Contents

S12 Session 12: Radiation detection technologies and radionuclide analytics – Oral presentations

S12-01 **State-of-the-art activity measurement and radionuclide metrology in radiation protection** 1818
Maringer, Franz Josef

S12-02 **Location and identification of radioactive materials on sea using airborne gamma-ray spectrometry** 1828
Nikkinen, Mika; Kettunen, Markku

S12-03 **Quantification of NaI(Tl) whole body counter spectra using the EGSNrc Monte Carlo System** 1833
Breustedt, Bastian; Eschner, Wolfgang

S12-04 **New opportunities of radiation portal monitors with plastic detectors** . . . 1843
Kagan, L.; Stavrov, A.

S12-05Y **Measurements and simulations of fission neutron spectra at the MEDAPP beam at FRM II and subsequent developments** 1850
Breitkreutz, Harald; Jungwirth, Michael; Schenk, Robert; Wagner, Franz M.; Petry, Winfried

S12-06Y **Feasibility study of a low cost wireless ionizing radiation sensor network** 1861
Kuipers, Tjerk; Franken, Yuri; van Doorn, Harry; Kemper, Ad; Koole, Iman

S12-07Y **Results of model calculations and algorithm development related to a 3D silicon detector dosimetric telescope** 1868
Hirn, Attila

S12-08Y **Sequential separation of alpha and beta emitters from natural samples by mixed solvent anion exchange and their subsequent determination** (ABSTRACT) 1878
Rozmaric Macefat, Martina

Contents

P12 Topic 12: Radiation detection technologies and radionuclide analytics – Poster presentations

P12-01 **Optically stimulated luminescence in salt tested against thermally stimulated luminescence in LiF and ambient survey measurements in a ^{137}Cs contaminated village in Belarus** 1879
Bernhardsson, Christian; Matskevich, Svetlana; Mattsson, Sören; Rääf Christopher

P12-02 **Visualization of hot particles in lung of radionuclide associated with emergency preparedness by means of clinical gamma cameras** 1887
Hansson, Mats; Rääf, Christopher

P12-03 **Whole-body counters for measurement of internal contamination in Finland** 1893
Huikari, Jussi; Pusa, Sauli; Muikku, Maarit

P12-04 **Determination of chest wall thickness of anthropometric voxel models** 1900
Hegenbart, Lars; Gün, Harun; Zankl, Maria

P12-05 **Measurements and Monte Carlo computation of the ^{241}Am counting efficiency pattern along the case #0102 USTUR leg phantom** (ABSTRACT) 1909
Broggio, D.; Capello, K.; Cardenas-Mendez, E.; El-Faramawy, N.; Franck, D.; James, A. C.; Kramer, G. H.; Lacerenza, G.; Lopez, M. A.; Lynch, T. P.; Navarro, J. F.; Navarro, T.; Perez, B.; Rhüm, W.; Weitzenegger, E.

P12-06 **Advanced Monitorin In Mixed Radiation Area – AMIRA** 1911
Bürkin, Walter; Dielmann, Rainer

P12-07 **Simple method to determine ^{234}U and ^{238}U in water using alpha spectrometry** 1916
Vesterbacka, Pia; Pöllänen, Roy

P12-08 **The progress in Minimizing Activity and Dose with Enhanced Image Quality by Radiopharmaceutical Administration (MADEIRA) project** (ABSTRACT) 1922
Hoeschen, Christoph; Mattsson, Sören; Cantone, Marie Claire; Mikuž, Marko; Lacasta, Carlos; Ebel, Gernot; Clinthorne, Neal; Giussani, Augusto

P12-09 **^{177g}Lu produced with high specific activity by deuteron irradiation for metabolic radiotherapy** (ABSTRACT) 1923
Bonardi, Mauro L.; Manenti, Simone; Groppi, Flavia; Gini, Luigi

P12-10 **High-grade radiochemical analyses act as a basis for good assessment in radiation protection** 1924
Vesterbacka, Pia; Vartti, Vesa-Pekka; Heikkinen, Tarja; Ikäheimonen, Tarja K.

P12-11 **Condition of liver, and iron and plutonium content** (ABSTRACT) 1933
Mussalo-Rauhamaa, Helena; Jaakkola, Timo; Miettinen, Jorma K.; Laiho, Kaino

P12-12 **^{240}Pu/^{239}Pu ratio in peat, lichen and air filter samples contaminated by global nuclear test fallout, the Chernobyl accident and other nuclear events** (ABSTRACT) 1934
Salminen, Susanna; Paatero, Jussi

P12-13 **Sensitivity of the standard and Fpg-modified comet assay for the estimation of DNA damage in peripheral blood lymphocytes after exposure to gamma rays** 1935
Garaj-Vrhovac, Vera; Gajski Goran; Miljanić Saveta

P12-14 **Gamma spectrometric sample measurements at STUK laboratories** 1943
Klemola, Seppo; Leppänen Ari-Pekka; Mattila Aleksi; Renvall Tommi

Contents

P12-15 **When is *in situ* gamma spectrometry motivated?** (ABSTRACT) 1950
Boson, Jonas; Nylén, Torbjörn; Ramebäck, Henrik

P12-16 **Review of modern application of gamma-beta spectrometer – radiometer MKGB-01 "RADEK"** 1951
Finkel, Felix

P12-17 **Radiation monitoring network with spectrometric capabilities: implementation of $LaBr_3$ spectrometers to the Finnish network** 1958
Mattila, Aleksi; Toivonen, Harri; Vesterbacka, Kaj; Leppänen, Mikko; Salmelin, Santtu; Pelikan, Andreas

P12-18 **Sample screening to locate active particles with position-sensitive alpha detector** 1967
Ihantola, Sakari; Outola, Iisa; Peräjärvi, Kari; Pöllänen, Roy; Toivonen, Harri; Turunen, Jani

P12-19 **Position-sensitive measurement system for non-destructive analysis** . . . 1974
Turunen, Jani; Ihantola, Sakari; Pelikan, Andreas; Peräjärvi, Kari; Pöllänen, Roy; Toivonen, Harri

P12-20 **Application of the MKGB-01 spectrometer-radiometer in the KX-gamma coincidences setup at the D. I. Mendeleyev Institute for Metrology** 1980
Moiseev, Nikolay; Tereshchenko, Evgeny

P12-21 **Comparison of two techniques for low-level tritium measurement – gas proportional and liquid scintillation counting** 1988
Barešić, Jadranka; Horvatinčić, Nada; Krajcar Bronić, Ines; Obelić, Bogomil

P12-22 **Multi-screen diffusion battery for radon progeny dispersion analysis** 1993
Zhukovsky, Michael; Bastrikov, Vladislav; Rogozina, Marina; Yarmoshenko, Ilya

P12-23 **Evaluating on-site monitoring cart conceptually developed for radiation workplace** 2000
Kawano, Takao; Nishimura, Kiyohiko

P12-24 **A new AMS system for actinides isotopic ratio measurements at CIRCE (Caserta, Italy)** 2006
Sabbarese, Carlo; Quinto, Francesca; De Cesare, Mario; Petraglia, Antonio; Terrasi, Filippo; D'Onofrio, Antonio; Roca, Vincenzo; Pugliese, Mariagabriella; Palumbo, Giancarlo; Alfieri, Severino; Esposito, Alfonso, Migliore, Gianluigi

P12-25 **Neural network method for activity measuring in environmental samples** 2014
Finkel Felix; Bystrov Eugeny

P12-26 **Whole body counting with large plastic scintillators as a tool in emergency preparedness – determination of total efficiency and energy resolution** 2023
Nilsson, Jenny; Isaksson, Mats

P12-27 **Examination of patients using the whole body gamma ray counter that is calibrated according to the individual anatomy properties** 2030
Yatsenko, V. N.; Borisov, N. M.; Korzinkin, M. B.

P12-28 **An extrapolation ionization chamber for α-ray detection and measurement** 2037
Bercea, Sorin; Cenusa, Constantin; Celarel, Aurelia; Sahagia, Maria; Stochioiu, Ana; Ivan, Constantin

State-of-the-art activity measurement and radionuclide metrology in radiation protection

Maringer, Franz Josef[1,2,3]
[1] BEV – Federal Office of Metrology and Surveying, Arltgasse 35, 1160 Wien, AUSTRIA
[2] BOKU – University of Natural Resources and Applied Live Science, LLC-Laboratory Arsenal, Faradaygasse 3, Arsenal 214, 1030 Wien, AUSTRIA
[3] TU – Technical University Vienna, Atomic Institute, Schüttelstraße 2, 1020 Wien, AUSTRIA
(franz-josef.maringer@bev.gv.at)

Abstract

Numerous issues in radiation protection require appropriate activity measurements. Although today many methods are established to assess radiation exposure to man by physical models and mathematical simulations, there is also a strong requirement in technologically adequate, fair accurate, traceable and reliable activity measurements techniques and radionuclide analytics.

To ensure effectively traceable measurement methods for all medically and technologically used radionuclides up to end-user applications, a network of primary and secondary national metrological activity standards are provided by national metrology institutes under the coordinative umbrella of the Bureau International des Poids et Mesures (BIPM) in Paris. The international progress of activity metrology and measurement is scientifically supported by the International Committee for Radionuclide Metrology (ICRM).

In this paper, an overview of state-of-the-art activity measurement methods for all categories of radiation protection is presented. Special focus is given on current developments in emerging medical application, radioecology, NORM and radon measurements, and uncertainty assessment. Recent improvements and practical implementation on the metrological quantification of radionuclide activity – from fundamental metrology to end-user applications – are covered. The scientific support of ICRM in the field of radionuclide metrology is illustrated. Eventually, international, European and national standards and scientific and technological co-operations and networks in radionuclide metrology and analytics are discussed with regard to upcoming necessities determined by recent ICRP recommendations and IAEA & EU Basic Safety Standard development.

Introduction

To step into radionuclide metrology and activity measurement, one has to consider a common understandable and mostly agreed definition of the quantity activity. A widely agreed common scientific definition can be found in IEC 60050:2003:

> Activity A: quotient, for an amount N of radionuclide in a particular energy state at a given time, of $\langle dN \rangle$ by dt, where $\langle dN \rangle$ is the expectation value of the number of spontaneous nuclear transitions from this energy state in the time interval of duration dt.

$$A = -\frac{\langle dN \rangle}{dt} = \lambda \cdot N \qquad (1)$$

where λ is the decay constant of the radionuclide.

This definition is amended by the simpler and more operational definition in ISO 921:1997, entry No 23:

> Activity *A:* number of spontaneous nuclear disintegrations occurring in a given quantity of material during a suitably small interval of time divided by that interval of time.

In any case the unit of the quantity activity is defined in the International System of Units SI (BIPM, 2006) to s^{-1} with the specific name *becquerel* (Bq).

In many applications of radiation protection measurements derived activity quantities like activity concentration or surface contamination with their specific units are established eg. $Bq \cdot kg^{-1}$, $Bq \cdot m^{-3}$, and $Bq \cdot m^{-2}$.

Metrological activity measurement methods

For metrological purpose adequate standardisation measurement methods for representing the unit *becquerel* for specific radionuclides are given in the *Generic grouping of nuclides* (CCRI(II), 2008). The state-of-the-art radiation detectors, measurement geometries, radiation types and counting modes, currently used for metrological radionuclide activity standardisation, are shown in Tab. 1 and Tab. 2. The international key comparisons for primary standard activity measurement is supported by the *International Reference System* SIR of the *Bureau International des Poids et Mesures* BIPM in Paris (SIR, 2010).

The currently achievable measurement uncertainties in activity primary standardisation methods depend on the applied method and the radionuclide of interest. The expanded relative uncertainties (coverage factor $k = 2$ according to JCGM, 2008) of state-of-the-art activity primary standardisation methods range from 0,4 % to 5,0 %.

The international coordination of primary standard activity measurement capabilities supports the calibration services for activity measurement instruments of national metrological institutes and designated laboratories. Radiation protection is only one of various applications of activity measurement (eg. nuclear medicine diagnostics, brachytherapie).

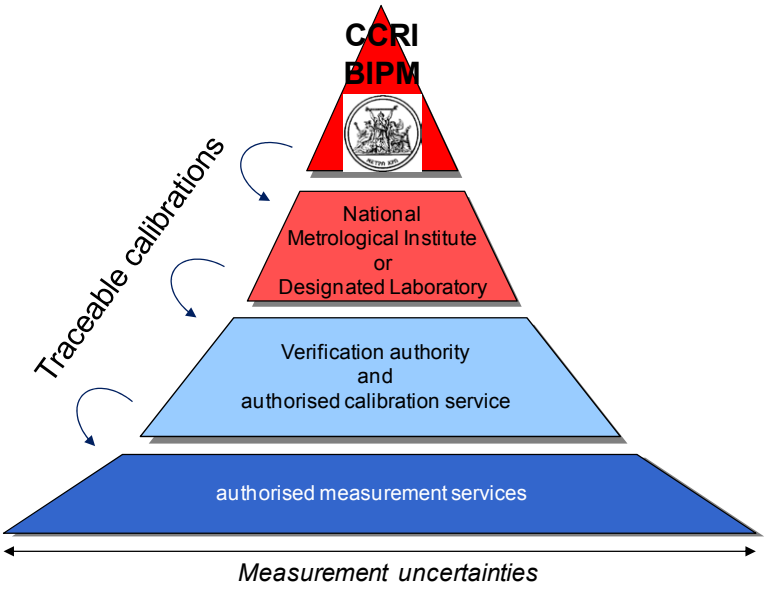

Figure 1. Traceability of measurements from CCRI - Consultative Committee for Ionising Radiation at BIPM - Bureau International des Poids et Mesures to authorised measurement services.

Comprehensive overviews on currently used methods for metrological radionuclide activity standardisation are given in Simpson & Judge (2007) and Pommé (2007).

Table 1. Radiation detectors and measurement geometries used in metrological activity standardisation measurement methods (source: Ratel, 2010).

Geometries	Radiation detectors
4π	Proportional counter
Defined solid angle	Pressurized proportional counter
2π	Liquid scintillation counting
Undefined solid angle	NaI(Tl)
	Ge(HP)
	Ge(Li)
	Si(Li)
	CsI(Tl)
	Ionization chamber
	Grid ionization chamber
	Bolometer
	Calorimeter
	PIPS detector

Table 2. Radiation types and counting modes used in metrological activity standardisation measurement methods (source: Ratel, 2010).

Radiation type	Counting mode
Positron	Efficiency tracing
Beta particle	Internal gas counting
Auger electron	CIEMAT/NIST
Conversion electron	Sum counting
Mixed electrons	Coincidence
Bremsstrahlung	Anti-coincidence
Gamma rays	Coincidence counting with efficiency tracing
X - rays	Anti-coincidence counting with efficiency tracing
Photons (x + γ)	Triple-to-double coincidence ratio counting
Photons + electrons	Selective sampling
Alpha - particle	High efficiency
Mixture of various radiations	Digital coincidence counting

The applicable primary standardisation measurement method depends on the decay scheme of the radionuclide of interest. In many cases high-geometry methods with solid angles of the sensitive detection volume around the radioactive source of almost 4π are chosen. For large-area sources 2π surface emission methods are used. Specific measurement methods used in high-geometry activity standardisation are 4π and 2π proportional counting including internal gas counting for gaseous samples, 4π gamma-ray counting, 4π beta + 4π gamma sum counting, 4π windowless sandwich spectrometer (CsI(Tl)) and liquid scintillation counting. Primary standardisation by LSC uses CIEMAT-NIST or triple-to double coincidence rate method. Some high-geometry methods are also high-efficiency methods. In this case, low and medium activity sources are suitable for satisfactory measurement uncertainties.

For alpha emitters defined solid angle methods taking into account the geometry factor $\Omega/4\pi$ are applicable. This method requires delicate sample preparation to avoid undefined self-absorption inside the source. The background rate for alpha detectors (PIPS) are comparable low around $1 \cdot 10^{-3}$ s^{-1}.

Coincidence counting is another applied method for activity primary standardisation. In this branch sum peak coincidence method, 4π beta-gamma coincidence and photon-photon coincidence counting has been implemented.

Examples for state-of-the art primary standardisation methods commonly used for metrological radionuclide activity determination are given in table 3. In this table the currently achievable expanded relative measurement uncertainties (coverage factor k = 2) are shown. These values are the metrological top level figures for traceable calibration of activity measurement instruments and methods.

Table 3. Examples of top-level primary standardisation methods for radionuclide metrology.

Geometry	Detector 1	Radiation 1	Detector 2	Radiation 2	Mode	Uncertainty range (*k*=2)
4π	liquid scintillation counter	beta particle or alpha particle or Auger electron or gamma ray or X-ray	---	---	CIEMAT/ NIST or triple-to-double coincidence ratio counting	0,4 to 3,5
4π	pressurised proportional counter	(beta particle or alpha particle) and gamma ray	---	---	high efficiency	1,0 to 4,0
4π	NaJ(Tl)	gamma ray	---	---	high efficiency	0,4 to 4,0
definded solid angle	PIPS detector	alpha particle	---	---	---	1,0 to 4,0
4π	proportional counter or pressurised proportional counter or liquid scintillation counter	beta particle or alpha particle	NaJ(Tl) or Ge(HP)	gamma ray	coincidence or anticoincidence	0,4 to 2,0

Activity measurement methods in operational radiation protection

Because radiation protection is mainly a health safety issue, activity measurements has to be carried out on a high quality level. This requirement leads to traceable calibration of activity measurement instruments. This means that any activity measurement done for radiation protection purposes have to been carried out by measurement instruments which are traceably calibrated at primary or secondary standards. In practice this technical claim is ensured by institutional authorisation or accreditation or verification of the used measurement instrument. The achievable measurement uncertainties of operational activity measurement methods are higher than metrological standardisation measurement methods due to uncertainty propagation in the calibration chain.

Different radiation protection branches (Tab. 4) require specific measurement methods.

Table 4. Radiation protection branches using activity measurement methods.

Radiation protection branches
Radiation protection of workers - operational RP
Individual monitoring – internal dosimetry
Environmental monitoring
NORM — Naturally occurring radioactive materials
Radon
Nuclear and radiological emergencies and incidents
Nuclear security and malevolent use of radioactive sources
Illicit trafficking
Radioactive waste management
Decommissioning of nuclear facilities
Education, training and research

In the following sections some general aspects of main relevant activity measurement method used in operational radiation protection are discussed.

Low-level gamma-ray spectrometry for environmental monitoring

Gamma-ray spectrometry for monitoring environmental material like water, air, soil, and food, is one of the most common radiometric method applied in radiation protection. Large volume high-purity germanium semiconductor detectors in special low-level shielding facilities support activity concentration measurement in different samples in the activity range from some mBq to some MBq, or expressed as activity concentration in the range from 10^{-5} to 10^{5} Bq·kg^{-1}.

Generally the Ge(HP) spectrometers are calibrated with standard reference activity sources and/or via Monte Carlo simulation methods. Depending on the efficiency of the detector / volume and geometry of the germanium crystal, sample volume and geometry, measuring time, and the decay scheme of the radionuclide of interest, achievable relative measurement uncertainties (k = 2) for this method are typically in the range of 4 % to 20 %. In most applications the achieved uncertainty fits the purpose because the measurement is done for environmental contamination assessment and not for individual monitoring.

One main problem of this method and restriction in measurement accuracy is the representative collection of samples. If enough measurement capacity is available, typically 15 to 30 samples of the monitored material are necessary to ensure similar uncertainty contributions as for the measurement itself.

Radon gas and radon progeny activity measurement

Dose exposition due to inhalation of radon progenies is of interest in radiation protection both at NORM workplaces and at home. Due to the simpler measurement of radon gas in many cases only radon gas activity measurements are legally regulated and carried out. To assess the lung and effective dose a mean equilibrium factor of typically 0,4 between radon gas and radon progenies indoor is applied. State-of-the-art

conventional radon gas and radon progeny detection systems are working in the activity range from some $Bq \cdot m^{-3}$ to some 10^5 $Bq \cdot m^{-3}$. Calibration of radon gas activity measurement instruments and radon detectors are done in radon chambers traceable to secondary or primary radon gas activity standards.

Again for these methods the representative collection of monitored air respectively the sampling position has large influence on the total uncertainty and individual dose determination. Whereas typical expanded relative uncertainties for measured Rn-222 activity concentrations in indoor air are in the range from 7 % to 20 %, the deviation between different sampling positions in the same room could be up to 30 % (eg. due to relative distance of the instrument / detector from fresh air and radon inflow ventilation flows inside the room). This fact leads to the necessity of careful detector / instrument positioning in the observed room.

Surface contamination activity measurement

This activity measurement method is widely used in all application branches of radionuclides eg. nuclear medicine, research laboratories or at NORM industrial workplaces. Purpose of this method is the safeguarding of radioactive contamination of workplaces to avoid unwanted exposition of staff members. Instruments for this purpose are hand-held and hand-foot-clothing monitors equipped with large-area proportional counters or plastic scintillation detectors.

Depending on the measured radionuclide, the covered activity-per-surface-area range goes from some 10^{-2} $Bq \cdot cm^{-2}$ to some 10^4 $Bq \cdot cm^{-2}$. Required expanded relative uncertainty vales ($k = 2$) are in the range from 15 % to 40 % depending on the specific application and the radionuclide of interest. In many countries these types of instruments are calibrated with large-area surface standard activity sources. In Austria the traceability of these instruments are assured via legal verification ('*Eichung*') each second year.

Liquid scintillation counting in radiation protection

For many radionuclides – especially such with very low beta particle energy emission like H-3 or C-14 and all type of alpha particle emitting radionuclides – liquid scintillation counting technology is a simply accomplishable and up-to-date activity measurement method. For example in activity concentrations of alpha emitters in water samples could be carried out with this method with satisfactory accuracy, linearity and reproducibility in the range from 10^{-5} $Bq \cdot kg^{-1}$ to 10^5 $Bq \cdot kg^{-1}$. For some radionuclides like uranium isotopes, radiochemical sample preparation is required before counting.

For simple activity measurement tasks like measuring the Rn-222 activity concentration in water, minimum expanded relative measurement uncertainties ($k = 2$) of 5 % could be achieved in very careful laboratory circumstances. In many cases the typical achievable range of the expanded relative uncertainty including sample preparation is from 10 % to 40%. Also these figures are useful for most applications in radiation protection like environmental and operational monitoring.

In Tab. 5 the currently most commonly used activity measurement detection systems and instruments are listed together with the available international IEC and ISO and European CENELEC (EN) standards. The Technical Committees for radiation

protection measurements instruments and methods are at IEC[1]: SC 45B 'Radiation Protection Instrumentation', at ISO[2]: TC 85/SC2 'Nuclear Energy / radiation protection' and at CENELEC[3]: TC 45B 'Radiation protection instrumentation'. In all these standards the application conditions and technical requirements of the specific instrument types are included. At CEN[4] no specific technical committee on ionising radiation protection measurement is established so far.

Table 5. Activity detection instruments for radiation protection applications.

Detector type	Traceability reference source	International & European standards
Portable *α, β, α/β* counter	Area source	EN 60325, (prEN 62363)
Hand, foot and clothing *β/γ* monitor	Area source	IEC 60325, IEC 61560, ISO 7503-1, 2, 3, EN 61098
Floor monitor	Area source	EN 60325, (prEN 62363)
Laundry monitor	Area source	IEC 61256
Well-type *γ* counter	Point source / volume source	IEC 61562, ISO 11929-1, 2
γ spectrometer	Point source / volume source	IEC 61563, IEC 61275, IEC 62002, ISO 11929-3
α spectrometer	Area source	
Liquid scintillation counter	Liquid source	
Whole body counter	Volume source	IEC 61582, EN 61582
Gate monitor	Area source	IEC 60325, IEC 61560, ISO 7503-1, 2, 3, EN 62022
Transit goods monitor	Area source	IEC 61098, IEC 61137, ISO 6980-1, 2, 3, ISO 8769-1, 2, (FprEN 62244)
β/γ water monitor	Liquid source	IEC 60861, IEC 61311, EN 60861
Noble gas monitor	Radioactive gas source	IEC 60761-3, IEC 61524, EN 60761-1, EN 60761-3
Tritium monitor	Liquid / gas source	IEC 60761-4, 5, 6, EN 60761-1, EN 60761-5
Iodine monitor	Gas source	IEC 60761-4, 5, 6, EN 60761-1, EN 60761-4
Dust monitor	Filter source	IEC 60761-1, 2, EN 60761-2
Radon monitor Passive radon detectors	Radon emanation source, radon chamber	IEC 61263, IEC 61577-1, 2, 3, IEC 61578

[1] www.iec.ch
[2] www.iso.org
[3] www.cenelec.eu
[4] www.cen.eu

The International Committee for Radionuclide Metrology - ICRM

The International Committee for Radionuclide Metrology[5] is an association of radionuclide metrology laboratories whose membership is composed of delegates of these laboratories together with other scientists actively engaged in the study and applications of radioactivity. It explicitly aims at being an international forum for the dissemination of information on techniques, applications and data in the field of radionuclide metrology and measurement.

The Bylaws were adopted at the General Meeting in Gaithersburg, Maryland (USA) in 1997. The ICRM as a formal organization grew from efficient contacts among radionuclide metrologists who participated in the First International Summer School on Radionuclide Metrology in Hercig Novi, Yugoslavia in summer 1972.

ICRM activities are largely the responsibility of its working groups. Each group is guided by a coordinator who acts as a net worker for ideas, joint projects and communications and may organize conferences and workshops. There are now six working groups in the following thematic fields:

- Radionuclide Metrology Techniques
- Life Sciences
- Alpha-Particle Spectrometry
- Gamma-Ray Spectrometry
- Liquid Scintillation Techniques
- Low-Level Measurement Techniques
- Non-Neutron Nuclear Data

The (biennially) recently held 17th International Conference on Radionuclide Metrology and its Applications," had been hold in Bratislava in September 2009[6]. The conference papers will be published shortly in *Applied Radiation and Isotopes*. The next conference will be hold in September / October 2011 in Tsukuba, Japan, organized by the National Metrology Institute of Japan, Advanced Industrial Science and Technology (NMIJ/AIST).

The recent conference of the Low-Level Measurement Techniques ICRM working group - the 5th International Conference on Radionuclide Metrology – Low-Level Radioactivity Measurement Techniques ICRM-LLRMT'08 - was held in Braunschweig, Germany, in September 2008 (Arnold, Jerome, Hult, 2009).

All ICRM conferences and workshops are announced on the ICRM homepage. The participation in ICRM conferences and workshops is open to all scientists and persons who are interested in the topics.

Conclusions and perspectives

The metrological basis of radionuclide activity measurement has been well developed on an international high quality level since the last five decades under the scientifical and technological umbrella of the *Bureau International des Poids et Mesures* BIPM in the frame of the Consultative Committee for Ionising Radiation CCRI(II). More than 60 metrological institutes and laboratories operate high-level primary and secondary

[5] http://physics.nist.gov/Divisions/Div846/ICRM/
[6] http://www.icrm2009.sk/

standards for metrological radionuclide activity measurement. The International Reference System SIR at the BIPM coordinates key comparisons for all radionuclides of interest in radiation protection. The international infrastructure in radionuclide metrology supports the high-quality activity measurement instrumentation in radiation protection. In most Europen countries the traceability of activity measurement instruments used in operational radiation protection is ensured by traceable calibration or verification. The increasing application of emerging radionuclides in medicine, industry and science generates permanent developments in activity measurement instrumentation. The necessary methodical developments are challenging tasks both for radionuclide metrologists and radiation protection experts. In Europe, the research and development network in metrology is scientifically and financially supported by the European Metrology Research Programme EMRP[7]. Within this co-ordinated research programme joint research projects in all branches of metrology and also in activity measurements are carried out to increase and ensure the necessary high-quality scientific and technological basis of radionuclide activity measurement instrumentation.

References

Arnold, D., Jerome, S., Hult, M. (eds.). 5th International Conference on Radionuclide Metrology – Low-Level Radioactivity Measurement Techniques ICRM-LLRMT'08. Appl. Rad. Isot. 67(5), 2009.

CCRI(II). Generic grouping of nuclides. KCWG(II), 2008. Comité consultatif des rayonnements ionisants. Bureau International des Poids et Mesures, Paris (www.bip.org/en/committees/cc/ccri/CCRIsection2/).

IEC 60050. International Electrotechnical Vocabulary, IEV No 393-14-12, IEC, 2003

ISO 921. Nuclear Energy – Vocabulary, ISO, 1997

JCGM. Evaluation of measurement data — Guide to the expression of uncertainty in measurement. JCGM 100 - GUM 1995 with minor corrections. Bureau International des Poids et Mesures, Paris. 2008.

Pommé, S. Methods for primary standardisation of activity. Metrologia 44(4), 2007, S17-S26.

Ratel, G. International Reference System for activity measurements of gamma-ray emitting nuclides (SIR). 38th circular letter, 2010. Bureau International des Poids et Mesures, Paris. 2010.

Simpson, B, Judge, S (edts.). Special issue: Radionuclide Metrology. Metrologia 44(4), 2007.

SIR. International Reference System. Bureau International des Poids et Mesures, Paris, 2010 (www.bipm.org/en/scientific/ionizing/radionuclides/sir/).

[7] http://www.emrponline.eu/

Location and identification of radioactive materials on sea using airborne gamma-ray spectrometry

Nikkinen, Mika[1]; Kettunen, Markku[2]
[1] Radiation and Nuclear Safety Authority, P.O. Box 14, 00881 Helsinki, FINLAND[a]
[2] Finnish Defence Forces Research Centre, P.O. Box 5, 34111 Lakiala, FINLAND

Abstract
Considering the nuclear security, one of the threats is that a nuclear device or radiological explosive device is transported to the harbour over the sea. A ship can carry rather large radiological device and if it is detonated close to densely populated areas or economically or strategically important locations the consequences may be severe. Possible source term can also be a marine nuclear reactor release or underwater detonation of nuclear weapon. In these cases the detection of source term is based on identification of fission and activation products that are spread and diluted to a large volume of sea water. The mapping is based on same methodology that is applied to the detection of radioactive fall-out on the ground. As the water masses are constantly moving, the radioactive materials are also changing the location and this requires constant monitoring activity for long period of time. As part of security measures, these scenarios can be exercised by using airborne gamma ray measurement devices on the sea. Measurement over sea is actually very sensitive method as the background from natural radiation is close to zero and the detection capability is significantly better over the sea than over the land. The experience gained through these exercises show that also high-speed jet plane can be used in the identification tasks as we need only few seconds measurement time over the source. The detection system and search logic are illustrated in the presentation.

Introduction
Typical problem in the mobile on-site gamma-ray measurement is to be able to track the radioactive source location with high efficiency and still be able to characterize the source by identifying and quantifying the radioactive substances and their activity. In fact, location, detection, identification and quantification are competing with each other; good location accuracy requires high measurement resolution (i.e. short measurement time for individual gamma-ray spectra) and this reduces the possibility to detect, identify and quantify the radioactive source. Multiple level measurement

[a] Currently at Preparatory Commission for Nuclear Test-Ban-Treaty Organization, Vienna International Centre, P.O. Box 1200, 1400 Vienna, AUSTRIA

strategy can be used to ensure the detection and location power together with good quantification and identification capability.

This type of measurement capability is needed in case a large radiation source or it's activity is released in the environment and there arises need to locate and assess the risks related on source strength and type. This kind of situation is possible for example due to:

- Release of radiation due to use or testing of nuclear weapon
- Accidental release of radiation from nuclear reactor, medical isotope production or other kind of facility handling radioactive materials.
- Release of radiation due to malevolent use of radiation
- Radiation due lost or forgotten radioactive source

This paper is presenting the results of an exercise that was performed by Finnish Defence Forces by using a mobile radiation source (Cs-137, 3 GBq) in a ship on the Baltic Sea. This exercise was set up to study the detection of mobile source and possible radioactive contamination in the water due to release of radioactive material. The measurements were performed using a jet-plane with both medium volume NaI detector (6x4") and HPGe detector (70% relative efficiency). Typical cruising speed was 370-400 km/h and altitude above the water was 100 meters. Each NaI spectrum was collected with 1 second integration time and HPGe spectra with 2 seconds integration time. This method was developed to ensure quick response measurement in case of nuclear or radiation emergency [1].

Results and discussion

In real time measurements, it is important to show the results immediately for the analyst performing the measurement. This requires that a graphical display with capability to visualize the radiation levels. A spectrogram display as shown in the figure 1 has to be able to show the energy and location of the source so that the operational staff can react on finding. This is the spectrogram of NaI detector. This feature has been built in the gamma spectrum analysis software UniSampo [2].

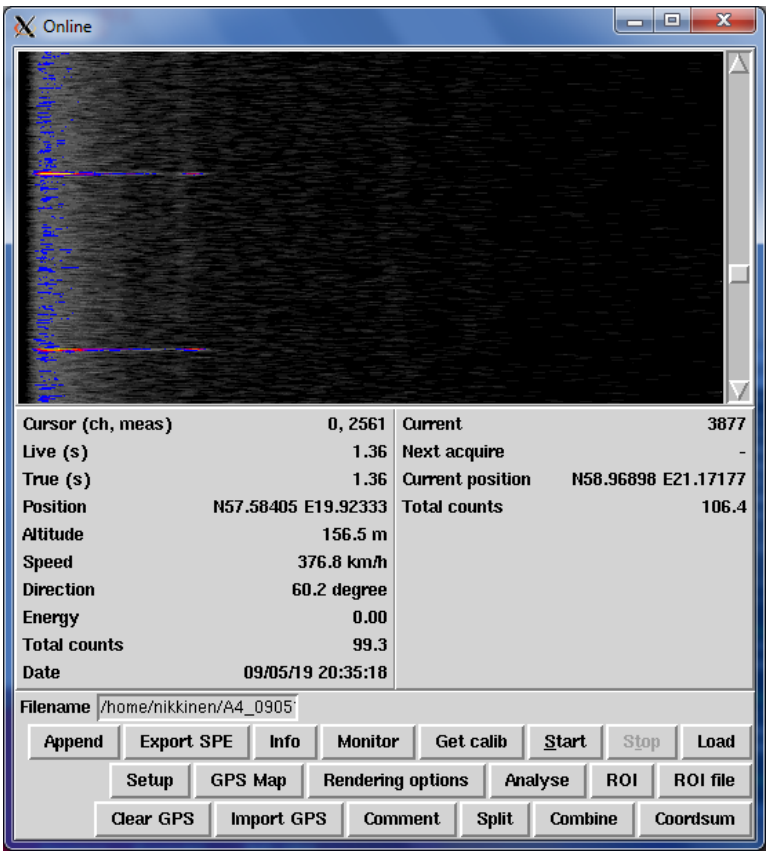

Fig. 1. Spectrogram display during the exercise (each horizontal pixel line represent one single spectrum, more intensive colour the pulses), high activity source is visible only in a few spectra. This view provides actual real-time detection and identification capability already during the flight.

Accurate post-processing is required to extract further information on source location and characteristics. It is possible also to lower the detection threshold using the post-processing. This is possible by combining the measurement points together and comparing the smoothed average with surrounding measurement points. In the measurements computer software GMLINT [3] has been used. The pulse rate of the background is used to calculate the critical limit in accordance with Currie [4]. As a result, it is possible to make a geographically referenced detection capability map as seen in figure 2 [5]. Possible source locations are highlighted in the processing window.

Number of corrections can be applied to the results:

- Distance between source and the detector (three dimensionally)
- Attenuation of the gamma rays in the air (gamma energy dependent)
- Attenuation of gamma rays in the body of the aircraft including angular response

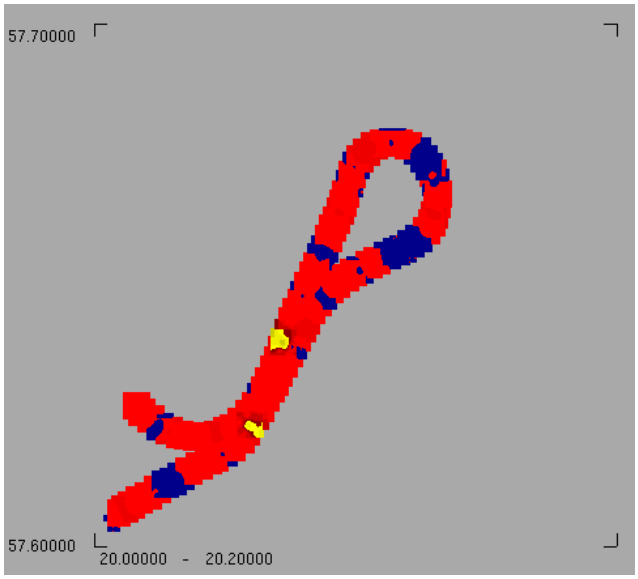

Fig. 2. Display of GMLINT software during the post-processing of data. Source location, uncertainty and critical limit can be displayed during the processing. This provides the end-user possibility to assess source locations and strengths. The yellow dot is showing the maximum source strength. As the ship was moving during the exercise the source was detected in two different locations.

More accurate information is available if HPGe detector information is combined with the analysis. In these kinds of measurements the background pulse-rate is relatively low and due to better energy resolution the pulses are concentrated on significantly more narrow energy window. As a result, the identification of the source is easier. Figure 3 shows one flight line and behaviour of pulse-rate for Cs-137 when by-passing the source during the exercise.

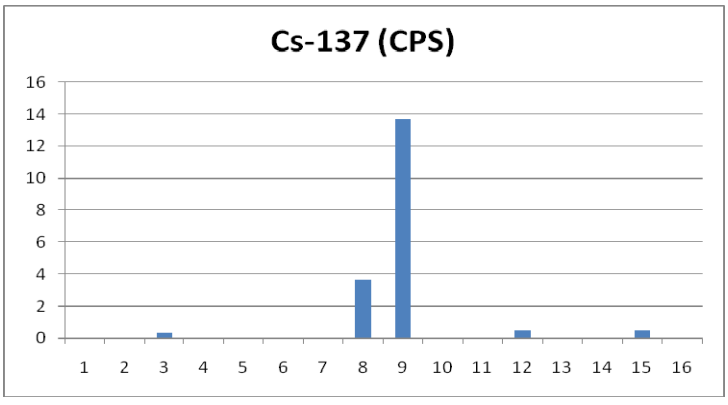

Fig. 3. Histogram display of HPGe detections, the maximum value is clearly detectable. Further analysis can be performed by calculating the weighted average to estimate the exact source location if when the gamma rays emitted are detected in more than one spectrum.

One additional question was where in the boat the source was located. As the size of the boat was rather large (218 meters long ship), it would be desirable to locate the source accurately during the over-flight. As the ship was moving, it was decided to bypass the ship by flying along the axis of the ship.

It is proposed to include also minimum and maximum source strength estimates to the automatic procedure. Maximum is the source strength if the measurement target is optimally located in the middle of integration time and the aircraft is flying exactly on the top of the source as shown in figure 4. Minimum would be if the source location maximum is in the end or beginning of integration time and the distance of the source is in the middle of measurement flight lines.

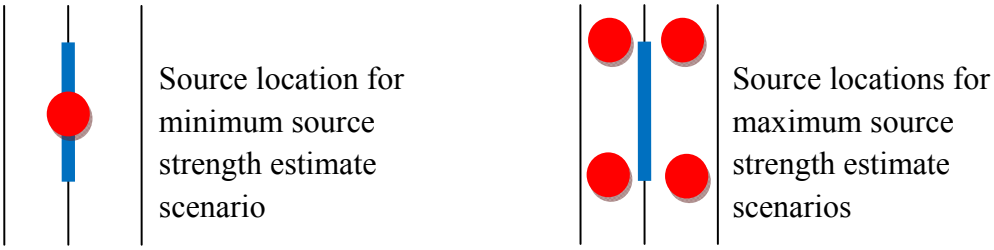

Fig. 4. Minimum and maximum estimates of the source strength. On the left side the source is right on the flight line (narrow line) and in the middle of integration line (thick line), this provides the minimum value for source strength. On the left side the possible source locations are in the end or begin of integration time and between the flight lines. This provides the maximum estimate for the source strength. All the source strength approximations should be between these two estimates.

Conclusions

As a conclusion the tools that are used for the radiation source detection and source location were working very well during the measurements. The flight team was able to locate the radioactive source carrying ship, to characterize the source type (open Cs-137 source) estimate the source activity. In this kind of measurement the uncertainties on source strength is large but the measurement team was able to give approximate source strength information in relatively good accuracy. It is also possible to calculate minimum and maximum source strength relative to source distance to the flight line.

References

1. Kettunen M, Nikkinen M. GammaJet - Fixed-wing gamma survey for the detection of radioactive materials. Finnish support to IAEA. STUK-YTO-TR 185. STUK, Helsinki 2002.
2. P.A. Aarnio, M.T. Nikkinen, J.T. Routti, “UniSAMPO, Comprehensive Software for Gamma-Spectrum Processing”, Journal of Radioanalytical and Nuclear Chemistry, 248 2 (2001) 371-375.
3. P.A. Aarnio, J.J. Ala-Heikkilä, T.T. Hakulinen, M.T. Nikkinen, “Gamma Spectrometric Monitoring of Environmental Radioactivity Using a Mobile Equipment.” Journal of Radioanalytical and Nuclear Chemistry, 233, 1-2 (1998) 217-223.
4. L.A. Currie, “Limits for Qualitative Detection and Quantitative Determination.” Analytical Chemistry, 40 (1968) 586.
5. M. J. Kettunen, M.T. Nikkinen, “Fixed-wing gamma measurement for the detection of radioactive materials”, Journal of Radioanalytical and Nuclear Chemistry, 263, 1 (2005) 241-243.

Quantification of NaI(Tl) whole body counter spectra using the EGSNrc Monte Carlo System

Breustedt, Bastian[1]; Eschner, Wolfgang[2]

[1] Institute for Radiation Research, Karlsruhe Institute of Technology, D-76021 Karlsruhe, GERMANY

[2] Department of Nuclear Medicine, University Hospital of Cologne, D-50924 Köln, GERMANY

(contact: bastian.breustedt@kit.edu)

Abstract

A generic EGSNRc-Monte Carlo model was developed for a whole body counter (WBC) with four NaI(Tl) detectors in a stretcher geometry - which is the setup both at Karlsruhe Institute of Technology (KIT) and at University Hospital of Cologne (UKK) – and the bottle phantoms previously used for their calibration. The main purpose of this work was to determine whether numerical calibrations can replace the ones based on measured spectra of known activity concentrations. Methods: Three main methods were developed and applied for the evaluation of measured spectra:

a) Simulation of nuclide decay and evaluation of total gross counts in a nuclide-specific region-of-interest (ROI), including the contribution of scattered photons
b) Simulation of nuclide decay and using these calibration spectra for a "full spectrum fit" to measured ones
c) Simulations of artificial "single energy" decays and deriving efficiency factors from a set of such simulations.

All methods were able to successfully replace the measured calibration spectra as proven at both institutions in a number of intercomparison exercises. A full set of "single energy" simulations offers a quick and flexible way to calculate efficiency factors for any nuclide without the need for further simulations or measurements. Moreover, Monte Carlo simulations offer the possibility to study the response of the counting system without the need of handling radioactive materials or relying on the properties of a real nuclide.

Introduction

Gamma spectrometry in whole body counters is used to detect and quantify radionuclides in man. This can be done as routine measure of incorporation monitoring or as means to assess doses after incidents. Further uses of whole body counting are measurements of the retention of pharmaceuticals labelled with radionuclides for medical diagnosis (ICRU 2003). All nuclides emitting gamma rays of sufficiently high energies (>100keV) with a significant emission probability (>3%) can be measured by in-vivo counting. Examples are fission or activation products such as ^{133}Ba, ^{137}Cs and

^{60}Co which are used in many nuclear applications or ^{99m}Tc, ^{201}Tl and ^{131}I from the field of nuclear medicine as well as naturally occurring ^{40}K.

Whole Body counters use an array of detectors placed around the person to be measured inside a shielding chamber. The person to be measured can either stand in front of the detectors, sit on a chair or lay on a bed. During the measurement the detectors may stay fixed or move around/along the patient (scanning mode). Detectors used for in-vivo counting are either scintillators such as NaI(Tl) or CsI(Tl) or semiconductor detectors like high purity germanium crystals (ICRU 2003). The activities of the identified nuclides can be calculated from the count rates in defined regions of the measured spectrum (ROI) using efficiency factors. The latter are classically determined from measurements of known activities in physical phantoms representing the human body. The phantoms used need to represent the properties of human body regarding scattering and absorption of radiation (ICRU 2003). Typically bottle phantoms filled with radionuclides diluted in water (e.g. BOMAB) or brick phantoms (e.g. IGOR) are used for calibration of whole body counters. Alternatively Monte-Carlo Methods can be used to simulate radiation transport during the measurement process. Such simulations can then be used to derive the efficiency factors. A Monte Carlo Code using the EGSNrc system (Kawrakow and Rogers 2000) was developed and applied to both installations. Several methods for the evaluation of simulated and measured calibration spectra have been tested and applied to both set ups. The results of this study will be presented in this paper.

Material and methods

The whole-body counters at Cologne-UKK and Karlsruhe-KIT

Both institutions, Karlsruhe Institute of Technology (KIT) and University Hospital of Cologne (UKK), operate whole body counters with a similar set up, referred to as “stretcher geometry”. The person lays on a bed which is surrounded by four fixed NaI(Tl)-scintillation crystals facing the person. Figure 1 shows the KIT whole body counter during the measurement of a bottle phantom. The nuclides are identified and their activity is determined from the sum of the four spectra of the measurement. The position of the detectors is optimized such that the count rates in the sum of the four spectra are as independent from the distribution of the source inside the person measured as possible. Properties of the two installations are summarized in table 1.

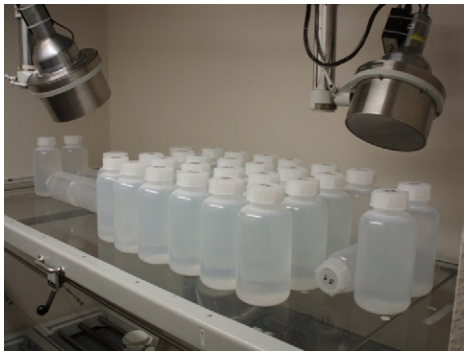

Fig. 1. The KIT whole body counter. A bottle phantom representing a 70kg person is placed on the bed. Only the upper two detectors can be seen in this figure.

Table 1. Properties of the two whole body counters used in this study.

	KIT	UKK
Chamber shielding	15/25cm Steel + 1.5mm Lead	16cm Steel + 3mm Lead
Detectors Postions Orientation	20.3 x 10.2 cm (8 x 4"), Fa. Bicron 2 above, 2 below the bed tilted around person's body axis	12.7 x 10.2 cm (5x4"), Fa. Scionix 2 above, 2 below the bed Parallell to bed
Channels in spectrum	256	1024
Energy Range	0 – 2500keV	0- 2000keV
Routine Counting Time	300 s	450 s

The Bottle Phantoms

The bottle phantom consists of a set of 2-1 and 1-l water-filled Cautex bottles in which a known amount of the radionuclide is diluted. A number of human shape geometries ranging from 10 kg/70 cm to 100 kg/190 cm can be arranged with different numbers of bricks/bottles. The concentration of the radionuclide in each bottle/brick was the same, thus a homogenous distribution of the nuclide within the body is assumed. In man, this is found only for some nuclides, e.g. ^{40}K or isotopes of cesium.

The EGSNrc usercode "Flaschenphantom"

A usercode for the EGSNrc Monte Carlo system has been developed (Breustedt and Eschner 2010). The EGNSrc system consists of several FORTRAN subroutines (called egscode) that provide the mechanisms for the radiation transport calculation. The geometry of the problem to be simulated and the tallying (extraction of information) has to be programmed by the user and is then coupled with the egscode by a defined set of subroutines (Kawrakow and Rogers 2000). The usercode "Flaschenphantom" provides the general geometry of the whole body counter chamber, the bed and the four detectors. A set of "bottles" (simulated as columns of water, without the bottles themselves) can be placed at the stretcher. All information needed by the usercode can be specified via a plain-text input file. Thus the code is flexible and can easily be adapted to other whole-body counters of the stretcher type. A set of input files describing the series of bottle phantoms (10kg -100kg) in the UKK and KIT set ups (including information on detector resolution and spectrum output) has been developed. Via the inputfile the user has to enter the geometry to be simulated, the nuclide which is assumed to be homogenously distributed in the bottles and the number of decays to be simulated. For some nuclides all information required (photon energies and emission probability, normalized beta spectrum if available) has been collected in text files, which can be addressed by the user. In order to study the response of the whole body counters as a function of photon energy, some artificial "one line" nuclides with a hundred percent emission probability were defined. After finishing the simulations the code will provide 5 output files (plain text format) which contain the spectra of the four detectors and the sum of the four spectra. Other information about the simulation is provided in a separate plain text file. All spectra are normalized to counts per decay simulated. This unit is equivalent to counts per second per Becquerel to which measured spectra can be normalized. The resolution of the detectors is taken into

account by a convolution of the simulated energy spectra with a Gaussian kernel of width according to photon energy. The parameters required for this Gaussian broadening can be determined from an observed FWHM vs. energy relation. Thus a direct comparison of measured and simulated spectra is possible, if the widths of the channels in the simulated spectra are chosen accordingly.

Methods for Evaluation of spectra

Three methods to assess the activities from the spectra have been applied ins this study. For each of the nuclides observed in the spectrum a dedicated region of interest ROI (usually centred around the full energy peak of the main emission line) was defined. Generally the count rate in the spectrum (or the parts thereof, ROI) is dependent on the activity of the nuclide measured. The proportionality factor eff(ROI ← nuclide) is called efficiency.

$$Cps\ in\ ROI = eff\,(ROI \leftarrow nuclide) \cdot Acitivity$$

The classical approach in gamma spectrometry takes only the full energy counts into account by using the net peak area which is determined by subtracting a scatter background below the peak. In in-vivo counting applications the spectra measured have very low count rates. This imposes problems on the determination of the scatter background below the peak. We tried to avoid these by using all counts in a given ROI for the determination of the activity. The scatter contribution to this gross count rate is taken into account by calculating efficiency factors of the form $eff(ROI_i \leftarrow nuclide_j)$ which then describe the probability of observing a count in the ROI for nuclide i after one decay of nuclide j. For each pair of nuclide and ROI this factor needs to be determined from calibration spectra which contain only counts of this nuclide. This requires a calibration measurement or simulation for each nuclide to be assessed. For whole body counting only a few nuclides are expected thus the overall effort to calibrate the counter still remains feasible. If more than one nuclide is present the efficiency becomes a matrix and the vector of activities A_j can be calculated from the observed vector of count rates C_i in the ROIs by inverting this matrix.

$$\begin{pmatrix} Bq\ nuclide\,1 \\ \vdots \\ Bq\ nuclide\,n \end{pmatrix} = \begin{pmatrix} eff\,(ROI\,1 \leftarrow nuclide\,1) & \cdots & eff\,(ROI\,1 \leftarrow nuclide\,n) \\ \vdots & \ddots & \vdots \\ eff\,(ROI\,n \leftarrow nuclide\,1) & \cdots & eff\,(ROI\,n \leftarrow nuclide\,n) \end{pmatrix}^{-1} \cdot \begin{pmatrix} cps\ inROI\,1 \\ \vdots \\ cps\ inROI\,n \end{pmatrix}$$

A shortfall of this matrix approach is that the assessed activities become dependent on each other due to the system of linear equations used to determine the activities. Nevertheless we used two methods for the Monte Carlo determination the elements of the efficiency matrix. One method (later referred to as “direct simulation”) is a complete simulation of the nuclide decay. The elements $eff(ROI_i \leftarrow nuclide_j)$ can then be calculated straightforward by integrating the simulated spectrum in the given ROI i. The second method (later referred to as “reference simulation” is based on simulations of artificial nuclides which emit only one energy with a 100 % probability per decay. Such nuclides were defined for 20, 40, . . . 1980 keV, 2000 keV. An example

for the derivation of efficiency factors eff($ROI_i \leftarrow nuclide_j$) for real nuclides from the set of "reference simulations" is given in the results section.

A second approach for the determination of activities from the measured spectra (later referred to as "fitting method") is also based on calibration spectra obtained with one nuclide at a time. Here the whole range of the spectrum, normalised to cps/Bq, is used to determine the activity. A weighted sum of the calibration spectra for the nuclides identified is built. A least squares fit to the measured spectrum (normalized to cps) is used to determine the weighting factors A_i which then are the activities. A prerequisite for the fitting of reference spectra to the measured spectrum is that all use the same energy calibration. This is ensured by the quality assurance procedures used in both labs, e.g. in the daily QA at KIT a point source is measured and the amplification factors are adjusted to fit the measured peaks in defined channels. Deviations between the different geometries are apparent in the scatter part of the spectrum at low energies. Thus it is useful to introduce a lower energy limit for the optimisation. We usually use only counts above 100 keV in the fitting procedure. In this method the assessed activities are also dependent on each other due to the common fitting.

Results

Several simulations in different geometries and for different nuclides were run. The photons were followed down to 1 keV, electrons down to 10 keV in these simulations. Usually 10 million decays were simulated, providing reasonably good counting statistics in the spectra. Depending on the nuclides' decay schemes the simulation runs took only a few hours on a modern computer. Simulated and measured spectra are in a good agreement. The direct comparison of the simulation and measurement of a 70 kg bottle phantom filled with ^{131}I in the UKK counter is shown in figure 2.

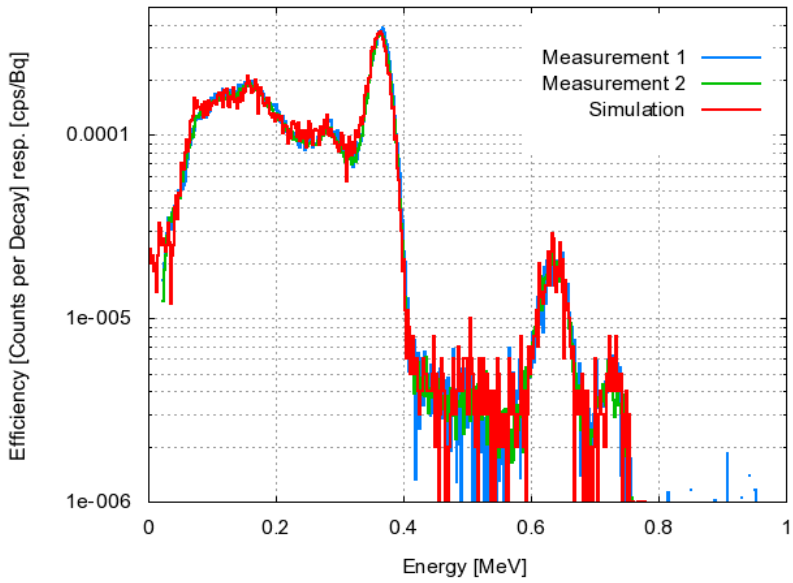

Fig. 2. Comparison of measured (blue, green) and simulated (red) spectrum of a 70 kg phantom filled with ^{131}I in the UKK whole body counter.

The only nuclide, where we observe deviations of measured and simulated spectra is ^{40}K. Here the spectra are in a good agreement above 250keV, below this energy the simulations underpredict the count rate in the spectra. The same effect could also be observed with another simulation code, MCNP5 (Brown 2002). Investigations on the reasons for these deviations are still in progress. Interestingly simulations with electron emissions only showed that the shape of the missing counts is that of a "Bremsstrahlung" spectrum for the electrons emitted by ^{40}K. If the electron emission in the simulations is artificially enhanced by a factor1 of ~4.4, the simulated 40K spectra are in good agreement with the measured ones (Breustedt and Eschner 2010).

Efficiency factors eff(ROIi ← nuclidej) were calculated in the different geometries (10 kg – 100 kg) for several combinations of ROI and nuclides. The efficiency factors determined by the two methods "direct simulation" and "reference simulation" are in a good agreement with each other and with the ones derived from a series of measurements. For calculating the efficiency(ROI_k ← nuclide) from the set of "reference simulations" all of the simulated spectra are integrated in the same ROI and the results are assigned to the simulated energy. These values eff(ROI_k ← E_γ) give the probability to observe one count in the ROI_k after the emission of one photon of E_γ in the phantom. An example of the resulting curve of 'efficiency in $ROI_{I\text{-}131}$ vs. emitted energy' is shown in Figure 3. $ROI_{I\text{-}131}$ is chosen from 316 – 411 keV centered around the ^{131}I line at 364 keV. The curves have a characteristic shape. For emitted energies below the ROI boundary, the efficiency values are zero. For emitted energies within the ROI high efficiency values are observed due to the photopeak being in the ROI. For higher energies only scatter events, which give lower efficiencies, are observed in the ROI.

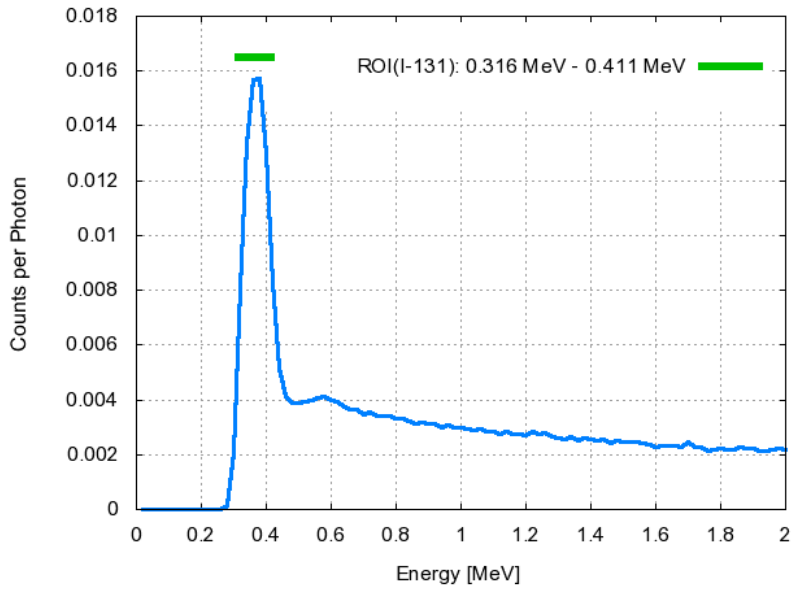

Fig. 3. Efficiency vs. energy curves (KIT counter) for ROI $_{I\text{-}131}$ centred around the peak at 364 keV. Here the ROI remains fixed and the efficiency for registering counts in this region of the spectrum after emission of a photon of a given energy is shown.

[1] Interestingly this factor is the same for both Monte Carlo systems EGSNrc and MCNP5.

Table 2. Calculation of efficiency from "Reference Simulations". Here the calculation of eff(ROI_{I-131} ← ^{58}Co), which gives the probability to observe one Count in ROI_{I-131} (from 316 – 411 keV) after the decay of one ^{58}Co nucleus in the phantom.

Energy [keV]	Emission Probability [%]	eff(ROI_{I-131} ← E_γ) [Counts per Photon]	contribution to eff(ROI_{I-131} ← ^{58}Co)
511	29,80	0.003876	0.001155
811	00,69	0.003329	0.003296
863	99,00	0.003131	0.000022
1674	00,52	0.002265	0.000012
		eff(ROI_{I-131} ← ^{58}Co) = 0.004485 **[cps/Bq]**	

Using the decay data of a nuclide the efficiency for the contribution of this nuclide to the count rate in a chosen ROI can then be calculated from such 'efficiency in ROI vs. emitted energy' curves. For each photon emitted by the nuclide its contribution to the efficiency is taken from the curve and summed up, weighted by the emission probabilities of the photons. The calculation of the nuclide specific efficiency factors from the curve shown in Figure 3 is shown in Table 2. Here eff(ROII-131 ← 58Co), which gives the probability to observe one count in ROII-131 (which again is centred around 364 keV, the main emission line of 131I) after one decay of an 58Co nucleus is calculated. Once a set of "reference simulations" is available for a given geometry, this method can be applied to derive efficiency factors for every nuclide. A contribution of Bremsstrahlung generated by emitted electrons is not taken into account. This may for some nuclides (e.g. 40K) lead to deviations. Nevertheless the efficiency factors eff(m, ROI ← nuclide) calculated with this method are consistent with the ones derived from direct simulations of the nuclide decay or from real measurements as can be seen in figure 3 which shows as example an plot of the "efficiency vs. mass" curve for 18F in the ROI which is centred around its main emission line at 511 keV. The mass dependency was parameterized by fitting a function of the type

$$eff(m, ROI \leftarrow nuclide) = a + b \cdot m^{-1} + c \cdot m$$

with free parameters a, b and c.

In the fitting procedure the main problem in the application of the simulated spectra was the underestimation of Bremsstrahlung counts in the spectrum of 40K. Thus the lower threshold needed to be raised as high as 250 keV in order to achieve good results for simulated spectra. If the 40K spectrum was replaced by a measured one, the lower threshold could by set down to 80 keV without any problems. Nevertheless the activities calculated by the application of simulated and measured spectra in the fitting method are in good agreement. The results were comparable to the ones calculated via ROI techniques.

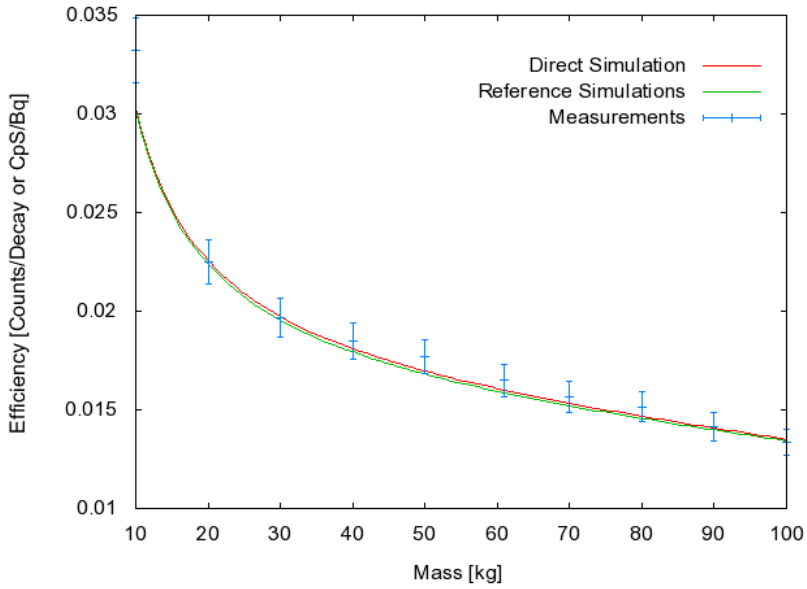

Fig. 4. Efficiency vs. mass curves for measurement of ^{18}F in a ROI centered around 511 keV. The lines show fits to efficiencies calculated from simulations (red: direct simulations; green: sets of reference simulations). Points show efficiencies derived from measured spectra.

Application example: Spectra from Intercomparison Exercises

Intercomparison exercises are one tool for quality assurance of in vivo measurement systems. The three methods described above were applied for the quantification of spectra during several intercomparison exercises. In these exercises, which are offered each year by the German federal office for radiation protection (Bundesamt für Strahlenschutz, BfS) (König et al. 2004), a brick phantom filled with activity (unknown to the participants) is measured by each participating institution. UKK and KIT participated regularly in the exercises of the last 10 years, which used the nuclides ^{133}Ba, ^{137}Cs, ^{60}Co and ^{40}K. All of the methods were able to quantify the reference activities within ±15%. As one example, the results for the KIT counter in the recent 2009 exercise are shown in table 3.

Table 3. Results of the 2009 intercomparison exercise at KIT. The activities calculated with the three approaches and the reference values provided by BfS are shown. The deviation from the reference values is given in brackets.

Nuclide	Reference Value [Bq]	Assessed Activity [Bq]		
		Direct Simulations of nuclide decay		Reference Simulations
		Fitting Method	ROI Method	ROI Method
K-40	2807	2605 (-7%)	2596 (-8%)	2631 (-6%)
Co-60	1176	1098 (-7%)	1045 (-11%)	1056 (-10%)
Cs-137	4332	3910 (-10%)	3895 (-10%)	3881 (-10%)
Ba-133	2564	2711 (+6%)	2403 (-6%)	2176 (-15%)

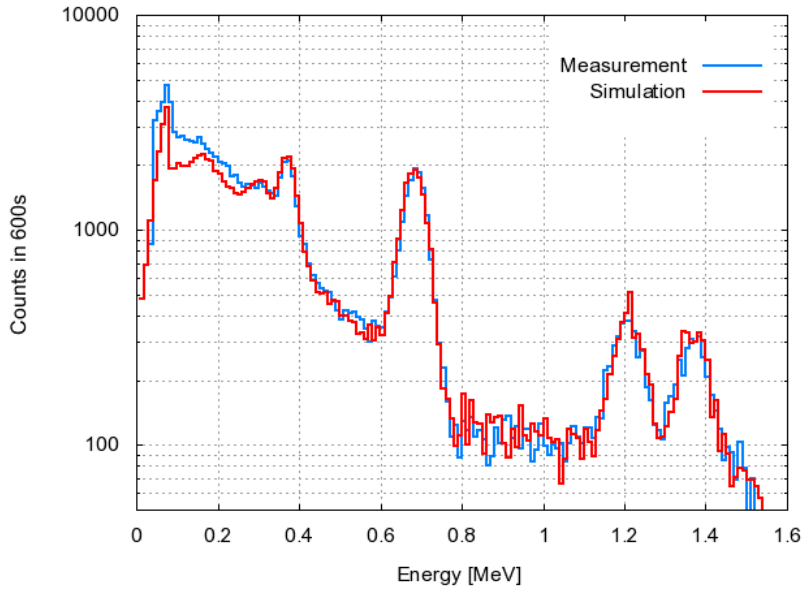

Fig. 5. Application of "fitting method" to spectrum of intercomparison exercise 2003 at KIT. The deviations below 250keV are due to Bremsstrahlung which is underestimated in the simulations. For the nuclide ^{40}K approximately half of the counts below 250 keV are due to Bremsstahlung.

Discussion and conclusions

None of the three methods we applied uses any algorithm to determine net peak areas. Only the gross counts in a Region of Interest need to be determined by an easy sum of counts in the according channels. This is an advantage especially in low count rate spectra as encountered in whole body applications, where net peak area algorithms may be hard to apply. The activities calculated are dependent on the other ones derived from the same measurement. This clearly is an disadvantage of the three methods and may lead to misinterpretations of the spectra. However, a large disagreement with activities derived from net peak areas algorithms has not been observed by us.

All Monte Carlo based methods were able to successfully replace the measured calibration spectra as proven at both institutions in a number of intercomparison exercises. The Monte Carlo Simulations offer the possibility to calibrate a whole body counter without the need of measuring activities. Thus single-nuclide spectra for the fitting method or the determination for efficiencies eff(ROI ← nuclide) become available for any nuclide needed. One problem observed by us is the improper simulation of Bremsstrahlung resulting from emitted electrons, which leads to an underestimation of low energy (< 250 keV) counts in the simulated spectra. This is observed for the nuclide ^{40}K which is always present in whole body counting. Studies to resolve this problem are currently done at KIT.

A full set of "single energy" simulations offers a quick and flexible way to calculate efficiency factors for any nuclide without the need for further simulations or measurements. Moreover, Monte Carlo simulations offer the possibility to study and evaluate the response of the counting system without the need of handling radioactive materials or relying on the properties of a real nuclide. A full calibration of the in-vivo counting system for using one of the three methods presented here may require a large

amount of calibration spectra. But using Monte Carlo Simulations these spectra can be calculated without large effort in a rather short time.

References

Breustedt, B. and Eschner, W. Monte Carlo Calibration of whole body counters with NaI(Tl) detectors in stretcher geometry. Radiation Protection Dosimetry 2010; Advance Access, doi:10.1093/rpd/ncp296

Brown FB, et al.. MCNP Version 5. Trans. Am. Nucl. Soc., 87:273, (2002).

International Commission on Radiation Units and Measurements (ICRU). Direct determination of the body content of radionuclides. ICRU Report 69 2003. Kent: Nuclear Technology Publishing.

Kawrakow, I. and Rogers, D. W. O. The EGSnrc Code System: Monte Carlo simulation of electron and photon transport. National Research Council of Canada Report NRCC-PIRS-0701 2000.

König, K., Buchholz, W., Dalheimer, A. and Hartmann, M. Ergebnisse der Ringversuche der Leitstelle Inkorporationsüberwachung des BfS [in German]. Strahlenschutz Praxis 2004(10): 22-24.

New opportunities of radiation portal monitors with plastic detectors

Kagan, L.; Stavrov, A.
TSA Systems, Ltd., Longmont, Colorado, USA

I. Introduction

The prevention of unauthorized transportation of nuclear and radioactive materials through borders of the states demands the creation of a high quality system of the radiation control. As it is shown by the international experience, radiation portal monitors intended for the first stage of the control, i.e. the detection of a radioactive source in an object which crosses a control zone, create the basis of such a system. In highly sensitive gamma-neutron radiation monitors, the detection of gamma sources is provided by plastic detectors. Despite of a rather low cost of such detectors, the creation of systems of the border (customs) radiation control is rather expensive as the total number of radiation monitors is very high. It is enough to mention the Sheremetjevo-2 airport in Moscow and the Rotterdam sea port [1, 2].

A tendency has recently appeared to use the monitors based on essentially new detectors, providing not only detection of sources, but also their identification (the so-called spectroscopic radiation portal monitors). However, these are so expensive that can hardly replace traditional monitors with plastic detectors. So, it is very important to search for ways to increase their efficiency.

In the present paper the authors consider a possibility to increase the efficiency of traditional monitors with the use of additional lead collimators installed on both sides of each plastic detector.

The purpose of this research was not the elaboration of certain design recommendations of radiation portal monitors, but the analysis of the general relationships of the collimator influence on the basic monitor characteristics.

II. Results and discussion

II.1. Decrease of the measured natural gamma background

As known, radiation portal monitors with plastic detectors for gamma source detection use the traditional algorithm connecting a threshold of detection (minimum detectable signal **S**) with the background value **B**

$$S = B + n \cdot \mathrm{sqrt}(B), \qquad (1)$$

where: **B** is value of the measured background;

sqrt (B) is the root-mean-square deviation of the background (so-called "sigma"),
n is the set number of "sigma" which defines both the false alarm rate, and the minimum detectable signal.

From the equation (1) it is clear, that a decrease of the background value measured by the given monitor should lead to a decrease of the minimum detectable signal other things being equal.

One of quite obvious technical decisions leading to a decrease of the measured gamma background is the use of a collimator installed on each plastic detector of the portal monitor. We have examined two versions of the lead collimator installation on the detector: collimator is perpendicular to the detector surface, and collimator is declined from the vertical by some angle (Fig. 1).

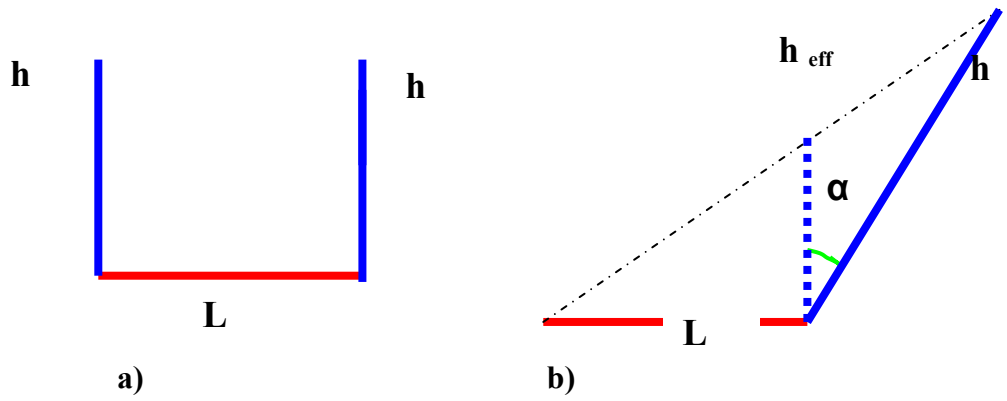

Fig. 1. Versions of collimator installation on the detector (top view):
a) collimator of the length h is perpendicular to the detector (L is the detector width);
b) collimator of the length h is declined from the vertical by an angle α (h_{eff} is the effective length of collimator).

Experiments were carried out with a VM-250AG vehicle portal monitor [3]. A distance between pillars was 6 m, collimators were installed on all four plastic detectors, width of the detector was 152 mm, and collimator thickness was 10 mm.

As a result of simple geometrical considerations it is possible to obtain the following dependence:

$$B/B_0 = 1 - [\text{arctg}\,(K \cdot h/L)]\,/90 \qquad (2)$$

where: B_0 is the natural background value without collimators;
B is the natural background value with collimators;
h is the collimator length, L is the detector width;
K is the numerical coefficient; its value can be found by calculations and experiments.

The equation (2) describes a version when the collimator is perpendicular to the detector surface (Fig. 1a). When the collimator is declined by an angle **α** from the

vertical (Fig. 1b), it is necessary to use its effective length $\mathbf{h_{eff}}$ instead of the actual collimator length **h** :

$$h_{eff} = (L \cdot h \cdot \cos \alpha)/(l + h \cdot \sin \alpha) \qquad (3)$$

Fig. 2 presents the calculated (by the equation (2)) and experimental data of relative background values when collimators of different lengths are installed perpendicular to the detector surface. As seen, the use of the collimator does significantly reduce the background value and, therefore, should result in a decrease of the minimum detectable activity (mass) of a radioactive source.

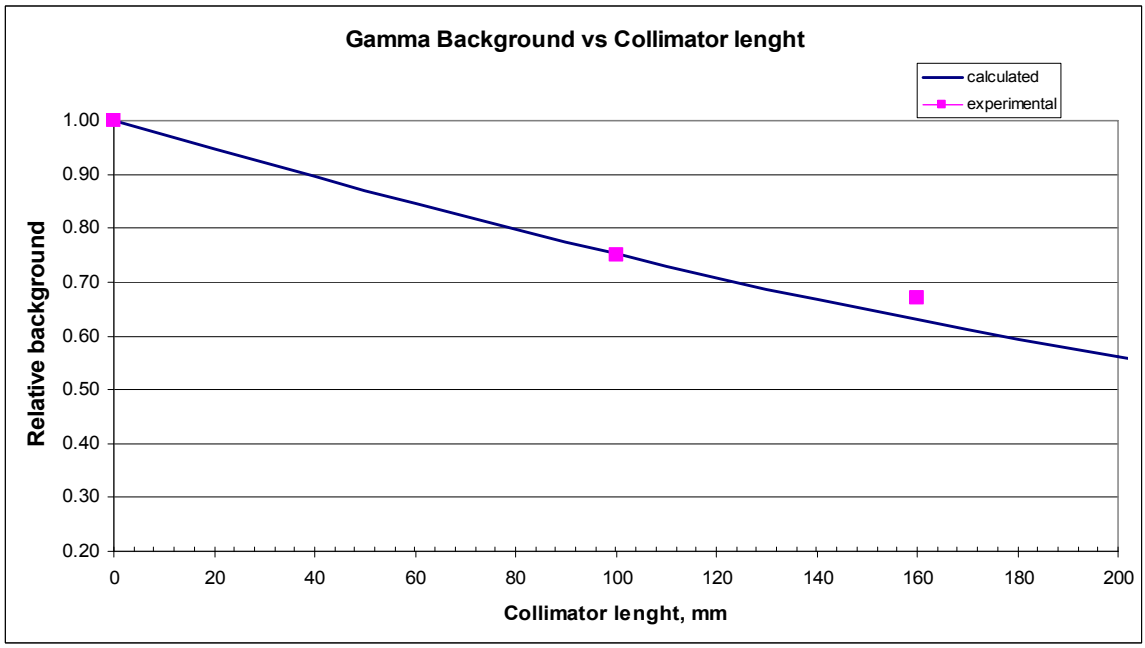

Fig. 2. Dependence of relative gamma background on collimator length (L=152 mm, K=0.625).

As known, when a vehicle is moving through the radiation portal monitor, the so-called "background suppression" effect, i.e. a decrease of recorded gamma background is observed. This effect is the cause of the fact that strong enough gamma sources which the monitor should detect easily become "invisible" [4]. Thus, a decrease of this effect also should promote the detection of weaker sources.

We have experimentally investigated the collimator influence on the "background suppression" effect by placing a truck between pillars of the portal monitor and measuring the gamma background values (Table 1). As seen from the data presented, the use of the collimator results in decreasing the " background suppression" effect both in absolute values (e.g. 90 cps instead of 160 cps for 160 mm collimator length), and in "sigma" values (2.9 instead of 4.3).

Table 1. Collimator influence on the background suppression caused by a truck inside of the radiation portal monitor.

Collimator length (alfa=0)	0 mm	100 mm	160 mm
Initial Background	1390 cps	1038 cps	933 cps
Backgr with truck	1230 cps	916 cps	843 cps
Backgr. suppression	-160 cps	-122 cps	-90 cps
Backgr. suppression	-4.3 sigma	-3.8 sigma	-2.9 sigma

II.2. Detection of the gamma sources.

The installation of a collimator results in two opposite effects. On the one hand, as it was stated above, there is a decrease of the natural gamma background measured by the monitor. On the other hand, the "field of view" of the detector is decreased and, as a consequence, the total time of a source exposition decreases too. Both of these effects depend directly on a ratio of the collimator and detector sizes. The efficiency of the collimator use is dependent on which of the effects is higher.

Let's consider the movement of a source with a speed of 2.2 km/s, in a distance of 3 m from the detector surface (a distance between the monitor pillars is 6 m). Fig.3 presents the experimental and calculated dependences of relative signal values on time without collimator and with collimator of 100 mm length. The Figure shows that the collimator installation causes a significant narrowing of the signal profile and, therefore, a decrease of the effective time of source exposition. If the collimator length is increased, the signal profile is even more narrowed.

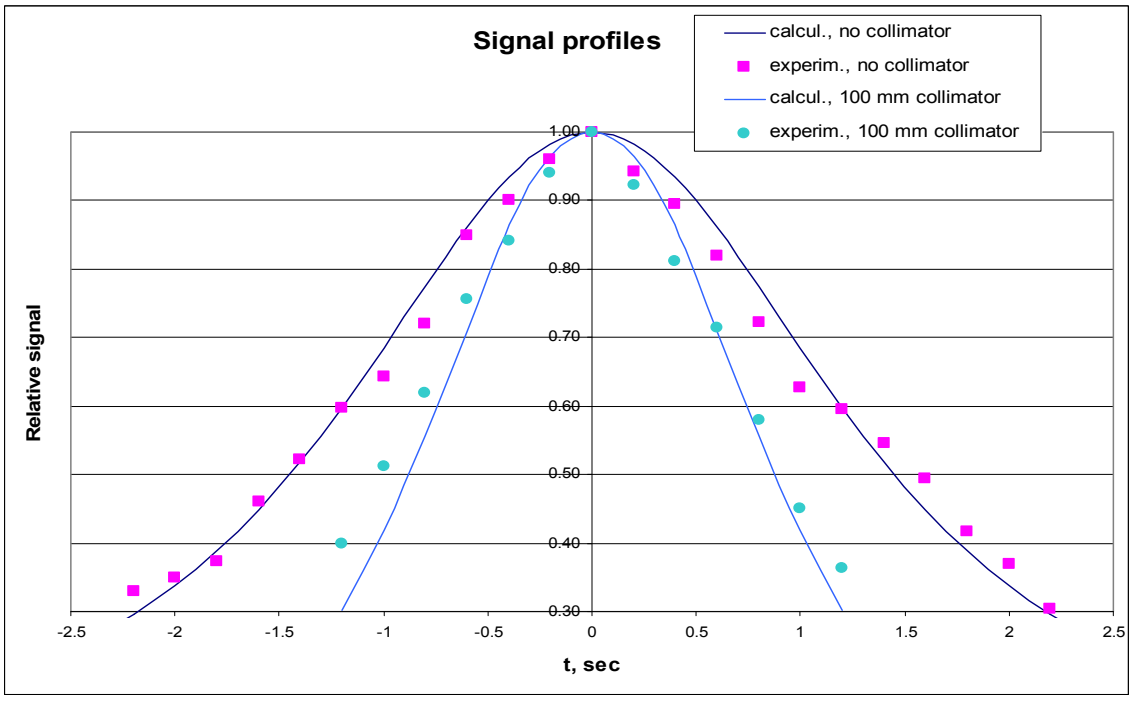

Fig. 3. Dependence of the signal profile on the collimator length.

It is possible to increase the source exposition time by changing an angle of the collimator declination (Fig.1), however, in this case the background also increases.

We estimated the results of mutual influence of these factors for collimators of different lengths installed under different angles Alfa to the vertical. The ratio of the maximum signal to the background "sigma" value was chosen as the studied parameter. The dependences obtained are presented in Fig. 4. As seen, the obvious maxima in the range of 20 degrees are observed for collimators of all the studied lengths.

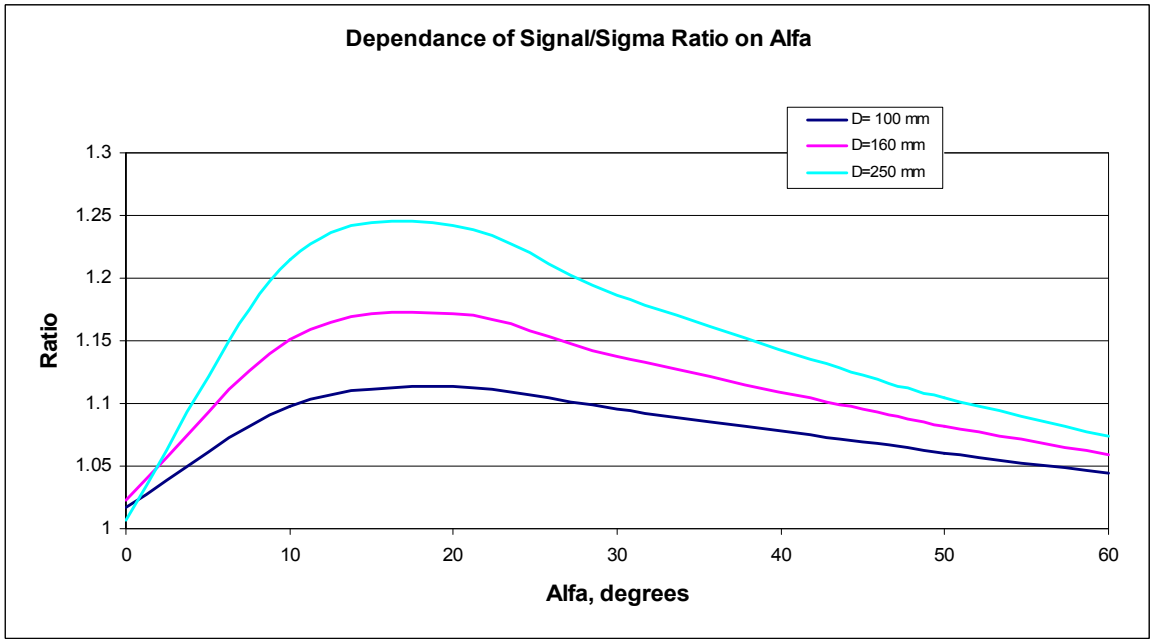

Fig. 4. Dependences of the signal/background ratio on the collimator declination angle Alfa for collimators of different lengths.

An increase in the signal/background ratio due to the collimator installation under an optimum angle results in an increase of the source detection probability. Dependences presented in Fig.5 testify that the collimator installation perpendicular to the detector surface (angle **α**=0) does not results in an increase of the source detection probability. However, the collimator installation at the optimum angle enables the monitor to detect a source (the detection probability is more than 90 %) which is practically not detectable without collimator (the detection probability is less than 60 %). Our calculations have shown that the collimator installation at the optimum angle results in a decrease of the minimum detectable signal by approximately 20 % (at the given detection probability).

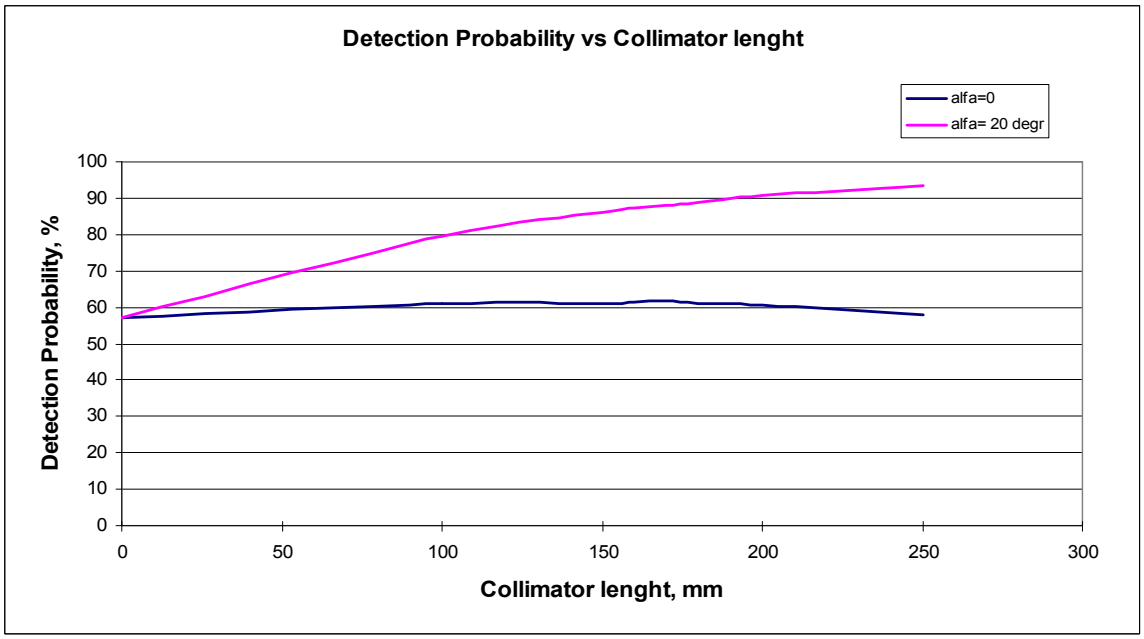

Fig. 5. Dependences of the source detection probability on the collimator length at different angles of the collimator declination to the vertical.

It is necessary to emphasize that the false alarm probability is the same for all the above cases as the alarm threshold (number of "sigma", equation (1)) was not changed in these calculations.

Conclusions

1. Installation of additional lead collimators on the plastic detectors of radiation portal monitors results in a decrease of the value of the measured gamma background. A decrease can reach 50% at collimator length of 250 mm.
2. Installation of the collimators causes as well a decrease of the detector "field of view" and, as a consequence, a narrowing of a signal profile; therefore, both the time of the source exposition and the probability of its detection decrease.
3. Installation of the collimators at some angle to the vertical results in an increase of the exposition time, however, the measured gamma background increases too. Calculations have shown that the maximum of the signal/background ratio for collimators of different lengths is observed at an angle of declination of 20 degrees.
4. Installation of the collimators at the optimum angle of 20 degrees provides an increase of the detection probability of the given source (or a decrease of the minimum detectable signal at the given detection probability) at the same false alarm probability.
5. We have paid the main attention to the collimator influence on **vehicle** portal monitors where the "field of view" of plastic detectors and the signal profile are of special importance. For **the pedestrian** portal monitors, a decrease of the measured gamma background can be more critical.
6. Additional advantages could be obtained with use of collimators of other shapes, for example, plate collimators [5].

References

1. N. Kravchenko, Organization of the Customs Control of Fissile and Radioactive Materials in the Russian Federation, The Second International Forum "Physical Nuclear Security – Counteractions to Acts of Nuclear Terrorism", October 26-28, 2006. Kiev, Ukraine.
2. R. de Goede, Border Monitoring Activities in the Netherlands, Research Coordination Meeting "Improvement of technical measures to detect and respond to illicit trafficking of nuclear and radioactive materials", 24-28 April 2006, Vienna, Austria.
3. http://www.tsasystems.com/products/portal_VM-250A.html
4. Kagan L., Stavrov A., Methodology of testing vehicle radiation portal monitors considering field operation conditions, INMM 51th Annual Meeting, Baltimore, MD (2010) (in press).
5. Walford, G.V., Bogard, J.S., Smith, S.E. and Solodov, A.A., High performance, directional gamma ray detector solutions for the detection and quantification of critical materials, INMM 50th Annual Meeting, Tucson, AZ (2009), paper # 310.

Measurements and simulations of fission neutron spectra at the MEDAPP beam at FRM II and subsequent developments

Breitkreutz, Harald; Jungwirth, Michael; Schenk, Robert; Wagner, Franz M.; Petry, Winfried

Forschungsneutronenquelle Heinz Maier-Leibnitz (FRM II), Lichtenbergstr. 1, 85747 Garching bei München, GERMANY

Abstract

The neutron spectrum of the fission neutron beam of the MEDAPP facility at FRM II was simulated with MCNPX and transmission calculations. The simulations were verified by multiple foil activation using threshold reactions. The measured spectra were unfolded and equalisation calculations performed. The full flux of the beam was determined by three methods: a specially developed gold-waterbath-method; by the calculation on the basis of dose measurements in a water phantom; and by the combination of the results obtained by activation foils.

It was shown that the geometric and spectral shape of the beam are widely independent. Together with the measurement of the gamma spectrum of the beam, this paves the way for a dose-planning system for tumour therapy at FRM II and further developments like the construction of a new collimator to enhance geometrical beam shaping. An overview of these developments is given.

Introduction

The MEDAPP facility is located at the Forschungsneutronenquelle Heinz Maier-Leibnitz (FRM II) (Wagner 2008). See fig. 1 for an overview of the facility. It possesses a neutron beam consisting of mainly non-moderated fission neutrons. They originate from a pair of uranium plates containing 540 g U, 93% enriched in ^{235}U, with an effective area of 15x15 cm², fed by thermal neutrons from the reactor core. The plates are positioned in contact to the entrance of the beam tube SR10. At the exit of SR10, thermal neutrons are captured by a boron filter. The beam quality (spectrum and neutron-to-gamma ratio) can be adjusted using filters of lead and polyethylene. Geometrical shaping is achieved by means of a multi-leaf collimator (MLC). For the tumour therapy, only one well-defined beam quality is used. Besides, numerous other biological and technical applications are possible.

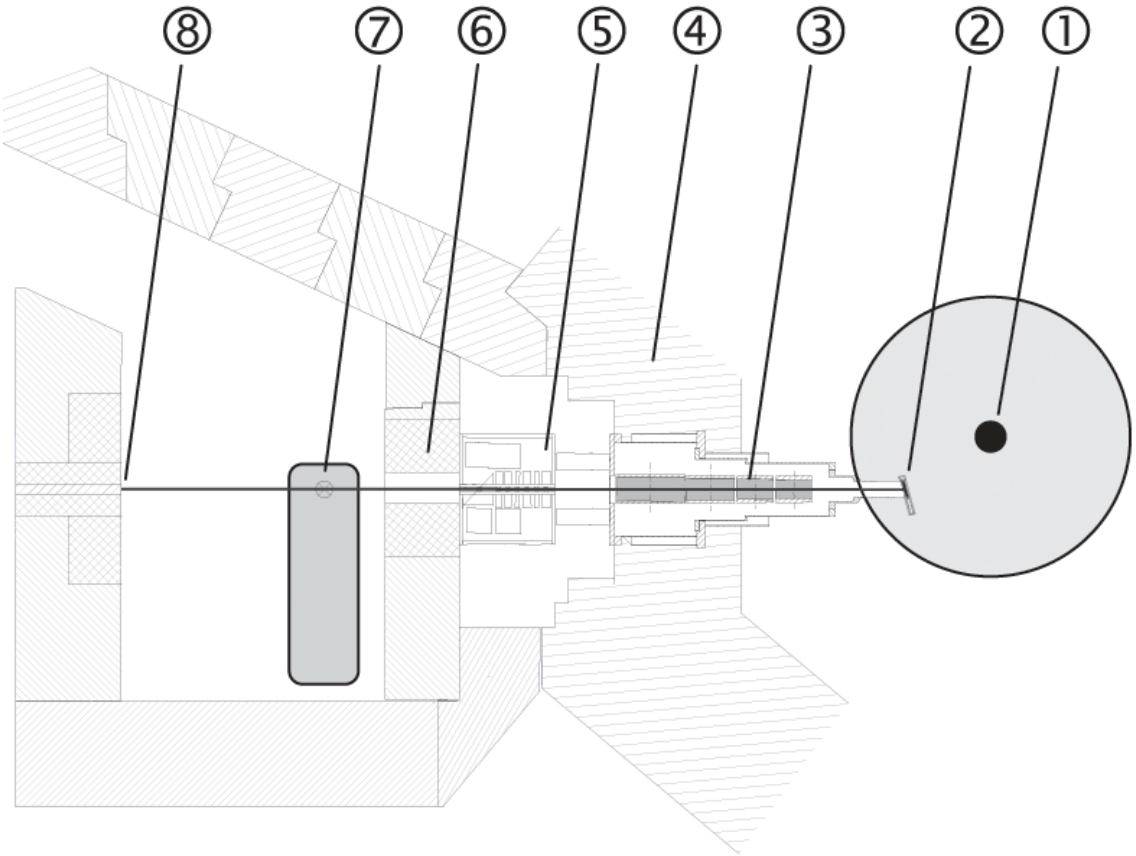

Fig 1. The MEDAPP facility. 1: Reactor core of FRM II inside a heavy water tank; 2: Converter plates; 3: Beam tube with shutters; 4: Biological shield (reactor pool wall); 5: Filter bench; 6: MLC; 7: Patient's position (SSD = 592cm); 8: Beam dump.

By now, the dose distribution is determined by measurements in a water phantom and results are transferred to the actual application at the patient. This delivers a sufficient accuracy for the irradiation of tumours situated near to the surface, although in the age of fast computers and modern simulation codes, a more precise-to-plan application is desirable. To develop such a dose planning system, five essential parameters of the beam must be known: Neutron spectrum and flux, gamma spectrum and flux and the correlations between the geometric position and those four items.

In a series of simulations and measurements, all parameters and correlations were determined. This paper mainly deals with the identification of the neutron spectrum, the neutron flux and the geometric correlations. In addition, an overview on the measurement of the gamma spectrum and a discussion on current developments based on these findings is given.

Neutron beam quality

Simulations

Prior to the measurements, simulations were carried out to be able to plan measurements more precisely and to lay the foundation for the unfolding of the spectra and the equalisation calculations. MCNP4C was used initially, later calculations were conducted using MCNPX, version 2.6.0. There was already a detailed model of the reactor core available which was used to calculate the first part of the simulation, from

the reactor core to the converter and further on to the entrance of the beam tube. The spectrum at this point was analysed and it was shown that it fully matches a reactor spectrum consisting of a Maxwellian distribution of thermal neutrons, an 1/E-distribution for intermediate energies, and the Watt spectrum for fission neutrons.

From thereon, the simulation was continued using RSSA files which were modified as described in (Breitkreutz 2007) using the program "ModRSSA" which was developed especially for this purpose. Using the technique of cell flagging, it could be shown that due to the collimation and a SSD (source skin distance) of nearly 6 m, the contribution of scattered particles to the resulting spectrum at the position of the patient is insignificant. It was therefore possible to calculate much more detailed spectra by means of straightforward transmission calculations applied to the spectrum at the entrance of the beam tube.

Due to the limited statistics that were achievable using RSSA files, it was not possible to extract the geometric-spectral correlations mentioned above in detail. However, there was no indication that such a correlation exists in an extent relevant for tumour therapy. As a consequence of this, the problem of the large source area and its projection onto the target could be solved by a straight-forward geometric approach, realised in a program called "ausleuchtung". This program calculates the geometric shape of the beam, i.e. the total neutron flux dependent on the geometric position in the treatment room, by summing up all visible source points (silhouettes / shadow image approach).

Measurements

The measurements consisted of three parts, namely the verification of the spectrum using threshold activation foils, the determination of the total neutron flux by a bath method, and the verification of the shadow image assumption used in "ausleuchtung", i.e. the determination of the beam profile after the MLC. (Breitkreutz 2008)

To measure the fission neutron spectrum, a total of 19 reactions with threshold energies ranging from 0.17 MeV, ^{103}Rh (n,n') ^{103m}Rh, to 12.40 MeV, ^{58}Ni (n,2n) ^{57}Ni, were used, with most reactions starting below 3.5 MeV. This high number of different reactions was possible due to the high intensity of the beam and barely no disturbing underground from thermal neutrons. After activation, the resulting radioactive isotopes were identified using a HPGe detector.

The total neutron flux density was determined using three different techniques: It was calculated from the activation foils with supplemental (n,γ)-reactions in combination with equalisation calculations below. Second, as the neutron spectrum was known, the fast flux could be calculated from depth dose measurements using the twin chamber method in a 200-l-water phantom (PTW-Freiburg). Third, the total flux was measured in the same water phantom in which gold foils were arranged in equidistant positions throughout its volume. This technique is similar to the well-known $MnSO_4$ bath method, but avoids handling large amounts of radioactive fluids and allows well to distinguish the contributions from thermal and epithermal neutrons. The horizontal beam was guided in the middle of the bath via an empty closed aluminium tube. The efflux from the bath was also determined using gold foils on its surfaces. This set-up is shown in fig. 2. The activation was again determined using a HPGe.

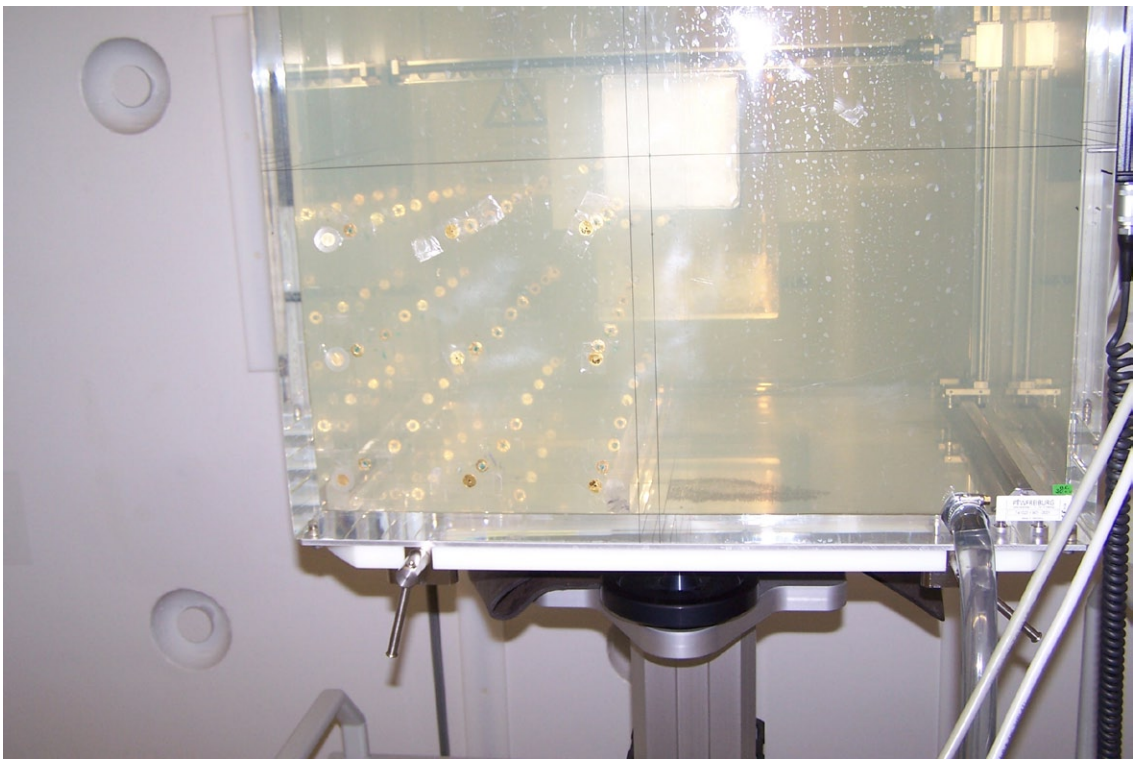

Fig 2. Measurement of the total flux by use of equally distributed gold foils in a big water bath. For symmetry reasons, it was sufficient to arrange about 150 foils in one quadrant around the beam.

To determine the correctness of the shadow image approach, a 1D flux profile was recorded using indium wires. The reaction ^{115}In (n,n') ^{115m}In has a threshold energy of 0.35 MeV. Of course, spectral changes can not be captured completely in this way, but it can be assumed that a significant spectral change goes hand in hand with a change of the flux above the threshold energy. Therefore, if the beam profile simulation and the 1D measurement agree well, it can be concluded that the spectral-geometric correlation is insignificant above this threshold. MCNPX calculations support this assumption.

As an additional verification, spectra at various positions in various depths inside a PE phantom were measured and simulated. It could be shown that the fission spectrum is hardened with increasing depth, though not significantly within the first five centimetres, and a thermal neutron flux in the same order of magnitude as the fast neutron flux builds up.

Equalisation calculations

Due to the low information density contained in the activation foil measurements and the high uncertainty in some of the cross sections for the fast reactions, it is hardly possible to unfold the spectrum from these measurements without any prior knowledge. Therefore spectra from transmission calculations and MCNPX simulations were used as start spectra. It turned out that the classic unfolding codes like MSANDB tended to converge to solutions that could not be explained by the materials in and the geometry of the beam. In fact, this behaviour could be suppressed when some measured reactions were excluded, but this approach is not easy to justify and, hence, was not followed up. Instead, equalisation calculations using MSITER were conducted. These calculations

roughly follow the procedure required by DIN 1319-4, even though the (co-) variances of cross section uncertainties are not taken into account.

Neutron results

All three flux measurements described above delivered a total neutron flux of $3.2(1)\cdot10^8$ n/(s cm²). The simulated neutron spectrum was essentially confirmed; only with slight adjustments above 5 MeV and in the intermediate range between thermal and epithermal neutrons, where. the MCNPX simulation showed large statistical errors.

The mean energy of the spectrum was determined to be 1.9(1) MeV, slightly lower than the 2.0 MeV of a pure fission spectrum. The final spectrum is shown in fig. 3.

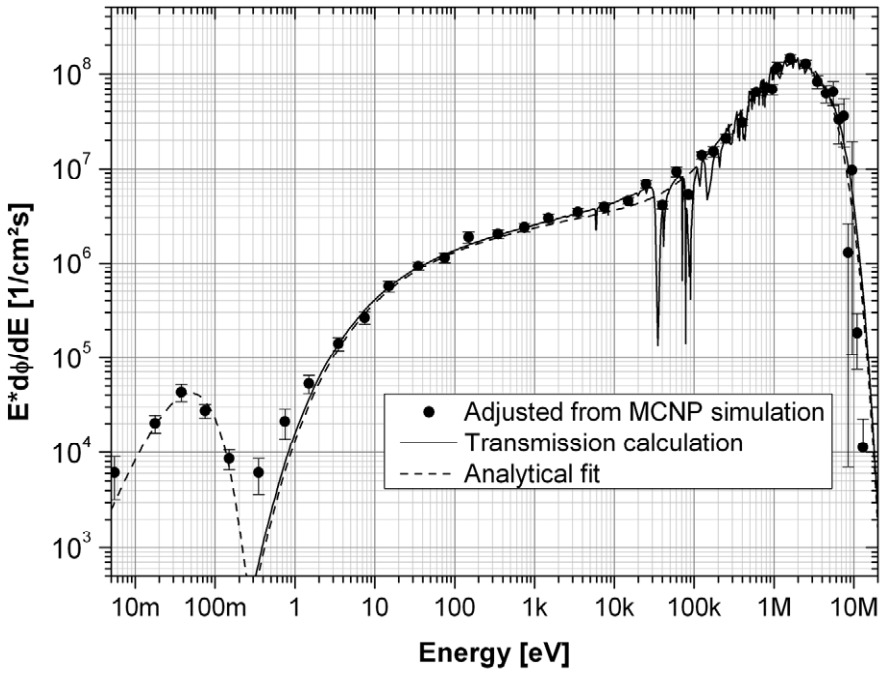

Fig 3. Neutron spectrum of MEDAPP at the patient's position. The small thermal peak results from scattering in the MLC which is not included in the transmission calculation. Due to the low resolution of the MCNP simulation (43 energy groups), the resonances from lead (filters) and aluminium (covers) clearly show up only in the transmission calculation.

Gamma beam quality

Simulation

A simulation of the gamma part of the beam was not fully possible until support for delayed gamma emission was added in MCNPX 2.6. Before, only the prompt gammas emitted during fission as well as on capture events in neutron-absorbing structure materials and the related Compton part could be simulated. With MCNPX 2.6, the delayed gammas emitted by fission products and activations due to neutron capture reactions were taken into account by means of an approach with 25 energy groups. Essentially the same models as for the older neutronic simulations were used for the simulation.

However, in the case of gamma radiation it was hardly possible to achieve satisfactory statistics by the original simulation approach using RSSA files at the beam tube entrance. To overcome this deficiency, the program "autospect" was developed. It is similar to "ModRSSA" but features some kind of peak detection routine as the complex gamma spectrum can not be fitted with a closed expression as easily as the neutron spectrum. "Autospect" starts to acquire the particles stored in the RSSA file with a high number of energy groups. It then detects peaks in this group structure by the unsteadiness of the statistic error and starts condensing the remaining energy groups until a specified level of statistics is reached. In this way, an inhomogeneous group structure is produced with sharp peaks and wider ranges in-between, all with an acceptable statistic error. With the spectrum gathered by "autospect", the simulation was continued at the entrance of the beam tube and brought further on to the patient's position. Fig. 4 shows the spectrum as determined by "autospect" and a transmission calculation to the patients position. Some important peaks like the 1779 keV ^{28}Al decay peak are missing as they are hidden in the coarse delayed gamma group structure mentioned above.

The measurements described below were simulated apart. For this, a MCNPX model of the detector was created.

Measurements

The measurement of the gamma spectrum proved to be a far higher cradle than the neutron spectrum. Due to the inevitable fission neutrons and the high intensity of the beam, the spectrum could not be measured directly in the therapy beam with a gamma detector (Jungwirth 2009).

Two measurements were conducted to determine the gamma spectrum: First, a measurement on the beam axis at very low reactor power (approximately 50 kW instead of 20 MW) with a 5" NaI using additional attenuators. At full reactor power, only scattered photons were measured under a defined angle apart of the direct beam using the 5" NaI detector and, for better resolution at lower energies, a HPGe detector. A special collimator was constructed for the latter measurement.

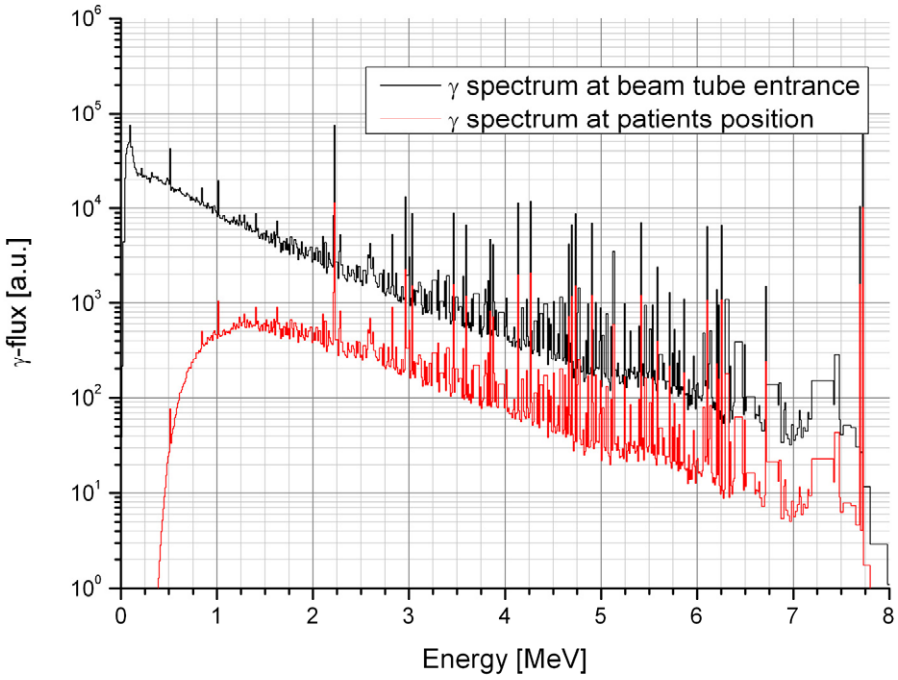

Fig 4. Gamma-spectrum determined by "autospect" and spectrum at the patients position calculated by transmission calculation.

Fig. 5 shows a measured gamma spectrum on the beam axis with partially closed shutters, i.e. with about 20 cm iron in the beam. In this case, all major peaks from fig. 4 can easily be identified, except decay peaks that were not included as line emission but within the 25 energy group structure in the simulation.

The total gamma flux was determined similarly to the neutron flux determination by evaluation of a depth dose curve in a water phantom in comparison to a simulated one. Of course, in this case a good knowledge of the spectrum is required, too.

Results

The simulated detector showed a drastic underestimation of the Compton spectrum. Peak efficiencies were ok (±4%). As a result of this, all measured spectra showed an increasing deviation in the high energy range starting from about 3.5 MeV up to the measured maximum of 10 MeV (or, in other words, an underestimation of the low energy part). Moreover, the depth dose curve showed deviations in depths larger than 5 cm, also pointing towards an overestimation of the high energy part in the simulations.

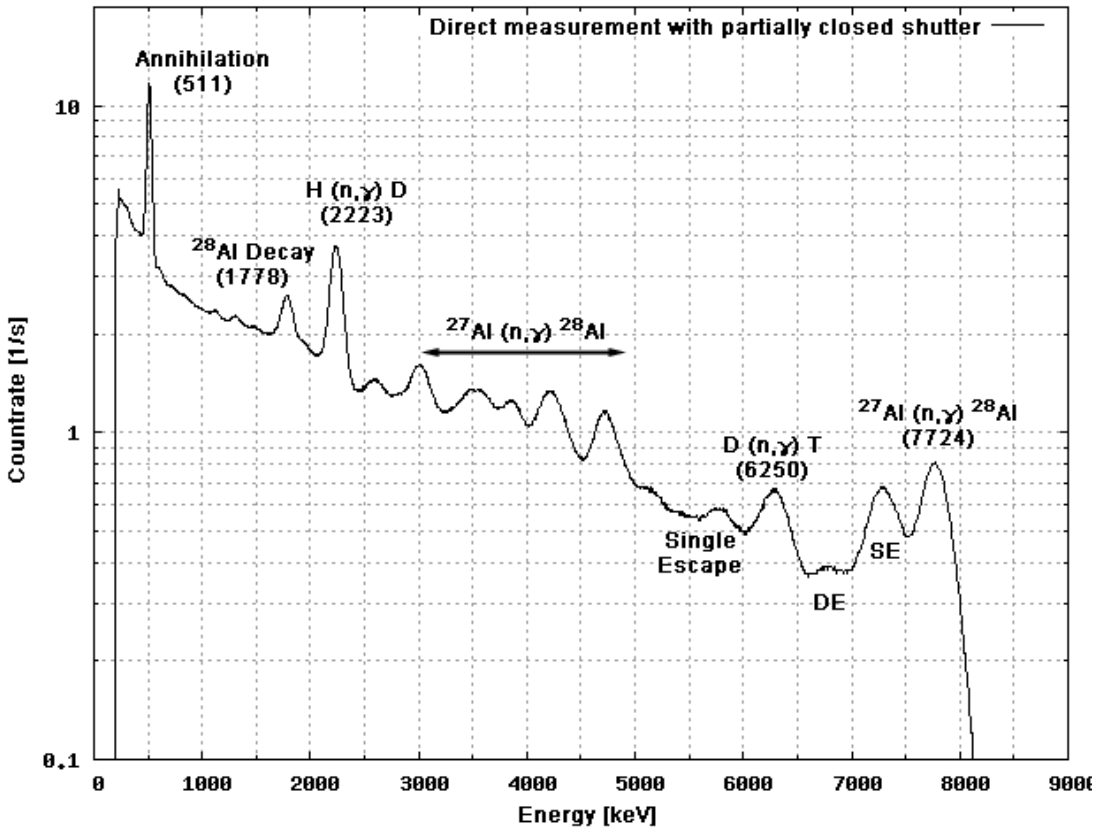

Fig 5. Measured gamma spectrum directly in the beam with partially closed shutters.

The mean energy of the gamma part of the beam is about 2.4 MeV, the total gamma flux 3.7(1) · 10^8 γ/s cm². As explained before, the accuracy of the total flux assignation depends on the correctness of the assumed spectral shape which is not the case here to the full extent. Therefore the total flux was determined from the first three depth dose points only. The uncertainty of the number given above is therefore by trend higher than quoted here. We are currently investigating the reasons for the deviations in the spectrum.

The spectral-geometric correlation has not been measured yet. However, results from simulations again suggest that there is no significant correlation.

Further Developments

A new MLC

As the current design of the beam collimator is not optimal regarding the large penumbra around the main beam, a new collimator is currently being constructed with improved field shaping and thereby increased radiation protection for the healthy tissue of the patient.

Based on the verified shadow image approach, a program “ausleuchtung” (see sec. 2.1) was developed which can be used to simulate the geometric shape of the beam depending on the collimator setting within seconds. With its help, the construction of the new collimator was optimised towards steep beam intensity edges for small fields as they are predominantly needed for irradiations of the head and neck (Schenk 2009).

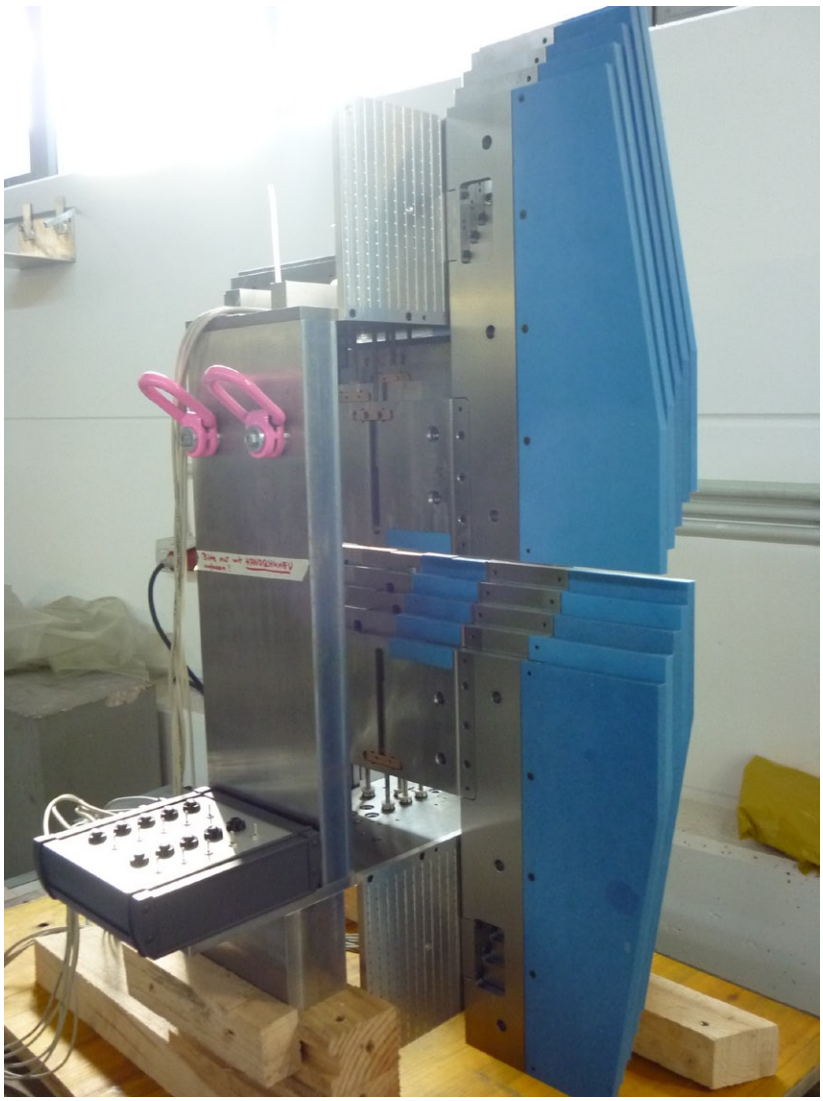

Fig 6. Prototype of a new collimator for MEDAPP.

Using the measured neutron and gamma spectra, the shielding and self-shielding against activation of the collimator is being optimised, yielding an increased radiation protection for the staff of MEDAPP. The collimator is electronically driven so that the collimator can be closed automatically and the medical staff is not exposed to the activated metal parts of the MLC.

Towards a dose planning system

For the development of a dose planning system, it is essential to know all the beam parameters mentioned in the introduction. As soon as the remaining discrepancies with the gamma spectrum are solved, all these parameters are known. In fact, spectral uncertainties play a minor role in the medical treatment because the photon component of the beam contributes only about 10 % to the total RBE-dose.

By now, based on the approach of “ausleuchtung” and MCNPX, a program was developed which utilises all the findings described above to simulate 3D depth dose distributions in a water phantom in a reasonable amount of time (some hours). The

errors which were introduced to the depth dose curve by all the measures like denying all spectral-geometric correlations and the adjustments made by neglecting scattered particles in the beam tube are assumed to be negligible compared to other uncertainties like the exact elemental composition of the patient's tissue or cross section uncertainties for fast reactions.

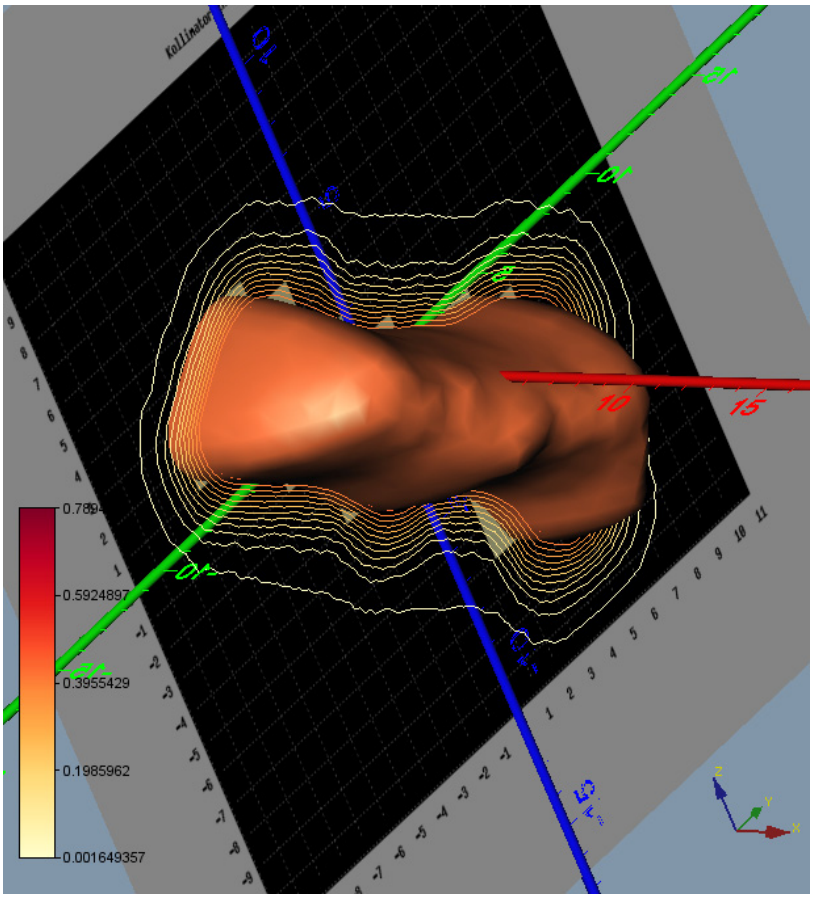

Fig 7. Example of a water phantom dose plan for MEDAPP: 2D and 3D iso-doses for a certain MLC setting (background image). The beam is entering along the red x-axis from behind through the MLC image.

Conclusions

The measurement of the neutron and the gamma spectrum and the determination of the spectral-geometric correlations have laid the foundation for the development of a dose planning system and a number of other programs. The radiation protection of the patient will be brought a good step forward when the dose planning system is eventually realised. The enhancements in radiation protection by the construction of a new collimator, which is optimised towards field shaping, again is mainly for the benefit of the patient. The staff profits from the enhanced activation self-shielding of the new collimator and more precisely calculable activation after long-term irradiations when the facility is used for technical applications.

References

Breitkreutz H, Wagner FM, Röhrmoser A, Petry W: Spectral fluence rates of the fast reactor beam MEDAPP at FRM II. Nuclear Instruments and Methods in Physics Research, Section A 2008; 593: 466-471

Breitkreutz H: Sektrale Charakterisierung des Therapiestrahls am FRM II. Diplomarbeit. Technische Universität München, 2009

Jungwirth M: Bestimmung des Gammaspektrums in einem intensiven Spaltneutronenstrahl. Diplomarbeit. LMU München, 2009

Schenk R: Entwicklung und Konstruktion eines Lamellenkollimators für die Neutronentherapie. Diplomarbeit. TU München 2009

Wagner FM, Kneschaurek P, Kampfer S, Kastenmüller A, Loeper-Kabasakal B, Waschkowski W, Breitkreutz H, Molls M, Petry W: The Munich Fission Neutron Therapy Facility MEDAPP at the Research Reactor FRM II. Strahlentherapie Onkologie 2008; 184: 643-646

Feasibility study of a low cost wireless ionizing radiation sensor network

Kuipers, Tjerk[1]; Franken, Yuri[1]; van Doorn, Harry[2]; Kemper, Ad[2]; Koole, Iman[2]
[1] Radiation Protection Department, Eindhoven University of Technology, THE NETHERLANDS
[2] Department of Applied Physics, Eindhoven University of Technology, THE NETHERLANDS

Abstract
The Radiation Protection Department at the Technical University Eindhoven has developed the operational need for an ionizing radiation monitoring instrument mapping real-time radiation emanated by industrial processes into the environment and workplace. Available instruments are energy consumptive, static and labor intensive in data collecting so this feasibility study will investigate an alternative. The aim of this feasibility study is to design a device collecting dosimetric data in a more economical and ergonomically manner. The end product is a modular, energy efficient wireless radiation sensor which constitutes automatically a flexible, secure and failsafe network with multiple modules. A module consists of a ZigBee protocol based transceiver capable of forming several types of network topologies and a MDA300CA sensor board interconnected with a custom-made ionizing radiation sensor. The radiation sensor is constructed using a widely used PIN-photodiode sensitive to photon energies ranging from 35 keV till 1173 keV. The received data streams are easily viewed and interpreted using an open-source PostgreSQL database. The wireless radiation sensor network is a real-time monitoring instrument which can be implemented in existing organizations and expanded on in several ways using commercially available components.

Introduction
For radiation protection of workers and environment a source oriented approach is indispensable. For such an approach to be effective, operational area monitoring is very helpful. Traditionally, area monitoring is done with handheld survey monitors or by fixed area monitors. The latter monitors are sometimes equipped with local or remote alarm indications. If source conditions in a workplace are relatively stable, periodic manual surveys are usually quite adequate. However, in situations like ours of strongly fluctuating source strengths or variable locations, real time monitoring is often desired.

Eindhoven University of Technology hosts a 30 MeV proton cyclotron, mainly used for large scale radionuclide production and radionuclide processing facilities. In all stages of production and processing there has been a growing need to monitor radiation levels in more detail in workplaces. Until now this has been done by a wired network of area monitors (wall mounted GM tubes) and by many small scale active and passive

dosemeters. We found the wired network to be inflexible and expensive; small standalone dosemeters fit our needs much better, but require of lot of manual work and manual data processing.

Therefore, we strive for an area monitoring system that is networked and flexible. The main goal of this study is to investigate the feasibility of a cost-effective modular area monitoring system, consisting of wireless sensors.

Material and methods

The system we designed has modules with ZigBee protocol based transceivers from Crossbow Technologies, capable of forming several types of network topologies and a MDA300CA data acquisition board with a custom made radiation detector. The detector was constructed using a widely used PIN-photodiode, capable of detecting photon energies ranging from 35 keV to 1332 keV.

Some properties like sensitivity, linearity and efficiency of the PIN-photodiode were investigated by using different calibration sources. Especially efficiency at low photonic energies was expected to be increased so filtration might be a crucial aspect (*C-R. Chen et al., 1993, R.H. Olser et al., 1991*). Calibration has been done with secondary standard calibrated Cs-137 sources with different activities (*P.W. Cattaneo, 1991*).

ZigBee

The ZigBee Alliance uses an energy efficient protocol IEEE 802.15.4 for wireless transmitting data (*P. Baronti et al., 2007*) and distinguishes three different devices. The *ZigBee coordinator (ZC)* is the most capable device. This coordinator forms the root of the network tree and might bridge to other networks. There is only one ZigBee coordinator in each network since it is the device that started the network originally. It is able to store information about the network, including acting as the Trust Centre & Repository for security keys. The *ZigBee Router (ZR)* runs application functions and is acting as an intermediate router, passing on data from other devices. The *ZigBee End Device (ZED)* contains just enough functionality to talk to the parent node (either the coordinator or a router); it cannot relay data from other devices. This relationship allows the node to be asleep a significant amount of time, combined with efficient use of memory, therefore giving long battery life.

In our experiments the integration of a ZigBee transceiver module, an experimental board (MDA300CA), the sensor and electronics and electromagnetically shielded wiring operates as a ZR or ZED, all powered by two LR6 (AA) batteries. The signals coming from the detector are sent to an internal counter in the microprocessor. This value is then stored, time-stamped and combined with data from other sensors and finally transmitted to the nearest module using the 2.4 GHz open band so the data collected by the sensory node in this network is eventually transmitted to the base node. There is no interference between other protocols, like 802.11a/b/g (WiFi), using the 2.4 GHz open band frequency. A ZigBee transceiver combined with an USB-connected programming board (MIB400) acts as a ZC.

The sensor

The sensor used is a daylight filtered PIN-photodiode (OSRAM BPW34FS) with a designed sensitivity range of 780 nm and 1100 nm. This semiconductor is commonly used for measuring infrared photons or X-rays but is also quite suitable for detecting photons in a range between 35 keV and 1173 keV.

A PIN-photodiode consists of three layers where the intrinsic (I) high resistance layer is important for detecting photon energies higher than 10 eV (*C-R. Chen et al., 1993*). The intrinsic layer reduces the leakage current between the P-N-junctions and also acts as an active volume for high energy photons and secondary electrons originated in the active volume or surrounding materials. Undiscriminated and unfiltered, the efficiency of a PIN-photodiode steeply increases at 10 keV and shows a decline until 10 MeV as seen in figure 1 (no filter).

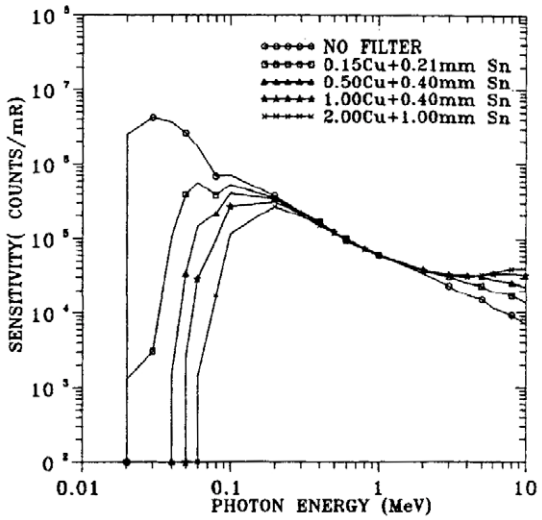

Fig. 1. Calculated sensitivities (in counts/mR) for several filter thicknesses (C-R. Chen et al., 1993).

We have limited our measurements between 35 keV and 2 MeV. Sensitivity and efficiency has been investigated by using several calibrated radioactive sources; Am-241, Ba-133, Cs-137, Mn-54, Co-60 and Na-22.

The electronic design

The used design is based on a PIN-photodiode (OSRAM BPW34FS) (*B. Denmark, 2003*). Major concern is noise reduction, therefore at the end of the amplification chain a discriminator cuts off the signal at low energies causing effects like reducing sensitivity as seen in figure 2.

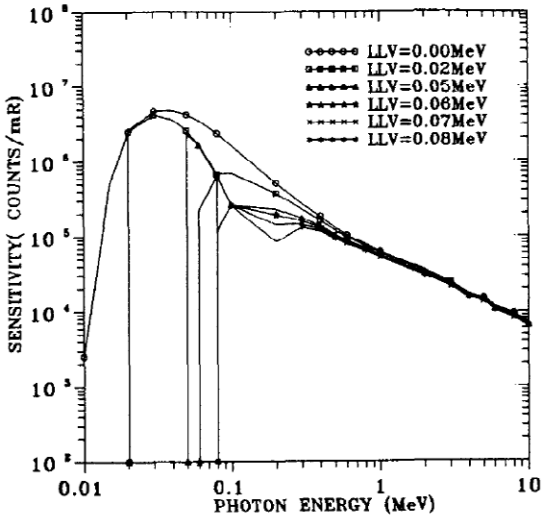

Fig. 2. Sensitivity curves with different settings of discrimination level (*C-R. Chen et al., 1993*).

The PIN-photodiode has a spectral range of sensitivity between 780 and 1100 nm. Exclusion of electromagnetic interference and daylight is achieved by a metal casing. The PIN-photodiode is embedded in the print so its angle sensitiveness is maximized.

In beneficially deploying this network power consumption of the sensor electronics had to be reduced. The energy consumption of the detector was about 80-90% of the total energy consumption of a node. The detector electronics consumes about 7 mA in active mode, for the greater part due to amplification electronics (4x MAX4475). The amplification electronics can be set in standby mode using an external digital pulse. Using this standby mode the power consumption of the detector electronics is about 0,001 mA.

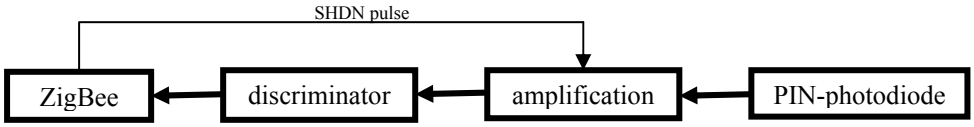

Fig. 3. Schematic view of the detector electronics.

The voltage ripple created in the PIN photodiode enters a four stage amplification line as seen in figure 3. After final amplification the pulse height is cut off with a pulse height discriminator so the pulse resembles a square wave. These square waves are used as input for the counter in the transceivers' microprocessor (ATMEL ATmega1281). To reduce power consumption the shutdown mode of the amplification chips (4x MAX4475) are routed to the transceiver module. This enables development of future measuring algorithms.

For valid representation of the collected data it is necessary to calibrate the detector. The calibration has been done with secondary standard calibrated Cs-137 sources with different activities. Using an Am-241 source (490 MBq) and the calibration installation of the Radiation Protection Service of the University of Technology Eindhoven the linearity of the detector has been investigated by verifying

the inverse square law. The measured data are stored in a provided open source SQL database (PostGreSQL) for further analysis.

Results

The discrimination level setting has a strong influence on the detector efficiency for photon energies up to several hundreds keV as seen in figure 4. There is an optimum between noise reduction and the low energy cut-off level. This reduces sensitivity and flattens the efficiency curve. Therefore sensor filtration was not required like in figure 1. Our prototype is capable of measuring photon energies from 35 keV, using I-125 seeds, up to 1173 keV, using a Co-60 source.

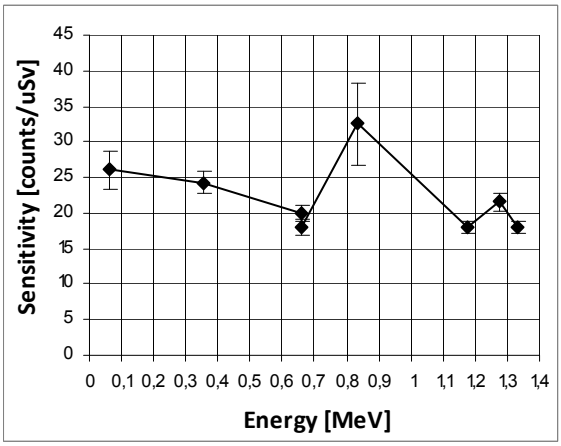

Fig. 4. Sensitivity of BPW34FS_no_filter using a set of calibration sources.

The measured sensitivity of the detector is about 20-25 counts per microSv.

The discriminator voltage is Vcc dependent. Battery voltage should not be below 2.3 V to prevent signal loss.

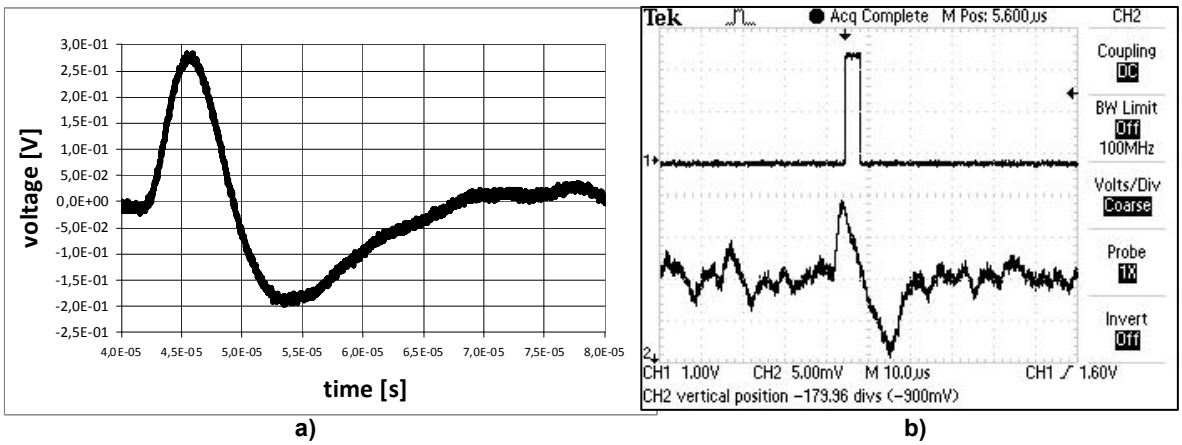

a) b)

Fig. 5. a) Non-discriminated pulse created using a Cs-137 source and b) X-ray photon pulse converted into a square wave.

The pulse width varies between 5 and 25 microseconds and increases with higher photon energies as seen in figures 5a en 5b. The internal counter is capable of detecting these short pulses so the transceiver can send every second a time-stamped data packet with the amount of counted pulses.

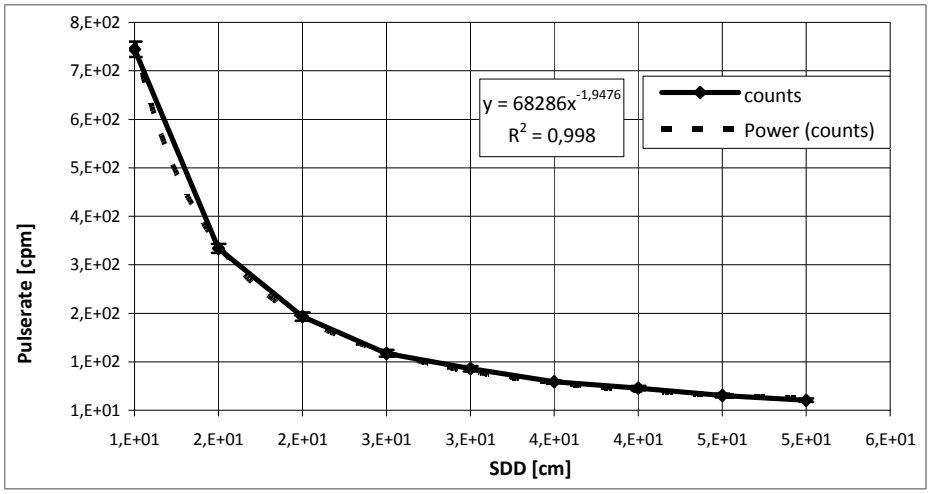

Fig. 7. Measured linearity of BPW34FS_no_filter using Am-241.

The linearity of the detector node has been tested using Am-241 (490 MBq). The pulserate measured in counts per minute follows the inverse square law indicated by figure 7.

Discussion

The first prototype with one gateway, one repeating node and one detector node was developed and tested successfully. The concept has good prospects for use in small to medium sized installations. Nevertheless, a complete wireless radiation sensor network has not been tested yet. In future detector nodes the node programs have to be modified so the frequency of emitting packets is reduced to a data packet every minute. This will also reduce power consumption.

Lowering the temperature of the PIN-photodiode by applying a Peltier element on the back of the PIN-photodiode could reduce noise by a factor 10 (*Z. Bian et al., 1985*).

For further sensitivity maximization a scintillation crystal can be mounted on the sensitive sides of the diode (*E. Fioretto et al., 2000*) or several PIN-photodiodes connected in series acting as one detector (*A. Sertap Kavasoglu et al., 2008*). The detector has not been tested in high frequency pulsed radiation fields.

The cost of a complete network system depends on the mapping detail degree, the size of the location, the signal attenuation between nodes, all in all, the amount of nodes. The cost of a detector node depends on further development of the hardware, like miniaturization of detector design, sensitization of the sensor and integration of detector and transceiver module in one design, and further development of software like data processing alarm algorithms, node programming and a comprehensible end-user software interface.

Conclusions

The development of a low cost reliable radiation detector is feasible. This study showed good sensitivity, efficiency and linearity of the detector. The wireless radiation sensor network is a real-time area monitoring instrument which can be implemented in existing organizations and workplaces. The wireless radiation sensor network can be expanded in several ways using commercially available components. Using a flexible wireless sensor platform creates a foundation for future applications determining activities in facilities for mapping radiation fields.

Acknowledgements

Gratitude goes to all my colleagues at the Radiation Protection Service at the University of Technology Eindhoven for support, my co-authors at the Department of Applied Physics for technological and programming support, Jan Weterings at the Department of Radiotherapy of the Catharina Hospital in Eindhoven for the iodine seeds and my girlfriend for endless patience and advice.

References

P. Baronti, P. Pillai, V.W.C. Chook, S. Chessa, A. Gotta, Y. Fun Hu. Wireless sensor networks: A survey on the state of the art and the 802.15.4 and ZigBee standards. Computer communications 30, 2007; 1655-1695.

Z. Bian, J. Dobbins, N. Mistry. The use of silicon photodiodes in a Cs(Tl) calorimeter. Nuclear instruments and methods in physics research A239, 1985; 518-526.

P.W. Cattaneo. Calibration procedure for irradiation tests on silicon devices. IEEE Transactions on nuclear science, June 1991; Vol. 38 (No. 3); 894.

C-R. Chen, S-H. Jiang. Energy response and filter compensation of PIN photodiode for personal dosimetrie application. IEEE Transactions on Nuclear Science, August 1993, Vol. 40 (No. 4), 857.

Crossbow Wireless Sensor Networks, *www.xbow.com*

B. Denmark. Circuit forms gamma-photon detector. EDN Electronics, Design, Strategy and News, April 24, 2003.

E. Fioretto, E. Innocenti, G. Viesti, M. Cinausero, L. Zuin, D. Fabris, M. Lunardon, G. Nebbia and G. Rete. CsI(Tl)-photodiode detectors for x-ray spectroscopy. IEEE Transactions on nuclear science, August 2000; Vol. 47 (No. 4); 1315.

R.H. Olser, Y. Eisen. A filter technique for optimising the photon energy response of a silicon PIN diode dosemeter. Radiation Protection Dosimetry, 1996; Vol. 67 (No. 4); 271-279.

PostgreSQL, www.postgresql.org

A. Sertap Kavasoglu, Nese Kavasoglu, Ethem Kose. Analysis and simulation of Si PIN photodiode anomalous I-V-T characteristic: modelling and experiments. Malatya-Turkey Balkan Physics Letters, 2008 Special Issue, Boğaziçi University Press.

ZigBee Alliance, *www.zigbee.org*

Results of model calculations and algorithm development related to a 3D silicon detector dosimetric telescope

Hirn, Attila
Hungarian Academy of Sciences KFKI Atomic Energy Research Institute, HUNGARY

Abstract

One of the many risks of long-duration space flights is the excessive exposure to cosmic radiation. The dose equivalent in orbit may be two orders of magnitude higher than that under the shield of Earth's atmosphere. In order to determine the dose equivalent on board different spacecrafts, the development of a 3D silicon detector telescope got underway in the Hungarian Academy of Sciences KFKI Atomic Energy Research Institute several years ago.

In the course of my doctoral research I was taking part in the R&D activities related to the instrument, such as designing the measurement system, developing the electronic system, reconciling the scientific, the electronic and the mechanical considerations of the development, working out the algorithms of the on-board software as well as coordinating, controlling and managing the development (Hirn 2009a). The present paper addresses two important issues of my work: the method of determining in almost real time the time intervals of the South Atlantic Anomaly (SAA) crossings of the International Space Station (ISS) and the calculations performed in relation with the anisotropy of the cosmic radiation field in low Earth orbit in order to compare the performances of 1D and 3D telescopes on board ISS. To switch between the SAA and non-SAA spectra I developed an algorithm, which has been tested with model time spectra generated from time spectra measured by the DOSTEL 1D telescope. I calculated the parameter of the algorithm such that the probability of false switching was less than 10^{-3}. With model calculations I also analyzed the effects of the angular dependence of the geomagnetic cut-off, the shielding of the Earth and the East-West asymmetry of the trapped particles on the measured deposited energy spectra. The results have shown that in case of the untrapped radiation the differences in the spectra could be attributed only to the shielding effect of the Earth. As for the trapped radiation a more pronounced directionality was obtained.

Introduction

Due to the lack of shielding provided by the atmosphere of our planet, the dose rates measured on the International Space Station (ISS, at an altitude of ~340 km) are about two orders of magnitude higher than those from cosmic origin measured on the Earth's

surface. Since dose equivalent, which characterizes the stochastic biological effects of the radiation, was defined in terms of a LET (linear energy transfer)-dependent quality factor, determining the LET spectrum and the quality factor of the cosmic radiation is necessary. For this reason, the development of a 3D silicon detector telescope (TriTel) started in the KFKI Atomic Energy Research Institute (AEKI) several years ago. The instrument comprises three mutually orthogonal, fully depleted PIPS detector pairs that are connected as AND gate in coincidence and has almost uniform sensitivity in 4π. A big advantage of TriTel, either as a stand-alone instrument or when operated together with the Pille thermoluminescent dosimeter system (Feher et al. 1981), is the capability of determining not only the absorbed dose but the LET spectrum and the average quality factor of the cosmic radiation as well (Pazmandi et al. 2006). From the absorbed dose and the quality factor the dose equivalent can be also determined.

Anisotropy of the cosmic radiation in low Earth orbit

The galactic cosmic radiation (GCR) in the near-Earth free space is approximately isotropic. However, because of the shielding effect of the Earth's magnetic field and the Earth itself, there is a lower limit on the energy of primary cosmic ray particles to enter given points in low Earth orbit from different directions (geomagnetic cut-off, Lemaître, Vallarta 1933). The solar component of the cosmic radiation also shows significant anisotropy. Its intensity on board ISS is usually negligible compared to GCR. However, its contribution to the radiation environment may be significant during solar particle events. My work did not address the anisotropy of the solar component.

Even at lower altitudes, due to a shift (~500 km) and tilt (~11°) of the geomagnetic axis compared to the Earth's rotational axis, the magnetic field is not symmetrical in relation to the rotational axis. Therefore in the region between South Africa and South America the inner radiation belt protrudes into lower altitudes (2-300 km). This designated region is called the South Atlantic Anomaly (Stassinopoulos, Staffer, 2007). The International Space Station passes the SAA in two time windows a day and in 2-3 consecutive orbits in a time window. The time elapsed between two time windows is approximately 8 and 16 hours respectively. When travelling through the SAA, astronauts are exposed to trapped radiation of the inner Van Allen belt, which shows a pronounced directionality. Although only about 5% of the mission time on board ISS is spent in the SAA, the astronauts may collect more than 50% of their total dose during this short time period (Apathy et al. 2007).

In case of ISS, which has usually an airplane-like attitude, i.e. the attitude is stabilized in the local vertical reference frame (ESA 2006), the anisotropies in the radiation field, such as the effect of the Earth's shadow, the angular dependence of the geomagnetic transmission factors and the East–West asymmetry in the SAA, might not be ignored in dosimetric measurements, unlike in case of Space Shuttle flights where, due to the changing orientation of the spacecraft, anisotropies usually tend to be averaged out (Badhwar et al. 1999). 1D telescopes used for dosimetry have strong directional sensitivity and therefore they might either under- or overestimate the dose equivalent. The application of 3D telescopes with three, mutually orthogonal axes improves significantly the measuring precision of the instrument.

A number of papers addressed the models of the anisotropic radiation environment on board ISS. The results of the calculations presented in (Wilson et al.

2006) have shown that the addition of the angular dependence of both the trapped protons and GCR transmission factors considerably increases the usefulness of the basic cosmic radiation models. Time resolved measurements performed with Liulin type silicon detector instruments on board ISS were used to evaluate the adequacy of the environmental revised models. The comparison has shown that further corrections are needed (Wilson et al. 2007). Nealy et al. presented validation of their revised environmental models in which they compared the results of the calculations with that of the measurements carried out with several passive and active detectors on board ISS. Albeit the agreement was found to be fairly good, they suggested further improvement of the models (Nealy et al. 2007).

Material and methods

The SAA switching algorithm

After a signal coming from a detector has been processed and digitized, the content of the appropriate channel in the active deposited energy spectrum is incremented. In order to collect the SAA and non-SAA spectra separately, it is necessary to switch automatically between them, i.e. to make the SAA spectra active when the ISS entered the SAA and the non-SAA spectra active when it leaves the anomaly. The algorithm for performing this procedure was developed based on the results of the measurements carried out with DOSTEL in different shielding configurations (Burmeister et al. 2000). The effectiveness of the method was tested with model time spectra calculated from the time spectra obtained by DOSTEL after taking into account the differences in the telescope geometry. Depending on the parameter of the algorithm and the expected number of counts, the switching between the SAA and non-SAA spectra might take place due to the statistics of the measurement. In order to determine the probability of this "false switching", statistical uncertainty was added to the calculated spectra by means of a pseudo-random number generator (Hirn 2009b).

Modelling the anisotropy of the GCR at low Earth orbit

In my calculations it is assumed that the 3D telescope is installed outside the wall and shielded by the space station from the nadir direction (Fig. 1). The x-axis of the telescope points along the orbital velocity vector, the z-axis toward the nadir direction, and the y-axis completes the right-handed coordinate system. Calculations are performed for ISS orientation with zero pitch, roll and yaw angles. Free-space GCR spectra for protons and alpha particles were obtained with the FLUX module of the CREME96 model (heavier ions were not included in the calculations).

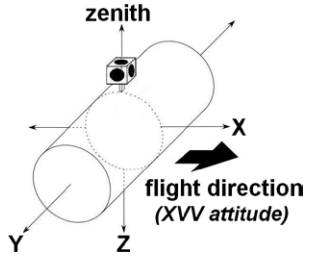

Fig. 1. Orientation and position of the telescopes.

The GTRN module of CREME96 can be used for evaluating geomagnetic shielding but only in a vertical cut-off approximation (Tylka et al. 1997). In order to determine the directional distribution of the geomagnetic cut-off rigidity, the expression developed by Stoermer for characterizing the interaction of a charged particle with a dipole magnetic field was used (Stoermer 1937)

$$R = \frac{C_D \cos^4 \lambda_M}{r_D^{\,2}\left(1+\sqrt{1-\cos^3 \lambda_M \sin\zeta \sin\psi}\right)^2} \qquad \text{Eq. 1.}$$

where R is the directional cut-off rigidity in GV, λ_M is the magnetic latitude, r_D is the distance from the magnetic dipole centre in Earth radii, ζ is the zenith angle, ψ is the azimuth angle measured clockwise from the magnetic north and C_D is a constant which is directly proportional to the dipole moment, and has a value of 59.6 GV for the 2000 IGRF (International Geomagnetic Reference Field) dipole. Geographical coordinates of the ISS as a function of the time were provided by the coordinate generator package included in ESA's Space Environment Information System (SPENVIS 2003; Heynderickx et al. 1996). The magnetic coordinates λ_M and r_D were obtained after coordinate transformations. At the altitude of the ISS the magnetic field of the Earth can be well approximated by the eccentric dipole model. The parameters of the coordinate transformations i.e. the colatitude (θ_N) and the azimuth (φ_N) of the point of intersection of the geomagnetic axis with the Earth's surface in the northern hemisphere in the centred dipole model as well as the translation in the x, y and z directions (η^*, ζ^* and ξ^*, respectively) are shown in Table 1.

Table 1. Parameters of the coordinate transformation.

Parameter	Value	Reference field model
θ_N	79.54°	IGRF 2000
φ_N	288.43°	IGRF 2000
η^*	–0.06308 R_{Earth}	IGRF 2000
ζ^*	0.04713 R_{Earth}	IGRF 2000
ξ^*	0.03149 R_{Earth}	IGRF 2000

Stoermer's expression does not account for the presence of the solid Earth. Since the details of how exactly the Earth's umbral shadow changes with altitude is still unknown (Smart et al. 2000, 2006), for the sake of simplicity, the Earth was considered as a solid sphere. At the altitude of the ISS the solid angle occulted by the Earth is 1.4π. The cut-off distributions as a function of the particle's energy and the angle of incidence were calculated in the reference frame fixed to the given telescope axis. The angle of incidence was discretized with a discretization step of 5°. With knowledge of the free-space GCR spectrum and the cut-off distribution, the LEO GCR spectrum was determined. To estimate the deposited energy spectra the FLUKA Monte Carlo transport code developed by the Italian National Institute for Nuclear Physics (INFN) and the European Organisation for Nuclear Research (CERN) was used (Ferrari et al. 2005; Battistoni et al. 2007). The geometry was simplified to two 300-micrometer-thick

silicon detectors at a distance of 8.9 mm with an active area of 222 mm^2 and an aluminium slab representing an effective shielding. Concerning the aluminium slab two different thicknesses were chosen:

– 0.5 mm of aluminium in front of the detectors (mechanical constraints);
– 74 mm (20 g/cm^2) of Al in the direction of the ISS.

Particles were generated from behind the slab. The deposited energy spectra were calculated with the DETECT card in coincidence mode. The minimum total energy to be scored in one event in the measuring detector region, as well as the coincidence threshold was 70 keV. Below this value the contribution of charged particles to the coincidence spectra is negligible (Hirn et al. 2007).

Modelling the anisotropy in the SAA

In the Earth's magnetic field charged particles are moving in spiral paths around the geomagnetic field lines bouncing back and forth between the mirror points. The SAA is also close to a mirror point where the pitch angle with respect to the magnetic field vector approaches and recedes from 90°. The proton flux is therefore maximized in the plane normal to the local magnetic field. Protons arriving from the west have trajectories with gyration about a point located above the reference observational point and hence they encounter less residual atmosphere than protons arriving from the east. This results in an asymmetry, where at a given point the flux of protons coming from the west is higher than the flux of protons coming from the east (Badavi et al. 2006). Although, there exist models (Watts et al. 1989; Badhwar, Konradi 1989) that are capable of predicting the directional flux of the charged particles, most of the cosmic radiation models that have been used for describing the cosmic radiation field are omnidirectional, including the "de-facto" standard AP8 and AE8 trapped proton and electron models.

Directionality of the proton flux then can be expressed as follows

$$\frac{J(\theta,\psi)}{J_{4\pi}} = F_N \exp\left[\frac{-(\pi/2-\theta)^2}{2\sigma_\theta^2}\right] \exp\left[\frac{r_g \cos I \cos\psi}{d_s}\right] \qquad \text{Eq. 2.}$$

where J is the vector flux, $J_{4\pi}$ is the omnidirectional proton flux provided by the AP-8 trapped proton models implemented in SPENVIS, θ and ψ are the pitch and azimuth angles respectively, d_s is the ionospheric scale height, I is the magnetic dip angle, r_g is the proton gyro-radius in km, σ_θ is the standard deviation of the pitch angle and F_N is a normalization factor (Kern 1994). To get a rough estimation of the directionality of trapped particles, calculations were performed with the positional version of the 'radiation sources and effects' package of SPENVIS. In the calculations, one single SAA transit was considered. The orbit was tailored to pass through near the centre of the SAA (centred near 29.4° S, 45.6° W in 2010).

Results

Performance of the SAA switching algorithm on model time spectra

Since the number of counts measured with TriTel depends on several factors (e.g. altitude, solar activity, shielding configuration), it might considerably change during a mission or from one mission to another. Therefore the switching algorithm developed is based not only on the absolute value of the number of counts but on its relative change

as well. The switching between the SAA and the non-SAA spectra takes place in real time. Passage through the anomaly is indicated by an SAA flag, its value outside SAA is 0 (the measured counts contribute to the non-SAA spectra). The number of counts in consecutive 60-second-long time intervals is registered in the time spectra. In case the relative change in the sum of the time channels of the x-, y- and z-axis exceeds a predefined δ value, the SAA flag changes to 1 and the number of counts starts to be registered in the SAA spectra. TriTel switches back to the non-SAA spectra (value of the SAA flag is 0) only if the number of counts decreases below the value registered at the time of the previous switch (Hirn 2009b).

From the calculations the value of δ at which the probability of false switching is less than 10^{-3} was found to be 0.34 and 0.25 for the spectra generated from the measurements with DOSTEL during the STS-84 mission and in the Matroshka-1 experiment, respectively. The difference in the two values can be attributed to the fact that during the STS-84 mission DOSTEL was inside the Space Shuttle, while in the Matroshka-1 experiment it was located outside the wall of the ISS. Therefore, in the former case, due to the smaller number of counts and so the higher standard deviation, the relative difference between the numbers of counts in two neighbouring time channels might be more significant. Since the number of SAA peaks in the model time spectra has shown weak statistics, no detailed statistical analysis has been performed on the maximum value of δ (δ has a nearly uniform distribution between 0.3 and 0.8).

In the view of the above I proposed $\delta = 0.35$. Fig. 2 shows the performance of the algorithm applied for the model time spectra generated from the STS-84 measurements of DOSTEL for this case.

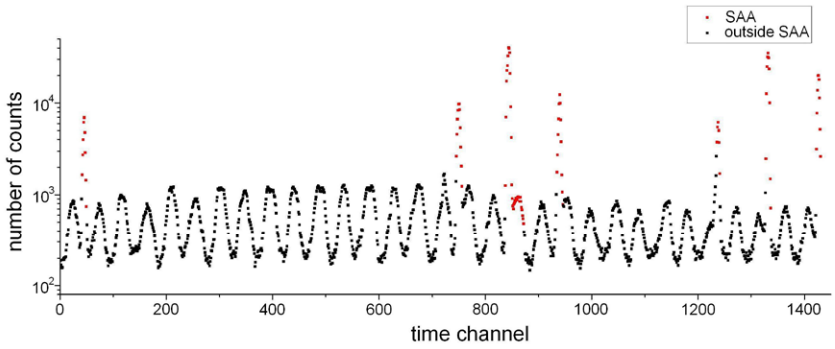

Fig. 2. A sample from the results of the SAA-switching algorithm applied to the model time spectra.

Effects of the anisotropy of untrapped GCR particles on the model calculations

The cut-off distributions for 0°, 20°, 40°, and 60° angles of incidence are shown in Fig. 3 in the case of a telescope axis pointing toward the geographical zenith direction. Below 10 GV, the four curves are practically identical. The contribution to this low cut-off region comes from segments of the orbit when the ISS is passing at higher latitudes where the change in the geomagnetic cut-off due to the change in the zenith and azimuth angles is not so significant. However, the differences in the curves above 10 GV originate from the zenith dependence of the cut-off at latitudes that are close to the geomagnetic equator.

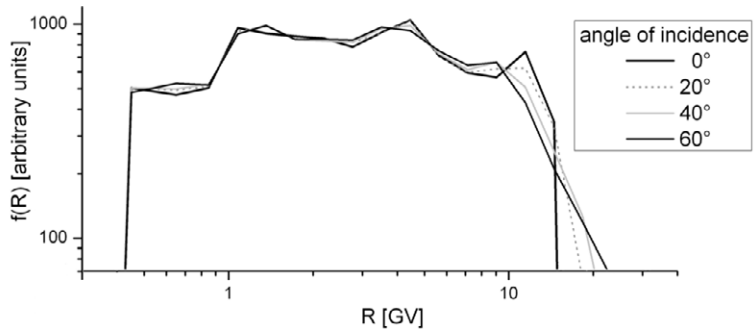

Fig. 3. Cut-off distribution for different angles of incidence for a telescope pointing towards the geographical zenith direction.

As for the total deposited energy spectra, the spectra in the x- and y-directions were found to be the same due to symmetry reasons and, in spite of the planar geometry of the detectors, no difference could be seen in the zenith direction either. Because of the planar geometry of the silicon detectors, the absorbed dose measured can be significantly higher for non-relativistic particles incident perpendicularly to the axis of the detector than for particles with normal incidence to the effective surface of the detector. Since the nadir, from which direction the radiation is considerably shielded by the Earth, is perpendicular to the axes of the x- and y-telescopes, the contribution of these higher energy deposits is lower in the total deposited energy spectra in the x- and y-directions. However, the lower cut-off values in the zenith direction have the opposite effect. In order to interpret the results in more details and determine the significance of the effects described above, further calculations are needed. The effects of the anisotropy of the galactic cosmic rays in LEO arise in the coincidence spectra and so in the calculated LET spectra, as well (Fig. 4).

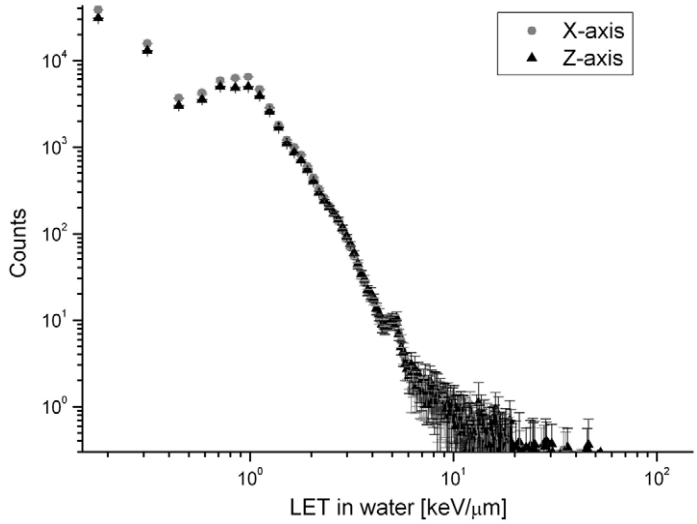

Fig. 4. LET spectra of protons and alpha particles determined from the coincidence spectra in the X and Z directions (the Y coincidence spectrum was found to be identical with the X spectrum; therefore it is not indicated in figure).

Contrary to the total deposited energy spectra, the number of counts in the LET spectra in the x- and y-directions is significantly higher than in the z-direction. The fact, that in case of the z-axis, 50% of the field of view is occulted by the Earth, while this ratio is only 30% in case of the x- and y-axis, might result in this effect (because the altitude of the spacecraft is 340 km, a considerable part of the particles coming from the –z directions can give a contribution to the coincidence spectra of the x- and y-axis).

Since only protons and alpha particles were considered in the calculations and the uncertainties in the number of counts related to the energy deposit of particles with a LET value higher than 10 keV/µm in water was high, no significant difference could be observed in the calculated quality factors. In order to study the differences in the quality factors, ions heavier than alpha-particles shall be included in the calculations as well (Hirn 2010).

Effects of the anisotropy of trapped particles in the SAA on the model calculations

The integral fluxes of trapped protons that can enter the sensitive volume of the detector are plotted in Fig. 5 as a function of the magnetic pitch angle. The fluxes were determined in seven distinct positions in the section of the orbit of the ISS crossing the SAA. Inside the SAA, protons arrive from directions within 10–15° of the plane perpendicular to the geomagnetic field line. Even if we take into account that the geographical and geomagnetic axis do not coincide, the velocity vectors of the trapped protons lie outside the field of view of the z-telescope. Therefore, these particles will contribute only to the coincidence spectra in the x- and y-directions but not the z-direction (Hirn 2010). A more quantitative description of the directionality of the trapped radiation can be performed by analyzing Eq. 2.

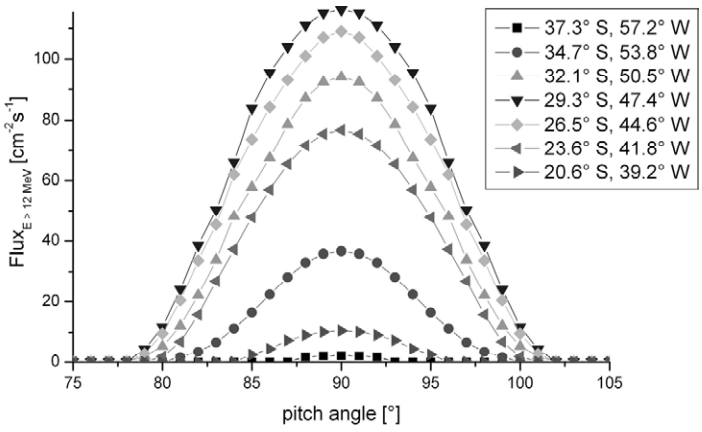

Fig. 5. The integral flux of trapped protons as a function of the pitch angle inside the SAA.

Discussion

The optimal value of the δ parameter of the SAA switching algorithm for a given experiment can be determined only after the first measurement data has been evaluated. However, the fine-tuning of the parameter is necessary. In the knowledge of the time spectra the effects of the time-shifts and the false switching might be corrected during the on-ground evaluation of spectra.

The calculations presented in the paper show that the effects of the directionality of the geomagnetic cut-off are negligible compared to that of the Earth's shadow when integrated over the orbit. In order to demonstrate the effects of the anisotropy of the untrapped radiation in the measured dose equivalents and quality factors, it will be necessary to take into consideration heavier ions as well. The trapped protons inside the SAA evidence an even more pronounced anisotropy. The velocity vectors of the trapped protons lie outside the field of view of a telescope pointing toward the zenith direction. However, with a 3D telescope, the LET spectrum of the trapped radiation can be studied as well. The author wishes to acknowledge the services provided by SPENVIS and CREME96 hereby.

Conclusions

In this paper only the anisotropy of the radiation field outside the ISS was addressed. Inside the space station, due to the complexity of the shielding distribution, simulating the deposited energy spectra is even more complicated; hence, 3D measurements on board the space station should be performed. In the light of the above, three different versions of the TriTel 3D telescope are being developed at AEKI. One version, in the framework of the European SURE project, will perform measurements on-board the Columbus module of the ISS, one in cooperation with the Institute of Biomedical Problems on-board the Russian segment of the ISS and finally another version will measure the LET spectra and the dose on board the ESEO satellite in the near future.

References

Apathy I, Akatov Yu A, Arkhangelsky V V, Bodnar L, Deme S, Feher I, Kaleri A, Padalka I, Pazmandi T, Reitz G, Sharipov S. TL dose measurements on board the Russian segment of the ISS by the "Pille" system during Expedition –8, –9 and –10. Acta Astronaut. 2007; 60: 322–328.

Badavi F F, West K J, Nealy J E, Wilson J W, Abrahams B L, Luetke N J. A Dynamic/Anisotropic Low Earth Orbit (LEO) Ionizing Radiation Model. NASA/TP-2006-214533; 2006.

Badhwar, G D, Kushin V V, Akatov Yu A, Myltseva V A. Effects of trapped proton flux anisotropy on dose rates in low Earth orbit. Radiat. Meas. 1999; 30: 415–426.

Battistoni G, Muraro S, Sala P R, Cerutti F, Ferrari A, Roesler S, Fassò A, Ranft J. The FLUKA code: description and benchmarking. In: Albrow M, Raja R (Eds.). Proceeedings of the Hadronic Shower Simulation Workshop. 2006 Sep 6–8; Fermilab, Batavia, Illinois. AIP Conference Proceedings; 2007; 896: 31–49.

Burmeister S, Beaujean R, Kopp J, Reitz G, Data on Radiation Belt and Solar Energetic Particles deduced from Dosimetry in Low Earth Orbits. 5th Workshop on Radiation Monitoring for the International Space Station, 2000 Sep 7–8; Louvain-La-Neuve, Belgium; 2000.

European Space Agency (ESA). European Users Guide to Low Gravity Platforms. UIC-ESA-UM-0001, Issue 2 Rev. 0. Noordwijk; Erasmus User Centre and Communication Office; 2006.

Feher I, Deme S, Szabo B, Vagvolgyi J, Szabo P P, Csoke A, Ranky M, Akatov Yu A. A new Thermoluminescent Dosimeter System for Space Research. Adv. Space Res. 1981; 1: 61–66.

Ferrari A, Sala P R, Fassò A, Ranft J. FLUKA: a multi-particle transport code, CERN 2005-10. INFN/TC_05/11; SLAC-R-773; 2005.

Heynderickx D, Lemaire J, Daly E J, Evans H D R. Calculating low-altitude trapped particle fluxes with the NASA models AP-8 and AE-8. Radiat. Meas. 1996; 26: 947–952.

Hirn A, Apathy I, Bodnar L, Csoke A, Deme S, Palfalvi J K, Pazmandi T, Szabo J, Szanto P. Development of a Complex Dosimetry Equipment for the Columbus Module of the International Space Station. In: 58th International Astronautical Congress. 2007 Sep 24–28; Hyderabad, India. Paper IAC-07-A1.9.-A2.7.01. ISSN 1995–6258 (CD-ROM); 2007.

Hirn A. Development of space dosimetry systems (in Hungarian). PhD thesis. Budapest, Hungary; BME NTI; 2009a.

Hirn A. Determining the time intervals of South Atlantic Anomaly crossings with the TriTel 3D silicon detector telescope (in Hungarian). Sugárvédelem. 2009b; 2(2).

Hirn A. Models of performances of dosimetric telescopes in the anisotropic radiation field in low Earth orbit. Acta Astronaut. 2010; 66: 1368–1372.

Kern J W. A note on vector flux models for radiation dose calculations. Radiat. Meas. 1994; 23(1): 43–48.

Lemaître G, Vallarta M S. On Compton's latitude effect of cosmic radiation. Phys. Rev. 1933; 43: 87.

Pazmandi T, Deme S, Lang E. Space dosimetry with the application of a 3D silicon detector telescope: response function and inverse algorithm. Radiat. Prot. Dosim. 2006; 120: 401–404.

Smart D F, Shea M A, Flückinger E O. Magnetospheric models and trajectory computations. Space Sci. Rev. 2000; 93: 271–298.

Smart D F, Shea M A, Tylka A J, Boberg P R. A geomagnetic cutoff rigidity interpolation tool: accuracy verification and application to space weather. Adv. Space Res. 2006; 37: 1206–1217.

Stassinopoulos E G, Staffer C A. Forty-Year Drift and Change of the SAA. NASA Goddard Spaceflight Center 2007.

Stoermer C. On the trajectories of electric particles in the field of a magnetic dipole with applications to the theory of cosmic radiation. Astrophys. Norv. 1937; II(4): 193–248.

Tylka A J, Adams J H, Boberg P R Jr, Brownstein B, Dietrich W F, Flueckiger E O, Petersen E L, Shea M A, Smart D F, Smith E C. CREME96: a revision of the cosmic ray effects on micro-electronics code. IEEE Trans. Nucl. Sci. 1997; 44: 2150–2160.

Watts J W, Parnell T A, Heckman H H. Approximate angular distribution and spectra for geomagnetically trapped protons in low-Earth orbit. In: Rester A C, Trombka J I Jr (Eds.). High-energy radiation in background space. AIP Conference Proceedings. New York Santibel Island, FL 1987; 1989.

Wilson J W, Cucinotta F A, Golightly M J, Nealy J E, Qualls G D, Badavi F F, de Angelis G, Anderson B M, Clowdsley M S, Luetke N, Zapp N, Shavers M R, Semones E. International Space Station: a testbed for experimental and computational dosimetry. Adv. Space Res. 2006; 37: 1656–1663.

Sequential separation of alpha and beta emitters from natural samples by mixed solvent anion exchange and their subsequent determination

Rozmaric Macefat, Martina
Rudjer Boskovic Institute, CROATIA

Abstract

Determination of alpha and beta radionuclides in environmental samples, food and drinking water is important from the aspect of human health and environmental protection. Low level activities determination of pure alpha and beta emitters in natural samples, prior to detection and quantitative determination, requires isolation of radionuclide from the sample and simultaneous separation from interfering elements. The extraction chromatography is mostly used method in last decade. However, due to chemical and mechanical stability and low price, ion exchangers are a good alternative to expensive extraction chromatographic resins because they don't lose their capacity with multiple usage, whereas resins do. It is very important, for the ion exchanger to be applicable in the separation, that its capacity is not a limiting factor (ion exchange must not be a dominant mechanism of bounding). This work will show that anion exchangers in nitric form, in combination with alcohol solution of nitric acid, can be used for separation of all kinds of cations. The effect of dielectric properties of solutions on the bounding strength of particular cations to anion exchangers in nitric form, its effect on exchanger selectivity conversion for Ca, Sr, Y, Pb, Th, U, Am and Pu from HNO_3 solutions in methanol, ethanol and acetone, as well as the separation possibility of various cations, based on changes in solution properties, will be presented. The effect of change in dielectric constant on the bounding strength of certain cations to the exchanger will be shown in temperature range from -50 to 20°C, and how it can be used in cation separation. For quantitative determination of certain isotopes, already existing methods have been modified (LSC, Cherenkov counting, alpha and gamma spectrometry, ICP MS). Finally, simple and rapid methods, which are used in daily Laboratory work, have been developed for isolation and quantitative determination of $^{89,90}Sr$, ^{210}Pb, and other isotopes.

Optically stimulated luminescence in salt tested against thermally stimulated luminescence in LiF and ambient survey measurements in a ^{137}Cs contaminated village in Belarus

Bernhardsson, Christian[1]; Matskevich, Svetlana[2]; Mattsson, Sören[1]; Rääf Christopher[1]

[1] Medical Radiation Physics, Department of Clinical Sciences Malmö, Lund University, Skåne University Hospital, SE-205 02 Malmö, Sweden

[2] Republican Research & Practical Centre of Radiation Medicine and Human Ecology, Ilyicha Street 290, BY-246 040 Gomel, Belarus

Abstract

Ordinary household salt (NaCl) have previously been investigated in the laboratory and has exhibited several promising properties for dosimetry, e.g. a linear dose response down to a few mGy and a low detection limit. In an attempt to test NaCl as a dosemeter outside the laboratory, we here report the first results from the use of NaCl as a dosemeter under normal environmental conditions, both indoor and outdoor. For this purpose, special dosemeter kits, each containing two chips of LiF and 2×10 mg of NaCl were designed. During the summers of 2008 and 2009 the dosemeter kits were positioned pair wise inside and outside the outer walls of 17 houses located in a village which was highly contaminated by ^{137}Cs from Chernobyl, in the Gomel region (Belarus). After 2.5 – 3 months the dosemeters were collected and read out using thermoluminescence (TL) and optically stimulated luminescence (OSL), respectively. The estimated dose rates from the two dosemeter systems were then compared for each kit and in addition, the dose rate at positioning and collection of the dosemeters was measured using a hand-held ambient dose survey meter (GR-110) based on a 5.0 x 3.8 x 3.8 cm^3 NaI(Tl)-detector.

The radiation level in the village was found to be highly inhomogeneous, even within the gardens around the houses. On average, the radiation level around the houses was 3 – 8 times higher compared to a normal background dose rate (0.10 μSv h^{-1}). Despite the relatively low signals, a strong correlation was observed between the results of the salt dosemeters and the portable NaI(Tl)-detector (r^2 = 0.89), but the correlation between NaCl and LiF was weaker (r^2 = 0.64). The repeated study in 2009 confirmed the potential for ordinary cheap household salt as a tool for retrospective dose estimates.

Introduction

In order to estimate radiation absorbed doses to the general public after an event that involves unwanted exposure of ionising radiation, several retrospective methods have been suggested, see e.g. (ICRU, 2002; Alexander et al. 2007). The Medical Radiation Physics group in Malmö has especially focused on optically stimulated luminescence (OSL) of household salt (NaCl) as a tool for retrospective dosimetry. The dosimetric properties of different brands of household salt have been investigated in the laboratory (Bernhardsson et al. 2009; Christiansson et al. 2008a; Christiansson et al. 2008b) and several promising properties for dosimetry have been found. The next step is now to test salt as a dosemeter *in situ*, under normal environmental conditions and during extended periods of time. This has been done in an environment that has been affected by a major surface contamination of anthropogenic radionuclides, mimicking a situation in which the dosemeters are aimed to be used in the future, after e.g. radiological and nuclear accidents as well as after antagonistic use of radiation and radioactive substances.

The Vetka district in the Gomel region (Belarus) was found to be an area that fulfils these conditions where one of the villages, Svetilovichi, was one of the most contaminated settlements outside the 30 km zone after the Chernobyl catastrophe. Parts of this district were decontaminated in 1986 – 1987, but not the village of Svetilovichi. The people living in this village were advised to relocate to areas with less contamination, but most of the inhabitants decided to stay instead of abandon their homes and village. However, in 1991 a more systematic decontamination was carried out in the village (roads and outside public buildings, i.e. kindergartens and the hospital). Thereafter, in 1999, and as part of the IAEA regional project RER/9/059 (Andersson K.G. et al. 2001), Svetilovichi was selected as a village for practicing and improving the existing techniques of decontamination. New equipment was bought and experts on decontamination were training the personnel at the federal state company Polesye (Gomel) who is specialized in cleaning contaminated buildings. Up till 2006, about 50 houses and gardens have been decontaminated according to the program and today, all of the most heavily contaminated houses have been decontaminated.

During the summers of 2008 and 2009, measurements of the gamma radiation level in the village of Svetilovichi were carried out by the Medical Physics group in Malmö (Lund University, Sweden) in cooperation with the Chernobyl Committee (Minsk, Belarus) and the federal state company Polesye (Gomel, Belarus). One of the aims of the project was to investigate household salt as an optically stimulated dosimeter (OSLD) when used in a contaminated environment.

Material and methods

The village of Svetilovichi is situated in eastern Belarus (Latitude: 52°47'43.76"N; Longitude: 31°19"11.88"E), between Gomel (Gomel region, Belarus) and Novozybkov (Bryansk region, Russia). Due to heavy rainout of the passing plume of the Chernobyl release, the Gomel region received an average ^{137}Cs surface deposition of 154 kBq m^{-2} [Drozdovitch V. et al. 2007]. Since 1990s, individual effective dose estimates of the internal and external exposure have been carried out in a number of the nearby villages, on the Russian side of the border, see e.g. (Thornberg C. et al. 2001; Thornberg C. et al. 2005; Bernhardsson C. et al. 2008).

Assemblying and positioning the dosemeters

To investigate the radiation level in some of the decontaminated and non-decontaminated houses in Svetilovichi, between 5 and 14 dosemeter kits were placed inside- and outside each of the houses described in Table 1. Each dosemeter kit contained two chips of LiF (TLD100, Harshaw) and two sections (about 10 mg each) of NaCl (Falksalt fint bergsalt, Hansson and Möhring, Halmstad, Sweden), a regular seasoning salt in Sweden. The TL-chips and the salt were placed between two 4 mm thick sheets of PMMA, thus forming a dosemeter kit with two different luminescent materials. Before the dosemeter kits were put together, during the night before the distribution, the salt was exposed to sunlight (bleached) in order to empty the stored dose information. To avoid further bleaching of the luminescence signal, all dosemeter kits were covered with light-tight black tape. Another precaution was to place the dosemeter kits in plastic bags filled with silica gel, to protect the dosimetric material from rain and moist during the varying outdoor weather conditions.

Table 1. Description of the houses and the extent of countermeasures carried out at each dwelling. Fifty-six dosemeters were used at houses 1-7 in 2008 and 69 dosemeters at houses 8-17 in 2009. The thickness of the outer walls on the wooden houses was about 0.2 – 0.3 m and 0.5 m on the brick houses.

House	Walls/Roof	Decontaminated[a]
1.	Wood/Aluminum sheet	Yes
2.	Wood/Eternit	No
3.	Wood/Eternit	Yes
4.	Bricks/Aluminum sheet	Partly[b]
5.	Wood/Eternit	Yes
6.	Bricks/Eternit	No
7.	Bricks/Eternit	No
8.	Wood/Eternit	No
9.	Wood/Eternit	No
10.	Wood/Eternit	No
11.	Wood/Eternit	Yes
12.	Wood/Eternit	Yes
13.	Wood/Eternit	No
14.	Wood/Eternit	No
15.	Wood/Eternit	Yes
16.	Wood/Aluminum sheet	No
17.	Wood/Eternit	No

[a] Decontamination of a building includes; cleaning of roofs and walls using high-pressure water as well as removal of the top soil layer (10 cm depth) from the house wall and 2 m out and replacing it with sand. Highly contaminated roofs were removed and replaced with new ones.
[b] Walls on houses made from bricks were not cleaned.

The investigated houses were all documented by Polesye and had a known history from the owners. In this way, only houses built after 1986 and where no major changes of the constructions (after 1986) had been carried out, were selected for the measurements. The dosemeter kits were fixed firmly on both the inside- and outside of the walls of the houses, in opposite positions on the wall where it was possible and about 1 m above the floor level. Rooms that were most frequently used e.g. living room, bedroom and kitchen were prioritised for the indoor measurements. The ambient dose rate at the position of the dosemeters was registered with a handheld 3.8×3.8×5 cm^3 NaI(Tl)-detector (GR-110, Exploranium, Canada). These measurements were repeated when the dosemeters were collected approximately 2.5 months later and a mean value of the two measurements was used as a reference value to the dosemeter readings. To compare the absorbed doses to the dosemeter kits with the readings of the GR-110 instrument, a general calibration coefficient (free in air using a ^{137}Cs source; SMM, Department of Emergency Preparedness and Environmental Monitoring, certificate No:06-08S01) of 1.15 nSv/h cps^{-1} has been used.

Read-out procedure

The dosemeters were distributed, at 56 positions in 2008 and 69 positions in 2009, during the last week of May and were re-collected in the middle of August. They were immediately transported back to Sweden and shortly after that, the LiF chips were read-out in a TL–reader (Toledo, Vinten Instruments Ltd., England) at Sahlgrenska University Hospital in Göteborg. To assess the signal in the salt, it was optically stimulated by blue light (λ = 470±30 nm) at the Medical Radiation Physics department in Malmö, using a TL/OSL-DA-15 reader (Risø National Laboratory, Roskilde, Denmark). The net OSL signal was defined as the registered luminescence during the first 2 s subtracted by the average luminescence after 10-12 s, 20-22 s and 31-33 s of stimulation. In order to convert the net OSL signal to an absorbed dose a pre determined calibration coefficient ($c_{specific}$ = 313 counts mg^{-1} mGy^{-1}) for this particular brand of salt was used (Bernhardsson et al. 2009). It should be noted that $c_{specific}$ is determined for a specific brand of salt, from a single jar, and then generalised to hold for all salt jars of the same brand, thereby assuming that the salt in all jars are identical. To account for changes between individual dosemeters and salts taken from different jars, there are other means of calibration that can be used. One approach is to use the single-aliquot-regenerative-dose (SAR) protocol (Murray et al. 1998) where successively increasing doses, in the range of the dose to be determined, are given to the salt after the read out. This approach was however impossible to carry out at the time of the readouts in 2008 and 2009 and hence the protocol and calibration coefficients described by Bernhardsson et al. (2009) have been used.

A correction for the additional dose originating from the exposure during transportation from Svetilovichi and storage before read-out has been carried out. To estimate the magnitude of this dose, ambient survey meters were used at various positions along the travel route from Belarus and the final destinations (the laboratories in Malmö and Göteborg, Sweden, respectively). From these measurements an average background dose rate was calculated and subtracted from the total dose accumulated during the probing time.

Results and discussion

The average dose rate during transportation and storage was determined to 0.10 μSv h^{-1}. The total dose accumulated during transit and storage varied individually and has hence been subtracted from the total dose registered by each dosemeter. Unfortunately, the dose to the TLDs used in 2009 was not possible to retrieve due to problems with the TLD-reader and therefore, the OSLD to TLD comparison was not achievable that year.

In Fig. 1 is the absorbed dose as determined by NaCl and LiF plotted as a function of the corresponding dose obtained from the handheld NaI(Tl)-detector at the position of the luminescent dosemeters. In spite of the low detector signals there is a fairly good correlation between the dosemeters and the radiation protection instrument. However, the OSLDs exhibit on average, a 15% higher absorbed dose than the TLDs. This might indicate a too small signal background subtraction of the NaCl batches, or a too high signal background subtraction of the LiF-chips. It could also be a consequence of sensitivity changes in the LiF-chips during the measuring period. Another explanation could be that anomalous fading of the signal is more rapid in the specific LiF-chips used, compared to NaCl, at least during the first 2 – 3 months.

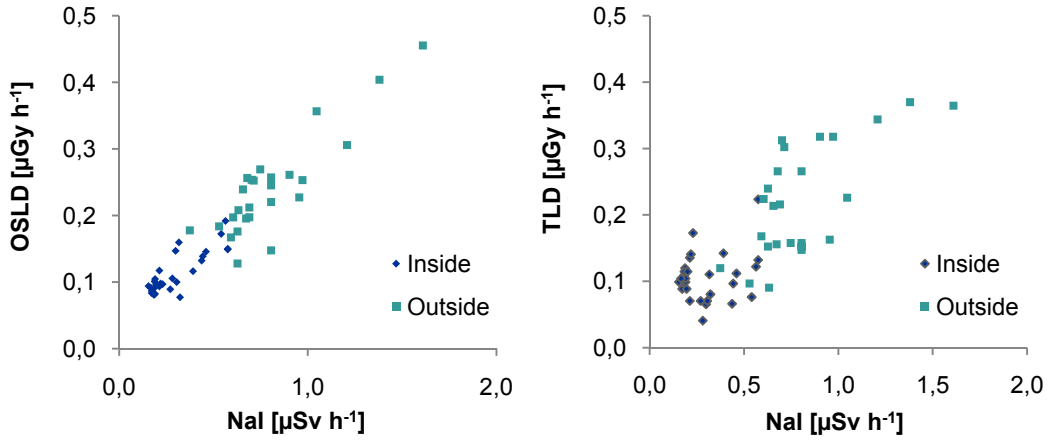

Figure 1. Absorbed dose in OSLD and TLD as a function of the dose registered by GR-110 (average of measurement at outset and pickup of the kits). Included in the figures are measurements from 56 dosemeter kits (positions) in 7 houses, during the summer of 2008. Different colours have been used to distinguish between dosemeters positioned inside and outside the buildings.

Generally, the dose rates indoor were rather low, comparable to the normal background radiation level in many European countries. Outside the houses the average dose rate was 3 – 8 times higher compared to the indoor values. The pair-wise correlation between the results of the 3 measurements in terms of Pearsons's r^2 was higher for the outdoor measurements compared to those inside. Nevertheless, there was a moderately or a strong correlation between all of the investigated dosemeters (Table 2). The correlation was strongest between the OSLDs and GR-110, which may partly reflect the similar responses between these two detectors for the photon energies studied. It is however apparent that some of the specific LiF chips used in this study exhibited a rather low sensitivity and this in turn may have adversity influenced the detection limit (0.01 mGy, as specified by the manufacturer).

Table 2. Covariance matrix (r^2-values), for the three dosemeters tested in the survey in 2008.

	OSLD	TLD	GR-110
OSLD	1	0.64	0.89
TLD	-	1	0.65
GR-110	-	-	1

The dose rates measured with the OSLDs, plotted as a function of the correspondingly dose rates of GR-110, in the years 2008 and 2009, is shown in Fig. 2. There is a noticeable difference in the linear relationship between the two years, with:

$$OSLD_{2008} = 0.24 \cdot NaI + 0.04 \qquad \text{Eq. 1}$$

$$OSLD_{2009} = 0.40 \cdot NaI + 0.10 \qquad \text{Eq. 2}$$

Even though it was not the same houses that were investigated, the dose response in the salt should not be affected by this factor. The ranges in the registered doses are similar in both years but the slope and intercept of the lines are significantly different (Eq. 1 and Eq. 2).

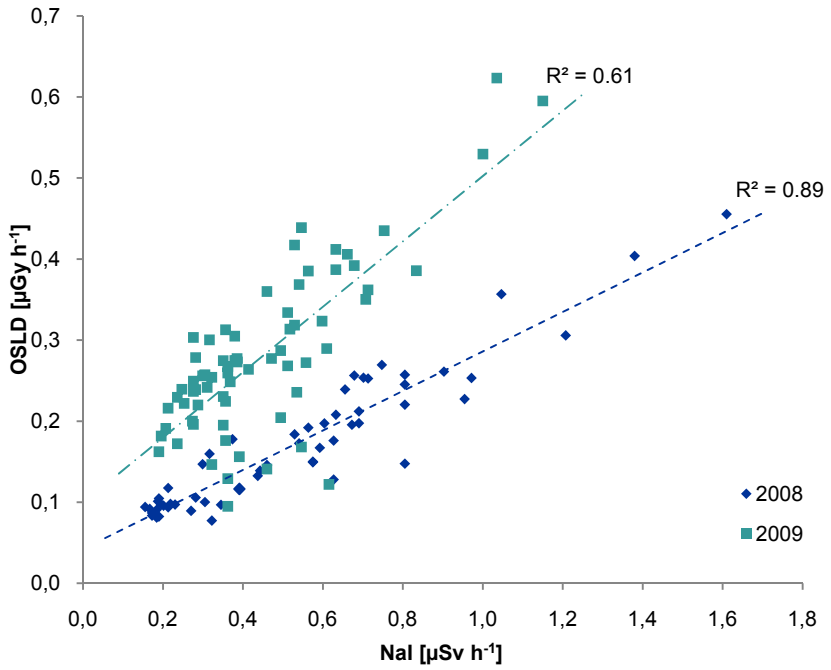

Figure 2. Absorbed dose rate as measure by the salt dosemeters in 2008 and 2009 as a function of the dose rate as measured with GR-110 at the position of the dosemeters.

The sensitivity is about twice as high in the salt used in 2009 compared to 2008, despite the fact that they are from the same brand of salt. The reason for this diversity is that the particular salts used were taken from different jars. The jar of salt used the first year was packed in December 2006 and the salt used in 2009 was packed in March

2009. Hence, the salts were probably extracted from different salt layers within the same, or different, mines and possibly mixed with salt from other deposits before it was packed and distributed. Changes in these fractions will accordingly change the properties of the salt as a dosemeter.

Another observation is that the salt used in 2009 appears to have a slightly weaker correlation to the GR-110 reading, compared to the salt used in 2008. One factor that influences this is the distribution of grain sizes within a particular package of salt. Large grains will generally give less luminescence per absorbed dose compared to small grains, at a given weight. Since the salt was not sieved (fractionated due to grain size), this might be one of the major factors for the discrepancy found in the OSLD measurements in 2008 and 2009 caused by using two different jars of salt.

Conclusions

Even though the study was carried out with pre-manufactured dosemeter kits, the salt demonstrates a promising potential as a tool for retrospective dose reconstructions. The salt in the dosemeter kits exhibits a good or a strong correlation to measurements carried out using a radiation protection instrument and TLDs. The repeated survey increases the confidence in salt as an OSLD, despite the fact that the measuring conditions were slightly different during the two different years.

Small changes to the experimental set-up by changing a few factors can further increase the usefulness of salt as a dosemeter. One of these is to sieve the salt before the read-out, thereby making the salt more homogenous and thus, minimising the risk of analysing inefficiently used grains. Another one is to use individual calibrations of each dosemeter, e.g. by the use of the SAR-protocol. One benefit with this approach is that changes in the sensitivity between two different jars of salt, from the same brand, will be incorporated in the calibration. Another benefit is that almost every salt on the worlds market becomes available as a potential dosemeter.

References

Alexander GA, Swartz HM, Amundson SA, Blakely WF, Buddemeier B, Gallez B, Dainiakg N, Goans RE, Hayes RB, Lowry PC, Noska MA, Okunieff P, Salner AL, Schauner DA, Trompier F, Turteltaub KW, Voisin P, Wiley AL Jr., Wilkins R. BiodosEPR-2006 Meeting: Acute dosimetry consensus committee recommendations on biodosimetry applications in events involving uses of radiation by terrorists and radiation accidents. Radiation Measurements 2007; 42:972-996

Andersson KG, Antsipov GV, Astashko GA, Balonov MI, Barkovsky AN, Bogachev OM, Golikov VY, Kenik IA, Kovgan LN, Matveenko SA, Mirkhairdarov AK, Roed J, Zombori P. Guide on decontamination of rural settlements in the late period after radioactive contamination with long-lived radionuclides. 2001 (IAEA Working Document: TC Project RER/9/059) 84 p.

Bernhardsson C, Christiansson M, Zvonova I, Jesko T, Jakovlev V, Rääf CL, Mattsson S. Long-term radiation exposure of inhabitants in the Bryansk region in southwestern Russia. Proceedings of the IRPA12 Congress [CD-ROM]. 2008 October 19-24; Buenos Aires, Argentina

Bernhardsson C, Christiansson M, Mattsson S, Rääf CL. Household salt as a retrospective dosemeter using optically stimulated luminescence. Radiation Environmental Biophysics 2009; 48(1):21-28

Christiansson M, Bernhardsson C, Mattsson S, Rääf CL. Optimization of read-out sequences for optically stimulated luminescence (OSL) of household salt for retrospective dosimetry. Proceedings of the International conference on radioecology and environmental radioactivity. 2008 June 15-20; Bergen, Norway

Christiansson M, Bernhardsson C, Rääf CL, Mattsson S. Test of household salt read by optically stimulated luminescence (OSL) as a personal dosemeter. Proceedings of the IRPA12 Congress [CD-ROM]. 2008 October 19-24; Buenos Aires, Argentina

Drozdovitch V, Bouville A, Chobanova N, V Filistovic, Ilus T, Kovacic M, Malátová I, Moser M, Nedveckaite T, Völkle H, Cardis E. Radiation Exposure to the population of Europe following the Chernobyl accident. Radiation Protection Dosimetry 2007; 123(4):515-528

ICRU (2002) Retrospective Assessment of exposures to ionising radiation. ICRU Report 68. Nuclear Technology Publishing, Ashford, United Kingdom

Murray A, Roberts, R. Measurement of the Equivalent Dose in Quartz using a Regenerative-Dose Single-Aliquot Protocol. Radiation Measurements 1998; 29:503–515

Thornberg C, Vesanen R, Wallström E, Zvonova I, Jesko T, Albinsson J, Börjesson J, Mattsson S. Long-term radiation exposure of inhabitants in the western Bryansk region of Russia as a consequence of the Chernobyl accident. Radiation Environmental Biophysics 2001; 40:287-294

Thornberg C, Vesanen R, Wallström E, Zvonova I, Jesko T, Balonov M, Mattsson S. External and internal irradiation of a rural Bryansk (Russia) population from 1990 to 2000, following high deposition of radioactive caesium from the Chernobyl accident. Radiation Environmental Biophysics 2005; 44:97-106

Visualization of hot particles in lung of radionuclide associated with emergency preparedness by means of clinical gamma cameras

Hansson, Mats; Rääf, Christopher
Medical Radiation Physics, Department of Clinical Science Malmö, Lund University, Malmö University Hospital, SWEDEN

Abstract
In a situation when radionuclides accidentally or deliberately are dispersed in the environment and individuals have been internally contaminated there is an urgent need for localization of the radionuclide in affected individuals. The aim of this study is to examine the possibilities to visualize hot particles of radionuclides with gamma energies close to and beyond the upper level of the pulse height analysers (PHA) of clinical gamma camera systems. The aim is also to examine the possibilities to visualize hot particles of pure β-emitters with a clinical gamma camera. An anthropomorphic phantom was used to mimic uptakes in the lung region of three different radionuclides associated with emergency preparedness ^{60}Co ^{137}Cs and ^{90}Sr/^{90}Y (0.8, 0.16 and 2.2 MBq respectively). The radionuclides were located in or outside the right lobe of the lung insert. The conclusion of this study is that point sources, mimicking a hot particle of a given radionuclide can clearly be visualized even in cases when the primary gamma photon energy exceeds the upper limit of the PHA. This study indicates also that point sources of pure β-emitters can be visualized. Hence gamma camera systems can be useful for rapid assessment of inhaled hot particles in connection with radiological and nuclear accident.

Introduction
There are a number of radionuclides of special concern within the emergency preparedness; for instance ^{60}Co, ^{137}Cs and ^{90}Sr/^{90}Y, which are frequently used in hospitals, in the industry and at research laboratories. In addition to these sources, nuclear power plants generate airborne aerosols and surface contamination of ^{60}Co as a result of neutron activation of stable cobalt in construction materials, which can accidently be ingested or inhaled by workers (D. W. Whillans, W. J. Chase and W. H. Wolodarsky 2007). Another source of radionuclides in nuclear power plants is fission products of ^{235}U such as ^{137}Cs and ^{90}Sr/^{90}Y. These radionuclides are generally not dispersed to the surroundings except in cases of severe nuclear reactor accidents, such as the Chernobyl accident in 1986. Other potential exposure pathways to humans are transportation accidents or releases in connection with terrorist activities where

radionuclides are involved (ICRP 96, 2003). In previous mention scenarios there is a need for methods to rapidly screen suspected intakes of e.g. ^{60}Co and ^{137}Cs in individuals by means of in-vivo measurements. Potential resources that are useful in case of nuclear and radiological emergencies must be explored. Equipment and personnel connected to radiological work at general hospitals are one such resource. Clinical gamma camera imaging systems, which are available in many hospitals, would be a valuable addition to the capacity of emergency measurements.

Wallström et al., (1998) examined the possibility to use a gamma camera for visualizing of ^{137}Cs in man by using bottle phantoms. The major part of the work was performed with a gamma camera consisting of a NaI(Tl)-detector with a crystal thickness of 1.2 cm. The limitations with many gamma camera systems are that some radionuclides associated with emergency preparedness scenarios emit gamma photons with energies beyond the upper level of the energy window of the PHA. Therefore, imaging of organ uptakes of the high energy photon emitters must be deduced by detection of scattered radiation. A previous study using a Siemens MultiSPECT 2 with various acquisition settings for imaging of ^{46}Sc and ^{60}Co in the lungs and abdomen were carried out at our department (Hansson et al., 2008).

The aim of this work is to evaluate the possibility to use clinical gamma camera systems for visualization of the presence of radionuclides associated with emergency preparedness in the lungs, also in cases where the primary photon energies exceed the normal operative range of the PHA. In addition to gamma emitters associated with emergency preparedness (e.g. ^{60}Co and ^{137}Cs) we aim to evaluate the possibility to visualise presence of pure beta-emitters (^{90}Sr/^{90}Y) by the detection of bremsstrahlung.

Material and methods

Gamma camera systems and imaging of high energy gamma quanta

Two gamma camera imaging systems have been used in this study, the principal measurements being carried out on a Siemens MultiSPECT 2 (Siemens, Erlangen, Germany), The MultiSPECT 2 is a dual-head imaging system with NaI(Tl)-detectors having a field-of-view of 53.3x38.7 cm^2 and a crystal thickness of 0.95 cm. Complementary pilot measurements have been carried out on a Symbia SPECT-CT (Siemens, Erlangen, Germany) which is a SPECT-system equipped with an low dose CT. The point source of the radionuclide was placed on the right lung lobe close to the heart compartment or inside the same lung compartment of the phantom (Fig 1). The first alternative was used when the physical size of the holder of the point source did not allow it to pass in to the inside of the lung compartment. When exploring the MultiSPECT 2 capability to visualise lung uptakes of point sources, the entire energy window, 45-535 keV, of the PHA was used. High energy collimator was used in connection with the MultiSPECT 2 measurements. The matrix size of the SPECT image was 128x128 and filtered back projection reconstruction algorithm was used. For the Symbia SPECT-CT an energy window of 100-300 keV was used, together with a medium energy collimator. The matrix size of the image was 64x64 and here an iterative reconstruction algorithm was used.

Phantom characteristics

An anthropomorphic phantom (Alderson-phantom, RSD 2008) specifically designed for calibration of imaging systems within nuclear medicine has been used in this study. The phantom is composed of different materials with attenuating properties comparable to human tissues. Phantom inserts shaped as human internal organs, such as lungs, liver and heart, can be filled with various radioactive solutions of known activity to simulate different organ uptakes. By supplying additional human tissue equivalent material on the anterior of the phantom torso, three different body sizes can be simulated. The body sizes are; *i.*) average male 74 kg, (personal communication Helen Kelly, RDS) *ii.*) large male more than 74 kg and *iii.*) large female more than 74 kg. Only the "average male" phantom was used in this study.

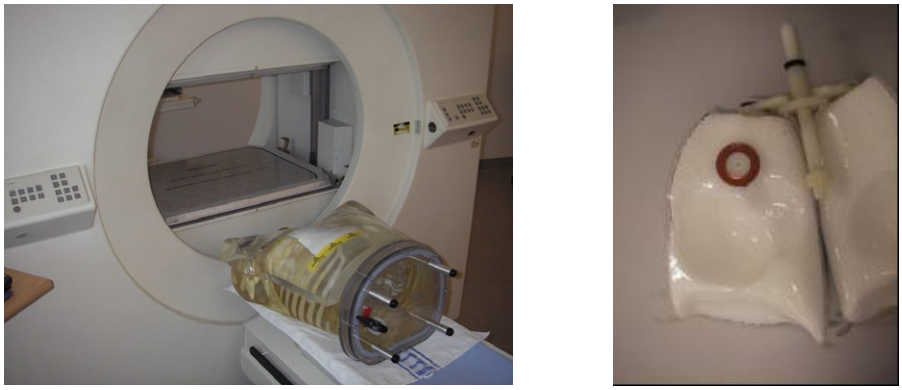

Fig 1. Left frame: The Alderson phantom positioned on the patient couch of the MultiSPECT 2 gamma camera. Right frame: The lung insert of the Alderson phantom with a point source on the outside.

Radionuclides

Three key radionuclides associated with the emergency preparedness scenarios as mentioned before were used in this study. The photon energies emitted by these radionuclides was 661.6 keV (^{137}Cs) and 1132 keV and 1332.5 keV, respectively (^{60}Co). The possibility to visualize uptakes of pure β-emitters in the lung has also been investigated using a commonly occurring β-emitters ^{90}Sr/^{90}Y ($E_{\beta,Average}$=0.196 MeV / $E_{\beta,Average}$=0.934 MeV). For the ^{90}Sr/^{90}Y the radiation detected by the gamma camera consists of the bremsstrahlung originating from the interaction between the high-energy β-particles within the tissue material. In Table 2 the investigated radionuclides and some of their properties are summarised.

Table 2. Strength of the point sources used simulating hot particles. ^{90}Sr was in equilibrium with the daughter ^{90}Y that emits the *β*-p.

Radionuclide	$T_{1/2}$ [year]	Main energy [keV]	γ-yield [%]	Activity [kBq]
^{60}Co	5.3	1173/1332	100/100	800
^{137}Cs	30	662	85	160
^{90}Sr /^{90}Y	29/0,0073	196/934 (average β-energy)	100/100	2200

Results and discussion

Visualisation of lung uptakes for different radionuclides

Fig 1-3 show images (matrix 256*256) obtained with the MultiSPECT 2 visualise ^{60}Co, ^{137}Cs and ^{90}Sr/^{90}Y in the Alderson phantom. An increased intensity at the position of the sources is clearly seen in all images compared to the background. The obvious disadvantage with planar gamma camera imaging in this case is the lack of correlation of the point source and the anatomy in the image. It could be a help to use so called landmarks in form of ^{57}Co sources of low activity placed on well defined points on the thorax of the internal contaminated person in the measuring situation. In fig 1 the image representing a hot particle in the lung containing ^{60}Co appears as a cloud with no distinct delimitation. Such an image may be of limited help in an emergency situation, but with another levelling of the SPECT image the area of the cloud can be reduced and become somewhat more guiding in terms of localisation of the particle. The general problem is that the high gamma energy (1173 keV/1332 keV) emitted from ^{60}Co is more than twice that of the ULD at 535 keV of the MultiSPECT 2.

Fig 4-6 show images (matrix 64*64) obtained with the Symbia SPECT-CT visualising hot particles of ^{60}Co, ^{137}Cs and ^{90}Sr/^{90}Y, respectively, in the Alderson phantom. The obvious advantage with fused SPECT-CT imaging compared to planar gamma camera image is the possibility to correlate the point source to a specific point in the anatomy. The correlation between the point source in the anatomy is not only given in one dimension but in three dimensions. N.B. that the image layers of the SPECT and CT are morphed at the coronal plane of the phantom.

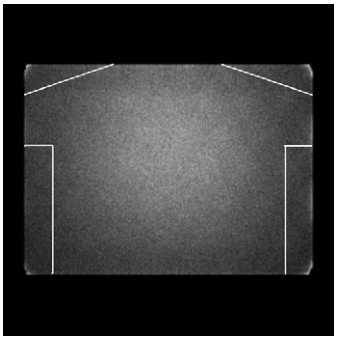

Fig 1. ^{60}Co, 800 kBq, point source positioned on the right lung lobe.

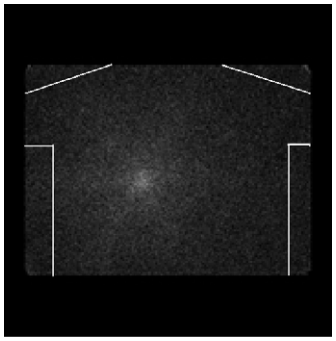

Fig 2. ^{137}Cs, 160 kBq, point source positioned on the right lung lobe.

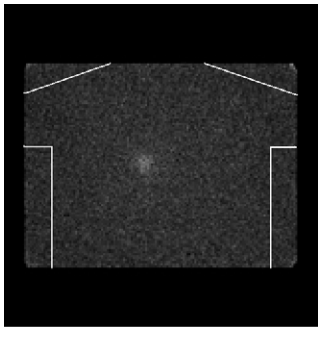

Fig 3. ^{90}Sr/^{90}Y, 2300 kBq, point source positioned in the right lung lobe.

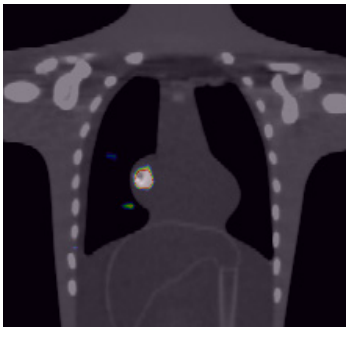

Fig 4. ^{60}Co, 800 kBq, point source positioned on the right lung lobe.

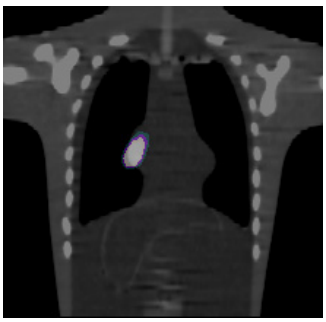

Fig 5. ^{137}Cs, 160 kBq, point source positioned on the right lung.

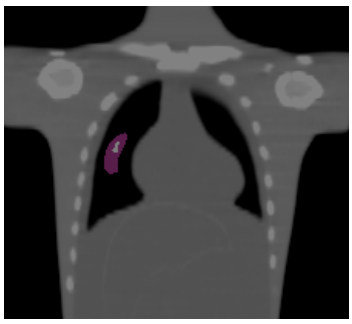

Fig 6. ^{90}Sr/^{90}Y, 2200 kBq, point source positioned in the right lung.

Conclusions

The conclusion of these pilot studies can be summarised as follows;

- Lung uptakes of a point source with gamma energy high above (^{60}Co) the ULD appear as a cloud with no clear delimitation by planar gamma camera and as a point with distinct delimitation by SPECT-CT imaging system.
- Lung uptakes of a point source with gamma energy close to or right above (^{137}Cs) the ULD can be visualized as a point with distinct delimitation both by planar gamma camera and by SPECT-CT imaging system.
- Lung uptakes of a point source of a pure beta-emitter (^{90}Sr/^{90}Y) can clearly be visualized as a point with distinct delimitation both by planar gamma camera and by SPECT-CT imaging system. In fact, the bremsstrahlung of ^{90}Sr/^{90}Y is more clearly delineates the hot particle in the planar image than do the scattered ^{60}Co radiation.

Our study thus indicates that clinical gamma cameras and SPECT-CT can be a useful instrument for visualisation of human lung contents of gamma emitting hot particle normally associated with emergency preparedness scenarios, and for pure β-emitting radionuclides as well. Future work is to examine which settings of the SPECT-CT are optimum for visualisation of high photon energy emitting sources in the inhalation tracts, and the detection limit in terms of activity for which the source can be visualised in an image at given acquisition times.

References

Kelly, H., E-mail contact (2009-10-22), Administrative Assistant at RDS, Radiology Support Devices, Inc. 1904 E. Dominguez Street, Long Beach, CA 90810

Hansson, M. (2008) Detection limits and quantification of ^{60}Co with gamma camera and handheld gamma detectors in human phantom.

International Commission on Radiological Protection, ICRP (1990) Annual Limits on Intakes of radionuclides by workers based on the 1990 recommendations, ICRP publication 61.

International Commision on Radiologial Protectiton, ICRP (2005) Protecting people against radiation exposure in the event of a radiological attack, ICRP Publications 96.

International Organization for Standardization, ISO/IEC Guide 98-3:2008. Guide to the expression of uncertainty in measurement (GUM:1995)(2008).

Radiology Support Devices, RDS, 1904 East Dominguez Street, Long Beach, CA 90810 USA.

Wallström, E., Alpsten, M., Mattsson, S., (1998) A gamma camera for measurements of internal contamination after a radiological accident. J. Radiol. Prot. Vol. 19 No 2143-154.

Whillans*, D. W., Chase, W. J., Wolodarsky, W. H., (2007, June 7). Does assessment for ingestion of an 330 kBq ^{60}Co hot particle. Radiation Protection Dosemetry , pp. 90-92.

Whole-body counters for measurement of internal contamination in Finland

Huikari, Jussi; Pusa, Sauli; Muikku, Maarit
STUK – Radiation and Nuclear Safety Authority, P.O. Box 14, 00881 Helsinki, FINLAND

Abstract

STUK - Radiation and Nuclear Safety Authority - has two whole body counters for measurement of internal contamination. Both counters use high purity germanium detectors. The stationary system is installed inside a 50-ton iron room. The new mobile unit is built on a truck chassis. Both counters are used to assess the internal exposure of radiation workers and that of the Finnish public in general. Up to now, information of the location of the internal contamination has not been available due to measurement geometry in the mobile unit.

For this reason, a project was started to design and build a new counter in order to obtain location information and to improve detection efficiency. Monte Carlo simulations exploiting MCNPX were used together with voxel phantoms to guide the design process. The mobile unit can also be mobilised in emergency situations and it provides a fast and reliable method for both screening and dose assessment purposes. The need for assessing internal radiation doses in emergency situations is evident and has been demonstrated after the accidents e.g. in Brasil and Ukraine. This paper describes a design for the new mobile counter and presents calculated predictions of detection limits and efficiency.

Introduction

Assessment of internal radiation doses can be done using results from direct measurement of people or indirectly by excreta measurements. Estimations can also be made using air concentration data or activity concentrations in food stuffs combined with consumption data. By experience from occupational contamination cases we have noticed that air concentration data tends to give too low an estimate of the intake as well as estimates done from dietary data. In principle, the dietary data gives estimate for the whole population. However, individual differences are significant, depending on how much each individual uses wild-caught fish or wild berries or mushrooms. Therefore, the need for reliable measurements is obvious. The aim of measurements is to determine the intake of radioactive substances. The internal radiation dose is then assessed using metabolic and dosimetric models. *In-vivo* measurements are used to assess the internal exposure of radiation workers as well as the exposure of the public. In cases with high internal contamination, the purpose of measurements is to help in

deciding if medical treatment or other types of measurement for more exact dosimetry is needed. In situations with prolonged exposure repeated measurements are recommended. In emergency situations direct measurements should be done as soon as possible after an alert to give support for decision making and to reassure the general public.

Equipment

STUK has obtained a new mobile whole-body counter for measurement of internal contamination (Figure 1). The unit has been built on standard Volvo FE 42R truck. The carrossery is insulated and equipped with air conditioning, along with electric and diesel heaters which makes all year usage comfortable. The monitoring unit uses 230 V AC. This external power is backed up by a UPS system consisting of a powerful sine wave inverter, a sophisticated battery charger, a high speed AC transfer switch and AC distribution in a single light weight and compact enclosure. A battery pack (24 V/400 Ah) has been added in order to maintain measuring devices 24 hours in case of loss of the external mains. This battery pack is also charged by the alternator of the truck when the engine is running.

Figure 1. A new mobile whole-body counter.

The whole-body monitor inside the carossery consists of two HPGe detectors and Dspec Pro digital electronics from Ortec (Ortec 2005). The present geometry used is a modified chair with a shadow-shield made of lead to reduce background in detectors (Figure 2). The detector set-up consists of a coaxial p-type HPGe-detector with a 90% efficiency and a GAMMA-X detector which is a coaxial n-type HPGe having an efficiency of 80%. The former detector is placed in the middle of the chair for whole-body measurements and the latter is placed closer to the upper body, providing the possibility to detect iodine accumulated in the thyroid, for example. The GAMMA-X has an ultra thin entrance window made of beryllium, providing good efficiency also for low energy γ -rays. The detectors are surrounded by a 5 cm thick lead shield. The typical time used in a routine measurement is 1000 s. Background is determined using

the background phantom consisting of 14 pieces of 5 kg sugar bags. If needed the measurement distance can be adjusted by moving the detectors and the lead shield up or down.

Figure 2. The present measurement set-up in the mobile unit. The modified chair is made of lead. The white shadow shield is also made of lead from "waist" down. Upper part is made of steel covering the detectors and supporting them.

The stationary whole-body counter is shown in Figure 3 below. This chamber is built of old steel in order to avoid background radiation (often tiny amounts of ^{60}Co) from freshly rolled sheets. This indoor unit, usually called Ironroom, uses scanning bed geometry, detectors being positioned in a fixed location surrounding the person. The detectors presently in use are two HPGe (both 80 % crystals) above the person and one 28% crystal under the bed. In addition, two NaI detectors are installed above and two below the bed. The analysis program provides also the total count rate versus location graph. However, as the detectors are not collimated, only a modest spatial resolution can be achieved.

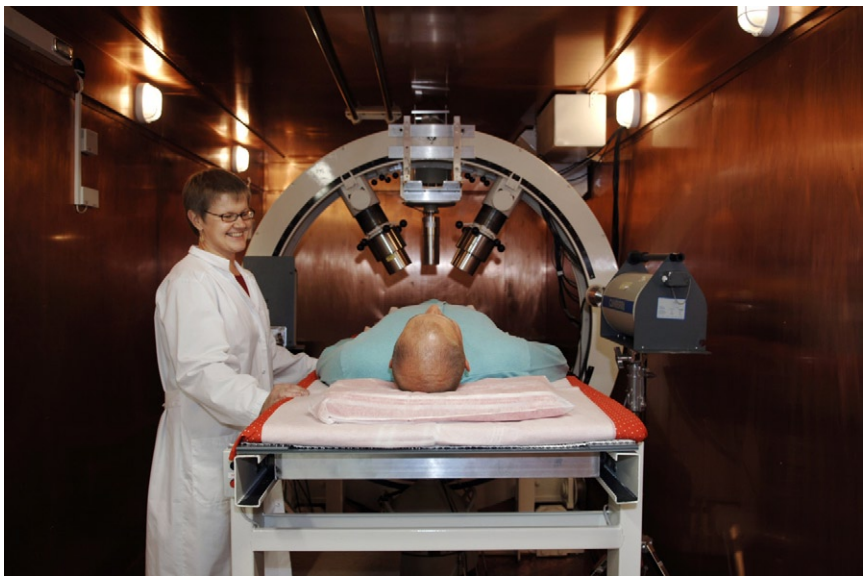

Figure 3. Inner view of the Ironroom. The indoor whole body counter uses HPGe and NaI detectors, some of which are visible above the person being measured.

The background phantom used in Ironroom is made of plastic containers filled with sugar. The containers include pieces for thorax, arms, legs, head and neck. The neck part can be replaced with a thyroid phantom.

Method

The efficiency calibration for both units is performed using the adult St. Petersburg whole-body phantom (Kovtun 2000) with ^{60}Co, ^{137}Cs, ^{40}K and ^{152}Eu rods (energy range 122-1460 keV). Figure 4 shows the efficiency calibration for a mobile unit. Both calculated and measured curves are shown. In addition, three St. Petersburg thyroid phantoms with ^{133}Ba capsules are available: adult, teenager (14 years old) and child (6 years old). Barium is used to imitate ^{131}I as its gamma energies are in the same energy range. The body burden of adult persons is determined roughly from knees to nose in the mobile unit. The Ironroom measures whole person. The whole-body phantoms from 12 kg to 110 kg corresponding ages from two-year old to adult were used to obtain the correction to the efficiency due to the size of the measured person. The correction factor ranges from 1.4 (12 kg) via 0.9 (90 kg) to 1 (110 kg).

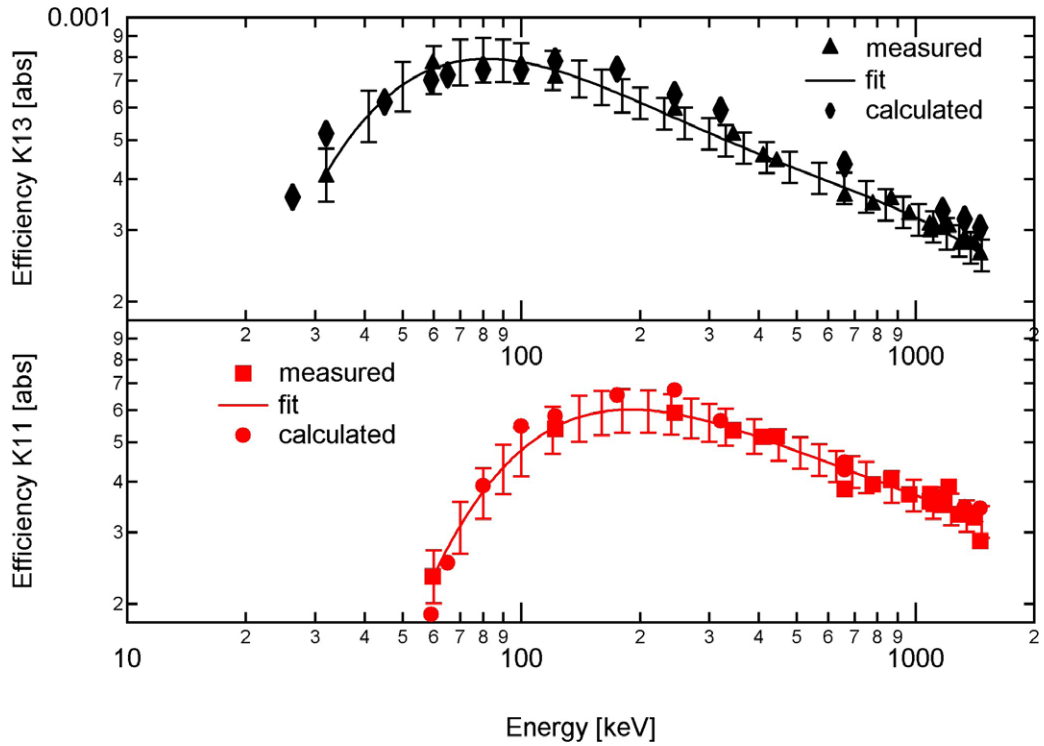

Figure 4. Efficiency curves for the p-type HPGe (K11, lower) and n-type GAMMA-X HPGe (K13, upper) detectors.

The uncertainty on the absolute γ-efficiency is 10 % for γ-rays >200 keV and goes up to 15 % towards lower energies. The final uncertainty on the activity measured will be determined by adding quadratically the statistical uncertainty of the identified γ-peak and that of the efficiency. For the most of the cases, uncertainties on the branching ratios and half-lives of the nuclei are so small that they can be neglected. The minimum detectable activities (MDAs) (Moilanen 2007) for the most commonly detected

artificial nuclei, ^{137}Cs and ^{60}Co have been determined to be of the order of 100 Bq. MDAs are roughly factor of two smaller in Ironroom. The minimum detectable activities for the most of the common radionuclides found in nuclear power plants, industry or radiopharmacy are sufficient from the point of view of radiation protection. As the MDA depends on the background level it should be determined when the background changes. In emergency situations the MDAs can be higher due to the higher background from the environment. However, as the MDA increases as a function of square root of background rate, the equipment will be able to handle it. *In-vivo* monitoring can also be used to follow prolonged exposure e.g. after a nuclear or radiological accident. Presently, the efficiency calibration assumes that the radionuclides are homogenously distributed in human body.

Mathematical calibrations and new set-up

STUK has launched the project in order to upgrade the measuring units. The main goal of the project is to obtain better treatment for the radionuclides that are not homogenously distributed in the body, for instance freshly inhaled radionuclides in the emergency situations. Other goals are to improve ergonomics for the person being measured and to gain more information about the location of the contamination in the body in the cases where intake path is not known. In addition, lower detection limits for some specific nuclei (like ^{241}Am, ^{123}I) which emit only low energy (<200 keV) gamma rays will be necessary to achieve. To begin with, Monte Carlo simulations will be used with voxel phantoms. The code selected is MCNPX (Monte Carlo N-Particle eXtended, Pelowitz 2005).

The simulations were started by reproducing the calibration for the present set-up where good measurements are available (Figure 4). For a new set-up, different possibilities were considered and ordinary chair geometry was chosen for a further study (Figure 5).

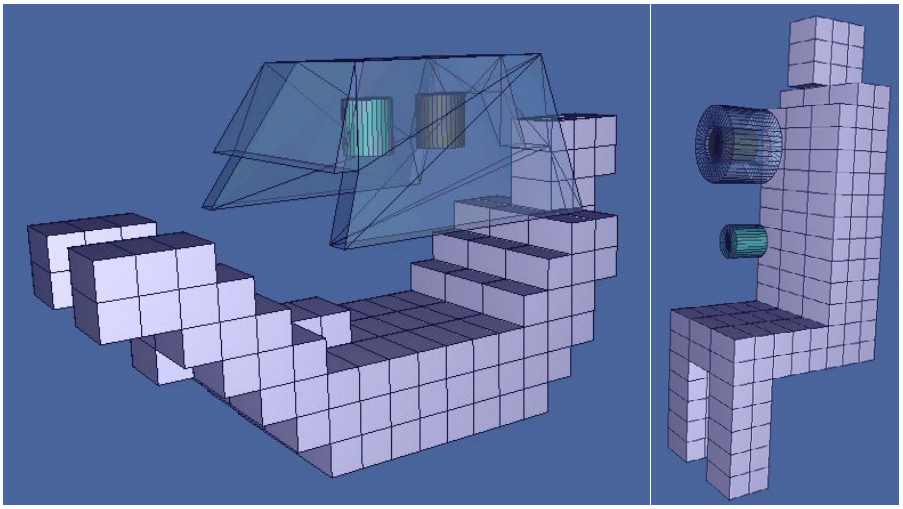

Figure 5. Models for MCNPX simulations. The present mobile unit set-up is on left and the new set-up is shown on the right. Transparent part is the lead made background shield. In the new set-up, shield of the lower detector is removed from the picture.

The background shield will be made of lead (not shown in Figure 5). There will be 5 cm of lead at the back, top and bottom and front side is open for a measurement. Cylindrical collimators around detector crystals can be moved along the axis, allowing fine tuning of the spatial resolution.

Figure 6 below presents calculated detection efficiency for a present and a new set-up in mobile unit. The overall efficiency with the new set-up will be better by a factor of 1.7 as the detectors can be closer. However, the detection efficiency will improve only for the region below the detectors. This can be compensated by using the sum spectrum for species like ^{137}Cs, which is known to be evenly distributed. For non-even distributions localisation of the activity can be done by comparing the measured two spectra. As can be seen in Figure 6, spatial resolution will be just enough to determine whether the activity is in lungs only or whether it has already been transferred further, for instance to liver as ^{60}Co would do.

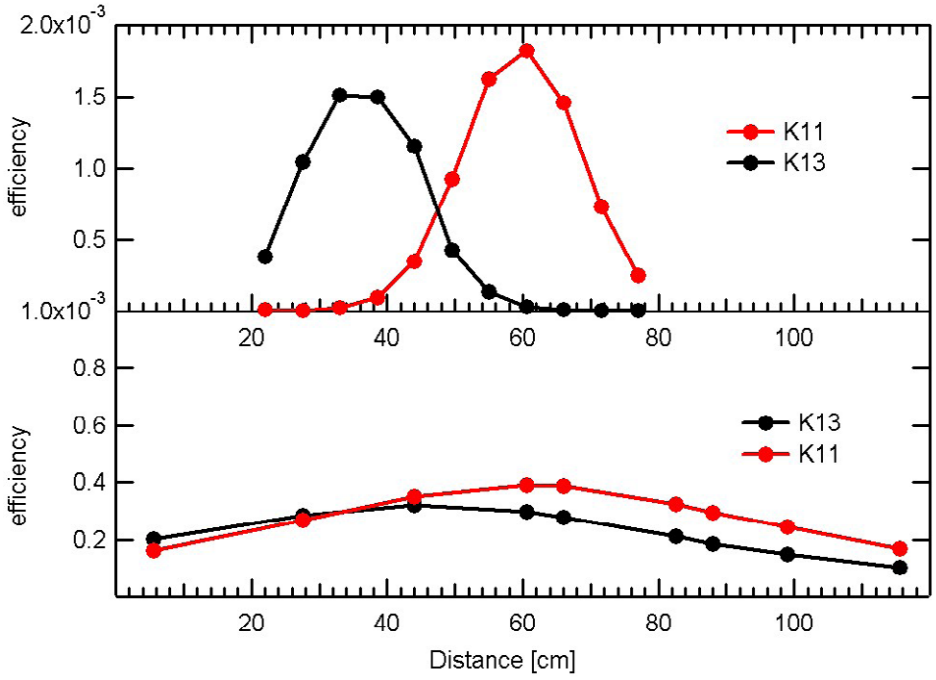

Figure 6. MCNPX simulation results for a polyetylene brick phantom. Each point has been calculated by placing 30 cm long cylinder of ^{137}Cs in different locations perpendicular to longitudinal axis of the phantom. The top curve displays the new set-up and the lower is for the present one.

Conclusions

In-vivo measurements are used to assess the internal exposure of radiation workers as well as the exposure of the public. The whole-body counters in STUK fulfil the requirements defined by the dose registration limits of radiation workers. In emergency situations it will be necessary to perform also direct measurements on people for reassurance of the public even if such measurements would not be necessary from a strictly radiation protection point of view. The new measurement unit will provide fast and reliable method for both screening and dose assessment purposes. The gamma ray detection efficiency for the whole energy range will be greatly increased. A significant

improvement will be the new feature of localisation of the internal contamination. In addition, it will give more precise information about possible ^{131}I accumulation in the thyroid. The new set-up presented above will be studied further in STUK. Calibrations with well defined calibration phantoms need to be performed before commissioning.

References

DSPEC Pro, Digital gamma-ray spectrometer, Hardware user's manual, ORTEC part no. 794380, manual revision C 2005, IL USA.

Kovtun, A.N., Firsanov, V.B., Fominykh, V.I. and Isaakyan, G.A. Metrological parameters of the unified calibration whole-body phantom with gamma-emitting radionuclides. Radiation Protection Dosimetry, 2000, **89**(3-4), 239-242.

Moilanen A, HPGe-ilmaisimia käyttävän kokokehomittauslaitteiston kalibrointi ja testaus (in Finnish). Helsinki University of Technology, Espoo, 2007.

Pelowitz, D., 2005. MCNPX™ User's Manual, Version 2.5.*0*. Los Alamos National Laboratory, Los Alamos, New Mexico, USA.

Determination of chest wall thickness of anthropometric voxel models

Hegenbart, Lars[1]; Gün, Harun[1]; Zankl, Maria[2]

[1] Institute of Radiation Research, Karlsruhe Institute of Technology (KIT), Hermann-von-Helmholtz-Platz 1, 76344 Eggenstein-Leopoldshafen, GERMANY

[2] Institute of Radiation Protection, Helmholtz Zentrum München GmbH (HMGU), Ingolstädter Landstraße 1, 85764 Neuherberg, GERMANY

Abstract

Chest wall thickness is a major quantity for the calibration of lung counting detector systems. A method for the determination of chest wall thickness of anthropometric voxel models is introduced and applied. The computer-aided method was compared successfully with mechanical measurements and found valid within small error ranges. This method allows the generation of three-dimensional, colour-coded profiles for visualisation of tissue thicknesses overlying an organ of interest. Furthermore Monte Carlo simulations of lung counting scenarios involving two germanium detectors were performed to show the performance of the method with a selection of voxel models.

Introduction

Chest wall thickness – an important counting efficiency calibration parameter for *in vivo* measurements

The detector efficiency for *in vivo* measurements of low energy photon emitters in the thorax (e.g. lung or liver) depends strongly on chest wall thickness (CWT). Hence, CWT is an important calibration parameter for counting efficiency. Systematic errors for the determination of counting efficiency can be reduced if the accuracy of the estimation of CWT can be improved.

The first challenge is a clear definition of CWT. For lung counting, the distance from the anterior skin surface of the thorax to the pleura (thin skin surrounding the lung) can be taken as a definition for CWT. However, this distance is not constant throughout the chest, but CWT can be averaged in the region that is covered by the detector. Consequently, position and size of detectors are important parameters for this definition.

Sumerling and Quant (1982) suggested a standard geometry for placing two scintillation detectors, one on the left, and one on the right side of the anterior chest. The centre of the detector was positioned in the intercostal space of the second and third rib. They performed ultrasound measurements on each side in the area of a circle with the detector's diameter to determine CWT.

Physical phantoms are used for calibrating counting efficiency. For example, the LLNL Torso Phantom (Griffith *et al.* 1978) has a set of overlays that can additionally be put onto the chest for the determination of counting efficiency. This way, counting efficiency can be described as a function of CWT.

Chest wall thickness of anthropometric voxel models

Anthropometric voxel models are increasingly used to calculate counting efficiencies for *in vivo* measurement systems numerically with radiation transport simulations based on Monte Carlo methods. An MCNPX (Hendricks *et al.* 2005) based Monte Carlo simulation environment for the partial body counter at KIT has been developed and validated (Hegenbart *et al.* 2009). Simulations can help to investigate counting efficiencies of radionuclides incorporated in arbitrary organs that might not be available in the laboratory's inventory. Thus, sensitive parameters can be identified which is helpful to develop strategies to reduce systematic errors of classical counting efficiency calibration.

Using voxel models can in principle help to represent an individual better than an ordinary physical calibration phantom, especially, if the model is customisable. Several novel techniques have been developed and allow generating customised anthropometric voxel models. The generation of customised voxel models for better representation of individuals should be based on biometric data of the individual. Hence, there is a demand to develop methods for measuring biometric data of voxel models in virtual reality. Those methods need to be comparable to conventional methods in reality. A previous example for this was the measurement of chest circumferences and cup sizes of a series of female voxel models (Hegenbart *et al.* 2008).

Since CWT is a sensitive biometric parameter for counting efficiency, it is meaningful to develop a method to determine the CWT of anthropometric voxel models.

Material and methods

Determination of CWT of voxel models

The determination of the CWT of anthropometric voxel models is based on measuring and averaging distances of body surface (skin) voxels to voxels of the target organ, i.e. the lung in case of lung counting.

The method is inspired by the determination of CWT with ultrasound, as for example presented by Sumerling and Quant (1982). The surface voxels are chosen according to a given detector diameter and its position and alignment onto the chest. The voxels lie in a cylindrical projection of the diameter of the detector along its axis onto the body surface. Starting from the surface voxels, the shortest distance – often perpendicular to the surface – to the nearest voxel of the organ of interest is determined. Depending on detector diameter and voxel resolution, hundreds to thousands of surface voxels are selected. Single distances x_i for each voxel are stored in a list.

The arithmetic mean can be calculated with the distances x_i from the list. Moreover, after defining a linear attenuation coefficient – suitable for the concerned tissue and photon energy – the *effective* CWT (Dean 1973, Kramer and Hauck 1997) can be calculated.

$$CWT_{eff} = -\frac{1}{\mu}\ln\left[\frac{1}{n}\sum_{i=1}^{n} e^{-\mu x_i}\right]$$

CWT_{eff}: effective chest wall thickness (mm)

n: number of list entries

x_i: distance i (mm)

μ: linear attenuation coefficient (mm^{-1})

The effective CWT takes the exponential attenuation law into account. Short distances are given higher weight, since photons can pass through them more likely. The higher the photon energy considered for the attenuation coefficient, the closer the effective CWT gets to the arithmetic mean. For photon energies starting from 60 keV, the effective CWT can be approximated with the arithmetic mean (Kramer 1999).

The introduced method for determination of the CWT of voxel models is integrated in the in-house developed software Voxel2MCNP (Hegenbart 2009). This software is able to generate and visualise *in vivo* measurement scenarios and furthermore to prepare and evaluate MCNP(X) Monte Carlo simulations with voxel models. The viewer of the software allows the generation of three-dimensional, colour-coded illustrations of the local distribution of the tissue thickness, i.e. a CWT-profile of a voxel model. This information can be used for optimisation of detector position and helps judging if a voxel model keeps a reasonable anatomy after customisation.

Validation of the method

The *in vivo* Measurement Laboratory (IVM) at KIT has a copy of the LLNL Torso Phantom (Griffith *et al.* 1978). The thicknesses were measured mechanically with a calliper within 14 cm diameter from the centre of the three concentric markings on the chest cover and on each overlay defining the detector position for lung and liver measurements. The physical phantom was compared with the voxel model of KIT's LLNL Torso Phantom, which was generated from computed tomography (CT) images performed at the Vincentius Kliniken of Karlsruhe by Prof. Dr. J. Lehmann and his team. The CT images were segmented and successfully used to validate Monte Carlo simulation of an *in vivo* measurement scenario (Hegenbart *et al.* 2009).

The mechanically measured data were compared to the corresponding CWT data obtained from the computer method from the voxel model. Furthermore, a comparison with effective CWT values from literature (Taylor 1997) was performed.

Monte Carlo simulations

Monte Carlo simulations of lung counting scenarios have been performed to investigate the relationship of voxel model's CWT and the corresponding counting efficiency. The voxel models used in this investigation were the

- MEET Man (Sachse *et al.* 1996) and Voxelman (Zubal *et al.* 1994) with organ density and material data from ICRP 89 (ICRP 2002),
- in-house developed voxel models of the LLNL-Phantom without and with four overlays with measured organ densities and materials specified by the manufacturer,

- LLNL-Phantom of the EURADOS Intercomparison on Monte Carlo modelling (Broggio 2009),
- ICRP Adult Male (ICRP 2009), and
- Godwin (Zankl *et al.* 2005) and Frank (Petoussi-Henss 2002) of HMGU.

With these voxel models *in vivo* counting scenarios were generated involving ^{241}Am-photon-emissions (Schötzig and Schrader 2000) homogeneously distributed in all lung voxels. The voxel models lie in supine position on a model of the examination table of KIT's partial body counter. In this scenario two detectors were placed on the chest using the validated model of the *in vivo* Measurement Laboratory's Canberra XtRa HPGe detector with a diameter of 7.5 cm (Marzocchi *et al.* 2009). The detector was inclined by 25° in order to be parallel to the skin surface of the chest with about 1 to 2 mm distance. The detector axis was centred on the third rib, 7 cm away from the centre of the sternum. This setup was symmetrical for one detector on the left and on the right side.

The CWTs (arithmetic means) of these voxel models have been determined with the above introduced method considering the detectors' positions and diameters. A CWT profile was generated for all phantoms.

MCNPX 2.6 (Hendricks *et al.* 2008) was used to simulate 10 million photon histories for each voxel model. The voxel model syntax for the MCNPX-input-file was generated with Voxel2MCNP according to recommendations by Taranenko *et al.* (2005). The code was run in MCNPX's mode p (photon transport only). The electron transport mode was skipped, because no significant differences were found in test calculations. Thus, it was possible to save computer time. The cross-section library PLIB=04p for photons and ELIB=03e for electrons were used.

MCNPX's F8 tallies were assigned to the active HPGe-crystal volumes. The counting efficiency was calculated in the energy range from 57.5 keV to 61.5 keV, which is about +/-1.5 FWHM. The net counting efficiency was determined subtracting the background with the trapezoidal rule from the full absorption peak of the 59.5 keV gamma line of ^{241}Am. Results from both detectors were summed up.

Results and discussion

Validation of the method

Table 1 shows a comparison of mechanically measured CWT values and calculated values from the corresponding voxel models. Both columns show the effective CWT with μ/ρ=0.93 cm^{2}g^{-1} for polyurethane tissue equivalent material with a muscle/adipose ratio of 50/50 for the overlays and μ/ρ=1.13 cm^{2}g^{-1} for 100% muscle for the chest cover, respectively, both at 17 keV (NIST 2009). The comparison of effective CWT values was preferred. The first reason for this was, to have a more strict comparison, which takes variances stronger into account. The second reason was, to make a comparison with literature values.

The values are in agreement with a maximum deviation of 1.0 mm. The values for the chest cover show the largest deviations. This is can be explained by the comparably large variances of the single measurements. 2σ-errors were estimated for the calliper measuring (0.1 mm) and for position inaccuracies (0.95 mm) on the voxel model. The

method for determination of effective CWT of voxel models can be taken as valid, considering an error of roughly 1 mm.

Most measured and calculated values lie in the range of values reported in the literature. Some phantom values are smaller than those reported by Taylor (1997). The investigated LLNL phantom at KIT is a third-generation, commercial version and might not be comparable with the second generation investigated by Taylor (1997). Manufacturer's specifications are unknown.

Table 1. Effective CWT of the mechanical measurements in the three concentric markings (liver, left and right lung) of the LLNL phantom of the phantom compared with the calculated values of the corresponding voxel model (Gün 2010). The obtained values are faced to literature values (average and range) from five laboratories, which owned the second generation of the LLNL phantom (Taylor 1997).

Configuration (concentric marking)	CWT_{eff} (mm) of phantom	CWT_{eff} (mm) of voxel model	Absolute deviation (mm)	Literature average values (range) (mm)
Chest cover (left lung)	15.4	16.2	0.8	16.4 (15.6-17.2)
Overlay B1 (left lung)	6.1	6.1	<0.1	6.6 (5.4-8.9)
Overlay B2 (left lung)	12.1	12.5	0.4	12.6 (11.2-14.5)
Overlay B3 (left lung)	17.2	17.3	0.1	17.6 (16.4-19.0
Overlay B4 (left lung)	24.0	24.2	0.2	24.7 (24.2-26.1)
Chest cover (right lung)	14.0	15.0	1.0	14.6 (13.3-15.0)
Overlay B1 (right lung)	6.3	6.5	0.2	7.0 (6.0-9.0)
Overlay B2 (right lung)	12.3	12.1	0.2	12.7 (10.8-13.8)
Overlay B3 (right lung)	17.0	17.4	0.4	17.9 (17.4-19.6)
Overlay B4 (right lung)	24.8	25.3	0.5	25.6 (24.8-27.2)
Chest cover (liver)	13.6	13.2	0.4	14.1 (12.9-15.2)
Overlay B1 (liver)	6.2	6.2	<0.1	6.8 (4.4-9.9)
Overlay B2 (liver)	11.2	11.1	0.1	11.8 (9.5-14.4)
Overlay B3 (liver)	16.4	16.3	0.1	18.1 (16.4-20.6)
Overlay B4 (liver)	24.5	24.4	0.1	24.7 (23.7-27.3)

CWT profiles

Figure 1 shows colour-coded CWT profiles (skin-pleura distance) of a selection of three voxel models. The profile of KIT's LLNL voxel model shows strong asymmetric shading due to the position of the heart, which covers partly the left lung lobe. This uncovers some limits of the LLNL phantom's anatomy in terms of realism. The other two models exhibit just a slight asymmetry. The ICRP Adult Male's chest wall is coloured partly in dark red, because he is less obese compared to the MEETMan. The red zones are suitable for placing detectors in order to get high count rates. Notable are local CWT minima near the second rib and at the lower end of the lung lobes. Such coloured profiles can be generated for every organ (e.g. the liver).

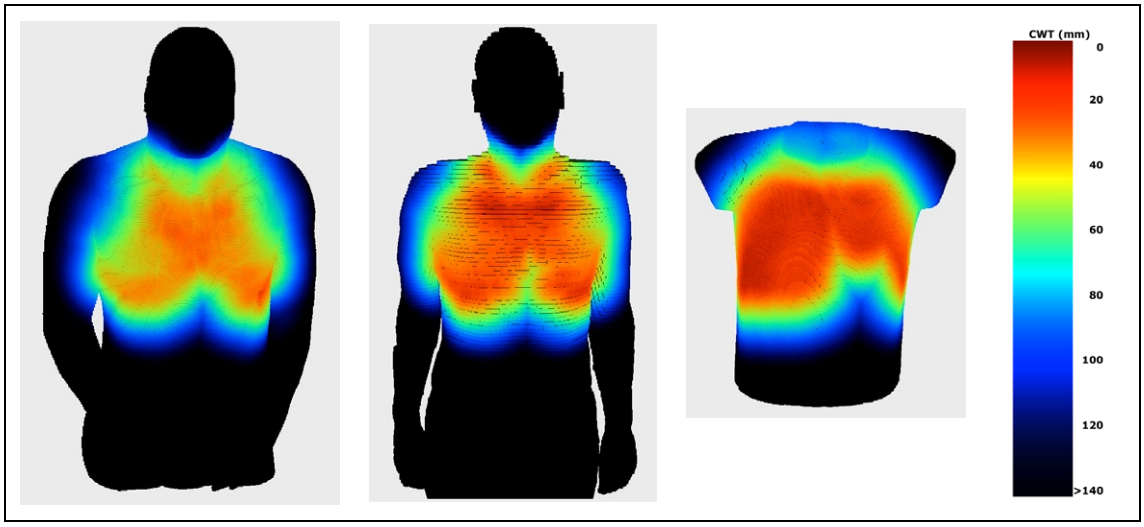

Fig. 1. CWT profiles of the MEETMan (left), the ICRP Adult Male (middle) and KIT's voxel model of the LLNL Phantom without overlay (right). Deep red colour indicates a small CWT (see legend, right). Larger CWT are indicated with the transition to shades of green. Dark-blue and black areas are not meaningful, since the distance to the lungs is too high and angles are not perpendicular to the skin surface anymore.

Monte Carlo simulations

Figure 2 shows the summary of the results. The left and the right detector's counting efficiencies for a ^{241}Am-lung-counting scenario were summed and plotted over the determined CWT (arithmetic mean of left and right) for each voxel model. Similar to routine *in vivo* measurements, the KIT's five LLNL voxel models were used to determine an exponential calibration curve. As a first approximation, the exponential calibration curve is suitable for most voxel models, except the ICRP Adult Male and Godwin. Their counting efficiencies are considerably higher. Yet unknown, the responsible parameters for the observed higher efficiencies need further investigation. The EURADOS LLNL voxel models P0 and P4 lie on the curve as expected. Since air cavities under the chest cover of these models were not considered, CWTs are higher and hence, counting efficiencies are lower compared to the corresponding KIT LLNL models. Two resolutions of the MEETMan were also investigated and compared. The plot shows that CWT and efficiency differ only slightly within the error bars.

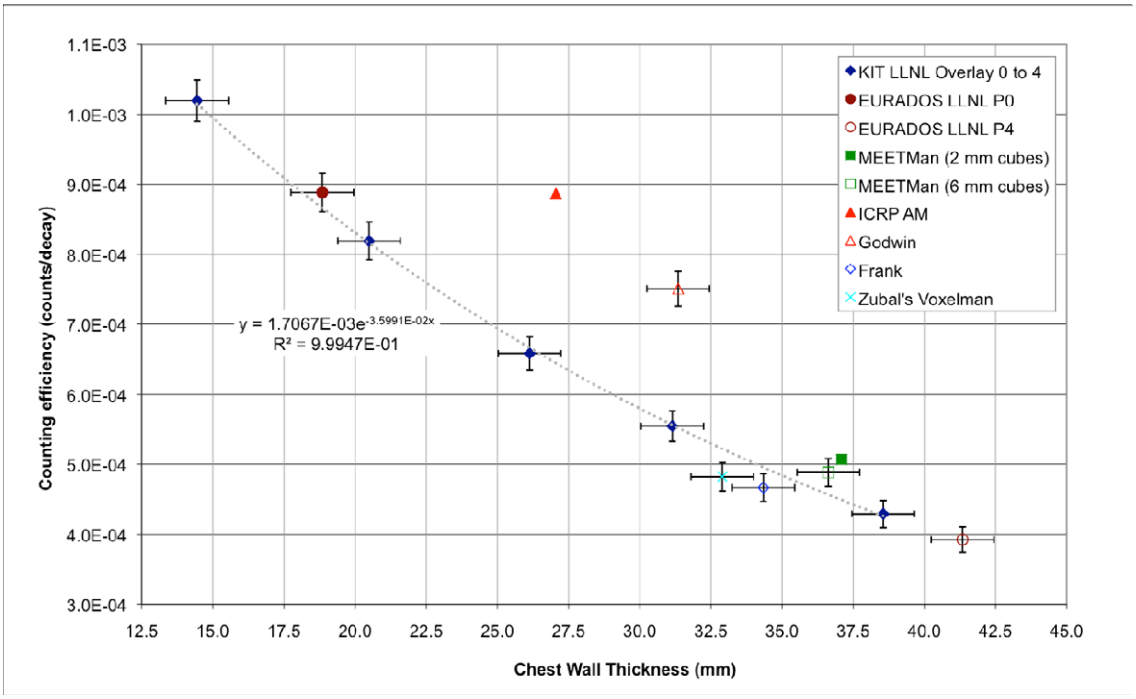

Fig. 2. Lung counting efficiencies calculated with MCNPX plotted against the determined CWT of various voxel models. An exponential fit (dotted gray line) was performed with Microsoft's Excel with data from the five KIT LLNL models (solid diamonds). The formula and the R2-coefficient are given in the plot. The horizontal and vertical error bars indicate the error (2σ) of the CWT and the net counting efficiency in the ROI (2σ).

Conclusions

The authors presented and validated a method for determination of CWT of anthropometric voxel model with an error of about 1 mm.

This method can also be used to generate colour-coded, three-dimensional CWT-profiles. The profiles are helpful for verifying the realism of anatomy of voxel models, i.e. models of man-made phantoms or customised/adapted models. Furthermore, it gives useful information for detector positioning.

An exponential calibration curve depending on CWT was generated from KIT's LLNL voxel models for a typical ^{241}Am-lung counting setup with germanium detectors. As a first approximation, the curve can be used for counting efficiency calculation for most voxel models considered in this investigation. The ICRP Adult Male and Godwin show that there are other important parameters that play a role in the determination of lung counting efficiency. Thinkable is another important quantity in the assessment of thoracic deposits of nuclides emitting low energy photons: the composition of the tissue in the anterior chest wall, i.e. the fraction of muscle, adipose and bone tissue. Next steps will involve the development of algorithms, which determine such fractions in voxel models.

Acknowledgements

The authors would like to thank Mr. Olaf Marzocchi of KIT for providing the HPGe detector model.

References

D. Broggio. Intercomparison on Monte Carlo modelling of *in vivo* measurements of lung contamination with a Livermore phantom. URL: http://www.eurados.org/MCIntercomp2009/intercomp2009.htm, last checked December 2009.

P. N. Dean. Estimation of chest wall thickness in lung counting for plutonium. Health Phys, 24(4):439-441, Apr 1973.

R. Griffith, P. N. Dean, A. L. Anderson, and J. C. Fisher. Fabrication of a tissue-equivalent torso phantom for intercalibration of in-vivo transuranic-nuclide couning facilities. In Symp. on Advances in Radiation Protection Monitoring, Stockholm, Sweden, Jun 1978.

H. Gün. Bestimmung der Brustwandstärke als Kalibrierparameter für Teilkörpermessungen. Diploma Thesis, University of Applied Science Giessen-Friedberg / Karlsruhe Institute of Technology, 2010.

L. Hegenbart, Y. H. Na, J. Y. Zhang, M. Urban, and X. G. Xu. A Monte Carlo study of lung counting efficiency for female workers of different breast sizes using deformable phantoms. Phys Med Biol, 53(19):5527-5538, Oct 2008.

L. Hegenbart, O. Marzocchi, B. Breustedt, and M. Urban. Validation of a Monte Carlo efficiency calibration procedure for a partial body counter system with a voxel model of the LLNL torso phantom. Radiation Protection Dosimetry, 133(3):158-164, 2009.

J. S. Hendricks, G. W. McKinney, M. L. Fensin, M. R. James, R. C. Johns, J. W. Durkee, J. P. Finch, D. B. Pelowitz, L. S. Waters, and M. W. Johnson. MCNPX 2.6.0 Extensions. Technical Report LA-UR-08-2216, Los Alamos National Laboratory, 2008.

ICRP. Basic anatomical and physiological data for use in radiological protection: reference values. Number 89 in ICRP Publication. ICRP, 2002.

ICRP. Adult Reference Computational Phantoms. Number 110 in ICRP Publication. ICRP, 2009.

G. H. Kramer and B. M. Hauck. Chest wall thickness measurements of the LLNL and JAERI torso phantoms for germanium detector counting. Health Phys, 73(5):831-837, 1997.

G. H. Kramer. Chest wall thickness measurements of the LLNL Phantom for small area germanium detector counting system. Health Phys, 79(2):203-206, 1999.

O. Marzocchi, B. Breustedt, and M. Urban. Characterisation, modelling and optimisation of the model of a HPGe detector with the aid of point sources. Applied Radiation and Isotopes, In Press, Corrected Proof, 2009.

NIST Photon Cross Sections Database http://physics.nist.gov/PhysRefData/Xcom/html/xcom1.html, last checked November 2009.

N. Petoussi-Henss, M. Zankl, U. Fill, and D. Regulla. The GSF family of voxel phantoms. Phys. Med. Biol. 47, 89-106, 2002.

F. B. Sachse, M. Glas, M. Müller, and K. Meyer-Waarden. Segmentation and tissue-classification of the visible man dataset using the computertomographic scans and the thin-section photos. In in Proc. First Users Conference of the National Library of Medicine's Visible Human Project, pages 125-126, 1996.

U. Schötzig and H. Schrader. Halbwertszeiten und Photonen-Emissionswahrscheinlichkeiten von häufig verwendeten Radionukliden. Number PTB-RA16/5. PTB, Braunschweig, 5th edition, 2000.

T. Sumerling and S. Quant. Measurements of the Human Anterior Chest Wall by Ultrasound and Estimates of Chest Wall Thickness for Use in Determination of Transuranic Nuclides in the Lung. Radiation Protection Dosimetry, 3(4):203-210, 1982.

V. Taranenko, M. Zankl, and H. Schlattl. Voxel Phantom Setup in MCNPX. In The Monte Carlo Method: Versatility Unbounded In A Dynamic Computing World. American Nuclear Society, 2005.

F. Y. Taylor. History of the Lawrence Livermore National Laboratory Torso Phantom. Master's thesis, San Jose State University, 1997.

M. Zankl, J. Becker, U. Fill, N. Petoussi-Henss, and K. F. Eckerman. GSF male and female adult voxel models representing ICRP Reference Man – the present status. In: Proceedings of The Monte Carlo Method: Versatility Unbounded in a Dynamic Computing World, Chattanooga, TN, 17.-21.04.2005 (Ed.: American Nuclear Society, La Grange Park, USA); Proceedings published on CD, 2005.

I. G. Zubal, C. R. Harrell, E. O. Smith, Z. Rattner, G. Gindi, and P. B. Hoffer. Computerized three-dimensional segmented human anatomy. Med Phys, 21(2):299–302, Feb 1994.

Measurements and Monte Carlo computation of the ^{241}Am counting efficiency pattern along the case #0102 USTUR leg phantom

Broggio, D.[1]; Capello, K.[2]; Cardenas-Mendez, E.[2]; El-Faramawy, N.[3]; Franck, D.[1]; James, A. C.[4]; Kramer, G. H.[2]; Lacerenza, G.[5]; Lopez, M. A.[5]; Lynch, T. P.[6]; Navarro, J. F.[5]; Navarro, T.[5]; Perez, B.[5]; Rhüm, W.[3]; Weitzenegger, E.[3]

[1] Institut de Radioprotection et de Sûreté Nucléaire, DRPH/SDI/LEDI, FRANCE
[2] Radiation Protection Bureau, Human Monitoring Laboratory, CANADA
[3] Helmholtz Zentrum München, Institute of Radiation Protection, GERMANY
[4] Washington State University, U.S. Transuranium and Uranium Registries, UNITED STATES
[5] CIEMAT, SPAIN
[6] Pacific Northwest National Laboratory, UNITED STATES

Abstract

Some Actinides like Americium are bone-seekers, and according to their biokinetics are retained in the skeleton after an intake. Because of the radiosensitivity of red-marrow and endosteum cells, the assessment of the bone activity is an important matter to take into account. *In vivo* counting of bone seekers is usually performed at the skull or at the knee, since the attenuation of radiation is here limited.

The USTUR (U.S. Transuranium and Uranium Registries) disposes of a unique physical phantom containing the left half of the skeleton of a donor significantly contaminated by ^{241}Am. The left leg phantom, containing bones from hip to foot, embedded in muscle equivalent plastic, has an activity of 1026 Bq. This phantom was measured in three European *in vivo* facilities and one Canadian laboratory; Monte Carlo (MC) simulations were also performed to assess the reliability of numerical calibration based on voxel phantoms.

Using different Germanium detectors the same efficiency pattern was found by participants, when counting positions were comparable. A sharp increase of counting efficiency is found at the patella level, about 10 times higher than at other locations, at this level a 5 cm displacement of detectors can result in 50% change in efficiency. Measurements on each side of the leg show a significantly different efficiency pattern.

A voxel phantom was build after acquisition of 234 CT scan images and used to simulate the measurements. Despite the gross feature of the efficiency pattern is reproduced by MC simulations, discrepancies larger than 50% have been found for some measurements. Several factors can explain these discrepancies: difficulties in building the voxel model and in reproducing the measurement conditions, uncertainty about the total activity and the activity distribution in bones.

Based on this study recommendations will be given to ensure reliable measurements, the efficiency obtained in this study will also be compared with other relevant data.

Advanced Monitorin In Mixed Radiation Area – AMIRA

Bürkin, Walter; Dielmann, Rainer
Saphymo GmbH, GERMANY

Advanced Monitoring In Mixed Radiation Area – AMIRA

AMIRA is the result of a research project in cooperation with the Radiobiological Institute of the University of Munich, a workgroup of the University of Saarland and Saphymo GmbH. An active, universal applicable dosimeter for radiation protection has been developed providing precise neutron and photon measurements within mixed unidentified radiation fields. AMIRA uses a miniaturized tissue equivalent proportional counter tube (TEPC), simulating a microscopic volume of 1 µm diameter. Using a microscopic detector offers the advantage that for each event of energy deposition not only the proportion of dose but also the lineal energy, the micro dosimetric analogon of the LET, can be determined. This allows assigning to each individual event the correct quality factor for the determination of the equivalent dose. Thus, a separate indication of neutrons and photons is not really required for radiation protection applications although it is principally possible.

The energy response of most conventional instruments is often varying by a factor of 10. Measuring results of PTB Braunschweig – Germany and IRSN Cadarache – France prove an extremely high energy response within the entire measuring range.

The latest version of the measurement device is based on reduced size and weight, disposes of an economized MCA with more than four decades dynamic measurement range and suppresses microphonic effects. The software saves the LET spectrum, calculates and saves the total dose according to ICRP60 as well as the neutron/photon dose by LET separation. Due to the small, compact construction it could be achieved for the first time to make use of the TEPC technology for applications everywhere where there is occupational exposition. Examples can be found with aircrew dosimetry or in the complete spectrum of the nuclear fuel cycle for the determination of the personal dose and dose rate.

Introduction

The exact measuring of the exposure rate gains more and more importance due to growing activities of human beings within radiation exposed areas (i.e. aviation, astronautics, medicine, nuclear techniques, etc.). People are mostly confronted with mixed radiation exposure composed of charged particles, neutron and photon rays. Therefore, at workplaces being subject to radiation exposure dosimeters for measurement of radiation, dose rate and environmental surveillance are applied.

Common dosimeters using semiconductor detectors cannot determine the correct proportion of neutrons and photons of the equivalent dose, although especially the neutron exposition is known to have a quite high injury potential to humans. This results from the great variety of interacting processes and their distinctive dependence from material composition and neutron energy. Further, the high and energy depending RBW (relative biological effectivity) requires the discrimination of neutrons and photons with most of the detector conceptions.

This fact as well as the growing interest in active electronic dosimeters providing lower detection limits as passive equipment, more flexibility in use and real-time monitoring features (e.g. alarm function) generated the motivation for the development of a new personal dosimeter. While official dosimetry is still exclusively applying passive detectors the in-plant use of electronic dosimeters for monitoring tasks is increasing. It is expected that the passive dosimeters will be replaced by electronic units in the medium term.

Along with the described AMIRA development the correct measurement of neutron radiation using a personal dosimeter based on the Tissue Equivalent Proportional Counter (TEPC) technology should be realized. Neutrons and photons within mixed unknown radiation fields should be accurately detected using an active handy measuring device.

Material and methods

The most important challenges with respect to this project were the reduction of mass and size of a sufficiently sensitive TEPC, the improvement of the gas booster's long-term stability as well as the elimination or reduction of the sensitivity against acoustic noise and shock (microphony) which is inherent to all TEPCs. Additionally, a miniaturization of all required electronic components and the reduction of power consumption should help to optimize the use of the new instrument as personal dose meter.

Apart of the detector the measuring system also includes a high-voltage supply, a charge sensitive pre-amplifier, a 4 decade multi channel analyzer, a display, PC-interface and power supply (rechargeable batteries). All components are designed for minimum power consumption.

Based on a tissue equivalent proportional counter (TEPC) with a simple geometry and modular design a plastic (A150) is used which due to its interaction with neutrons simulates the characteristics respectively the features of a biological tissue with a microscopic volume of 1µm diameter. The Radiobiological Institute of the University of Munich (SBI) already proved the basic technical feasibility of such detectors.

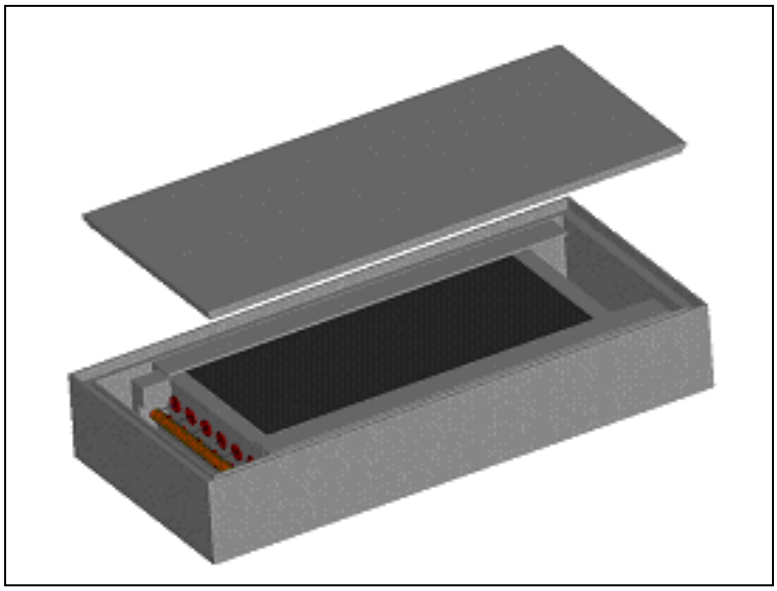

Fig. 1. Miniaturized multi-element TEPC (Tissue Equivalent Proportional Counter).

Within applications in the radiation protection area tissue equivalent micro dosimetric proportional counters offer the great advantage that they are simulating the energy deposition within the tissue - that means the so called lineal energy - the micro dosimetric analogon to the LET (= linear energy transfer) is determined for each individual event of energy deposition. This measuring method is therefore able to allocate a quality factor to each given radiation contribution. It therefore allows giving evidence about the biological radiation effect within mixed radiation fields (determination of equivalent dose).

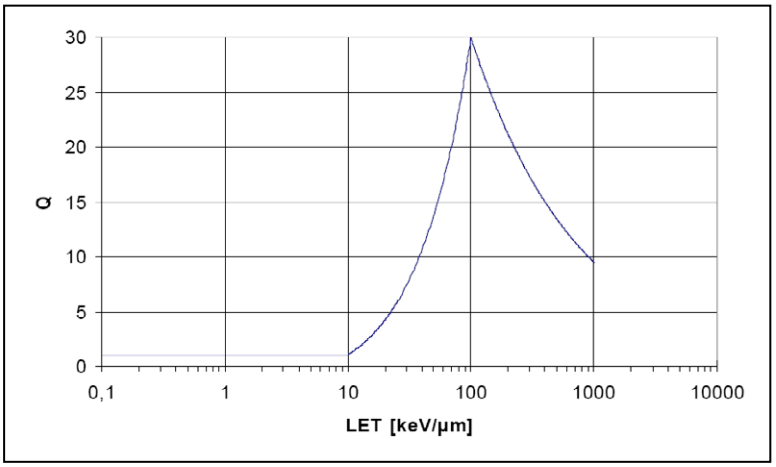

Fig. 2. Quality factor Q as function of LET L [1].

Equivalent dose and dose rate are calculated in a five second interval and displayed. Determination of absorbed dose contributions of neutron and photon radiation is not required as the different radiation components are automatically evaluated according to the respective LET. Analogous to each measured impulse a

weighting factor Q according to ICRP 60 is assigned to allow to indicate the result using the measuring categories $H_p(10)$ respectively $H^*(10)$. Fig. 3 shows the LET spectrum of Cs-137.

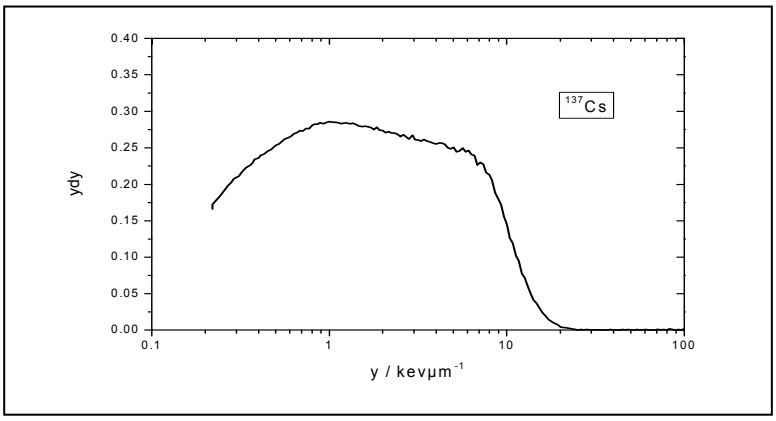

Fig. 3. LET spectrum for Cs-137.

An alarm function with simply settable dose rate thresholds is available. The accumulated event spectrum can be downloaded to a PC and can then be displayed and analysed in detail.

Fig. 4 shows a block diagram of the miniaturized electronics. The signal received from the TEPC reaches the pre-amplifier as a negative slope. This charge sensitive component is acting as trans-impedance amplifier and is adjusted to an optimal signal-noise-ratio. Subsequently, the signal is sampled by a fast high resolution ADC and transferred to a micro processor which registers the pulses using digital filter algorithms.

For dose meter configuration and data download the instrument provides an integrated RS-232 interface. The software running on PC also allows displaying the spectra of lineal energies – almost in real-time.

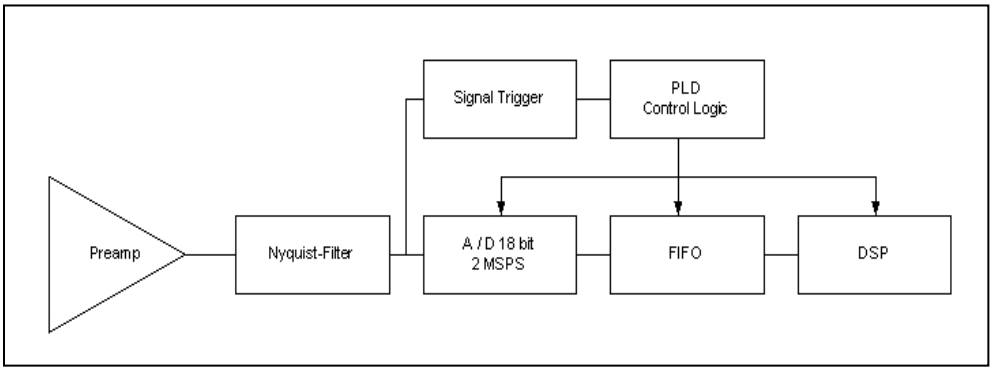

Fig. 5. Block diagram of the signal unit.

Results

Since the energy of neutron fields spreads over several decades the measuring technique is faced with a big challenge. The energy dependency of most of the commercially available measuring equipment is varying up to a factor 10 about this range. Fig. 5 is demonstrating that the new TEPC-design concept features an extremely high energy response across the entire field.

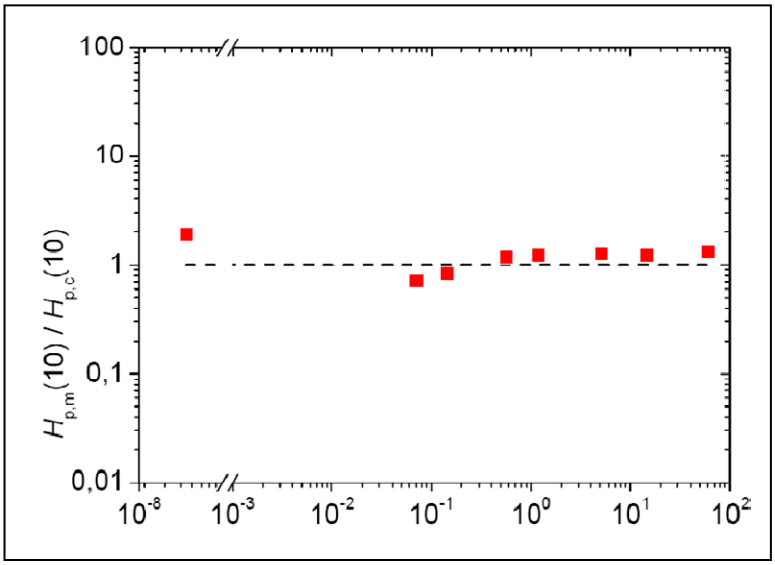

Fig. 6. Energy response. Source: H. Roos (IRSN-measurements).

References

[1] Wimmer, S.: Entwicklung, Bau und Test eines mikrodosimetrischen Vielelement-Proportionalzählers. Dissertation an der Medizinischen Fakultät der Ludwig-Maximilians-Universität München, München 2006

Simple method to determine ^{234}U and ^{238}U in water using alpha spectrometry

Vesterbacka, Pia; Pöllänen, Roy
STUK – Radiation and Nuclear Safety Authority, Laippatie 4, 00880 Helsinki, FINLAND

Abstract
A simple method was developed to determine the activity concentration of ^{234}U and ^{238}U in water using alpha spectrometry. The method is based on rapid evaporation of water, mounting the residue into a vacuum chamber of an alpha spectrometer, alpha particle counting and subsequent spectrum analysis using a novel analysis program known as Adam. The method was compared to liquid scintillation spectrometry and alpha spectrometry with radiochemical sample processing. Consistent results were obtained.

Introduction
In a nuclear or radiation emergency or in nuclear security there is a need for rapid and simple off-line and on-line analysis methods to detect radionuclide threat agents in water. Efficient tools are necessary especially when screening the samples with low and medium activity concentrations. Simplified methods have recently been developed for example for liquid samples (Semkow et al., 2009), swipe samples (Ihantola, 2009) and air filters (Pöllänen and Siiskonen, 2006). Nevertheless, there still room to develop the methods.

Radiochemical sample processing is often prerequisite for successful measurements in alpha spectrometry. However, the processing may be too tedious and time-consuming especially in the case when the analysis results must be obtained rapidly. In addition, operations in the field pose special requirements although the processing is typically performed in a fixed laboratory.

In the simple and rapid off-line method investigated here, water samples were evaporated and the residues were counted as such using alpha spectrometry, i.e. without further radiochemical sample processing. A novel spectrum analysis tool known as Adam (Advanced deconvolution of alpha multiplets) was used to unfold the alpha spectra. The results were compared to those obtained by scintillation spectrometry and alpha spectrometry with radiochemical sample processing. The main focus was put on the congruity of the results obtained using different methods.

Material and methods

Simplified method for alpha spectrometry

Eleven drilled well water samples were selected for the study. An aliquote of 15 ml was evaporated in Teflon container to stainless disc under IR lamp. After evaporation the alpha particles were counted in an alpha spectrometer (AlphaAnalyst, Canberra) for one week (Fig. 1). The samples were measured from shelf one, where the distance from the semiconductor (PIPS, Canberra) detector is 2 mm. The area of the detector was 450 mm^2.

After evaporation, the walls of the Teflon container were rinsed using 1M HCl acid to determine the influence of possible adsorption. The activity concentration of rinsing acid was determined using liquid scintillation spectrometry (Quantulus 1220, Perkin Elmer), and the final results were corrected accordingly.

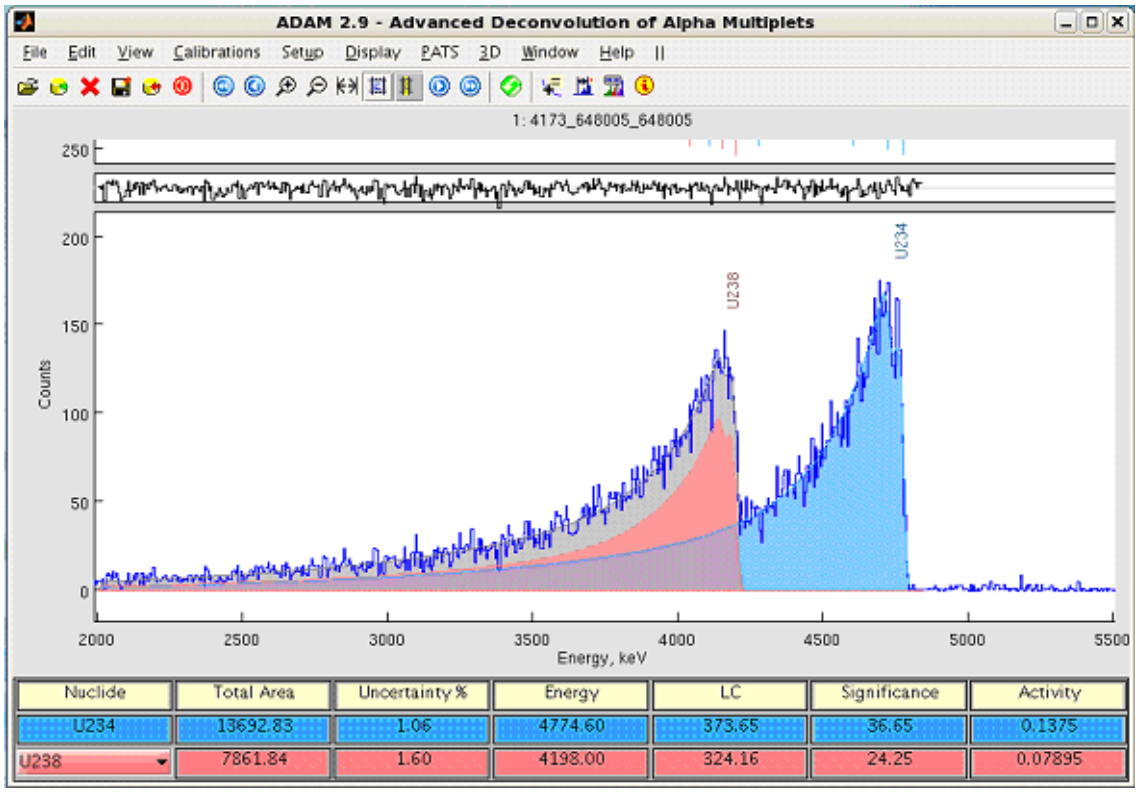

Fig. 1. Screen snapshot of an alpha spectrum from evaporated residue (sample ID 4173 in Figs. 2 and 3). The families of the peaks of ^{238}U and ^{234}U were fitted using Adam. All peaks are assumed to have the same shape. ^{234}U was not taken into account in the fitting. Reduced residual is shown at the top.

Gross alpha analysis

Sum activity concentrations were determined by liquid scintillation method (Salonen 1993, Salonen and Hukkanen 1997). The measurements were performed to screen the level of occurrence of the long-lived alpha-particle emitting (^{238}U and ^{234}U, ^{226}Ra and ^{210}Po) radionuclides in water. The samples (38 mL) were prepared by evaporating water into dryness with a freeze-dryer in a Teflon-coated polyethylene vial. The residues were dissolved in small amount of HCl acid and then scintillation cocktail Ultima Gold AB was added. The sample was counted one month after the sample preparation. During

that time ^{226}Ra attains equilibrium with ^{222}Rn and its short-lived daughters. Gross alpha and beta are determined with a low-background liquid scintillation spectrometer (Quantulus 1220, Perkin Elmer).

Radiochemical uranium determination

Radiochemical processing of the samples was performed to determine the activity concentrations and ratios of uranium isotopes (Sill and Williams 1981, Sill 1987). The water samples were concentrated by applying iron scavenging. The precipitate was dissolved in concentrated HCl. Uranium was separated from other radionuclides by ion exchange method (using Dowex 1x8, 50/100 mesh). Uranium was co-precipitating with CeF3 for the alpha counting (AlfaAnalyst, Canberra). Minimum detectable activity was 2.0 mBq for one litre water sample and 180 hour counting. ^{232}U was used as a chemical yield tracer.

Spectrum unfolding using Adam

Adam is a spectrum analysis tool for alpha spectrometry (Toivonen et al., 2009). The peaks of a nuclide are treated as a family of individual peaks with energies and yields obtained from a nuclide library. Because of the omission of radioelement separation there may be a number of peaks of different radionuclides present in the spectra.

In the fitting the peaks of each radionuclide are treated as a group which enables efficient spectrum unfolding even in the case of complex alpha spectra. The shape of the peaks of the nuclides used in the analysis was same. Convolution of a Gaussian distribution with low-energy side double exponential tail is used in the fitting. The energy region considered in the analyses was 2–8 MeV. In the measurements the number of the channels was 1024 (5.9 keV per channel).

Uncertainty estimation

The activity uncertainty of the ^{232}U tracer used in the radiochemical analyses was 5%. The uncertainty for the geometrical detection efficicency used in the simple method was estimated to be 10%. The uncertainty (Δf) of the $^{234}U/^{238}U$ ratio between the simple method and the radiochemical determination was calculated according to the following formula

$$\Delta f = \sqrt{\left(\frac{\Delta x}{y}\right)^2 + \left(\frac{x \times \Delta y}{y^2}\right)^2} \times f\,, \qquad (1)$$

where Δx is the uncertainty of $^{234}U/^{238}U$ ratio in the simple method, Δy is the uncertainty of $^{234}U/^{238}U$ ratio in the radiochemical determination and f is the abovementioned isotopic ratio between the simple method and the radiochemical determination.

Results

The correlation between the activity concentrations obtained by the simple method to those determined by liquid scintillation method and radiochemical analyses was good (Fig. 2). The calculated correlation coefficients between the rapid method and gross alpha determination and radiochemical analyses were 0.98 and 0.99, respectively. For the method developed here the adsorption onto the walls of the evaporation container was on the average 8% (range 5–14%).

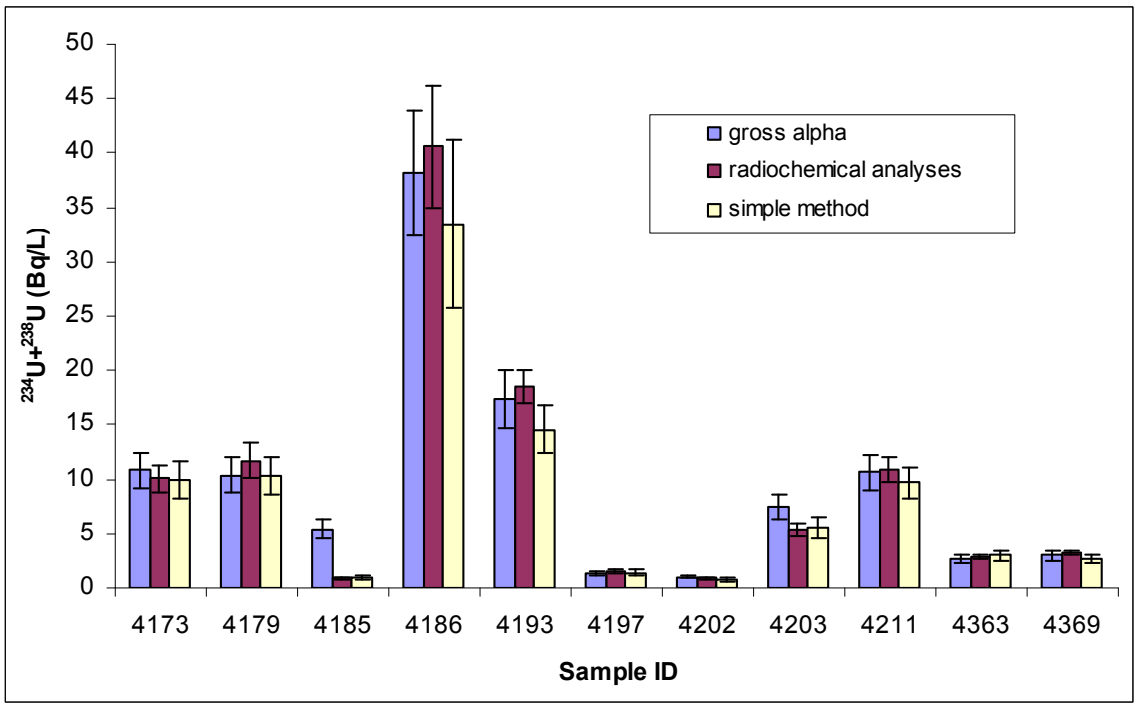

Fig. 2. Total activity concentration of uranium (^{234}U + ^{238}U) obtained from gross alpha determination, radiochemical sample processing and the rapid evaporation method developed here. Numbers in the x-axis refer to the sample identification number.

U isotope ratios obtained by the rapid method developed here and those obtained by radiochemical analyses were close to each other (Fig. 3). The difference was 10% on the average.

The presence on ^{226}Ra (main peak alpha energy 4784 keV is only 10 keV larger than that of ^{234}U) must be taken into account to unfold the spectra correctly. Among the 11 samples considered here there were three samples that contained notable amounts of ^{226}Ra (Fig. 4). Radium contribution was accounted for in the present analysis.

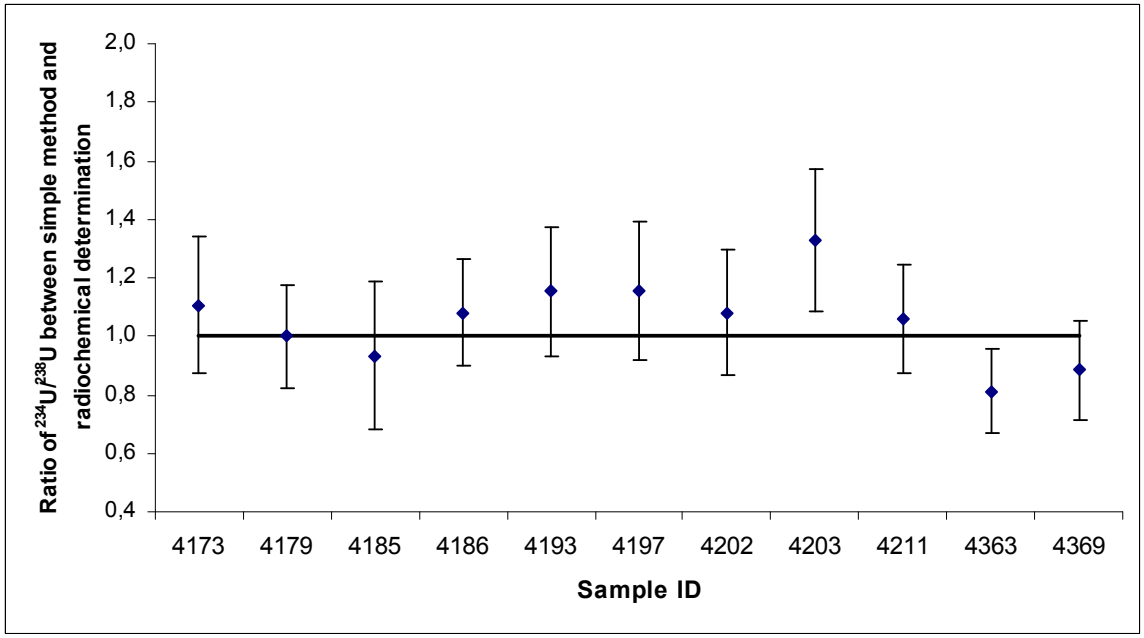

Fig. 3. $^{234}U/^{238}U$ activity ratio for different samples determined by alpha spectrometry with radiochemical sample processing relative to that of the simple analysis method developed here. Error bars refer to 2σ uncertainty and the numbers in the x-axis refer to the sample identification code.

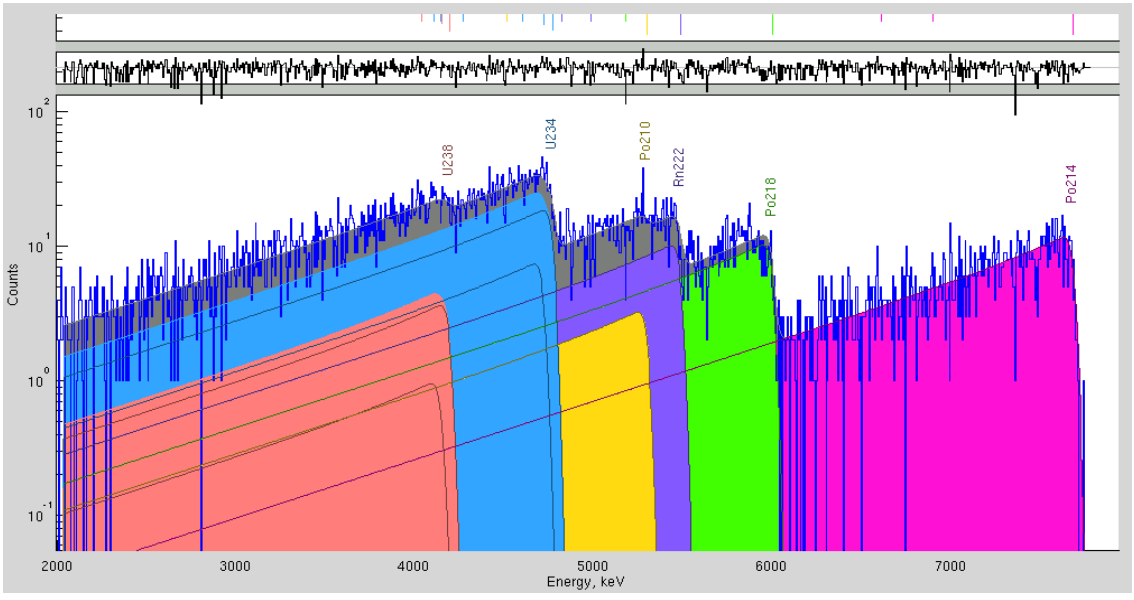

Fig. 4. Alpha particle energy spectrum from the sample 4185 (see Figs. 3 and 4) containing notable amounts of radon and its progeny (^{218}Po, ^{214}Po and ^{210}Po). Here (in this figure), the contribution of ^{226}Ra is not taken into account in the fitting.

Discussion and conclusions

Simplified sample manipulation with sophisticated analysis methods is advantageous when obtaining the results rapidly is of importance. However, straightforward water evaporation cannot entirely replace the radiochemical sample processing. This is because peak broadening in the alpha spectrum, caused by the absorption of the alpha particles in the evaporation residues, makes spectrum analysis challenging and, thus, influences the identification of the radionuclides. Too thick residues may even prohibit the analysis and since no radioelement separation is performed for the source, unequivocal nuclide identification may sometimes be impossible.

Despite of the drawbacks mentioned above the method developed here has many advantages: The sample manipulation is simpler, more rapid and inexpensive compared with radiochemical processing. If the samples could be counted without major sample manipulation (or using only minor processing) it gives the possibility to redirect resources in a laboratory towards sophisticated data analysis. This does not require expensive investment for the laboratory facilities. In addition, the information from several alpha-particle emitting radionuclides can be obtained in only one measurement.

In the present paper it was shown that simple and rapid water sample processing gave comparable results to those obtained with radiochemical processing and gross alpha analysis. The method gave information on all alpha-particle emitting radionuclides present in a water sample. Although the spectrum analysis software Adam is currently under evaluation it worked well and was capable to unfold complex alpha spectra reliably. Using the method presented here the sample preparation is simple and availability of the results is fast.

References

Ihantola S. Surface sampling methods for non-destructive radionuclide analysis. Master's Thesis. Helsinki University of Technology, Faculty of Information and Natural Sciences; 2009.

Pöllänen R, Siiskonen T. High-resolution alpha spectrometry under field conditions – fast identification of alpha particle emitting radionuclides from air samples. Journal of Environmental Radioactivity 2006; 87: 279-288.

Salonen L. A rapid method for monitoring of uranium and radium in drinking water. The Science of the Total Environment 1993; 130/131: 23-35.

Salonen L, Hukkanen H. Advantages of low-background liquid scintillation alpha-spectrometry and pulse shape analysis in measuring ^{222}Rn, uranium and ^{226}Ra in groundwater samples, Journal of Radioanalytical and Nuclear Chemistry 1997; 226: 67-74.

Semkow T M, Khan A J, Haines D K, Bari A. Rapid alpha spectroscopy of evaporated liquid residues for emergency response. Health Physics 2009; 96: 432-441.

Sill S, Williams R. Preparation of actinides for spectrometry without electrodeposition. Analytical Chemistry 1981; 53: 412-415.

Sill S, Precipitation of actinides as fluorides or hydroxides for high resolution alpha spectrometry. Nuclear and Chemical waste management 1987; 7: 201-215.

Toivonen H., Pelikan A, Pöllänen R, Ruotsalainen K. ADAM - Advanced Deconvolution of Alpha Multiplets. User manual of Adam 2.8. STUK - Radiation and Nuclear Safety Authority, Helsinki 2009.

The progress in Minimizing Activity and Dose with Enhanced Image Quality by Radiopharmaceutical Administration (MADEIRA) project

Hoeschen, Christoph[1]; Mattsson, Sören[2]; Cantone, Marie Claire[3]; Mikuž, Marko[4]; Lacasta, Carlos[5]; Ebel, Gernot[6]; Clinthorne, Neal[7]; Giussani, Augusto[1]

[1] Helmholtz Zentrum München, German research center for environmental health, Institute of radiation protection, GERMANY

[2] Lund university at Malmö, Medical radiation physics, SWEDEN

[3] Universita degli studi di Milano, Department of Physics, ITALY

[4] Jozef Stefan institute, Ljubljana, Experimental particle physics department, SLOVENIA

[5] Consejo superior de investigaciones cientificas, Valencia, Instituto de fisica corpuscular, SPAIN

[6] Scivis wissenschaftliche Bildverarbeitung GmbH, Göttingen, GERMANY

[7] University of Michigan at Ann Arbor, Department of Radiology, UNITED STATES

Abstract

The introduction of new and more beneficial diagnostic procedures combining CT and PET or SPECT is related to a rapid growth of medical exposures. The European collaborative project MADEIRA (Minimizing Activity and Dose with Enhanced Image Quality by Radiopharmaceutical Administration) within the 7th EURATOM FP aims to improve 3D nuclear medical imaging in terms of increase of spatial and temporal resolution and also of reduction of the radiation exposure. The project is organized in 5 work packages, which are identified as: WP1 assessment of clinical data, WP2 PET magnifier probe development, WP3 physics-based image processing; WP4 biokinetic and dosimetric modelling; WP5 training and dissemination activities. In particular in WP1 quantitative biokinetic data were collected in patients after administration of 18F-choline and those data were used to develop detailed compartmental models and to evaluate the internal dose to the patient. Moreover, the biokinetic models were used as a basis to define more efficient protocols for data collection (WP4). The collected tomographic images were used to test different reconstruction algorithms (WP3) including some newly developed ones for which a patent is pending. In addition a special phantom for checking image quality in nuclear medicine imaging was designed and also for this a patent is pending. WP2 deals with the construction of a PET insert probe. The different modules of the probe have been developed and their performances monitored, and the probe prototype is going to be tested in clinical conditions with the use of the developed reconstruction methods. Finally, training and dissemination activities include the organization of two training courses (Milano, November 2008; Malmö November 2009), and the Malmö Conference on Medical Imaging (June 2009) as well as the tutoring of graduate and doctoral students and young post-doctoral researchers.

^{177g}Lu produced with high specific activity by deuteron irradiation for metabolic radiotherapy

Bonardi, Mauro L.[1]; Manenti, Simone[1]; Groppi, Flavia[1]; Gini, Luigi[2]
[1] Università degli Studi di Milano & INFN of Milano, L.A.S.A. Laboratory, Physics Department, ITALY
[2] INFN of Milano, L.A.S.A. Laboratory, ITALY

Abstract

Nowadays metabolic radiotherapy is in constant progress and there is a range of new radionuclides (RNs) and radiopharmaceutical compounds on the market. Although the production of RNs is improved, often it is not possible to achieve high AS, even in NCA conditions, and sometimes long-lived radionuclidic impurities are co-produced.

^{177g}Lu (t1/2 = 6.734 d, β-emission 100 %, $E_{\beta\text{- max}}$ = 489.3 keV and E_{γ}= 208.4 keV) is one of the therapeutic γ emitting RNs, which is starting to find several applications in nuclear medicine, especially for metabolic radiotherapy of cancer and radioimmuno-therapy, thanks to its favorable decay characteristics (half-life of the order of few days, relative low energy of negatrons and gamma emission suitable for detection). Presently, the production of ^{177}Lu is carried out mainly in thermal nuclear reactor either in carried added (CA) form by direct neutron capture reaction ^{176}Lu(n,γ)^{177}Lu on enriched ^{176}Lu target, or by neutron capture reaction on enriched ^{176}Yb target, followed by negatron decay. This second method produces a high specific activity (AS) no-carrier-added (NCA) radionuclide, since ^{177}Yb decays to the ground state ^{177g}Lu only.

We started to study an alternative method for the production of ^{177}Lu by the deuteron activation of natural or enriched Yb targets. In order to optimize the irradiation conditions, the thin target yields were experimentally determinated in the energy range from the threshold up to 19 MeV. The thick target yields were measured in order to compare with the production yield by neutron activation route. The contamination from the long-lived metastable level was evaluated too. Moreover a suitable radiochemical separation of Lu radioisotopes from Yb target and from the contaminants was pointed out.

High-grade radiochemical analyses act as a basis for good assessment in radiation protection

Vesterbacka, Pia; Vartti, Vesa-Pekka; Heikkinen, Tarja; Ikäheimonen, Tarja K.
STUK – Radiation and Nuclear Safety Authority, Laippatie 4, 00880 Helsinki, FINLAND

Abstract
High-level risk assessment is mostly based on results of qualitative and accurate radioactivity measurements. Accreditation is one of the most effective tools to maintain high quality in the laboratory. This means, for example, proficiency of the personnel, documented working procedures, validated methods, participating in intercomparisons, maintenance of measuring equipment, workable laboratory information management system and continuous improvement of the working practices in the laboratory. By maintaining quality system and accredited determination methods STUK assures high-grade quality in radiochemical analyses that are used as basic data of doses in risk assessment in radiation protection work.

Introduction
High-level risk assessment is mostly based on results of qualitative and accurate radioactivity measurements. In future, the need for knowledge of low doses increases and raises requirements for research infrastructure and quality management in laboratory. It means documented working practices, traceability of the results, method validation, active participating in intercomparisons, good professional skills of personnel, stability of measurement equipment, proper data management, uncertainty estimations, plan of action in case of errors and continuous improvement of working practices. It also creates the need for accredited determination methods.

At STUK, development of a uniform and modern quality system started in 1997. Accreditation of laboratory processes was awarded by FINAS (The Finnish Accreditation Service) in 1999 and was renewed twice in 2003 and 2007 according to the European Standard EN ISO/IEC 17025. The accreditation field is "Test of radiation safety and related environmental sampling". Fields of testing in radiochemical analyses are both artificial and natural radionuclides. Other fields of testing are gammaspectrometric analyses, direct measurements of people, airborne ^{222}Rn concentrations, chromosome analyses, sampling for control of radioactivity and method for local laboratories (NaI(Tl) detector).

STUK's radiochemical analyses are carried out at two different locations, in the main office in Helsinki, and in the regional laboratory in Rovaniemi, in northern Finland. The facilities comprise a total of 50 laboratory rooms for pre-treatment of

samples, radiochemical and biological treatment and analysis of samples as well as measuring rooms.

Radiochemical analyses are made from foodstuffs, all kinds of environmental samples, swipe and urine samples. ^{3}H and ^{222}Rn are determined without radiochemical separation using direct measurement by liquid scintillation spectrometry. Ion chromatographic extraction is used in $^{89,90}Sr$ and ^{210}Pb separation and ion exchange in $^{239,240}Pu$, ^{238}Pu, ^{241}Am, ^{234}U, ^{235}U, and ^{238}U separation. ^{210}Po is determined via spontaneous deposition onto silver disk and measured using alpha spectrometry. Low-background proportional counter is used with $^{89,90}Sr$ measurements, liquid scintillation spectrometry with ^{90}Sr and ^{210}Pb measurements and alpha spectrometry with measurement of actinides. The radiochemical analyses are validated and their quality is maintained by participating regularly in intercomparison exercises and professional tests. All data from samples and measurements are stored either in LIMS or LINSSI databases in order to maintain traceability of the results.

By maintaining quality system and accredited determination methods STUK assures high-grade quality in radiochemical analyses that are used as basic data of doses in risk assessment in radiation protection work.

Analyses methods

Radiochemical determination demands nearly always digestion of the sample and elemental separation. Elemental separation is done because of the interference of other elements. Radiochemical analyses are made from all samples that can be digested into liquid form. Sample types analysed are environmental samples (e.g. sediments, soil, mushroom, various berries, lichen, moss, water), drinking water and food samples, excretion samples (urine), swipe samples and industrial products. Summary for the detection limits for radionuclides ^{90}Sr, $^{239,240}Pu$, ^{3}H, ^{222}Rn, ^{226}Ra, ^{228}Ra, $^{234,235,238}U$, ^{210}Pb, ^{210}Po, gross alpha and gross beta are given in Table 1.

Artificial radionuclides

Strontium ($^{89,90}Sr$)

Strontium separation from interfering nuclides is performed with extraction chromatographic resin, Sr resin (Triskem International) and measured either with low-background proportional counter (Risø or LB770 Berthold) or liquid scintillation counter (Quantulus). Proportional counter is used if both ^{89}Sr and ^{90}Sr are to be measured, liquid scintillation counter is used if only ^{90}Sr is to be measured. In proportional counter method the strontium is precipitated after Sr separation as a carbonate onto filter paper, and ^{89}Sr and ^{90}Sr together with its ingrowing daughter nuclide ^{90}Y are measured as soon as possible. After a minimum of 18 days, the ingrowth daughter nuclide ^{90}Y is separated together with stable Y from Sr and measured few times in a couple days. ^{90}Sr is calculated from the ^{90}Y measurements and ^{89}Sr from the first measurement by subtracting the ^{90}Sr contribution. In liquid scintillation method the ^{90}Sr is measured together with its ingrowth daughter ^{90}Y after a minimum of 18 days from the Sr separation (Fig. 1 (B)). The chemical yield is determined with inactive Sr and Y carriers. The efficiency in proportional counting is typically 40-50% and in liquid scintillation counting ~200%.

Plutonium (^{239,240}Pu)

The routine method for separation of plutonium is based on ion exchange with Dowex 1x4 anion exchange resin. Radioactive tracer ^{242}Pu is added and the sample is brought into solution either by wet ashing or microwave digestion. The sample is introduced into ion exchange column (Dowex 1x4, 50-100 mesh, in NO_3^- -form) in 8 M HNO_3, washed with 8 M HNO_3 and concentrated HCl, and the Pu fraction is eluted with conc. HCl + 1 M NH_4I solution. The plutonium is electrodeposited on stainless steel disc and counted with an alpha spectrometer. The chemical yield is determined with the radioactive tracer ^{242}Pu. The counting efficiency is approximately 35-40%.

Tritium (^{3}H)

Tritium measurements are made from water, urine and swipe samples. Water and urine samples are distilled for purification. Aliquote from a distilled sample is taken and UltimaGold uLLT scintillation cocktail is added to the 20-ml plastic scintillation vials. In Figure 1, the tritium spectrum of a water sample is presented. Swipe samples are measured with no pre-treatment. Pori-Vuoltee-groundwater is used for a background sample. Counting efficiency is determined measuring also a ^{3}H standard sample in every sample sequence. Activity concentration of tritium is determined with a low-background liquid scintillation spectrometer 1220 Quantulus.

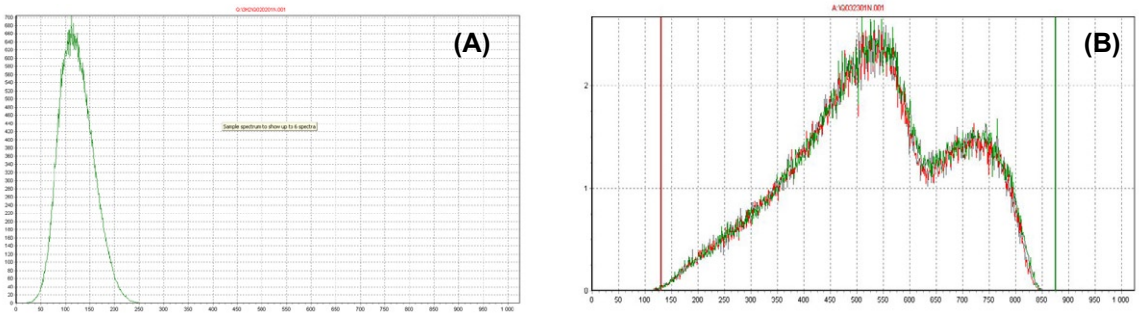

Fig. 1. Tritium spectrum of water sample (A). Strontium-90 spectra together with its ingrowth daughter ^{90}Y measured with Quantulus 1220 liquid scintillation spectrometer (B).

Natural radionuclides

Gross alpha and beta

The gross alpha and beta measurements are performed mainly in order to screen for the level of occurrence of the long-lived alpha-emitting (^{238}U and ^{234}U, ^{226}Ra and ^{210}Po) and beta-emitting (^{40}K, ^{210}Pb and ^{228}Ra) radionuclides in water. The sample (38ml) is prepared by evaporating water into dryness with a freeze-dryer in a teflon-coated polyethylene vial. The residue is dissolved in small amount of HCl acid and then scintillation cocktail Ultima Gold AB is added. The sample is counted one month after the sample preparation. During that time ^{226}Ra attains equilibrium with ^{222}Rn and its short-lived daughters. Gross alpha and beta are determined with a low-background liquid scintillation spectrometer 1220 Quantulus. An example of the gross alpha spectra of a drilled well water sample is given in Figure 2(A).

Radon (^{222}Rn)

Radon is measured in a homogeneous solution with a liquid scintillation spectrometer 1414 Guardian. The sample is prepared by adding 10 ml of water into a glass vial (equipped with a cap containing an aluminium foil) pre-filled with liquid scintillation cocktail Ultima Gold XR. The concentration of ^{222}Rn is calculated from the alpha spectrum in the window which covers the most part of the alpha peaks. The alpha counting efficiency of radon in the selected alpha window is 268%±3%.

Radium (226Ra) and Radium (228Ra)

^{226}Ra activity is calculated from the gross alpha spectrum on the basis of the counts measured in window set on the area of the ^{214}Po peak. This will give quite accurate results to ^{226}Ra because no other natural or artificial radionuclide has alpha emissions in the same energy range >7.5 MeV. The counting efficiency of ^{214}Po (and thus of ^{226}Ra) in the selected window is 86±3%. ^{228}Ra is determined via its daughter nuclide ^{228}Ac using gamma spectrometric measurement.

Uranium (^{238}U, ^{234}U and ^{235}U) and Thorium (^{232}Th, ^{230}Th and ^{228}Th)

Uranium and thorium are analysed by a radiochemical method. It allows the accurate determination of each uranium and thorium isotope separately. The water sample is concentrated by applying iron scavenging and the iron precipitate is dissolved in concentrated HCl. The other environmental samples are digested by either wet ashing or microwave digestion. Uranium and thorium are then separated from other radionuclides by ion exchange method (by using Dowex 1x8, 50/100 mesh). Uranium and thorium are coprecipitated with CeF_3 for the alpha measurement. The sample is counted with AlfaAnalyst spectrometer (Canberra). ^{232}U is used as a chemical yield tracer in the uranium analysis and ^{229}Th in the thorium analysis.

Lead (^{210}Pb) and polonium (^{210}Po)

^{210}Pb and ^{210}Po concentrations were determined using spontaneous deposition of ^{210}Po on silver disk and alpha spectrometric measurement (AlphaAnalyst) of the ^{210}Po activity (Fig. 2 (B)). The solution, remaining from the ^{210}Po deposition, is stored at least for 200 days to allow the in-growth of ^{210}Po which is a daughter product of ^{210}Pb. The second ^{210}Po deposition is then carried out and its ^{210}Po activity is counted. The final ^{210}Po result is calculated using the results from these two depositions. The ^{210}Pb result is calculated from the second ^{210}Po deposition. ^{209}Po and ^{208}Po are used as chemical yield tracers. Lead can also be determined using extraction chromatography. ^{210}Pb is separated from other radionuclides by Triskem´s Sr-resin. The sample is counted after a 30-day period during which ^{210}Bi attains nearly 100% equilibrium with ^{210}Pb. The result is then calculated from ^{210}Bi and ^{210}Pb together. Inactive lead is used for yield determination.

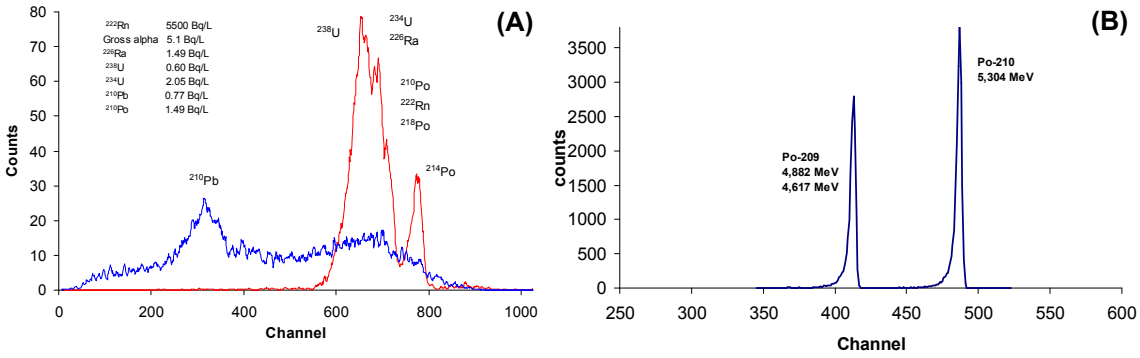

Fig. 2. The alpha and beta spectra of the Quantulus from a drinking water sample with different radionuclide contents (A). Alpha spectrum of ^{209}Po and ^{210}Po isotopes measured with Alpha Analyst (Canberra). ^{209}Po is used as tracer (B).

Table 1. The minimum detection limits for radionuclides ^{90}Sr, ^{239,240}Pu, ^{3}H, ^{222}Rn, ^{226}Ra, ^{228}Ra, ^{234,235,238}U, ^{210}Pb, ^{210}Po, gross alpha and gross beta at 95% confidence level. The amount of samples used in analyses depends on material. In this table MDA is calculated for the sample amount given in the table.

Nuclide	Equipment used in the measurement	Examples from amount of sample used in analysis (L, kg)	Counting time (h)	MDA (Bq/sample)
^{90}Sr	Quantulus 1220, proportional counter	30 L	15	0.005
^{239,240}Pu	AlphaAnalyst (Canberra)	100 L	60	0.0005
^{3}H	Quantulus 1220	0.008 L	10	0.008
^{222}Rn	Guardian 1414	0.01 L	1	0.0017
^{226}Ra	Guardian 1414, Quantulus 1220	0.04 L	3	0.00004
^{228}Ra	HPGe detector (Ortec, Canberra)	2 L	16	0.14
^{238}U	AlphaAnalyst (Canberra)	1 L, kg	180	0.002
^{235}U	AlphaAnalyst (Canberra)	1 L, kg	180	0.002
^{234}U	AlphaAnalyst (Canberra)	1 L, kg	180	0.002
^{210}Po	AlphaAnalyst (Canberra)	1 L, kg	180	0.002
^{210}Pb	AlphaAnalyst (Canberra)	1 L, kg	180	0.002
^{210}Pb	Guardian 1414, Quantulus 1220	1 L, kg	3	0.02
Gross alpha	Guardian 1414, Quantulus 1220	0.04 L	3	0.00012
Gross beta	Quantulus 1220	0.04 L	3	0.008

Quality control in radiochemical laboratory

Good laboratory practices carried out at STUK in analytical work for radiochemical and gammaspectrometric analyses are described in detail in publication Ikäheimonen et. al 2006. A short summary of these practices is described here. Concerning radioactivity determinations there are only few international standards available. Therefore, almost always the methods used are laboratory-developed methods.

Proficiency of personnel and working practices

Proficiency of the personnel must be on a level where everybody knows what he is doing and why. Skilful laboratory personnel know what things can affect the result. Working with environmental samples with low radioactivity levels implies that the analysts must be qualified and aware of good laboratory practices. Especially, attention needs to be paid on contamination. This means that glassware and equipment are classified for different purposes according to the activity concentration of the sample. Also separate rooms are organized for pre-treatment of the sample, analyses and measuring equipment. In a laboratory with good working practices all instructions are found in written form in laboratory manuals.

Measurement rooms

STUK has four laboratory rooms for low-background alpha and beta measurements. The rooms are constructed of a special concrete containing an extremely low amount of natural radioactive elements and are equipped with a special air ventilation system. Measuring equipment is separated according to the measured radionuclide and activity concentration of the sample. Monitoring of temperature and humidity in the measurement rooms is arranged and all data is stored for further evaluation. The measurement rooms are equipped with uninterruptible power supplies (UPS) and outside backup generator to assure continuous power supply.

Equipment stability

STUK has a large number of high-quality measurement equipment used for radiochemical analyses. The equipment are three alpha spectrometer systems from Canberra (AlphaAnalyst), three Guardian 1414 liquid scintillation spectrometers, three Quantulus 1220 liquid scintillation spectrometers and three proportional counters (Fig. 3).

Confidence in the performance of equipment is maintained by regular calibrations and service, routine checks and control charts. Additionally, for good flow of information regular instrument meetings, four times per year, are arranged. In the meetings, all changes in operations of the equipment are documented. Equipment is operated only by authorized personnel. Up-to-date instructions on the use and maintenance of equipment are found in equipment manuals. All significant information from software and item of equipment is documented.

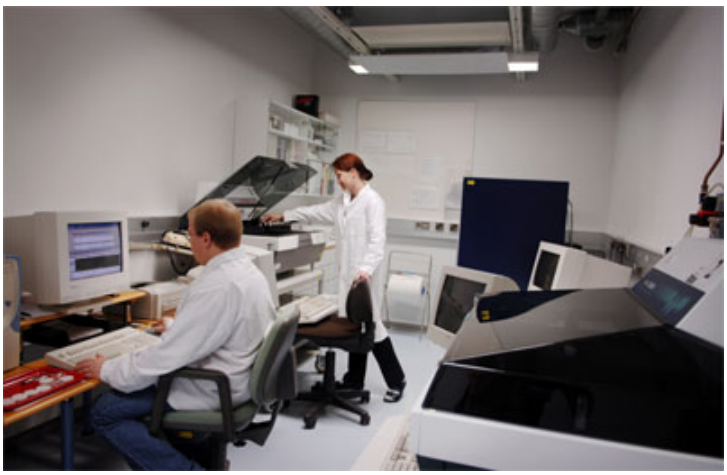

Fig. 3. Activity concentrations of tritium, Rn-222, C-14 and Sr-90 are determined using Guardian 1414 liquid scintillation spectrometer.

Regular calibrations

Standard 17025 requires that the calibration programmes are established for the equipment having significant effect on the results. At STUK the equipment used for radioactivity measurements are calibrated regularly. For all the analysis methods the interval for calibration is determined. For example, ^{222}Rn determination is calibrated between 3 to 5 years and ^{89,90}Sr between 5 to 7 years. Calibration procedure and the results are documented as closed circuit technical documents (TecDocs). With methods where internal standard is used as tracer, no regular calibrations of equipment are needed e.g. Pu. In these cases the activity of the tracer used is controlled regularly. The results are documented as a TecDoc in order to attain traceability of the results.

Control measurements

The laboratory needs to maintain confidence on its calibration status. This is done by making control measurements using blank samples, background and reference samples and internal measurements of the equipment (alpha spectrometer) indicating that calibrations are valid during activity measurement. All measurements are done regularly and the results are documented in x-cards (Fig. 4).

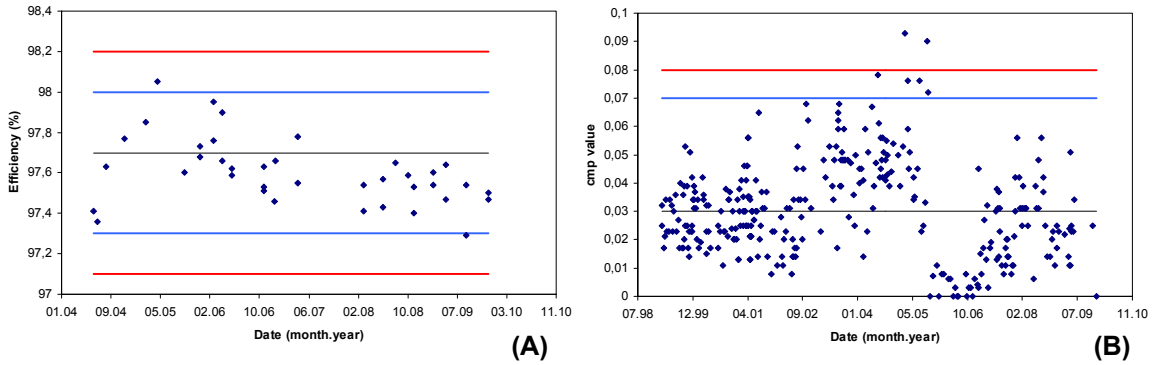

Fig. 4. Regular C-14 measurements of the reference sample (A) and background measurements from gross alpha determination (B) using Quantulus 1220 liquid scintillation spectrometer. Blue line presents the alarm level and red line the action level.

Regular maintenances

Confidence in the performance of equipment is maintained by regular service which is done by authorized personnel. Typically, measurement equipment is maintained once a year.

Intercomparions

The laboratory takes regularly part in internal and international intercomparison exercises or proficiency tests. These are good tools to assure high quality of analyses and also excellent tools for analysis development. STUK participates in 5 to 10 international intercomparisons per year (Fig. 5). Additionally, internal intercomparisons are arranged to ensure convergent results and personnel competence.

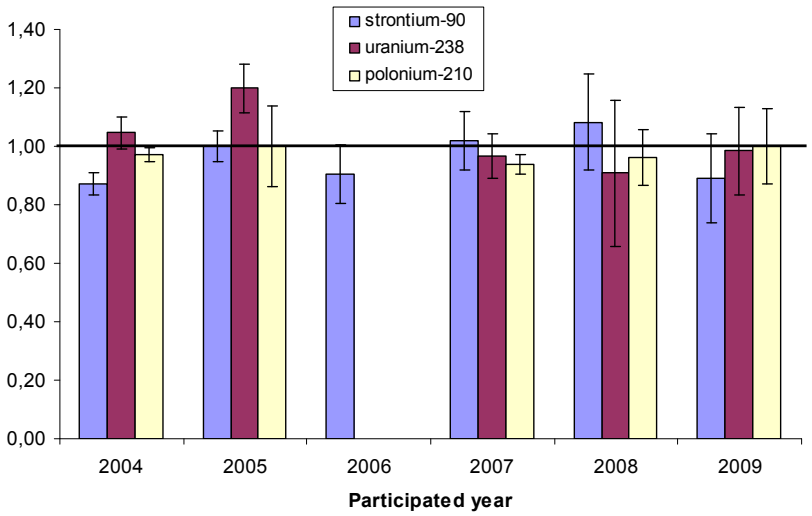

Fig. 5. Intercomparison results for ^{90}Sr and ^{238}U in 2004 – 2009. Analyzed samples were urine, lake water, sea water, drinking water, spinach and milk power.

Laboratory information management system

A uniform Laboratory Information Management Systems, LIMS and LINSSI, are used for data management, follow-up samples and chemicals, and analysis flow control. The system is password-protected and access is given only for authorized persons. The system helps the management of laboratory work, data management, traceability of the results, reporting and quality assurance in the laboratory. In the future, the same system will manage also the equipment used with radioactivity determinations.

Development of laboratory work and analyses methods

The most important issues in accredited laboratory are continuous improvement of laboratory work and analyses methods as well as the whole quality management system. New analyses methods are first tested, then validated and taken in use if they are found eligible for the analysis. Validation procedure is planned and all work tasks are documented as closed circuit technical documents (TecDocs). The laboratory work is enhanced by self-assessments, external and internal audits, various customer surveys and regular meetings with customers.

Conclusions

Radiochemical analyses are demanding analyses and demand proficiency of the whole personnel, well documented working procedures and properly controlled equipment. Validation of a new analysis method is a long procedure and requires a careful plan before the actual work can begin. In routine work, attention is needed on regular control measurements and contamination in order to maintain high quality of the analyses and measurement equipment. Workable laboratory information management systems provide an effective tool for evaluation of control measurements.

Accreditation is an excellent way to bring clarity in the routine work and regular external assessors improve the continuous maintenance of laboratory work. Laboratory work can be continuously improved by self-assessments, internal audits and customer surveys or regular meetings with customers.

References

EUROPEAN STANDARD EN ISO/IEC 17025, General requirements for the competence of testing and calibration laboratories (ISO/IEC 17025:2005): 2005.

Ikäheimonen TK, Klemola S, Vesterbacka P.: Towards quality excellence in radioanalytical laboratories at STUK, Finland. In: Povinec PP, Sanchez-Cabeza JA (eds.) Radionuclides in the environment. International Conference on Isotopes in Environmental Studies. Radioactivity in the environment 8, 2006: 629–639

Condition of liver, and iron and plutonium content

Mussalo-Rauhamaa, Helena[1]; Jaakkola, Timo[2]; Miettinen, Jorma K.[2]; Laiho, Kaino[3]
[1] University of Helsinki, Department of Public Health, FINLAND
[2] University of Helsinki, Department of Radiochemistry, FINLAND
[3] University of Helsinki, Department of Forensic Medicine, FINLAND

Abstract

Plutonium and iron share a common metabolism in transportation and accumulation in human body. This was also supported by this study, where the accumulation of plutonium and iron in liver was investigated. The ^{239,240}Pu and iron contents in liver correlated positively (Rs = 0.378) in healthy livers, but not in livers having pathological changes. In contrast to iron content , the plutonium content of fatty degenerated or cirrhotic livers was significantly lower than that in normal livers. This difference suggests that plutonium and iron are not similarly accumulated or excreted in fatty degenerated and cirrhotic livers. The plutonium contents in lung and bone of these persons did not differ from the average values of the same age group, which may suggest that plutonium is excreted from the liver cells mainly by feces, instead of having been recirculated.

$^{240}Pu/^{239}Pu$ ratio in peat, lichen and air filter samples contaminated by global nuclear test fallout, the Chernobyl accident and other nuclear events

Salminen, Susanna[1]; Paatero, Jussi[2]
[1] Laboratory of Radiochemistry, University of Helsinki, FINLAND
[2] Finnish Meteorological Institute, FINLAND

Abstract

The $^{238}Pu/^{239+240}Pu$ activity ratio by alpha spectrometry is a useful method for separating the influences from nuclear weapons testing and the Chernobyl fallout. However, $^{238}Pu/^{239+240}Pu$ activity ratios in global nuclear test fallout and weapons-grade Pu are nowadays so similar, that it is difficult to reliably distinguish the two Pu sources by using this activity ratio. Besides, the activity concentration of ^{238}Pu is usually relatively low compared to ^{239}Pu and ^{240}Pu in environmental samples, leading to high uncertainties in $^{238}Pu/^{239+240}Pu$ activity ratio. As a complementary method for alpha spectrometry, ICP-MS provides the tool for identifying the origin of the Pu from global fallout or weapons-grade Pu, since the $^{240}Pu/^{239}Pu$ mass ratio is clearly different in Pu from nuclear weapons testing and weapons-grade Pu.

$^{238}Pu/^{239+240}Pu$ and $^{241}Pu/^{239+240}Pu$ activity ratios have been determined for peat and lichen samples collected in Finland immediately after the Chernobyl accident in 1986, air filter samples collected in Sodankylä in 1963 and air filter samples collected in Astana, Kazakhstan, in 2002. The Pu activity ratios indicated contamination from global nuclear test fallout in air filters from Sodankylä, and in peat and lichen samples Pu has been deposited from global fallout and the Chernobyl accident. $^{238}Pu/^{239+240}Pu$ activity ratio in air filters from Astana corresponded with the ratio in nuclear fuel of high burnup. In this study, a more exact estimation about the origin of Pu in these different types of samples from Finland and Kazakhstan was sought by determining their $^{240}Pu/^{239}Pu$ mass ratios.

The membrane filters used for alpha counting were decomposed and the resulting solutions containing Pu were purified with extraction chromatography. Mass concentration of ^{239}Pu and ^{240}Pu in the samples was determined by quadrupole ICP-MS. Results from $^{240}Pu/^{239}Pu$ mass ratio determinations for the investigated samples will be presented in detail in the poster.

Sensitivity of the standard and Fpg-modified comet assay for the estimation of DNA damage in peripheral blood lymphocytes after exposure to gamma rays

Garaj-Vrhovac, Vera[1]; Gajski Goran[1]; Miljanić Saveta[2]
[1] Institute for Medical Research and Occupational Health, Mutagenesis Unit, CROATIA
[2] Ruđer Bošković Institute, Laboratory for Radiation Chemistry and Dosimetry, CROATIA

Abstract

The comet assay is a rapid and sensitive technique for measuring DNA damage. This assay detects single and double stranded breaks, sites of incomplete repair, alkali labile sites, DNA-DNA and DNA-protein cross-links. In addition, particular enzymes such as formamidopyrimidine glycosilase (Fpg) can be used for detection of oxidative damage at the level of DNA molecule by cleavage of 8-oxodG, FaPyGua, FaPyAde and other ring-opened purines caused by reactive oxygen species (ROS). The aim of this study was to test the sensitivity of both standard alkaline and Fpg-modified comet assay and to detect the type of DNA damage caused by gamma rays. In that manner, human lymphocytes were exposed to gamma radiation doses of 0.1 Gy and 4 Gy *in vitro*. With the standard assay increase in DNA damage was noticed for both exposure doses but it was significant only at higher dose of 4 Gy whereas at lower dose there were no statistically significant increase in neither of the standard comet assay parameters. Fpg-modified protocol showed significant increase in all the parameters measured for both exposure doses indicating that the modified version is capable of detecting wider scale of DNA damage induced by gamma radiation. In addition, with modified protocol it is possible to detect ROS mediated DNA damage, thus significant increase in modified comet parameters in comparison to the standard ones suggests that gamma radiation did induce oxidative damage in DNA molecule. Correlation between different protocols of the comet assay suggests that Fpg-modified version is more sensitive to gamma radiation by virtue of measuring oxidative DNA damage in addition to the basal DNA strand breaks. Results obtained lead to the conclusion that gamma rays affects DNA molecule by ROS that are the most frequent product of gamma radiation. Additionally, human lymphocytes proved to be sensitive to ionizing radiation depending on the radiation dose and are suitable biomarkers for this type of research.

Introduction

Ionizing radiation is nowadays omnipresent in human lives because of the increasing development of technology, industry and medicine. People live and work near nuclear facilities and places of testing nuclear weapon and also use nuclear (gamma) radiation in medical purposes. In each case, human organism bears the strong genotoxic effect making the structure of the DNA molecule unstable and causing the genesis of many changes in it (Mettler and Voelz 2002). The damage of the genetic material caused by ionizing radiation is one of the best precondition indicators for development of malign diseases such as breast, gall-bladder or thyroid cancer (Cooke and Evans 2006). Gamma radiation affects the DNA structure directly, causing strand breaks, or indirectly causing cleavage of the water molecules and damaging the DNA molecule by reactive oxygen species (ROS) (Ito et al. 2007). These changes can be examined in human lymphocytes using different cytogenetic techniques.

The comet assay is a rapid, simple, visual and sensitive technique for measuring and analyzing DNA damage at the single cell level (Fairbairn et al. 1995, Faust et al. 2003, Møller 2006, Olive 1999, Singh 1988). This technique can be performed at the level of individual cells and requires a small number of cells per sample. Single cells can be used *in vivo* and *in vitro* as well as in biomonitoring of population exposed to radiation or chemical mutagens (Faust et al. 2003, Garaj-Vrhovac et al. 2002). The comet assay detects single and double stranded breaks at the level of DNA molecule, sites of incomplete repair, alkali labile sites, DNA-DNA and DNA-protein cross-links. Besides, the comet assay can be used for detection of the level of the DNA fragmentation in apoptosis (Collins 2004, Husseini et al. 2005, Olive 1999, Piperakis et al. 1999). Particular enzymes such as formamidopyrimidine glycosilase can be used for detection of oxidative damage at the level of the DNA molecule caused by ROS (Collins et al. 1993, Speit et al. 2003).

The aim of this study was to detect the type of DNA damage caused by ionizing radiation. For that purpose human peripheral blood lymphocytes were exposed to gamma radiation doses of 0.1 Gy and 4 Gy *in vitro*. Considering that, two forms of the comet assay, standard alkaline and Fpg-modified were used.

Material and methods

Blood sampling

The study was performed on peripheral blood samples obtained from a healthy female non-smoking donor (age 24 years). The donor was not exposed to ionizing radiation, vaccinated or used medicals for a year before blood sampling. Whole venous blood was collected under sterile conditions in heparinised vacutainer tubes (Becton Dickinson, Franklin Lakes, NJ, USA) containing lithium heparin as anticoagulant. After collection, blood was divided into a large number of samples. All experiments were conducted on peripheral blood lymphocytes cultivated at 37ºC in an atmosphere of 5% CO_2 in air.

Exposure conditions

The whole blood samples were irradiated with gamma radiation on the ice. As a source of radiation Gammacell 220 (Ruđer Bošković Institute, Zagreb, Croatia) was used. Vacutainers (volume 5 cm^3) containing blood samples were exposed to radiation doses

defined as doses in the water, but irradiation was performed in the air. Samples were irradiated with radiation doses of 0.1 Gy and 4 Gy that is equal to radiation periods of 32.3 s and 23 min and 9 s at the temperature of 21°C. Significance of the absorbed dose was 3% (Miljanic et al. 1994). To get homogenate samples, they were stirred after irradiation, cooled to 4°C, transported to the laboratory on ice and processed as quickly as possible.

Alkaline comet assay

The comet assay was carried out under alkaline conditions, basically as described by Singh et al. (1988). Fully frosted slides were covered with 1% normal melting point (NMP) agarose (Sigma, St Louis, Mo, USA). After solidification, the gel was scraped off the slide. The slides were then coated with 0.6% NMP agarose. When this layer had solidified a second layer containing the whole blood sample mixed with 0.5% low melting point (LMP) agarose (Sigma) was placed on the slides. After 10 min of solidification on ice, the slides were covered with 0.5% LMP agarose. The slides were then immersed for 1 h in ice-cold freshly prepared lysis solution [2.5 M NaCl, 100 mM disodium EDTA, 10 mM Tris–HCl, 1% sodium sarcosinate (Sigma), pH 10] with 1% Triton X-100 (Sigma) and 10% dimethyl sulfoxide (Kemika, Zagreb, Croatia) added fresh to lyse cells and allow DNA unfolding. The slides were then placed on a horizontal gel electrophoresis tank, facing the anode. The unit was filled with fresh electrophoresis buffer (300 mM NaOH, 1 mM disodium EDTA, pH 13.0) and the slides were placed in this alkaline buffer for 20 min to allow DNA unwinding and expression of alkali-labile sites. Denaturation and electrophoresis were performed at 4°C under dim light. Electrophoresis was carried out for 20 min at 25 V (300 mA). After electrophoresis the slides were rinsed gently three times with neutralization buffer (0.4 M Tris–HCl, pH 7.5) to remove excess alkali and detergents. Each slide was stained with ethidium bromide (20 µg/ml) and covered with a coverslip. The slides were then stored in sealed boxes at 4°C until analysis.

Fpg-modified comet assay

The analysis of oxidized purines was performed using an Fpg FLARE™ assay kit (Trevigen Inc, Gaithersburg, Maryland, USA) with some modification (Comet Assay interest group website: http://cometassay.com/). Within the kit the manufacturer provided all the reagents used. Fully-frosted microscopic slides were prepared. Each slide was covered with 1% normal melting point (NMP) agarose (Sigma). After solidification, the gel was scraped off the slide. The slides were then coated with 0.6% NMP agarose. A low melting point (LMP) agarose was melted and stabilized in a water bath at 37 °C. For each sample and control, 5 µl of cell homogenate was mixed with 100 µl of LMP agarose (provided with the FLARE^{TM} assay kit) and placed on the slides. After 10 min of solidification on ice, the slides were covered with 0.5% LMP agarose. The slides were then immersed in a pre-chilled lysis solution (provided with the FLARE^{TM} assay kit) and kept in a refrigerator at 2 °C for 60 min. Followed the immersion in the FLARE^{TM} buffer, three times for 15 min. After lysis, the slides were treated with 100 µl of Fpg enzyme (1:500 in REC dilution buffer). The enzyme was diluted right before use. Control slides were treated with 100 µl of REC dilution buffer only. The slides were placed horizontally in a humidity chamber at 37 °C for 30 min.

All slides were then immersed in an alkali solution (0.3 M NaOH, 1 mM Na_2EDTA; pH 12.1) for 40 min. Followed electrophoresis in a pre-chilled alkali solution (0.3 M NaOH, 1 mM Na_2EDTA; pH 12.1) at 1 V/cm for 20 min. After electrophoresis, the slides were rinsed gently three times with neutralization buffer (0.4 M Tris–HCl, pH 7.5) to remove excess alkali and detergents. Each slide was stained with ethidium bromide (20 µg/ml) and covered with a coverslip. Slides were stored at 4°C in sealed boxes until analysis.

Comet capture and analysis

A total of one hundred randomly captured comets from each slide were examined at 250x magnification using an epifluorescence microscope (Zeiss, Oberkochen, Germany) connected through a black and white camera to an image analysis system (Comet Assay II; Perceptive Instruments Ltd., Haverhill, Suffolk, UK). The analysis did not include the edges and damaged parts of the gel as well as debris, superimposed comets, and comets without distinct head ("clouds", "hedgehogs", or "ghost cells"). To quantify DNA damage, the following comet parameters were evaluated: tail length, tail intensity (percentage of DNA in tail), and tail moment. Differences in the tail length, tail intensity and tail moment between samples obtained with standard alkaline comet assay and Fpg-modified comet assay were considered as oxidative DNA damage in a single cell.

Statistical analysis

The various parameters measured in the exposed and control groups were evaluated using Statistica 5.0 package (StaSoft, Tulsa, Okla, USA). Each sample was characterized for the extent of DNA damage by considering the mean ± SE (standard error of the mean), median and range of the comet parameters. In order to normalize the distribution and to equalize the variances, a logarithmic transformation of data was applied. Multiple comparisons between groups were done by means of ANOVA on log-transformed data. Post-hoc analysis of differences was done by Scheffé test. The level of statistical significance was set at $P<0.05$.

Results

Results of the standard alkaline comet assay are presented in the Figure 2A. These results showed statistically significant increase of the mean values for all three parameters of the standard comet assay ($P<0.05$) in the sample irradiated with the dose of 4 Gy in contrast to control sample and sample irradiated with the dose of 0.1 Gy. Sample irradiated with the dose of 0.1 Gy showed slightly increased values for all parameters measured but there were no significant differences in compare to the corresponding control. Results of the Fpg-modified comet assay are presented in the Figure 2B. These results showed statistically significant increase in all three parameters of modified comet assay ($P<0.05$) for both irradiation doses in compare to the control sample. Generally, the mean values of all three Fpg-modified comet assay parameters were significantly higher than of the standard comet assay. These findings suggest that the Fpg-modified comet assay is more sensitive to gamma irradiation than the standard alkaline comet assay.

Discussion

Our goal was to test the sensitivity of the standard alkaline and Fpg-modified version of comet assay after exposure to different doses of gamma radiation. This type of radiation is a potent carcinogen mainly due to it potential as oxidative-induced damage agent. It produces variety of primary lesions in DNA such as single and double strand breaks, DNA-DNA and DNA-protein cross-links, alkali-labile sites and damage to purine and pyrimidine bases as well as oxidize bases and abasic sites (Cadet et al. 1999, Đurinec et al. 2006, Garaj-Vrhovac and Zeljezic 2004, Sudprasert et al. 2006).

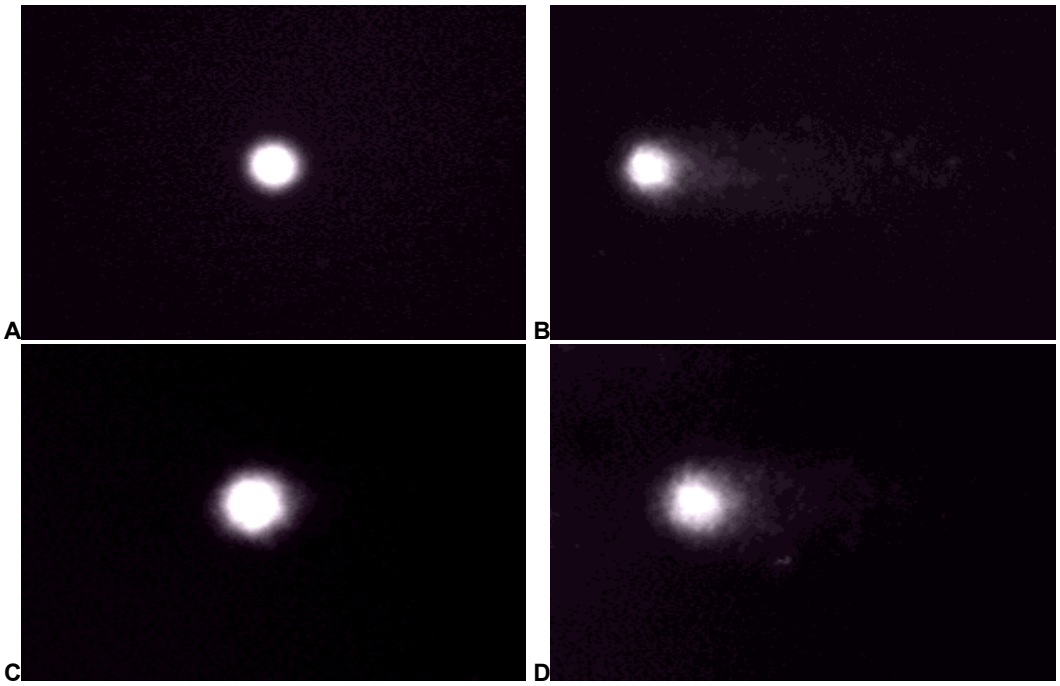

Fig. 1. Comet assay microphotographs represent undamaged lymphocyte from the un-exposed sample (A). Image (B) represents damaged lymphocyte that has comet appearance. Fpg-modified comet assay microphotographs represent undamaged lymphocyte from the un-exposed sample (C). Image (D) represents damaged lymphocyte that has comet appearance. Cells were stained with ethidium bromide. Cells were photographed under the fluorescent microscope using a 60x objective equipped with a 515 nm to 560 nm excitation filters and a 590 nm barrier filter.

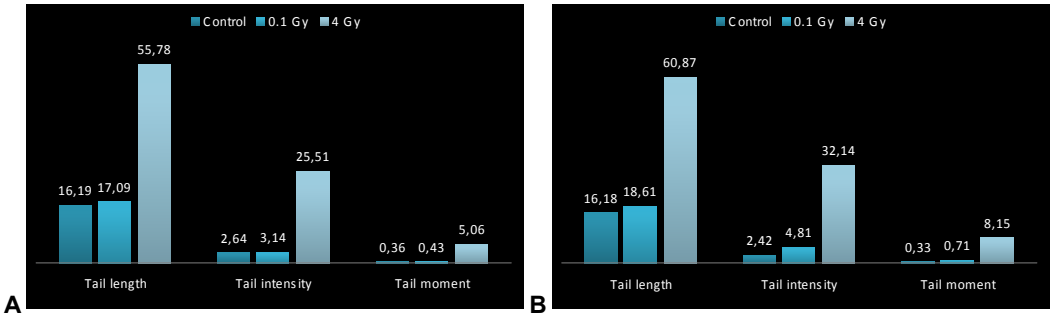

Fig. 2. Parameters of the alkaline comet assay (A) and Fpg-modified comet assay (B) (tail length, tail intensity and tail moment), in human peripheral blood lymphocytes exposed to 0.1 Gy and 4 Gy gamma irradiation.

Both protocols used in this study showed genotoxic effect of gamma rays on DNA molecule of human peripheral blood lymphocytes *in vitro*. With the standard alkaline comet assay increase in DNA damage was noticed in both exposure doses but it was significant only at higher dose of 4 Gy whereas at lower dose there were no statistically significant increase in neither of the standard comet assay parameters. Usage of the Fpg-modified protocol showed significant increase in all the parameters measured at both exposure doses indicating that the modified version of this assay is capable to detect wider scale of DNA damage induced by gamma irradiation. In addition, with modified protocol it is possible to detect ROS mediated DNA damage, thus significant increase in modified comet parameters in comparison to the standard one suggests that gamma radiation did induce oxidative damage in DNA molecule *in vitro*.

Some of the previous studies also showed that the Fpg-modified version of the comet assay is more sensitive for detection of DNA damage than the standard alkaline one (Domijan et al. 2006, Fracasso et al. 2006, Husseini et al. 2005, Garaj-Vrhovac et al. 2002, Rössler et al. 2006). According to that fact, scientists revealed that using the standard alkaline comet assay it is possible to detect damages at radiation doses from 5 cGy to 10 cGy and in some adapted experimental conditions (*e.g.* addition of the Fpg enzyme) it is possible to detect damages even at radiation doses of 0.6 cGy (Dusinska and Collins 1996, Malyapa et al. 1998, Verbeek et al. 2007). The additional reason why the Fpg-modified comet assay is more sensitive than the standard alkaline one is that the Fpg enzyme helps to detect oxidative damage of the DNA molecule by cleavage of 8-oxodG, FaPyGua, FaPyAde and other ring-opened purines (Karakaya et al. 1997).

Conclusions

In this study correlation between different protocols of the comet assay was made suggesting that Fpg-modified version is more sensitive to gamma radiation by virtue of measuring oxidative DNA damage in addition to basal DNA strand breaks. Results obtained lead to the conclusion that gamma radiation affects the DNA molecule by ROS that are most frequent product of the gamma radiation effect. Human peripheral blood lymphocytes proved to be sensitive to ionizing radiation depending on the radiation dose and are suitable biomarkers for this type of research.

References

Cadet J, Delatour T, Douki T, Gasparutto D, Pouget JP, Ravanat JL, Sauvaigo S. Hydroxyl radicals and DNA base damage. Mutation Research 1999; 424 (1-2): 9-21.

Collins AR. The comet assay for DNA damage and repair: principles, applications, and limitations. Molecular Biotechnology 2004; 26 (3): 249-262.

Collins AR, Duthie SJ, Dobson VL. Direct enzymatic detection of endogenous oxidative base damage in human lymphocyte DNA. Carcinogenesis 1993; 14 (9): 1733-1735.

Comet Assay interest group website: http://cometassay.com/

Cooke M, Evans M. Oxidative damage to DNA in non-malignant disease: biomarker or biohazard? Genome Dynamics 2006; 1: 53-66.

Dusinská M, Collins A. Detection of oxidised purines and UV-induced photoproducts in DNA of single cells, by inclusion of lesion specific enzymes in the comet assay. Alternatives to Laboratory Animals 1996; 24: 405-411.

Domijan AM, Želježić D, Kopjar N, Peraica M. Standard and Fpg-modified comet assay in kidney cells of ochratoxin A- and fumonisin B_1-treated rats. Toxicology 2006; 222 (1-2): 53-59.

Đurinec M, Želježić D, Garaj-Vrhovac V. Phytohaemagglutinin as a modulator of DNA repair measured by chromosome aberration analysis in micronucleus assay in ionizing radiation biodosimetry. Radiology and Oncology 2006; 40 (1): 43-49.

Fairbairn DW, Olive PL, O'Neill KL. The comet assay: a comprehensive review. Mutation Research 1995; 339 (1): 37-59.

Faust F, Kassie F, Knausmüller S, Boedecker RH, Mann M, Mersch-Sundermann V. The use of the alkaline comet assay with lymphocytes in human biomonitoring studies. Mutation Research 2003; 566 (3): 209-229.

Fracasso ME, Doria D, Franceschetti P, Perbellini L, Romeo L. DNA damage and repair capacity by comet assay in lymphocytes of white-collar active smokers and passive smokers (non- and ex-smokers) at workplace. Toxicology Letters 2006; 167 (2): 131-141.

Garaj-Vrhovac V, Kopjar N, Ražem D, Vekić B, Miljanic S, Ranogajec-Komor M. Application of the alkaline comet assay in biodosimetry: assessment of in vivo DNA damage in human peripheral leukocytes after a gamma radiation incident. Radiation Protection Dosimetry 2002; 98 (4): 407-416.

Garaj-Vrhovac V, Želježić D. Comet assay in the assessment of the human genome damage induced by γ-radiation in vitro. Radiology and Oncology 2004; 38 (1): 43-47.

Husseini GA, O'Neill KL, Pitt WG. The comet assay to determine the mode of cell death for the ultrasonic delivery of doxorubicin to human leukemia (HL-60 Cells) from Pluronic P105 micelles. Technology in Cancer Research and Treatment 2005; 4 (6): 707-799.

Handerson L, Wolfreys A, Fedyk J, Bourner C, Windebank S. The ability of the Comet assay to discriminate between genotoxins and cytotoxins. Mutagenesis 1998; 13 (1): 89-94.

Ito K, Takubo K, Arai F, Satoh H, Matsuoka S, Ohmura M, Naka K, Azuma M, Miyamoto K, Hosokawa K, Ikeda Y, Mak TW, Suda T, Hirao A. Regulation of reactive oxygen species by Atm is essential for proper response to DNA double-strand breaks in lymphocytes. Journal of Immunology 2007; 178 (1): 103-110.

Karakaya A, Jaruga P, Bohr VA, Grollman AP, Dizdaroglu M. Kinetics of excision of purine lesions from DNA by Escherichia coli Fpg protein. Nucleic Acids Research 1997; 25 (3): 474-477.

Leonard A, Rueff J, Gerber GB, Leonard ED. Usefulness and limits of biological dosimetry based on cytogenetic methods. Radiation Protection Dosimetry 2005; 115 (1-4): 448-454.

Malyapa RS, Bi C, Ahern EW, Roti Roti JL. Detection of DNA damage by the alkaline comet assay after exposure to low-dose gamma radiation. Radiation Research 1998; 149 (4): 396-400.

Mettler FA, Voelz GL. Major radiation exposure--what to expect and how to respond. The New England Journal of Medicine 2002; 346 (20): 1554-1561.

Miljanić S, Ražem D, Ranogajec-Komor M. Dosimetric calibration of an annular 60 Co gamma-ray source. Journal of Radioanalytical and Nuclear Chemistry 1994; 185 (1): 101-108.

Møller P. The alkaline comet assay: towards validation in biomonitoring of DNA damaging exposures. Basic and Clinical Pharmacology and Toxicology 2006; 98 (4): 336-345.

Olive PL. DNA damage and repair in individual cells: applications of the comet assay in radiobiology. International Journal of Radiation Biology 1999; 75 (4): 395-405.

Piperakis SM, Visvardis EE, Tassiou AM. Comet assay for nuclear DNA damage. Methods in Enzymology 1999; 300: 184-194.

Rössler U, Hornhardt S, Seidl C, Müller-Laue E, Walsh L, Panzer W, Schmid E, Senekowitsch-Schmidtke R, Gomolka M. The sensitivity of the alkaline comet assay in detecting DNA lesions induced by x-rays, gamma rays and alpha particles. Radiation Protection Dosimetry 2006; 122 (1-4): 154-159.

Singh NP, McCoy MT, Tice RR, Schneider LL. A simple technique for quantitation of low levels of DNA damage in individual cells. Experimental Cell Research 1988; 175 (1): 184-191.

Speit G, Schütz P, Bonzheim I, Trenz K, Hoffman H. Sensitivity of the FPG protein towards alkylation damage in the comet assay. Toxicology Letters 2003; 146 (2): 151-158.

Sudprasert W, Navasumrit P, Ruchirawat M. Effects of low-dose gamma radiation on DNA damage, chromosomal aberration and expression of repair genes in human blood cells. International Journal of Hygiene and Environmental Health 2006; 209 (6): 503-511.

Tice RR, Agurell E, Anderson D, Burlinson B, Hartmann A, Kobayashi H. Single cell gel/comet assay: guidelines for in vitro and in vivo genetic toxicology testing. Environmental and Molecular Mutagenesis 2000; 35 (3): 206-221.

Verbeek F, Koppen G, Schaeken B, Verschaeve L. Automated detection of irradiated food with the comet assay. Radiation Protection Dosimtery 2007; 128 (4): 421-426.

Gamma spectrometric sample measurements at STUK laboratories

Klemola, Seppo; Leppänen Ari-Pekka; Mattila Aleksi; Renvall Tommi
STUK – Radiation and Nuclear Safety Authority, FINLAND

Abstract

In this paper, the facilities and applications for gamma spectrometric sample measurements at the Finnish Radiation and Nuclear Safety Authority (STUK) will be presented. The Department of Research and Environmental Surveillance has 15 HPGe spectrometers operated in specially constructed counting rooms. The software for the spectrum analysis and detector calibration are the key components of the accredited method. Integrated Laboratory Information Management System (LIMS) databases offer tools to manage the large amount of data involved in spectrum analyses.

Applications of STUK's gamma spectrometry include surveillance of environmental radioactivity in Finland, radioecological studies of both natural and artificial radionuclides and contracted services to industry and trade and for various organisations and institutes. STUK's laboratory is also one of the Radionuclide Laboratories certified by the Comprehensive Nuclear Test Ban Treaty Organisation (CTBTO). One of the tasks of the Department is to maintain measurement standards for radioactivity determinations.

Introduction

Finnish Radiation and Nuclear Safety Authority (STUK) has more than 40 years of experience in gamma spectrometric analysis of environmental samples.

Since 1999, the method of gamma spectrometric sample measurements has been accredited according to the Standard EN ISO/IEC 17025. The method of analysis of environmental samples, biological samples and foodstuffs is two-graded: 1) measurements of ^{137}Cs, ^{134}Cs, ^{131}I, ^{40}K and natural decay series of U and Th, 2) advanced analysis of all radionuclides emitting gamma-rays in energy range of 30 keV-2700 keV. The accreditation has been renewed in 2003 and 2007.

More than 4 000 samples are analysed annually in the Department of Research and Environmental Surveillance, and more than 500 additional quality control measurements are performed.

Laboratories and equipment

The sample measurements are carried out in three separate counting rooms; two of them are located in Helsinki and one in Rovaniemi, in the premises of the Regional

Laboratory of Northern Finland. The Helsinki counting rooms are constructed from selected concrete and mortar materials where the abundance of natural radionuclides is low. In addition, the rooms are equipped with special air conditioning in order to decrease background radiation due to indoor radon, and also to prevent contamination of the laboratory during an incidence of fallout. Continuous monitoring of temperature, humidity, air pressure and ambient radon is arranged in order to evaluate changes in detector background and in operation of the measurement equipment. The measurement rooms are equipped with uninterruptible power supplies (UPS) and a reserve power generator (Fig 1.).

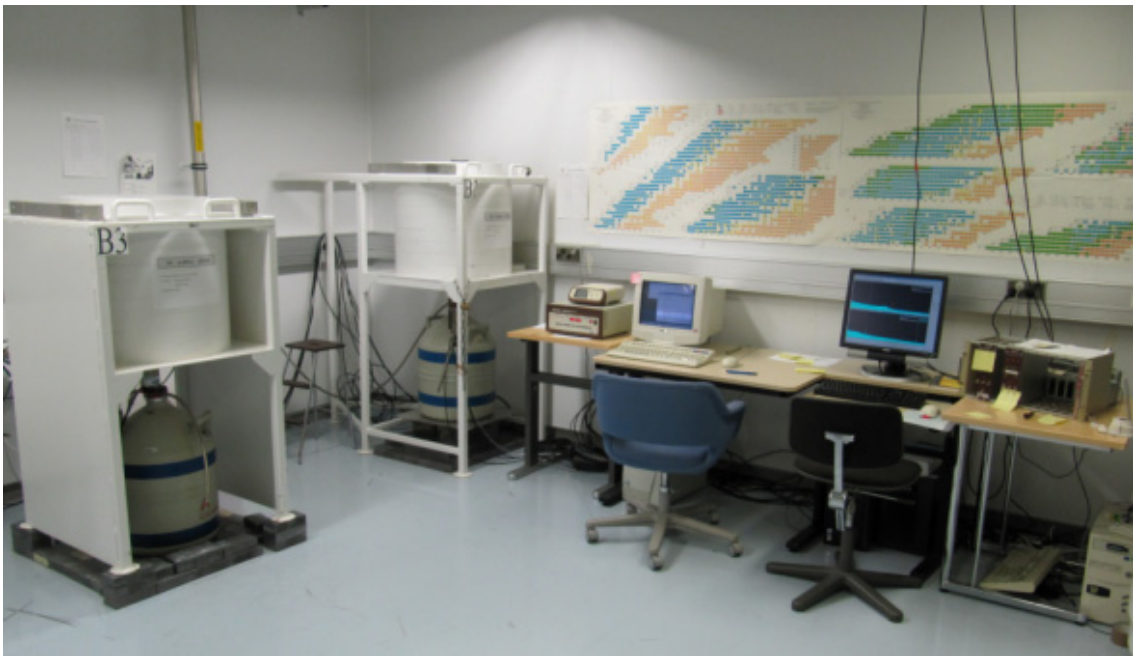

Fig. 1. One of the gamma spectrometry laboratories in the Research and Environmental Surveillance department. HPGe detectors are installed in heavy lead shields.

Currently there are altogether 14 low-background, high-resolution spectrometers at STUK laboratories for sample measurements (Table 1). In addition, two high-resolution spectrometers are employed for environmental monitoring sample measurements at sampling stations. The p-type HPGe detectors are of coaxial design with vertical cryostats. The relative efficiencies of the detectors range from 33% to 90% and energy resolution from 1.6 keV to 2.1 keV at 1.33 MeV. The detectors are installed in 12-14 cm thick lead background shields which are lined on the inside with cadmium and copper. The electronics of the spectrometers are either conventional NIM-modules or all digital stand-alone units. Measurement control and spectrum analysis are performed at a local microcomputer or on any network computer with the proper software installed. Lowest reachable detection limit is a few mBq/sample.

The laboratories in Helsinki use liquid nitrogen for cooling of spectrometers. The supply of nitrogen is arranged with vacuum insulated pipelines from a storage tank outside the building. All the detectors at Rovaniemi laboratory are electrically cooled.

Table 1. HPGe spectrometers for sample measurements at STUK laboratories.

Detector code	Manufacturer and model	Relative efficiency %	Energy resolution keV at 1.33 MeV	Purchase year
G1	ORTEC GEM-35185	33	1.76	1985
F5	ORTEC GEM-35190	38	1.70	1986
F6	ORTEC GEM-35190	39	1.75	1986
V2	ORTEC GEM-18190	18	1.90	1988
P1	ORTEC GEM-30185	30	1.69	1989
F9	ORTEC GEM-90205	87	1.87	1994
N2	ORTEC GEM-80190	78	1.80	1995
P3	ORTEC GEM-30190	36	1.74	1996
B1	Canberra BE5030	50	2.00	1999
P4	ORTEC GEM-35200	38	1.85	2001
G2	ORTEC GEM 50-S	70	1.85	2004
B4	Canberra BE5030	50	1.90	2005
B3	Canberra BE5030	50	1.88	2005
B5	Canberra BE5030	50	1.80	2007
F1	ORTEC GEM-8530	50	1.74	2008

For sample measurements there are three standard measurement geometries at the laboratory. Two of them are simple cylindrical plastic beakers with diameters of 42 mm and 74 mm, correspondingly. The height of beakers is 26 mm, and the volumes are 35 and 105 ml, correspondingly. The third beaker in use is a standard 0.5-l Marinelli beaker (Fig. 2.).

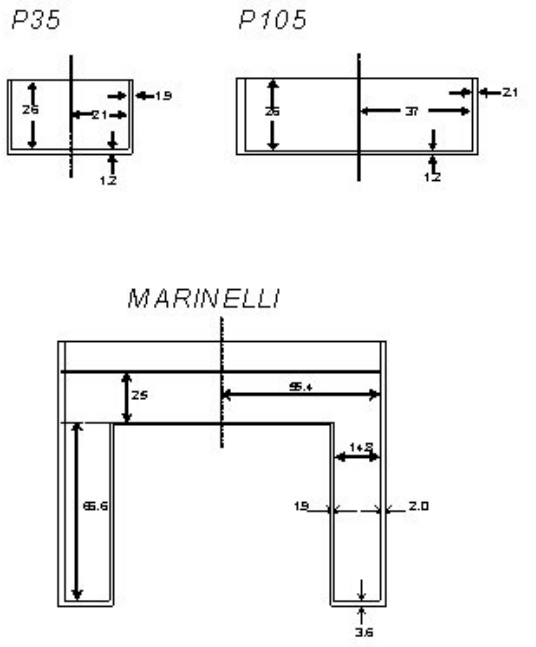

Fig. 2. Three standard measurement geometries for sample measurements at STUK.

All the beakers are measured right on top of the detector end-cap. The efficiency calibrations for other measuring geometries, densities or sample matrices can be obtained using a semi-empirical computer method developed to transfer full-energy peak efficiency to other geometries for the same detector (Ugletveit et al. 1989, Aaltonen et al. 1994).

The experimental efficiency calibrations of the detectors have been obtained with both separate single-line nuclides in water solution and multinuclide standard sources. The following nuclides have been used: ^{40}K, ^{51}Cr, ^{57}Co, ^{60}Co, ^{65}Zn, ^{88}Y, ^{109}Cd, ^{113}Sn, ^{137}Cs, ^{203}Hg, ^{210}Pb and ^{241}Am.

Analysis software and databases

In the early 1980s STUK developed a spectrum analysis programme especially for the analysis of low-level environmental sample measurements. The original GAMMA-83 code was written in Fortran language and run in a mainframe computer (Sinkko 1981, Sinkko and Aaltonen 1985). In the late 1980s, the code was ported to microcomputers and MS-DOS operating system. A MS-Windows version of the programme was written in 1997. This version introduced several new features, e.g. interactive user interface, evaluation of detection limits for selected nuclides, various optional output files.

GAMMA-99 programme searches peaks, evaluates their area and, after subtracting the background, calculates activity concentrations for identified nuclides. The varying heights and densities of the samples and the effect of true coincidence summing are taken into account in calculating the results. The program can be operated either in interactive or automatic mode. The updated master nuclide library has at present 139 nuclides and 1027 gamma lines, including decay data for calculation of coincidence summing corrections.

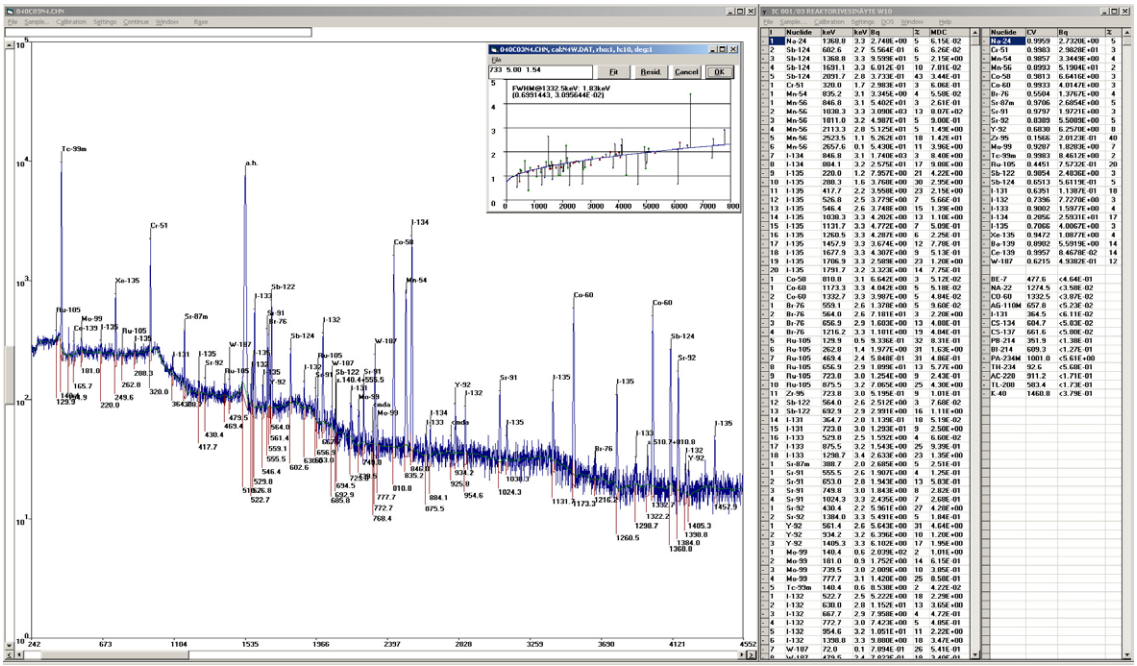

Fig. 3. GAMMA-99 user interface; spectrum, result and energy resolution views.

Recently, the laboratory has implemented and validated a new analysing software package, Unisampo/Shaman. UniSampo is the newest member of the Sampo family of gamma-ray spectrum analysis programs. UniSampo carries out the first part of the analysis, i.e. determination of the peak energies and intensities with the corresponding uncertainty estimates (Aarnio et al. 2001) .Peak analysis results from UniSampo are the input for Shaman programme which is a rule-based expert system for qualitative and quantitative radionuclide identification. Shaman utilizes a reference library with 3 648 radionuclides and 80 062 gamma lines extracted from the ENSDF and NUDAT databases. The programme takes into account e.g. true coincidence summing and is capable of identifying also sum peaks, escape peaks, and X-ray peaks (Aarnio et al. 1995, Ala-Heikkilä et al. 1995).

In 2004, uniform Laboratory Information Management System (LIMS) software was taken into use at the analytical laboratories at STUK. All analytical data, including basic information on sampling and samples, raw measuring data and results, are stored in the database.

In 2010 especially for gamma spectrometry designed database, LINSSI, will be integrated into the LIMS system. LINSSI (Linux System for Spectral Information) is a MySQL database that covers the whole production chain from sample preparation to final analysis results. Also full control of calibrations and their histories is supported, providing complete traceability of the results. As a database system specifically designed for gamma spectroscopy, LINSSI allows for more comprehensive recording of various quantities related to a spectral analysis than LIMS. LINSSI is being developed in collaboration with STUK, Helsinki University of Technology and Health Canada (Aarnio 2006).

Quality assurance

Confidence in the performance of equipment is maintained by regular calibration and servicing, routine checks and control charts. The most important control charts, background, energy resolution and detection efficiency, are based on regular QC measurements. Computerised techniques record the performance characteristics of spectrometers and software. These include peak widths and positions, which are evaluated during the spectrum analysis of every sample measurement, thus decreasing the frequency of regular QC measurements. The obtained values are recorded in a log file.

Corresponding warning limits and action limits are set, taking into account the different characteristics of spectrometers. The acceptance criteria in the charts are normally set as warning limits of 2σ and an action limit of 3σ above and below the long-term average data. However, with low-level measurements the differing behaviour of various background components requires careful consideration. While count rates of the peaks due to ^{40}K and cosmic background can be considered as stable, the count rates from daughter nuclides of ambient radon might vary either periodically or irregularly. ^{210}Pb in detector material and shielding is a special source of background, since it decays at a constant rate and can even be calculated for the future. Each of these components might require separate update frequency, also taking into account the contribution of the background to the total uncertainty of a particular result.

The dominant uncertainty contributions in gamma-ray spectrometry of environmental samples are usually those of count rate, full-energy peak efficiency and

source-detector geometry. In special circumstances other sources of uncertainty will have a major contribution. Examples of these are the same or higher background count rate of a nuclide compared to sample activity, low energy gamma-rays from high density samples, and cascade-summing correction of the poorly-defined decay scheme of a rarely analysed nuclide (Ikäheimonen et al. 2006).

Successful participation in proficiency tests and inter-laboratory comparisons is highlighted as the best way of proving good quality. Since it is not possible to have exercises for all the gamma-emitting nuclides, it is important to show quality of the analyses of a few nuclides representing a variety of situations, especially including the wide range of gamma-ray energies.

To test and demonstrate proficiency also for short-lived nuclides, STUK co-organizes intercomparisons of reactor water analysis. The nuclear power plant coolant water samples are taken and prepared by NPPs and delivered promptly to the participating laboratories. Since all the participants get their sample within a few hours, it is possible to analyse and compare results of nuclides with half-lives shorter than one hour (Klemola 2008).

Applications

Applications of gamma spectrometry at STUK include surveillance of environmental radioactivity in Finland, radioecological studies of both natural and artificial radionuclides, contracted services for industry and trade and for various organisations and institutes. These applications provide a wide variety of sample types to be analysed including air, deposition, water, milk, foodstuffs, biota, sediments, swipe samples, building materials and various export products.

Since 2003, STUK has been one of the radionuclide laboratories certified by the CTBTO (Comprehensive Nuclear Test Ban Treaty Organisation) to support the network of radionuclide air sampling stations. These laboratories perform additional analysis of a suspect air filter samples to verify presence or absence of fission or activation products. Radionuclide laboratories also analyze samples from stations as a part of network quality control program. The main requirements for the CTBTO certification are quality system, documented procedures for sample analysis and good quality of analytical results. Certified laboratories are required to participate in proficiency test exercises organised by the CTBTO.

One of the tasks of the gamma spectrometry laboratory is to maintain measurement standards which ensure the traceability and accuracy of activity measurements of gamma-emitting radionuclides. Measurement standards are accurate spectrometers with traceable calibration, validated methods, or radiation sources. STUK is a member in a network for ionising radiation standard laboratories and participates in the activities of International Committee for Radionuclide Metrology (ICRM) and its Gamma-Ray Spectrometry Working Group.

Gamma spectrometry gives also support to radiation and nuclear safety authorities at STUK performing analyses for dosimetry, metrology, inspections, NPP radiation safety, safeguards and quality assurance. Gamma spectrometry is the most efficient method also for emergency preparedness, which presents a special challenge for the maintenance and development of software and equipment and also personnel competence for rapid response.

References

Aaltonen H, Klemola S, Ugletveit F, Validation of a method for computer calculation of germanium detector efficiencies. Nucl. Instr. and Meth. in Phys. Res. A 1994; 339: 87–91.

Aarnio P, Ala-Heikkilä J, Hakulinen T, Routti J. Expert System for Nuclide Identification in Gamma Spectrum Analysis. Journal of Radioanalytical and Nuclear Chemistry 1995; 193 (2): 219–227.

Aarnio P, Nikkinen M, Routti J. UniSampo, Comprehensive Software for Gamma-Spectrum Processing. Journal of Radioanalytical and Nuclear Chemistry 2001; 248 (2): 371–375.

Aarnio P. Linssi–SQL Database for Gamma-Ray Spectrometry. Part I: Database, Version 1.1. Report TKK-F-A841, Publications in Engineering Physics. A. Espoo: Helsinki University of Technology; 2006.

Ala-Heikkilä J. Expert System for Nuclide Identification in Environmental Gamma Spectra. Report TKK-F-B159. Otaniemi: Department of Technical Physics; 1995.

Ikäheimonen TK, Klemola S, Vesterbacka P. Towards quality excellence in radioanalytical laboratories at STUK, Finland. In: Povinec PP, Sanchez-Cabeza JA (Eds.). Radionuclides in the environment. International Conference on Isotopes in Environmental Studies. Radioactivity in the environment; 2006. 8: p. 629–639.

Klemola S. Inter-laboratory comparisons of short-lived gamma-emitting radionuclides in nuclear reactor water. Applied Radiation and Isotopes 2008; 66: 760–763.

Sinkko K. Computer analysis for gamma-ray spectra in sample measurements. Licentiate thesis, Helsinki: University of Helsinki, Department of Physics; 1981 (in Finnish).

Sinkko K, Aaltonen H. Calculation of the true coincidence summing correction for different sample geometries in gamma-ray spectroscopy. STUK-B_VALO 40. Helsinki: Finnish Centre for Radiation and Nuclear Safety, Surveillance Department; 1985.

Ugletveit F, Aaltonen H, Sinkko K. A simple method for efficiency calibration of germanium detectors. In: Proc XVth Regional Congress of IRPA. 1989 Sep 10–14; Visby, Sweden, 1989. The Radioecology of Natural and Artificial Radionuclides. p. 562–567.

When is *in situ* gamma spectrometry motivated?

Boson, Jonas; Nylén, Torbjörn; Ramebäck, Henrik
Swedish Defence Research Agency, FOI, SWEDEN

Abstract

In situ gamma-ray spectrometry has since the introduction of portable germanium detectors been a widely used method for the assessment of radionuclide ground deposition activity levels. It is, however, a method that is most often associated with fairly large and poorly known uncertainties. A large part of the combined uncertainty originates from the source characterization, e.g. soil density and activity depth profile. In order to reduce this uncertainty soil sampling and subsequent laboratory analysis is often needed. The more samples collected for this characterization, the lower uncertainty in the *in situ* measurement result. However, if a large enough number of soil samples are collected, the uncertainty in the ground deposition activity measure directly obtainable from soil sample measurements will surpass the uncertainty of the *in situ* measurement. This will then render the *in situ* measurement superfluous. In this work we have considered *in situ* gamma ray spectrometry from a decision-maker-point-of-view; at which uncertainty level is *in situ* gamma ray spectrometry fit-for-purpose, and at which uncertainty level are laboratory measurements of soil samples preferable.

Review of modern application of gamma-beta spectrometer – radiometer MKGB-01 "RADEK"

Finkel, Felix
Scientific and Technical Center "Radek" ltd., RUSSIAN FEDERATION

Review of a modern application of spectrometer- radiometer of gamma-beta-radiation MKGB-01 "RADEK"

In the year 2001 STC "RADEK" Ltd. company produced spectrometer- radiometer of gamma-beta-radiation MKGB-01 "RADEK". Since then the device is widely used by various scientific and educational institutions, certification authority, research laboratories and organizations of nuclear fuel cycles. Apart its common use as a measuring instrument of activities of γ-radiating radionuclides in samples of ground, vegetation, water, foodstuff, materials of construction and other substances, it was also applied as a basis for the construction of unique spectrometric units.

Thus, the Railway Service Institute uses MKGB-01 as a measurement instrument of radionuclide contamination of railway acres and roads. On basis of MKGB-01 the underwater gamma-radiation spectrometer was developed for Geologic Institute, allowing the radioactivity measurement of bottom silt with the moving of detector along the bottom. The same spectrometer was also produced for the Federal Security Guard Service of Russian Federation for installation on boats patrolling water area.

The special place in radioactivity measurement of radionuclides belongs to spectrometry of body radiation. So the SEG-10P was developed as a modification of MKGB-01. It is completely implemented in the form of armchair and allows to measure the activity of incorporate γ- emitting radionuclides. The apparatus is used by nuclear power plants and medical centres.

In 2006 in the Russian Centre of Emergency and Radiation Medicine the expert spectrometric unit for human radiation measurement was constructed and put into operation. It is completely composed of analyzers of MKGB-01 spectrometer (14 pieces) and different types of detectors (scintillation and semiconductor detector). The unit is presented by steel chamber with 4x2x2 meters dimensions edged by lead, cadmium and copper. The chamber is provided by scanning operation.

Due to STUK Finland has about 50 devices of such kind.

Introduction

Nuclear-physical analysis methods of samples are widely used in various fields of science and technology. It provides an opportunity to resolve the tasks in such spheres as medicine, ecology, geologic intelligence, atomic industry, etc. To study the

radionuclide composition of samples, among others, gamma- and beta spectrometric methods of analysis are used.

In the beginning of 2001 the company STC "RADEK" manufactured a spectrometer-radiometer of gamma and beta radiation MKGB-01 "RADEK". Since that moment this device is widely used in different scientific, educational organizations, centers of certification, research laboratories and enterprises of NFC (Nuclear Fuel Cycle). Besides the standard use of this device by way of mean of measuring of γ and β radiating radionuclides activities in samples of ground, vegetation, water, foodstuffs, constructing materials and other substances, a unique spectrometric complexes are also constructed on its base.

Review

Thus, the institute of railway transport (VNIIZhT, Russia, Moscow), uses MKGB-01 by way of mean of measuring of radionuclide contamination of railroad track right of way and of automobile roads[1]. This complex is called "Main gamma-spectrometer of high sensivity (MGSHS)" and is placed in laboratory rail car of VNIIZhT. High sensitivity of gamma-spectrometer is determinated by a large volume of scintillator.

Constructively the spectrometer MGSHS consists of two DSU (detection and selection unit with 2 detectors each); unit for summing signals; four analog-digital converters (ADC) MD-129; three high-voltage power supplies; low-voltage power supply and PC. Functionally and programly the complex allows to use a signal from GPS - receiver, to turn on the alarm signal (bleeper, light, etc.), means of objective control, etc. Each DSU has 2 detectors in it on the base of crystals NaI(Tl) with size 100x200 and a PMT-49 (Photomultiplier Tubes) for registration of external gamma-radiation, and a stabilization unit based on beta-gamma coincidence (detector on the basis of scintillating plastic and PMT-85 for stabilization, source of ionizing radiation on the base of ^{60}Co with activity less than the minimum significant).

Conducted in 2007 the induction and performance tests on the known contaminated territories showed, that during the correlation of graphs of ^{137}Cs density contamination measurements, performed with an interval of 17 years, paying respect to the decay and migration of radionuclide correction, the discrepancy doesn't exceed 20%. At this moment the spectrometer is used in laboratory rail car, belonging to VNIIZhT [1].

Also an underwater gamma spectrometer on the basis of MKGB-01 is developed for geological institute, which allows to measure the radioactivity level of bottomset beds through the aid of the detector moving along the bottom. The spectrometer consists of a detector towed on bottom and of an onboard analytical complex. The full consist of the complex includes: a sealed shock-proof sleeve with an obstacles bypass system "Eel", containing a scintillation gamma-radiation detector with crystal CsJ(Tl) with size 80×80 mm; an analytical unit, containing an analog-digital converter board (ADC); power supplies and amplifiers (Fig.1); control PC with appropriate software; armored towing - connecting cable [2].

To stabilize and to control the amplification, a reference source of ^{113}Sn mounted in the detector sleeve was used, which allowed to change operatively the amplifying coefficient depending on the involving facts. The spectrometer is calibrated in the measurement units of specific activities on the volumetric, saturated for gamma-

radiation state standard norms. Estimated minimum detected activity with the exposure time of 30 seconds is as follows for ^{137}Cs - 4 Bq/kg, ^{226}Ra - 10 Bq/kg, ^{232}Th - 7 Bq/kg, ^{40}K - 90 Bq/kg. The working depth of spectrometer sleeve immersion - 500 meters, and by towing with speed 3–4 knots, using 600 meters of a tow cable-hemp – to 200 meters. By towing the underwater gamma-spectrometer the exposition set of each spectrum was about 30 seconds. The towing speed – 3 knots. Thus, in average each single spectrum corresponds to 50 meters of profile.

Fig. 1.

An example of underwater use of spectrometer MKGB-01 in geological purposes is the charting of ferromanganese nodules fields (FMK) in the gulf of Finland of Baltic sea. It's well known that FMK of marginal and inland seas sorb intensively the ^{226}Ra and are largely enriched with it. At the same time the accumulation of ^{137}Cs by nodules is insignificantly to the aleuropelite precipitations, which are intensively accumulating ^{137}Cs in zones, related to the impact of the Chernobyl disaster. These provisions give a theoretical basis of FMK fields charting by means of underwater gamma-spectrometry. Conducted in the gulf of Finland the experimental-methodological works have confirmed the assumptions made above. It can be stated a fairly reliable charting method of FMK fields on the ratio ^{226}Ra/^{137}Cs. Besides it the underwater gamma-spectrometry directly on the activity of ^{137}Cs, and also on the ratio ^{137}Cs/^{40}K and ^{226}Ra, ^{232}Th/^{40}K in many cases allows to separate and to chart the fields of aleuropelite sediments, of sands and boulder-pebble material.

Another successful example of underwater gamma-spectrometer use in geoenvironmental purposes was its application for radiogeochemical situation study in bottom sediments on the mass burial areas of PDUO (potentially dangerous underwater objects), representing the container landfills, containing radioactive waste, or single large objects, containing large quantities of radioactive substances. The researches of four burial plots showed, that by one of the profiles, passing close to two sunken ships with radioactive substances and containers landfill, an extended anomalous zone with ^{137}Cs activity up 1500 Bq/kg was detected. In a container burial area with radioactive waste, a local anomaly with length about 100 meters with ^{137}Cs activity in the maximum of 80 Bq/kg was also detected by another profile. Besides, in different sectors, the ^{137}Cs anomaly with activity from 40 to 60 Bq/kg were allocated by several

profiles. It should be noted, that all the identified anomalies are located in the distribution area of aleuropelite precipitations, which, as known, sorb intensively ^{137}Cs. Cesium background activity for the entire area was vastly negligible and ranged from values below the MDA (minimum detectable activity) to 7 Bq/kg.

Thus, the towed underwater spectrometric complex MKGB-01 proved to be quite suitable for solving problems of ^{137}Cs areal distribution study in bottom sediments and of local pollution identification in bottom sediments, associated with specific objects [2].

The same spectrometer was created by order of Federal Security Guard Service of the Russian Federation (FSGS RF) for installation on boats, patrolling the water areas.

A special place in the measurement of radionuclide activity is occupied by spectrometry of human radiation. In this field a spectrometer of human radiation SEG-10P is developped, it's a modification of MKGB-01. It is designed as a chair with console module on the anvil, aimed at the geometric center of the chair (Fig.2).

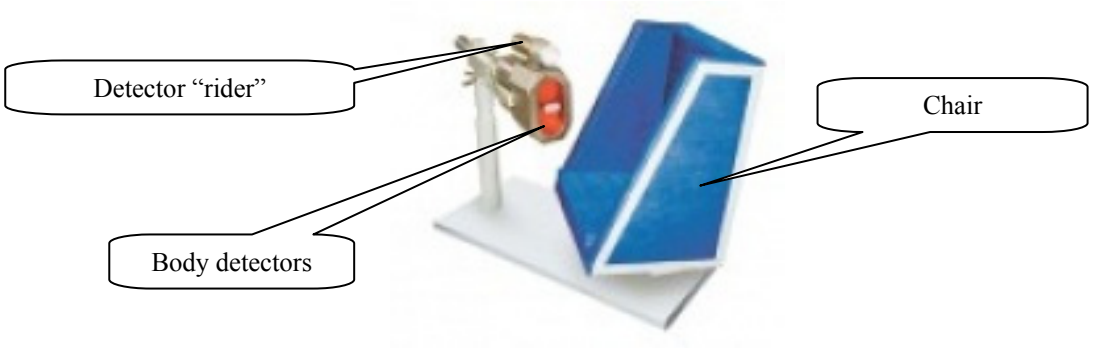

Fig. 2.

The module consists of two body detectors and so-called detector "rider", and allows to evaluate the activity of incorporated γ- radiating radionuclides in human body, lungs and thyroid. The spectrometer calibration is made by means of unified phantoms UF-02T (body) and FSZ-04T (thyroid). The phantoms are made of rectangular polyethylene blocks with bulk 1 kg with openings for placing the rod sources of radioactive material. The spectrometer is widely used on nuclear power plants and in medical centers.

In 2006 in the center of emergency and radiation medicine in Saint-Petersburg an expert low-background spectrometric complex of high sensitivity "SICh-E" for measuring human radiation was manufactured and was put into operation. In fact it's a totality of low-background spectrometers of human radiation and consists of 28 different spectrometric tracts (scintillation and semiconducting), based on electronic modules of spectrometer-radiometer MKGB-01 (14 two-channel analyzers MD-198, Fig.6). The low background of spectrometer is provided by its construction, which represents a steel chamber with size 4x2x2 meters, plated from the inside by lead, cadmium and copper (Fig.3,4,5).

Fig. 3. Chamber of spectrometer of human radiation inside view.

Fig. 4. Detectors view inside the chamber without couch.

Fig. 5. Detectors view inside the chamber with couch and with phantom.

Fig. 6. View of 14 analyzers MD-198 from the front side in the control cabinet.

The complex is intended for expert surveys of the content of incorporated radionuclides of persons, exposed to the radiation in various accidents and incidents, of nuclear technology cycle factory staff during the current and periodic monitoring of internal irradiation, and also of people, living in the radioactively contaminated areas [3]. The works performed on the spectrometer:

- identification of radionuclide composition and measurement in the linear longitudinal scanning mode of low activity levels of gamma - radiating radionuclides throughout the human body in minimum dependence from the character of their distribution in organism and from variations of examined body anthropometric parameters (the contingent of examined people – adults and children from 5 y.o.);
- identification of radionuclide composition and gamma – radiating radionuclides activity measurement in particular human organs: lungs, thyroid, liver, reins, etc.;
- measurement of ^{90}Sr radionuclide content in bones by the bremsstrahlung spectrum as in skeleton entirely, and in separate skeleton parts (in frontal bone, shin bone, etc.);
- measurement of content in the lightweight transuranic radionuclides with low photon radiation energy: plutonium, americium, etc., and also of gamma-radiating radionuclides content with energy less than 300 keV;
- research of radionuclides metabolism in human body in the estimation of parameters;
- research of homeostasis (on potassium metabolism by measuring the ^{40}K radionuclide activity in human body).

The widespread use of MKGB-01 is not limited only by RF. Thanks to STUK (Radiation and Nuclear Safety Authority) Finland has about 50 such devices. Since the mid 1980's in local laboratories of Finland from 6 to 20 counters Mini-Assay were used for evaluation the specific and radioactive substances volumetric activity in foodstuffs and of radon in potable water. The counters showed the total intensity of gamma radiation in samples, and when they began to fail, STUK started to develop a modernization plan of radiometric control equipment. Thus, a new equipment was purchased – gamma-spectrometer MKGB-01, which is used for radionuclide evaluation in samples. The spectrometer consists of a detector NaI(Tl) with size 63×63, located in

a lead protection with thickness 60 mm, computational electronics and of a gamma radiation spectrums processing program. Two measurement geometries are used – Marinelly container with volume 1l for liquids and cylindrical cuvette with volume 320 ml for solid foodstuffs. The minimum detectable specific activities of ^{137}Cs with measuring time - 1000 sec. in laboratory - 50 and 30 Bq/kg for cuvette with volume 320 ml and Marinelly container, respectively. The spectrometer is calibrated for samples density from 0,2 to 2,0 g/cm³ [4].

Referring to the scientific-research sphere of application of spectrometer MKGB-01, it's necessary to mention its use in the maquette of device, which realizes the method of KX-gamma coincidences, created in the ionizing radiation measurements department of D.I. Mendeleev Institute for Metrology (VNIIM). The activity evaluation results, obtained on this maquette, enable to recommend it for inclusion in the primary standard of RF [5].

Another example of MKGB-01 use in the research activity can be the Nephrology Department of Saint-Petersburg Medical University, where spectrometer MKGB-01 is used as an equipment for reins function study. For this, a so-called parameter GFV (glomerular filtration velocity) is evaluated. A patient is injected by a certain amount of radioactive medication (DTPA ^{99m}Tc) with known (measured in syringe on the spectrometer) activity, then after some time the blood of the patient is sampled, centrifuged and the activity in blood plasma is measured, some time later the blood is sampled, centrifuged again and the activity is measured again too. Then, according to the given algorithm, a so-called clearance is evaluated, with the help of which the reins function is studied.

Thereby, the gamma-beta spectrometer MKGB-01 have found a wide application in various applied and scientific problems, and, therefore, the realization of this project can be considered as successful.

References

1. Environmental safety on railway transport: Reference book. P.1 Environmental safety/Edited by V.V. Reshetov - SPb: IPK "KOSTA", 2007.
2. Grigoriev A.G., Zhamoida V.A., Vladimirov M.V.. Application of gamma-spectrometer towed on water area bottom in geological and geoenvironmental purposes. Materials of XVII International Scientific Conference of Marine Geology. Moscow, 2007.
3. The Complex of human radiation spectrometers SICh-E. Operating manual., Saint-Petersburg, 2008.
4. M. Muikku, T. Rahola. Emergency preparedness in Finland: improvement of the measurement equipment used in the assessment of internal doses. Helsinki, Finland.
5. N. Moiseev, E. Tereschenko.. Application of spectrometer-radiometer MKGB-01 in the device of KX-gamma coincidences in VNIIM of D.I. Mendeleev. Saint-Petersburg. VNIIM. 2010.

Radiation monitoring network with spectrometric capabilities: implementation of $LaBr_3$ spectrometers to the Finnish network

Mattila, Aleksi[1]; Toivonen, Harri[1]; Vesterbacka, Kaj[1]; Leppänen, Mikko[1]; Salmelin, Santtu[1]; Pelikan, Andreas[2]

[1] STUK – Radiation and Nuclear Safety Authority, P.O. Box 14, 00881 Helsinki, FINLAND

[2] Dienstleistungen in der automatischen Datenverarbeitung und Informationstechnik, Vienna, AUSTRIA

Abstract

Dose rate monitoring networks equipped with Geiger-Müller or proportional counters can provide an alarm with sensitivity to approximately 0.1 µSv/h increase over the ambient background. For airborne activity the 0.1 µSv/h increase translates to activity concentrations in the kBq/m^3 range. Better sensitivity and nuclide identification can be achieved by gamma spectrometers with sufficient energy resolution.

$LaBr_3$ scintillators provide a good energy resolution of about 2.5 % at 662 keV enabling the separation of I-131 (364.9 keV) and Pb-214 (351.9 keV) lines. The detectors are large enough to yield an adequate sensitivity, making them suitable for dose rate monitoring network applications. Major drawbacks of $LaBr_3$ detectors are the radioactive impurities in the material and the gain variation as a function of temperature. A fitting algorithm based on the La-138 and K-40 multiplet at 1430-1470 keV was developed to stabilize the detector. With fully automatic software controlling the $LaBr_3$ spectrometer during data acquisition the system gain is stable and provides environmental spectra of excellent quality. The same fitting algorithm is also applied to the analysis of the whole spectrum.

Spectrometers have recently been installed around the Finnish nuclear power plants. They send measurements to a central database at STUK headquarters over a secure wireless TETRA network at ten minute intervals. The spectra are automatically analyzed and checked for the presence of small signatures of man-made activity. Airborne or fallout nuclide activity concentrations and the dose rate are calculated from the spectra. The detection limit for I-131 is roughly 40 Bq/m^3. In comparison, an activity concentration of 1700 Bq/m^3, yielding an increase of 0.1 µSv/h in the dose rate, would be needed to create an alarm in the Geiger-Müller monitors.

In summary, the $LaBr_3$ spectrometer system now in operational use in Finland, is an excellent enhancement to the country-wide radiation monitoring network providing nuclide identification with high sensitivity.

Introduction

The Finnish ambient dose rate monitoring network consists of 255 monitoring stations. The network covers the whole country, with several stations around the Finnish nuclear power plants in Olkiluoto and Loviisa. Ambient dose rate at the station is monitored with three independent Geiger-Müller counters, with two identical counters for low dose rate and one counter for high dose rate. Instrumentation also includes a rain sensor. The measurement data from the stations is sent in ten minute intervals to the Radiation and Nuclear Safety Authority (STUK) headquarters to form a real-time picture of the dose rates. An increase in dose rate over a predefined limit, verified by the three independent Geiger-Müller counters at the station, generates an alarm at the regional Emergency Response Centres in addition to alerting STUK's duty officer.

The Geiger-Müller counters of the monitoring network can discern about 0.02 µSv/h change in the ambient dose rate. With the natural background in Finland varying between 0.05 µSv/h - 0.30 µSv/h, the alarm limit has been set to 0.4 µSv/h. In addition to a fixed alarm limit, a station-specific comparison of the latest dose rate value to a smoothed background over the last 7 d measurements is used to detect anomalous cases of concern. The alarm level is set to a 0.1 µSv/h increase over the average. For I-131, an air concentration of 1700 Bq/m^3 is needed to raise the dose rate by 0.1 µSv/h. Countermeasures, however, are needed already at the concentration levels of 1000 Bq/m^3 of I-131. Another drawback is the fact that Geiger-Müller counters do not provide identification information on the possible radionuclides responsible for an increased dose rate. An illustrative case is a weather-related increase in the radon progeny concentration of the surface air leading to elevated dose rate. Discerning these cases with natural origin reliably and promptly from events that might require further action can be a challenge to network operators, if spectroscopic measurements are not available.

The Finnish dose rate monitoring network was updated in 2005-2007. The prospects of adding spectrometric instrumentation to achieve better detection limits and nuclide identification was envisaged, but the NaI scintillators considered at the time did not provide sufficient energy resolution for e.g. resolving the I-131 gamma line at 364.9 keV photon energy from the Pb-214 radon progeny gamma line at 351.9 keV. Despite the lack of suitable spectrometers the monitoring station structure was designed to be flexible, with several interface options for adding new instrumentation.

Recently, a new scintillator material $LaBr_3$, has emerged as a viable alternative. The Cerium-doped $LaBr_3$ presents a scintillation photon output higher than NaI(Tl), (63,000 photons/MeV) at a wavelength suited for a photocathode. In addition, the crystals have an excellent energy resolution and are available at sizes suitable for gamma spectrometric measurements (Dorenbos et al. 2004, van Loef et al. 2001, Pani et al. 2007). The energy resolution of $LaBr_3$ scintillators is 2.5-2.9 % at 662 keV, whereas the resolution of NaI scintillators is 6-7 %. The operational lifetime of a $LaBr_3$ scintillator coupled with a suitable photomultiplier tube and related signal processing electronics is estimated to be several years.

$LaBr_3$ scintillators also exhibit problematic characteristics that need to be considered when designing a measurement system. The $LaBr_3$ material contains radioactive La-138 and Ac-227 impurities, which contribute to the background complicating the analysis of the spectrum. La-138 in particular has a disturbing impact

on the detection limits due to the increase of spectral baseline. In addition, the gain variation of the detector and the coupled photomultiplier tube may be of several percentages depending on the temperature and the detector orientation in terrestrial magnetic field.

Despite these complications, the overall performance of $LaBr_3$ scintillators is good enough for continuous environmental monitoring applications. In this paper, we show how the problems related to $LaBr_3$ material and gain instability have been overcome. We discuss how these detectors have been added to a geographically sparse monitoring network and show that automatic analysis procedures can be applied to process the environmental spectra from $LaBr_3$ scintillators.

Material and methods

Measurement setup and data processing

The $LaBr_3$ scintillators installed to the Finnish dose rate monitoring network utilize Saint-Gobain BrilLanCe 380 crystals with a height and diameter of 1.5 inches. The detector, including Hamatsu photomultiplier tube (R6231-100) is connected to a Princeton Gamma-Tech Instruments MCA2500 multi-channel analyser (MCA). The MCA2500 is connected via an ethernet interface, allowing cable lenghts up to 100m without a separate signal amplifier. This is an advantage for the typical monitoring station installation, where the central unit is located indoors and the sensors stand outside at some distance from nearby buildings.

The detector and the MCA are housed inside a weather resistant and insulated casing. The casing insulation has been tested in the expected outside temperature range of -30 Cº … +30 Cº to keep the detector and the MCA unit inside a manufacturer specified operational temperature range of 0 °C ... +50 °C, while preventing the condensation of humidity on the electronic components. The aluminium casing has a wall thickness of 1.5 mm at the scintillator end, not preventing the detection of low energy gamma radiation.

The monitoring station central unit is running on an embedded Linux computer. The Intel PXA255 computer has no moving parts ensuring long life time, with the open Linux software architecture offering software vendor independence and flexibility, including monitoring station software updates with user scripts and installation of additional programs written with C/C++ programming language. The control unit has several interfaces for external equipment and sensors, such as the ethernet connection used to interface with the $LaBr_3$ detector's MCA.

Individual stations communicate via a TETRA-based, closed government radio network called VIRVE (Fig 1). The VIRVE network is mainly used by law enforcement authorities and rescue services to relay voice communications, but the TETRA network also supports TCP/IP protocol and text messaging, with both services utilized by the radiation monitoring network stations to relay measurement data. The setup allows for two-way communication enabling remote management and software updates.

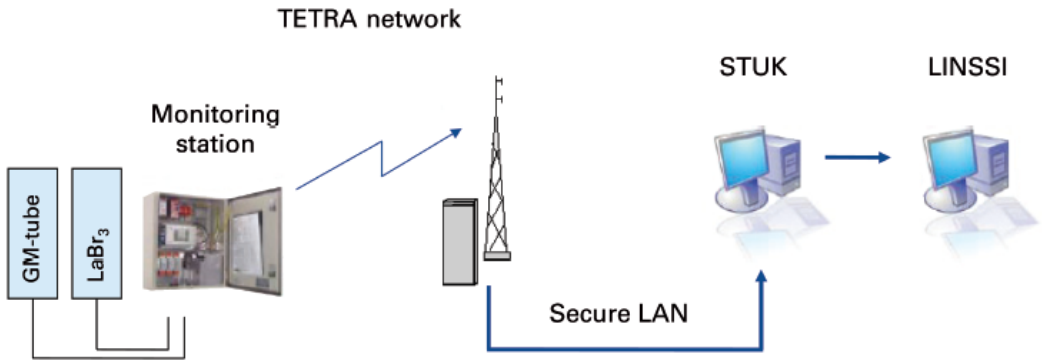

Fig. 1. Architecture of the Finnish radiation monitoring network.

The $LaBr_3$ detectors are operated in the same data acquisition mode as the Geiger-Müller counters, with a spectrum reading interval of ten minutes. The MCA conversion gain is set to 2048 channels, with the energy range extending up to 3200 keV. After a spectrum is read, it is processed at the monitoring station by a specialized multiplet fitting algorithm *mufi*. The purpose of the *mufi* algorithm is to stabilize the energy calibration against gain fluctuations induced by changes in external temperature. The program analyses the position of the La-138/K-40 multiplet at the photon energy region of 1430 keV - 1470 keV. If the multiplet peak positions have moved from their nominal values, *mufi* returns the channel shift, which is converted to a change in the amplifier gain. A new gain setting is then sent to the MCA unit to keep the energy calibration stable.

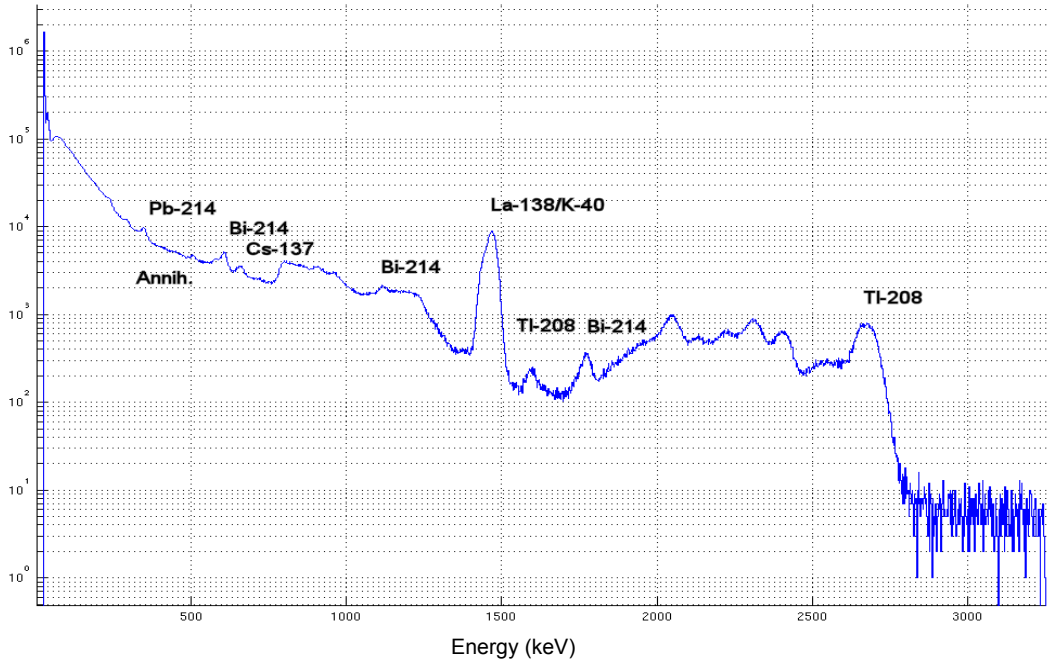

Fig. 2. A spectrum of the background radiation measured with the $LaBr_3$ detector. The La-138/K-40 multiplet is used to stabilize the energy calibration against gain fluctuations induced by changes in temperature. Measurement time was 24 h.

The spectral data and the *mufi* analysis results are then send from the monitoring station to a central server at STUK and stored to a gamma spectrometry database *Linssi* (Aarnio et al. 2006). A summation spectrum with a length of 60 min is formed from the individual 10 min spectra. These are automatically analyzed by a second multiplet fitting algorithm *jmufi*, which analyses predefined spectral regions for the presence of interesting gamma peaks. The *jmufi* software provides nuclide identification and count rates, detection limits and error estimates for the various quantities. In addition to nuclide identification, dose rates are calculated from the 10 min spectra to compare with the the Geiger-Müller counter values. The *jmufi* program and the dose rate calculation method are discussed in detail in Toivonen, 2008. A spectrum of the background radiation integrated over a 24 h measuring period is shown in fig. 2. Several radon progeny related peaks are apparent in the spectrum, with the La-138/K40 multiplet peak being the most prominent feature.

As of spring 2010, 19 monitoring stations have been equipped with $LaBr_3$ detectors. Most of these spectrometric stations are situated around the Finnish nuclear power plant sites in Olkiluoto and Loviisa (Fig 3.). Installations will continue with few additional $LaBr_3$ spectrometers during the year 2010.

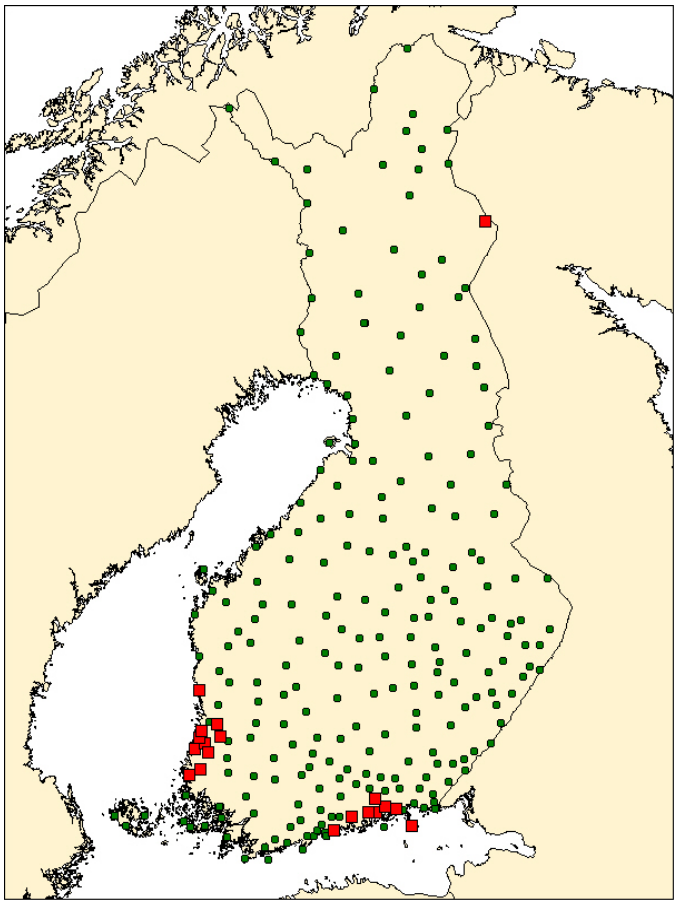

Fig. 3. Ambient dose rate monitoring network. Stations with $LaBr_3$ detectors are shown with red squares.

Conversion of detector count rates to activity concentrations

The nuclide specific count rates recorded at the spectrometers need to be converted to more general quantities. For a dose rate monitoring network, two distinct cases are of interest. In the first case, the radioactive nuclides are airborne and the nuclide specific air concentrations (Bq/m^3) need be derived from the respective count rates. In the second case, the radioactive nuclides are deposited on the ground and the interesting quantity is the fallout (Bq/m^2). The efficiency curves relating the nuclide-specific count rates to the different concentrations are also needed to estimate the detection limits (contamination level) which would generate the alarm. To this end, we have developed a semi-empirical method to derive the peak efficiency calibrations for the two different cases outlined above. We have derived equations for the efficiency curves of extended source geometries, utilizing a point source peak efficiency curve at a fixed source-detector distance.

The point source peak efficiencies can be easily measured with a selection of well calibrated sources at some finite source-detector distance *r*. From this data, the point source efficiency at an arbitrary distance is calculated. For airborne radioactivity one needs to consider the $1/r^2$ counting geometry dependance and the absorption of the radiation in air. The angular dependence can be neglected in the present case as the $LaBr_3$ crystals with equal height and diameter have only a small directional sensitivity. Finally, the point efficiency is integrated over the involved space to give the peak efficiency curve for the volume source. A similar approach is used to derive the peak efficiency curve for the fallout. A more detailed discussion of the method is given by Toivonen et al. 2009.

We obtained the experimental point source efficiency data at five different photon energies with a detector-source distance of 5 m. The experimental data set was supplemented by Monte Carlo calculations at different photon energies to yield a point efficiency curve over the whole energy region of interest. Fig. 4 shows the efficiency curve for the volume concentration, together with a scaled point source efficiency curve. With the calculated efficiency curves the nuclide specific count rates can be converted to corresponding air concentrations and fallout.

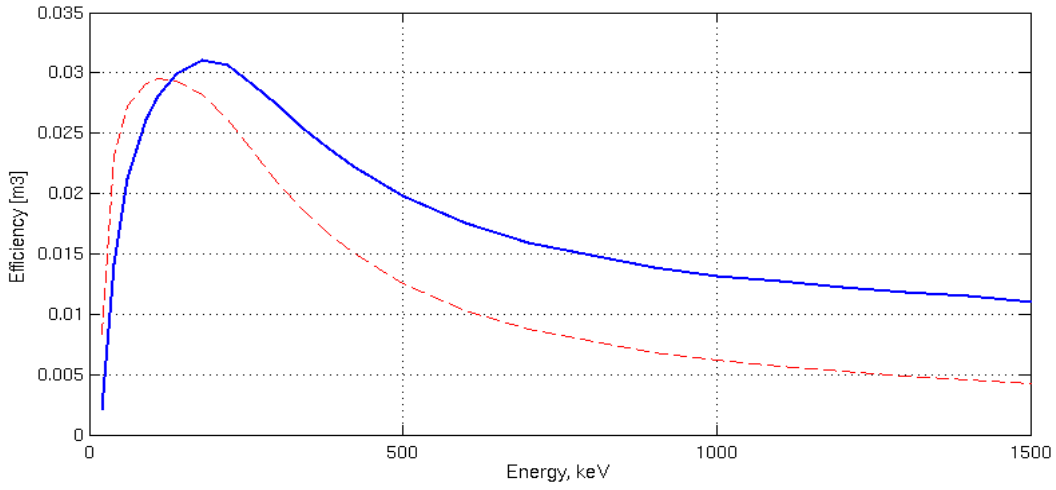

Fig. 4. Efficiency curve for the air concentration. The dashed line is provided for the reference; it is the shape of the point source efficiency at 5 m, multiplied by a factor of 10,000

Results

After deriving the efficiency curves for the relevant source geometries we proceed to discuss the detection limits of nuclides and compare the situation with a monitoring station equipped solely with Geiger-Müller counters. One of the most important benchmark nuclides is I-131 due its relevance in nuclear power plant accident scenarios, where significant amounts can be released into the atmosphere. Then the dose delivered to the thyroid gland by the inhaled or ingested iodine is of high concern.

Using *jmufi*, the main gamma line of I-131 at 364.9 keV photon energy is well separated from the Pb-214 radon progeny gamma line at 351.9 keV in the $LaBr_3$ spectra. As discussed before, an activity concentration of 1700 Bq/m^3 of I-131 in the air would increase the dose rate by 0.1 µSv/h, triggering an alarm at the Geiger-Müller counters of the Finnish monitoring network. For $LaBr_3$ detector, with typical background count rates and a 10 min measurement, the decision limit (Lc) for I-131 at risk level of 10^{-6} (type I error with $k\alpha = 4.75$) yields to approximately 30 Bq/m^3 using the derived peak efficiency shown in fig. 4. The MDA (Ld) is 40 Bq/m^3 at risk level of 5 % (type II error), which is a factor of 40 smaller compared to the alarm level of Geiger-Müller counter.

For Cs-137, in a 10 min measurement, the decision limit is approximately 26 Bq/m^3 and MDA (Ld) is 35 Bq/m^3.

Table 1 summarizes the detection limits of some nuclides in a 10 min measurement with the $LaBr_3$ detector. For a comparison, the activity concentration increasing the dose rate by 0.1 µSv/h is given. For many of the nuclides the $LaBr_3$ detection limits are better by a factor of 30-100.

Table 1. The $LaBr_3$ spectrometer detection limits for airborne nuclides. For a comparison, the alarm limit (increase of 0.1 µSv/h in the dose rate) for the Geiger-Müller counter is also given.

Nuclide	Gamma energy (keV)	LaBr3 Detection limit (Bq/m^3)	GM-tube alarm limit (Bq/m^3)
Am-241	59.5	200	33000
Co-60	1332	20	250
Cs-137	662	30	1100
I-123	159	50	4000

Discussion

The value of nuclide specific information in addition to dose rate is well demonstrated by an event in Olkiluoto area in November, 2009. At a late evening of 22nd of November starting 23:00 UTC, the dose rate at some of the monitoring stations near the Olkiluoto nuclear power plant site started to rise (Fig.4). The values did not at any time during the event cross the alarm limits. However, the change was noticed at a very early stage and an investigative action was taken. Although the rain sensors and weather data of the monitoring stations indicated a rain shower passing over the area, suggesting radon progenies related event, it was not possible to confirm this conclusively from the dose rate data only. The dose rate reached the peak values at 00:10 UTC on the 23rd of November, with a dose rate of 0.20 µSv/h measured at Eurajoki monitoring station.

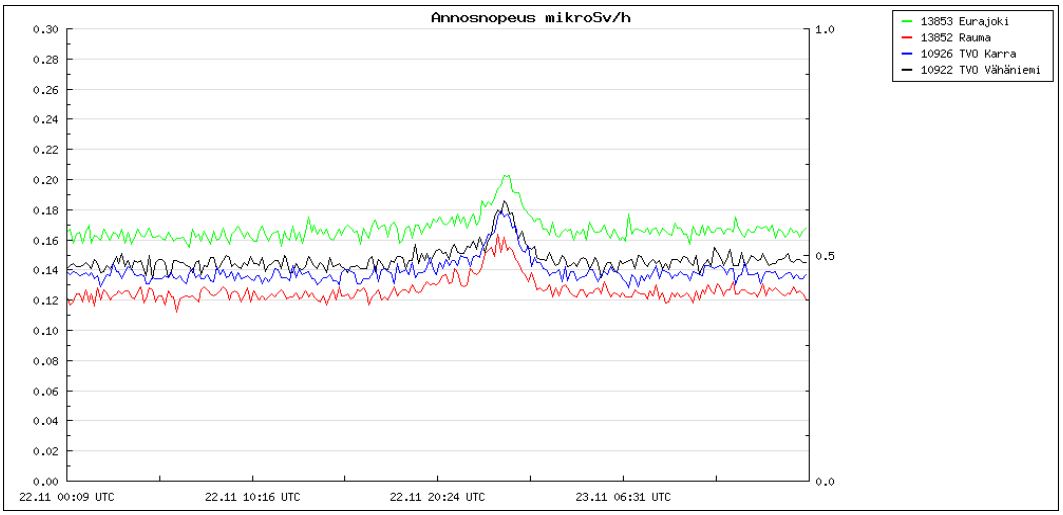

Fig. 4. Dose rates from four monitoring stations around Olkiluoto between 12:00 UTC 22.11.2009 - 12:00 UTC 23.11.2009.

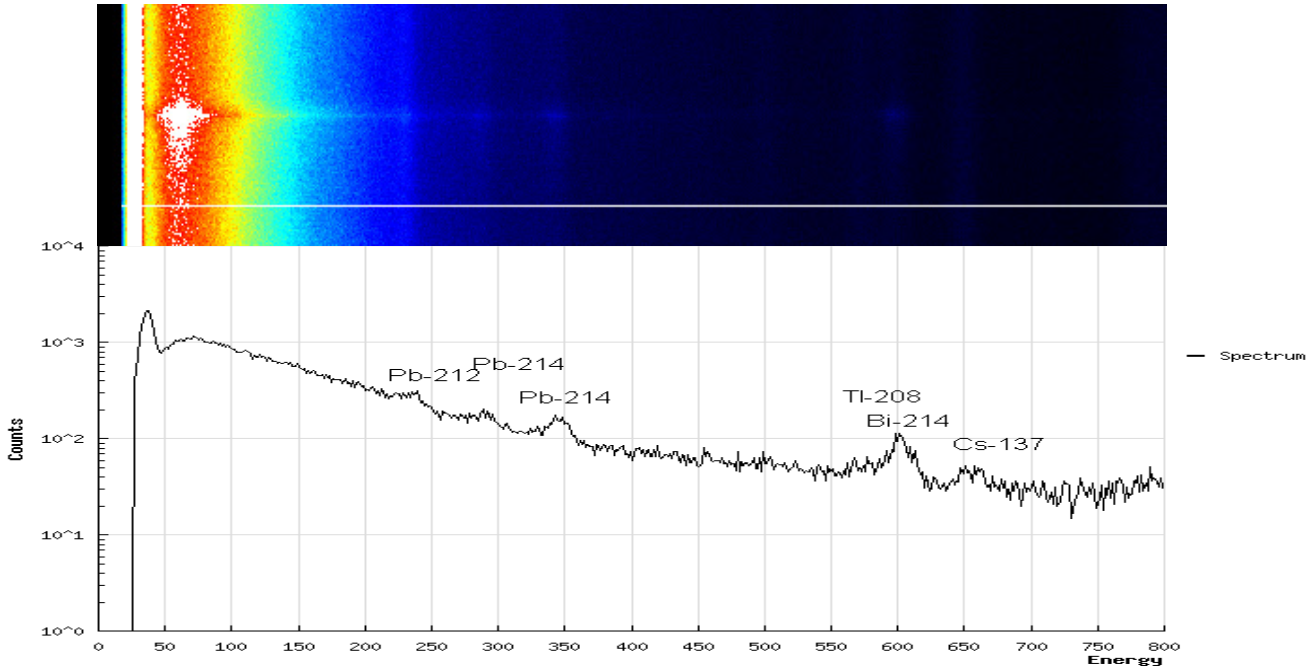

Fig. 5. Waterfall plot of the $LaBr_3$ spectra from Eurajoki monitoring station between 12:00 UTC 22.11.2009 - 12:00 UTC 23.11.2009. The energy scale (x-axis) is from 10 keV to 700 keV, while the y-axis is time. Increase in the intensity of several radon progeny related peaks is observed around midnight. A spectrum recorded at 23:40 UTC shows that the prominent peaks are related to radon progenies.

At that time, the spectra of the $LaBr_3$ detector installed at the Eurajoki station were investigated, and increase in radon progenies was immediately confirmed to be the culprit for the dose rate rise. A waterfall plot of the spectra between 12:00 UTC 22.11.2009 - 12:00 UTC 23.11.2009, shown in fig. 5, reveal several radon progeny related gamma peaks gaining in intensity starting at 22.30 UTC. A single spectrum

measured at 23:40 UTC shows that the most prominent peaks can be associated with Pb-212, Pb214 and Tl-208. The waterfall plot clearly shows how the rise and decay in the intensity of these peaks closely follows the dose rate curve. Even though the event did not generate an alarm in the dose rate monitoring network, as the radon-related events almost never because the typical dose increase is below 0.1 µSv/h, the value of $LaBr_3$ scintillators is clearly demonstrated. With the spectroscopic information at hand, the network operator was quickly able to verify the origin of the dose rate increase and confirm the non-alarming nature of the event.

Conclusions

The Finnish dose rate monitoring network has been equipped with 19 $LaBr_3$ spectrometers. These spectrometers have been installed to monitoring stations near the nuclear power plants. This fully automated $LaBr_3$ spectrometer subnetwork provides environmental spectra of excellent quality. Nuclide-specific activity concentrations can be derived from the measured gamma peak count rates. The detection limits for many nuclides are better by a factor of 30-100 compared with the standard Geiger-Müller counters of the monitoring network.

References

van Loef EVD, Dorenbos P, van Eijk CWE, Krämer KW, Güdel HU. High-energy-resolution scintillator: Ce^{3+} activated $LaBr_3$. Applied Physics Letters 2001; **79**: 1573-1575.

Dorenbos P, de Haas JTM, van Eijk CWE. Gamma ray spectroscopy with a Ø19 × 19 mm^3 $LaBr_3$: 0.5% Ce^{3+} scintillator. IEEE Transactions on Nuclear Science 2004; 51: 1289-1296.

Aarnio, P., et al., SQL Database for gamma-ray spectrometry, Helsinki, 2006. http://linssi.hut.fi/.

Pani R, et al. $LaBr_3$:Ce crystal: The latest advance for scintillation cameras. Nuclear Instruments and Methods in Physics Research Section A: Accelerators, Spectrometers, Detectors and Associated Equipment 2007; 572: 268-269.

Toivonen H, Vesterbacka K, Pelikan A., Mattila A. and Karhunen T, $LaBr_3$ spectrometry for environmental monitoring. IRPA 12 – Strengthening Radiation Protection Worldwide. The 12th International Congress of the International Radiation Protection Association. 2008 Oct 19–24; Buenos Aires, Argentina. Buenos Aires: Sociedad Argentina de Radioprotección; 2008. p. 15.

Toivonen H, Mattila A., Vesterbacka K., Efficiency Calibration for *in-situ* Gamma Spectrometry of Airborne Activity and Fallout. Radiation and Nuclear Safety Authority. TTL-TECDOC-2009-018, Helsinki. 2009.

Sample screening to locate active particles with position-sensitive alpha detector

Ihantola, Sakari; Outola, Iisa; Peräjärvi, Kari; Pöllänen, Roy;
Toivonen, Harri; Turunen, Jani
STUK – Radiation and Nuclear Safety Authority, FINLAND

Abstract
In order to speed up the analysis of collected samples, new sample screening techniques are required both in nuclear safeguards and nuclear forensics. One promising approach is using a position-sensitive alpha detector. In this work, screening is performed with a Double-Sided Silicon Strip Detector (DSSSD) supported with a novel analysis algorithm. The method is shown to accurately locate the most active particles from a sample containing multiple micrometer-sized particles consisting of weapons-grade plutonium. In addition to the particle locations, the DSSSD also gives the alpha spectrum that can be used to perform a preliminary isotope analysis. Compiling isotope and location information allows further assay methods to be focused only on the spots containing the key isotopes.

Introduction
Analysis of samples containing potentially radioactive particles is a complicated, multi-phased process. Typically, the samples are first screened in order to select the most probable spots. Thereafter, more time-consuming destructive assay methods, such as mass spectrometry, can be used to investigate the selected spots in detail. In increasing the throughput of the analysis without losing any interesting particles, the accuracy of the screening method has a crucial role. In addition to speed and accuracy, it is often essential that the method used is non-destructive to ensure that the sample stays intact for possible subsequent analyses.

Traditional gamma spectrometry is often very inefficient for detecting small amounts of heavy alpha-active isotopes. The gamma yields of such isotopes are typically orders of magnitude smaller than the alpha yields, or the emitted photons have too low energies to be measured. These properties also apply to many isotopes of plutonium and uranium that are of particular interest in nuclear safeguards and nuclear forensics. Thus, to ensure that these isotopes are not ignored during the screening, the screening method cannot only rely on gamma spectrometry but the emitted alphas must be detected as well.

In this work, a new screening method for particles emitting alpha radiation is presented. The particles are located with a position-sensitive Double-Sided Silicon Strip

Detector (DSSSD) and novel software. The performance of the method is investigated by analysing a sample containing multiple micrometer-sized particles from a nuclear bomb. The results are also compared with autoradiography performed to the same sample.

Measurement

The sample analyzed in this work contained pieces of an actinide particle on a filter. The original particle, containing ^{241}Am and ^{239,240}Pu, was isolated from a soil sample collected from Thule, Greenland (Roos et al., 2010) near the location where a US bomber carrying thermonuclear weapons crashed in 1968 (see Eriksson 2002 and references therein). Following chemical treatments with nitric acid and other reagents broke the particle down into several smaller particles. These smaller particles were collected on a filter paper with a pore size of 0.45 μm. All particles in the sample were too small to be visible with the naked eye. To image the sample, it was measured for a few days with the same autoradiography method as in Pöllänen et al. 2004. The autoradiography image obtained is shown in Fig. 1. As can be seen from the image, there are several particles in the sample, two of them having a significantly higher activity than the others.

The measurement of the sample was performed with the alpha-gamma coincidence setup of Particle And Non-Destructive Analysis (PANDA) testbed (Turunen et. al 2010). This setup contains a broad-energy HPGe gamma detector and a position-sensitive alpha detector connected to an event-mode data acquisition system. However, in this work, only the data from the alpha detector were utilized. The alpha detector in PANDA is a Double-Sided Silicon Strip Detector, consisting of 32 active strips in x and y directions. The width of each stripe is 2 mm, and thus, the stripes generate a 64×64-mm² grid consisting of pixels with a size of 2×2 mm². The typical energy resolution of this type of detectors for alphas from ^{241}Am is 55 keV (Micron 2010).

For the measurement, the sample was set inside the measurement chamber of PANDA, and the pressure inside the chamber was pumped to less than 10^{-5} mbar. The surface of the sample matrix was parallel to the alpha detector, and the distance from the detector to the sample was 3.5 ± 0.5 mm. The sample was located approximately at the centre line of the DSSSD. The sample was measured for one week, and the number of accepted alpha hits used in the analysis was about 33 000.

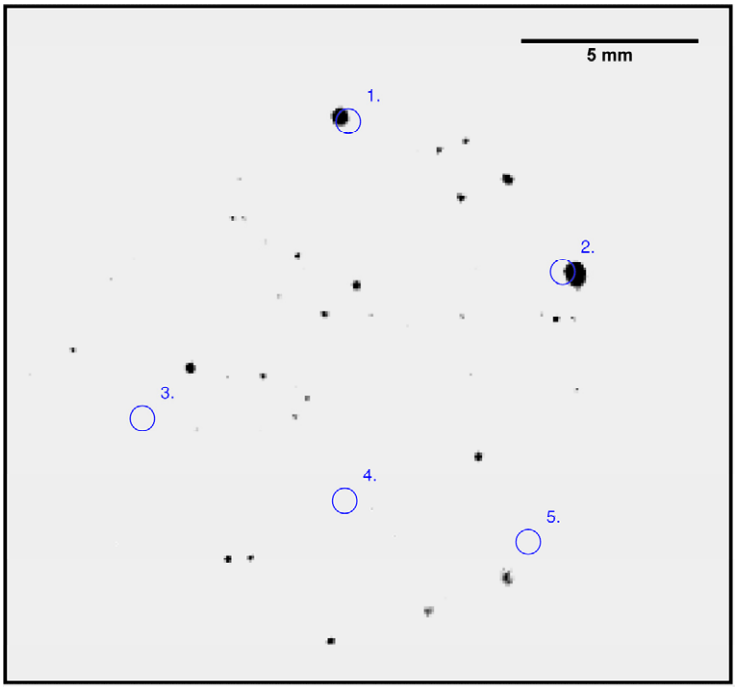

Fig. 1. Autoradiography image of the sample. The blue circles refer to the particle locations obtained with automated analysis (see Table 1) .

Methods

Let us assume that the DSSSD detects every alpha particle hitting the front surface of the detector. In this case, the absolute detection efficiency of each pixel (ε_{abs}) only depends on the solid angle of the pixel (Ω) seen from the source location:

$$\varepsilon_{\text{abs}} = \Omega/(4\pi).$$

For a rectangular pixel, Ω can be analytically calculated with the following equation

$$\Omega = \arctan\left(\frac{(x_2-x_p)(y_2-y_p)}{z_p\left[(x_2-x_p)^2+(y_2-y_p)^2+z_p^2\right]^{1/2}}\right)$$
$$-\arctan\left(\frac{(x_1-x_p)(y_2-y_p)}{z_p\left[(x_1-x_p)^2+(y_2-y_p)^2+z_p^2\right]^{1/2}}\right)$$
$$-\arctan\left(\frac{(x_2-x_p)(y_1-y_p)}{z_p\left[(x_2-x_p)^2+(y_1-y_p)^2+z_p^2\right]^{1/2}}\right)$$
$$+\arctan\left(\frac{(x_1-x_p)(y_1-y_p)}{z_p\left[(x_1-x_p)^2+(y_1-y_p)^2+z_p^2\right]^{1/2}}\right)$$

where (x_p, y_p, z_p) is the location of the source and $(x_1, y_1, 0)$ $(x_2, y_2, 0)$ locations of the opposite corners of the pixel (Gotoh et al. 1971). If the location of the source and

number of alphas emitted (C) are known, an estimate for the number of alphas detected with one pixel can be calculated as

$$c = C\Omega(x_p, y_p, z_p)/(4\pi) .$$

The location and activity of a particle can be determined by finding the parameters that maximize the probability of the detected counts to be produced by the model. Due to the small pixel size of the DSSSD and the low activity of the sample, the number of counts on many pixels is small. Thus, the number of counts does not follow Gaussian statistics, and only properties of the Poisson distribution can be used.

Results

Fig. 2 shows the measured hitmap (counts per pixel). As can be seen from the figure, without further analysis, only one particle can be clearly detected from the raw data. However, by analysing the spectrum with the software designed, the detected hitmap can be explained with five point sources. The parameters of the particles that explain best the shape of the hitmap are shown in Table 1. Fig. 3 shows a hitmap that was simulated by using a set of particle positions and activities obtained from the fit. Comparison of Fig. 2 and Fig. 3 reveals that the simulated hitmap resembles the measured one.

The locations of the fitted particles are also shown in Fig. 1 together with the autoradiography image of the sample. This figure reveals that the automated analysis of the DSSSD data successfully located two particles. The other particles found are not real but describe the shapes in the hitmap generated by multiple small particles close to each other.

Since DSSSD also has a relatively good energy resolution, the measurement produces not only the alpha hitmap but also the alpha spectrum of each pixel. Fig. 4 shows an alpha spectrum obtained by summing the spectra from the pixels near the active particles in the sample. This spectrum already reveals that the particles in the sample probably contain ^{241}Am and ^{239}Pu or ^{240}Pu. If more detailed information of the isotopes is required, the spectrum could be deconvoluted with Adam (see Vesterbacka et al. 2010).

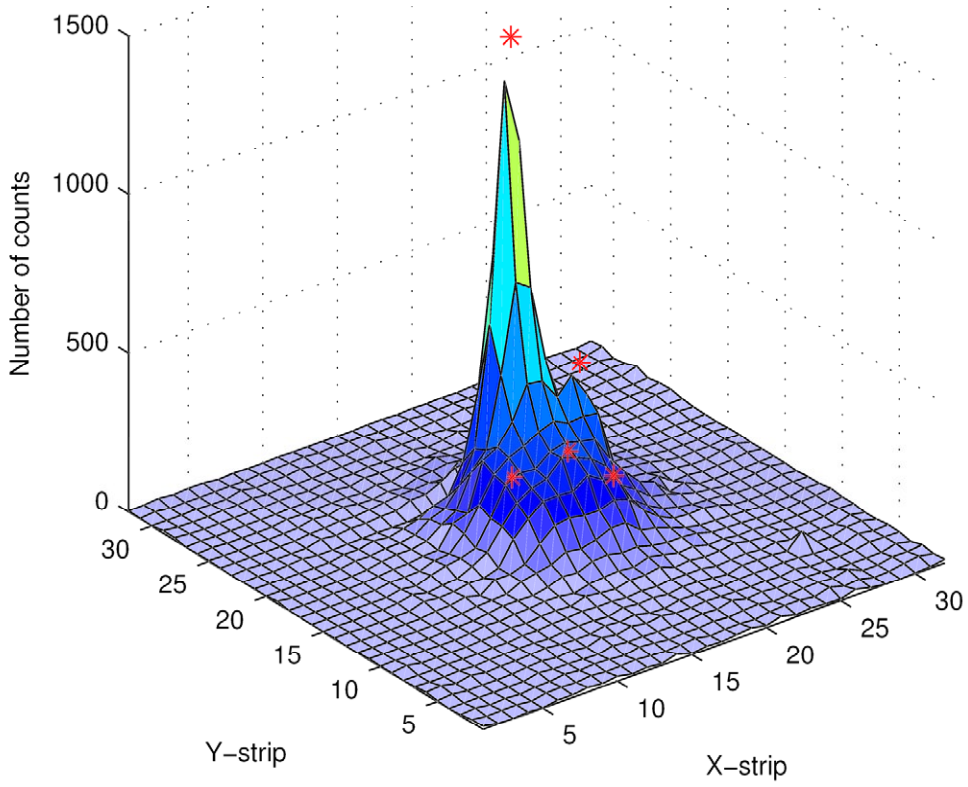

Fig. 2. Measured hitmap and locations of the fitted particles.

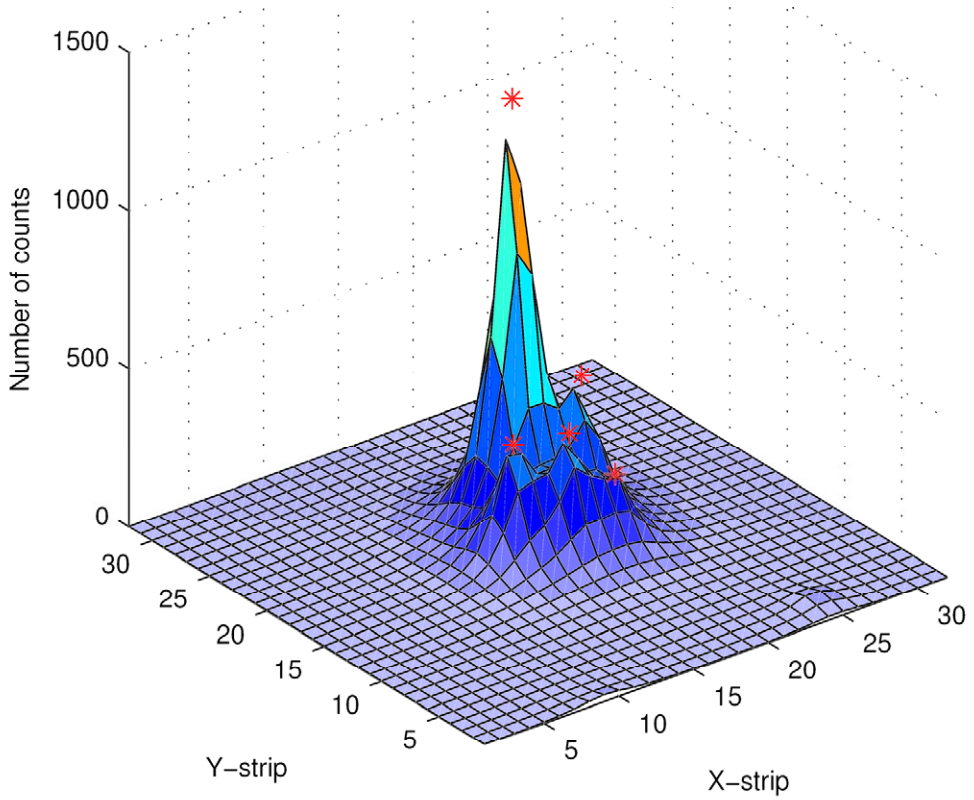

Fig. 3. Simulated hitmap and locations of the fitted particles.

Table 1. Parameters for the fitted particles. The origin of the coordinate system is located at the centre of the detector.

Particle ID	Number of alphas, C	X-coordinate, x_p (mm)	Y-coordinate, y_p (mm)
1	39884	6.8	1.7
2	10151	2.4	7.6
3	9970	-1.3	-4.4
4	9094	-3.8	1.3
5	5086	-5.1	6.4

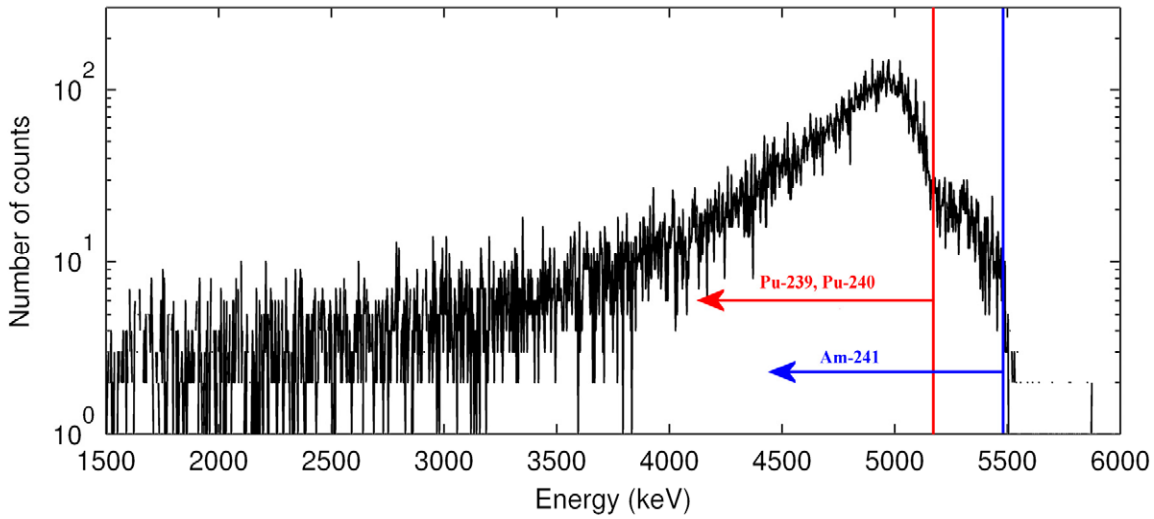

Fig. 4. Summed alpha spectrum from the pixels near the active particles.

Discussion and conclusions

Our research clearly showed that a Double-Sided Silicon Strip Detector can be used to locate alpha-active particles with very low activity. From the analysed sample, the method was able find one particle having a significantly higher activity than the other particles in the same sample. In addition, it was clearly shown that this one particle cannot explain all counts detected but the sample must contain multiple particles. The locations of the other particles given by the analysis software are not as precise but can still be used to determine the most interesting spots for more comprehensive analysis.

Compared to traditional autoradiography, DSSSD has several advantages for sample screening. First, DSSSD does not only give the locations of the particles but also accurate estimates for their activities. Second, the particle locations from the measured data are obtained fully automatically. Third, even though the pixels of the DSSSD are typically very large compared to the pixels in autoradiography images, preliminary tests have shown that with a dedicated location algorithm, the particles can easily be located with an accuracy of less than the pixel size (here 2×2 mm²).

Fourth, unlike in autoradiography, DSSSD also measures the alpha spectrum that can be used to find out the isotopes of the particles. Comparing the alpha spectra of different pixels, even differences in the isotope composition between the particles can

be detected. To determine the isotope compositions of the particles, the data from the gamma detector in PANDA can be utilized as well. For example, generating an alpha hitmap only of those counts in coincidence with 59.5 keV gammas from ^{241}Am may be very helpful in locating particles containing plutonium.

On the other hand, using DSSSD to locate particles has also some limitations compared to autoradiography. The greatest disadvantage of DSSSD is the relatively large pixel size that makes it impossible to distinguish particles close to each other. In addition, since DSSSD can only be operated in a high vacuum and each strip of the detector must be read individually, the measurement system is fairly complex. However, there are already similar detectors on the market with a pixel size as small as 400×400 µm² (Micron 2010). Therefore, the locations could be determined with significantly higher accuracy than what is presented in this work.

References

Turunen J, Ihantola S, Pelikan A, Peräjärvi K, Pöllänen R, Toivonen H. Position-sensitive measurement system for non-destructive analysis. IRPA 2010.

Roos P, Outola I, Nygren U, Ramebäck H, Sidhu R. Assessment of weathering and leaching rates of Thule hot particles. NKS-215, Roskilde, Denmark, 2010.

Eriksson M. On weapons plutonium in the Arctic Greenland (Thule, Greenland). Ph.D. Thesis, Risø National Laboratory, 2002: pp. 1–146.

Pöllänen R, Siskonen T, Vesterbacka P. High-resolution alpha spectrometry from thick sources. Radiation measurements 2004; 39 (5): 565-568.

Micron Semiconductor ltd, Product catalogue 2010; Special detectors for nuclear physics, Double sided DC microstrip detectors

Gotoh H, Yagi H. Solid angle subtended by a rectangular slit. Nuclear instruments and methods 1971; 96: 485-486.

Vesterbacka P, Pöllänen R. Simple method to determine U-234 and U-238 in water using alpha spectrometry. IRPA 2010.

Position-sensitive measurement system for non-destructive analysis

Turunen, Jani[1]; Ihantola, Sakari[1]; Pelikan, Andreas[2];
Peräjärvi, Kari[1]; Pöllänen, Roy[1]; Toivonen, Harri[1]
[1] STUK – Radiation and Nuclear Safety Authority, FINLAND
[2] Dienstleistungen in der automatischen Datenverarbeitung und Informationstechnik, AUSTRIA

Abstract

The Finnish Radiation and Nuclear Safety Authority, STUK, is conducting research on non-destructive sample analysis. One of the main tools used for this research is called PANDA (Particles And Non-Destructive Analysis).

Rather than just being a device tailored for a specific use, PANDA is more like a development platform. It has two vacuum chambers; the first is for loading and changing the samples and the second for the measurements. The currently operational measurement set-up consists of an HPGe detector to detect gamma radiation and a Double-Sided Silicon Strip Detector (DSSSD) to detect alpha particles. These detectors are placed face to face in PANDA's measurement position 1 (MP1). Samples are transported from the loading chamber and placed in the middle of these detectors using a linear feedthrough. The distance between the HPGe and DSSSD is about 8 mm. This setup allows simultaneous alpha-particle screening of large-area samples (around 40 cm^2), position-sensitive alpha-gamma and gamma-alpha coincidence studies and various half-life investigations. For example, alpha-gamma coincidence technique provides nearly background-free gamma spectra of alpha-decaying nuclides.

After the sample is screened in MP1, it can be transported to the measurement position 2 (MP2) where the interesting parts of the sample can be further investigated. At first, MP2 will host a single small-area (10 mm^2) silicon drift detector that has superior energy resolution as compared to the detectors of MP1. The main focus of MP2 will be in detecting conversion electrons, alpha particles and X-rays.

The data of MP1 are recorded in event mode, i.e. all events are timestamped. The resulting binary event files are then converted to xml-format and transferred to a database. Various analysis algorithms are currently being developed to facilitate the analysis process. The performance of PANDA is presented through the measurement and analysis of various environmental samples.

Introduction

A novel device for non-destructive sample analysis has been designed and built [1, 2]. This device is called PANDA (Particles And Non-Destructive Analysis). PANDA broadens measurements and analysis prospects of radioactive samples by applying techniques and instruments typical of basic research. These are, for example, double-sided silicon strip detectors, event mode data acquisition and software-based coincidences.

PANDA

PANDA is not only a measurement setup but rather a development platform to study different methods to measure and analyze radioactive samples. Two vacuum chambers are installed side by side on an aluminium pedestal (Fig. 1). The chambers are connected to each other with a gate valve. One chamber is for loading the samples and the other for making the measurements. The samples are transported from the loading chamber to the measurement chamber with a linear feedthrough.

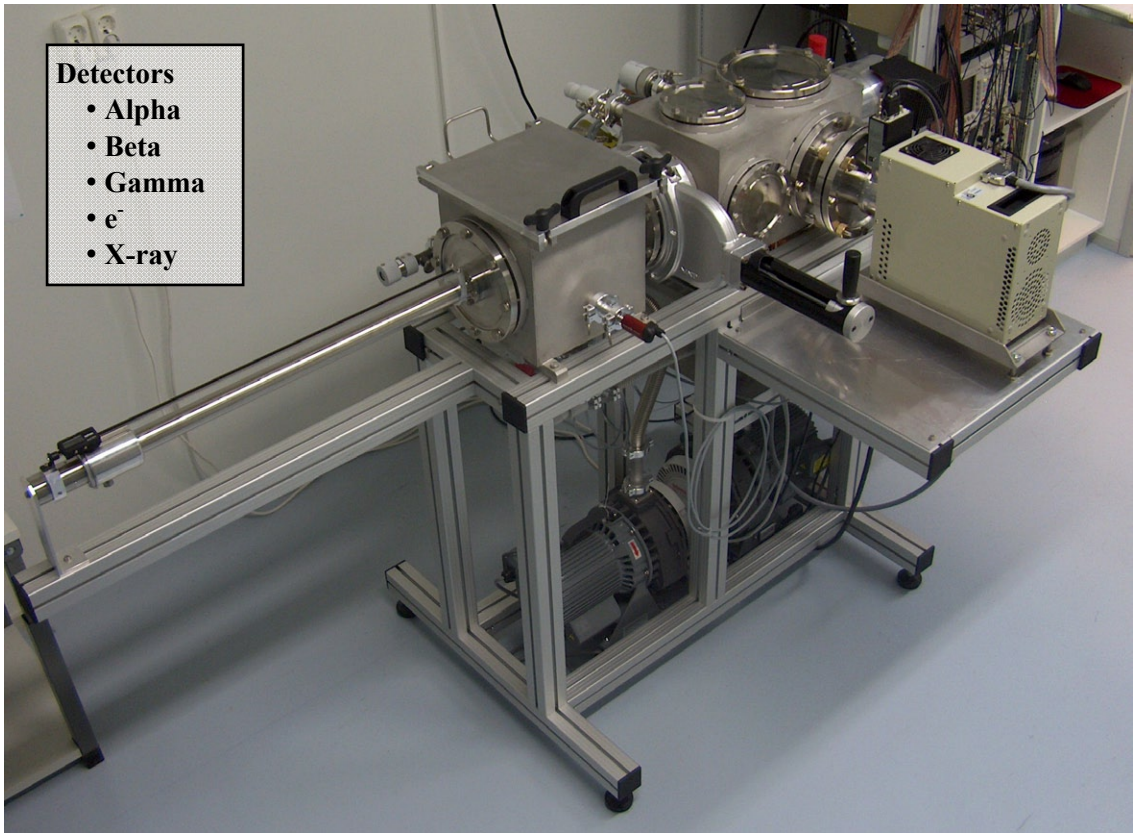

Fig. 1. The PANDA measurement setup.

The measurement chamber has two measurement positions. Measurement position 1 (MP1) is primarily meant for screening of large-area samples such as air filters. It hosts a High Purity Germanium (HPGe) detector and a Double-Sided Silicon Strip Detector (DSSSD) facing each other. The HPGe is used to detect photons and the DSSSD is intended for alpha particles. The samples are transported with the linear

feedthrough between the two detectors, see Fig. 2. The source-to-detector distance can be adjusted from a few millimetres to a few centimetres to fit different sample types.

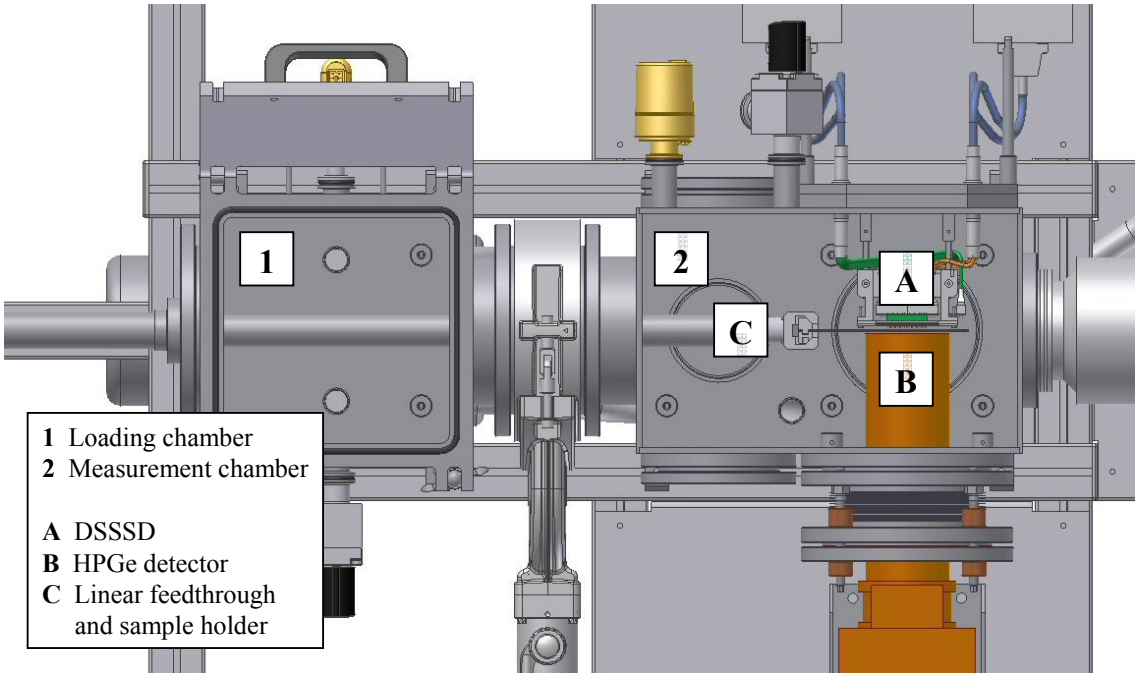

Fig. 2. Top view of PANDA's vacuum chambers.

The position sensitive DSSSD is used to locate interesting radioactive particles. It has 32 front and 32 back strips. Each strip is 2 mm wide and 64 mm long, so the active area of the DSSSD is 64 x 64 mm^2. It can be considered as 1024 individual pixels with a pixel size of 2 x 2 mm^2. After the location and partial analysis of the particles in MP1, the further analyses can be continued in measurement position 2 (MP2). It is devoted to the studies of individual radioactive particles and chemically processed samples. The first version of MP2 has a small silicon drift detector that can be used to detect conversion electrons, alpha particles and X-rays. This detector has an excellent energy resolution, about four times better for low energy photons as compared to the HPGe of MP1. Later on, MP2 will be expanded to include two or more detectors.

PANDA records data in event mode and the events are timestamped. This provides a lot of flexibility and additional possibilities to the data analysis. It enables, for example, to create alpha-gated gamma spectra that are nearly free of background [1]. Analysis of such spectra is simplified, since all gamma peaks are created by the alpha-decaying nuclides. In the near future similar gating can be done to beta-emitting radionuclides as well. This will be done by adding a third detector to MP1. The data are stored to a database and various analysis algorithms are being developed to further improve and intensify the analysis sequence.

Air filter measurement with PANDA

For performance evaluation, PANDA is tested with different kinds of samples. For initial tests, a measurement with an air sample was carried out (Fig. 3). The following results are taken from [2]. The air sample was collected to a Fluoropore filter with a

small commercial sampler. The collection time was 2.2 h and the total air flow through the filter was 12.7 m^3. The measurement with PANDA was started 0.5 h after the sample collection ended. The total acquisition time was 3 d 5 h.

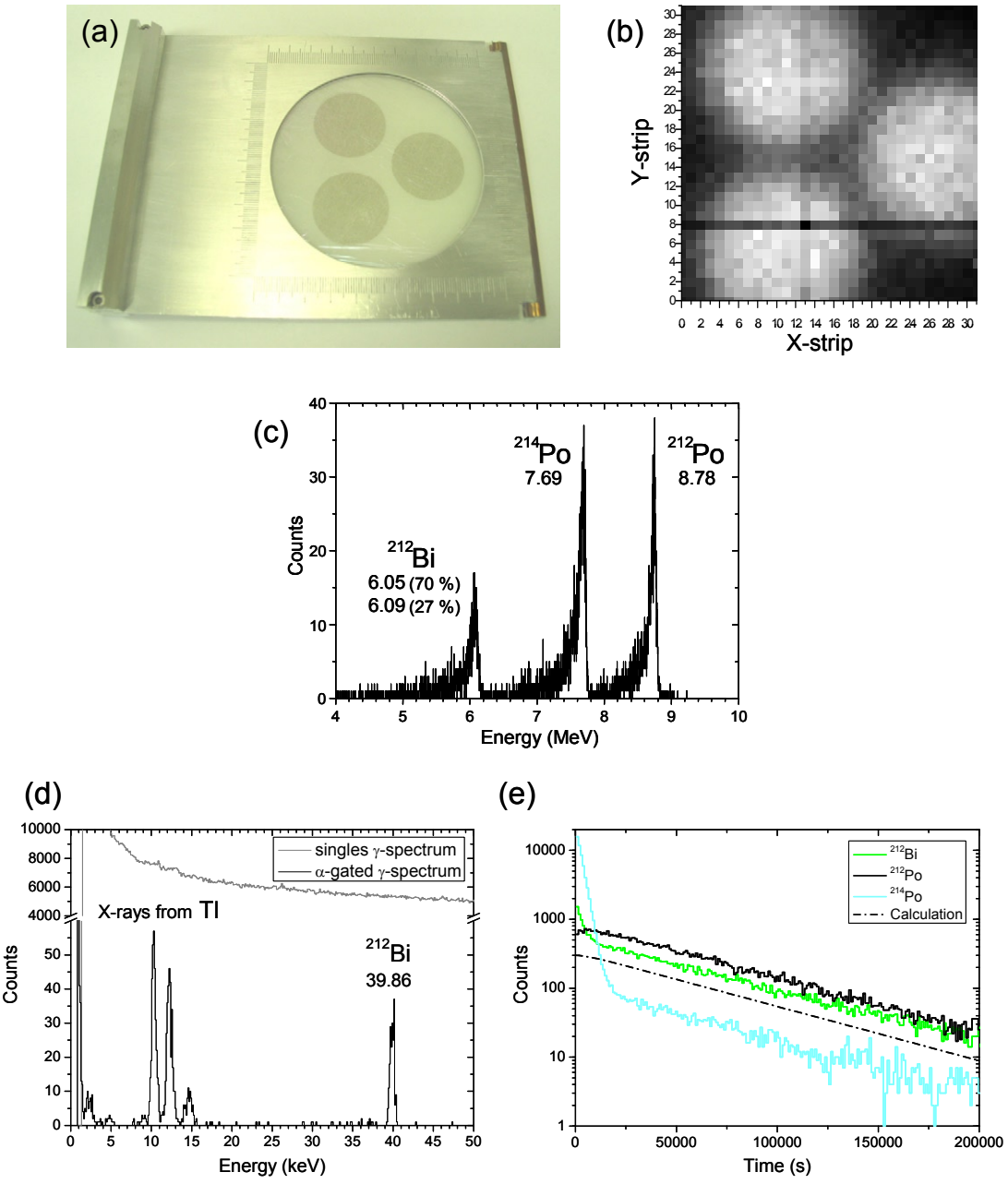

Fig. 3. An air sample measurement made with PANDA. (a) Air filter installed to a sample holder. (b) XY-hitmap of the DSSSD. (c) Alpha spectrum from a single strip. The alpha peaks are from radon daughters ^{212}Bi, ^{214}Po and ^{212}Po. (d) Conventional gamma spectrum and an alpha-gated gamma spectrum made using data from ^{212}Bi alphas. (e) Time behaviour of ^{212}Bi, ^{212}Po and ^{214}Po activity and a theoretical curve showing the shape of the ^{212}Bi and ^{212}Po. Figures 3b-e are taken from [2].

The air filter installed to a sample holder is presented in Fig. 3a. There is a 0.5 µm Mylar foil in front of the filter to protect the DSSSD from contamination. Figure 3b shows an alpha XY-hitmap recorded by the DSSSD. The highest alpha particle count

rate is in the brightest pixels. An alpha spectrum of a single strip is shown in Fig. 3c. Three significant alpha peaks belonging to radon daughters ^{212}Bi, ^{214}Po and ^{212}Po are clearly visible.

Figure 3d presents both the singles and the ^{212}Bi alpha-gated gamma spectrum. The alpha gate drastically reduces the background. In the alpha-gated gamma spectrum the 39.9 keV gamma peak related to ^{212}Bi alpha decay and Tl X-rays are easily visible.

With the timestamp data it is possible to study the time behaviour of interesting nuclides in the samples. The time behaviour of ^{212}Bi, ^{212}Po and ^{214}Po activities are shown in Fig. 3e. The graphs are made by gating the timestamp data with the three energy regions where the alpha peaks are located, see Fig. 3c. In the present case, the tailing of the two peaks with the highest energy corrupt the data from the peaks below them. The shape of the time behaviour of ^{212}Po agrees well with the calculated curve since it is not affected by other nuclides. The shape of the calculated curve comes from ^{212}Pb which is the grandmother nuclide of ^{212}Po. Note that since ^{212}Pb is a beta decaying nuclide it is therefore not directly visible in the recorded alpha spectrum. The count rate in the ^{214}Po region is initially dominated by genuine ^{214}Po counts (effective half-life 26.8 min). Later, tailing effects from the ^{212}Po peak (effective half-life 10.64 h) takes over. The ^{212}Bi count rate initially shows contributions from the ^{214}Po peak tails which quickly decay off and show the genuine ^{212}Bi count rate (with a very little fraction attributable to ^{212}Po tailing counts). The flat cap of the ^{212}Po count rate, however, shows the delay in reaching the equilibrium between ^{212}Pb -> ^{212}Bi -> ^{212}Po.

Impactor sample measurements with PANDA

The second sample used here to demonstrate PANDA's abilities is a sample from air monitoring of Thorium with a Berner low-pressure impactor. Figure 4 presents three different measurements of the same sample. In Fig. 4a there is an image of the sample made using autoradiography technique. As seen, the sample consists of 26 active spots that form a spiral shape (diameter ~ 23-28 mm, distance between consecutive spots ~ 3 mm). The same number of spots in the same formation is also clearly visible to the naked eye just by looking at the sample's surface.

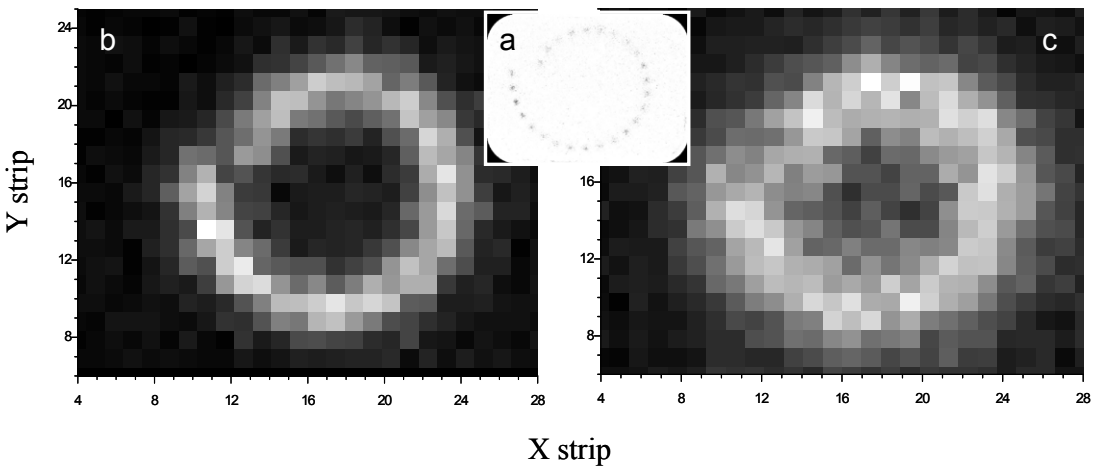

Fig. 4. Impactor sample. (a) Measured with autoradiography technique. (b) XY-hitmap of the DSSSD when sdd is 3 mm. (c) XY-hitmap of the DSSSD when sdd is 4 mm.

Figures 4b and 4c show two alpha particle hitmaps measured using PANDA's DSSSD. The source-to-detector distances (sdd) used were 3 mm and 4 mm, respectively. These hitmaps show only a portion of the DSSSD that is close to the size of the imaging plate shown in Fig. 4a.

As can be seen from the two hitmaps in Fig. 4, the quality of the image obtained with the DSSSD is strongly depended on the source-to-detector distance. There are limitations to how close to the detectors the samples can be installed in PANDA and, at the moment, 3 mm is close to the minimum. Also, since the pixel size (2 mm * 2 mm) in the DSSSD is quite large, it is very difficult to distinguish particles located only a few millimetres apart. When comparing Fig. 4b and 4c, it is clear that even one millimetre in the source-to-detector distance can make a great difference. More about finding and locating particles are discussed in Ihantola et al. [3].

Discussion

With the alpha-gamma coincidence technique, it is possible to reduce the background to nearly zero and improve the detection limits greatly. For example, PANDA is able to detect and locate a particle containing 10^{-9} g of ^{239,240}Pu in a few minutes [1]. Notice that the interesting alpha region for Pu and U is between 4 to 6 MeV and, as shown, the contribution of the radon daughters to the alpha spectra is mainly at energies above 6 MeV.

Using the DSSSD in a close geometry instead of a single large area silicon detector reduces the evenly distributed, naturally occurring alpha background significantly. This is because it is possible to use only the pixels right above an interesting spot of the sample in the analysis, i.e., the background recorded by these pixels is only a fraction of the background recorded by the entire detector [1].

As demonstrated, PANDA is a measurement setup that can, for example, greatly improve the analysis of air samples in Certified Laboratories. However, the sampling and subsequent sample preparation must be non-destructive, similar to the sample treatment at Cinderella-type air sampling stations [4].

Acknowledgements

The authors would like to thank Rudolf Engelbrecht, Seibersdorf Labor GmbH and Erich Hrnecek, EC JRC ITU for providing us the impactor sample.

References

[1] Peräjärvi K, Hakala J, Jokinen A, Moore ID, Penttilä H, Pöllänen R, Saastamoinen A, Toivonen H, Turunen J, Äystö J. Event mode data acquisition for characterization of samples containing radioactive particles. IEEE Transactions on Nuclear Science 2009; 56 (3):1444-1447.

[2] Turunen J, Peräjärvi K, Pöllänen R, Toivonen H. PANDA - A novel instrument for non-destructive sample analysis. Nuclear Instruments and Methods in Physics Research Section A 2010; 613: 177-183.

[3] Ihantola S, Outola I, Peräjärvi K, Pöllänen R, Toivonen H, Turunen J. Screening samples for locating alpha-active particles with position-sensitive detector and novel software. In: Abstracts of Third European IRPA Congress 2010. 2010 Jun 14-18; Helsinki, Finland.

[4] Medici F. Particulate sampling in the IMS radionuclide network of the Comprehensive Nuclear-Test-Ban Treaty. Kerntechnik 2001; 66 (3): 121-125.

Application of the MKGB-01 spectrometer-radiometer in the KX-gamma coincidences setup at the D. I. Mendeleyev Institute for Metrology

Moiseev, Nikolay; Tereshchenko, Evgeny
D.I. Mendeleyev Institute for Metrology (VNIIM), Saint-Petersburg, RUSSIAN FEDERATION

Abstract
The prototype of setup that implements of KX-gamma coincidences technique developed at the ionizing radiation department of the D.I. Mendeleyev Institute for Metrology is described. The basic element of setup is MKGB-01 spectrometer-radiometer (STC "Radek"). MKGB-01 units - NaI(Tl) crystals of 100 µm x 40 mm and 80 x 80 mm are used for photon radiation detection. The standard set of “CAMAC” units is used as a secondary electronic part. Original design multi-channel counting system is used for counting rate measurements. The main metrological characteristics of the setup model were determined: a long-term stability, background, dead time, resolution time.

Using the described setup the electron-capture radionuclides ^{54}Mn, ^{57}Co, ^{65}Zn, ^{88}Y, ^{139}Ce activity was measured. The combined uncertainty (K=2) of activity was estimated in the range 0,5-1,0 %. Using KX-KX coincidences technique ^{125}I activity was measured with combined uncertainty of 1,0 % (K=2). The results obtained are in good coincidence with international comparisons results.

The main result of investigations is a conception of a new KX-gamma coincidence setup based of the MKGB-01 serial spectrometer-radiometer. A number of requirements for the secondary electronic units have been declared, a device for source positioning has been designed and an achievable uncertainty of the KX-gamma coincidence method has been evaluated. The supplementary investigation for determination of possibility to use the MKGB-01 spectrometer-radiometer for realization in beta-gamma coincidence technique.

Introduction
The photon sources based on ^{54}Mn, ^{57}Co, ^{65}Zn, ^{88}Y, ^{139}Ce and ^{125}I radionuclides are used for spectrometers calibration, applied in radio-ecological measurements. Moreover, ^{125}I based sources are applying in nuclear medicine. These radionuclide disintegrates via electron capture (1) which is accompanied by characteristic radiation from the K, L shells, etc., and the excited state of daughter atom without delay becomes stable with gamma radiation emission (accompanied by the conversion characteristic radiation). The positron emission can also be present.

The main problem is the activity measurement of radionuclides in covered sources, when it is impossible to use beta-gamma coincidence methods (2). X-ray and γ-radiation coincidence method is practically the only method to measure radionuclides activity directly in the covered source.

In our opinion, the most appropriate, is the coincidences of KX and γ-radiation. The detector with thin crystal and Be entrance window was used for KX-radiation, and detector with large crystal and Al entrance window for γ-radiation. The crystals design provides registration mainly only one type of radiation in each detector, and the entrance windows construction excludes registration of KX-KX and KX-LX coincidences. The ^{125}I activity was measured by KX-KX coincidences method using two thin crystals NaI(Tl) (3).

Materials and methods

STC «Radek» produces spectrometer-radiometer MKGB-01, equiped by several detecting units of different type. In the ionizing radiation department at the D. I. Mendeleyev Institute for Metrology a prototype of setup for realisation of KX–γ и KX-KX coincidences method based on this commercially available device has been constructed.

The detecting units based on NaI(Tl) crystals 100 mkm*40 mm and 80*80 mm respectively were used for registration of KX and γ-radiation. For realization of KX-KX coincidences method two NaI(Tl) crystals, 40 mm diameter and 100 mkm thickness were used. Background radiation was shield by using 10 mm thickness lead screen. The prototype block-diagram is shown on Fig.1.

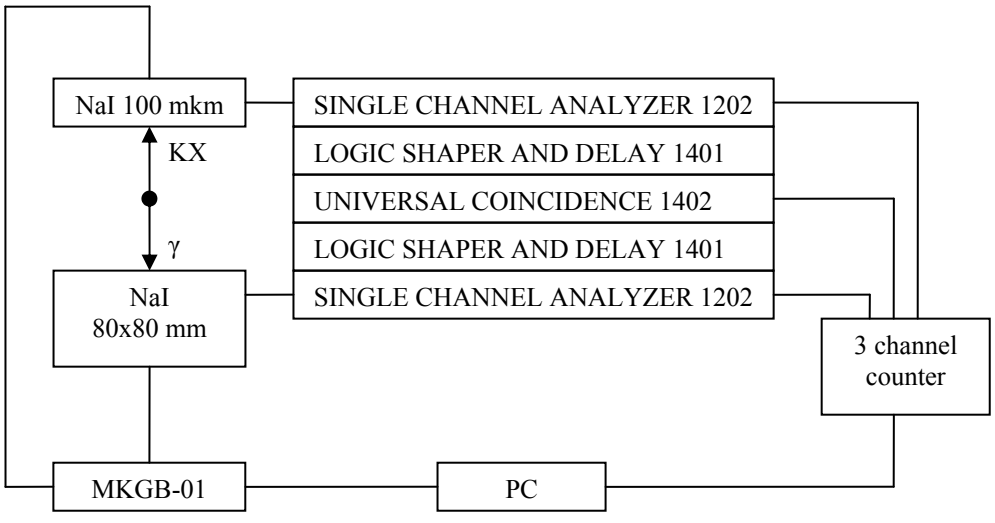

Fig.1. Prototype of setup block-diagram.

The control of spectrometer operating modes (PMT high voltage, preamplifier gain factors and etc.) was carried out using the MKGB-01 firmware.

The registration system is created using set of CAMAC module and consist of single-channel analyzer, pulse shaper and coincidence unit. X-rays, gamma-rays and coincidence counting rates are measured using original design multichannel counting system.

Before making the measurements the main characteristics of the measurement system were determined. These characteristics are following:

Warming time is the time interval, after which the device readings satisfy the requirement:

$$\left|N_i - \bar{N}\right| \le 3 \cdot S(\bar{N})$$

Where N_i is the device reading of the i-th measurement; $\bar{N}$ is the mean value of the device readings calculated as a result of m measurements performed two hours after the device has been turned on; $S(\bar{N})$ is the standard deviation of the mean value calculated by equation:

$$S(\bar{N}) = \sqrt{\frac{\sum (Ni - \bar{N})}{\sum (m-1)}}$$

Reproducibility after turning off is the relative deviation of the device reading after it has been turned off and turned on again at the unchanging (invariable, constant, permanent) irradiation field:

$$R = \frac{\left|N_i - N_j\right|}{N_i} \cdot 100\% ,$$

where N_i and N_j are the device readings before and after turning off.

Instability during the working day is the maximum deviation of detector readings from the mean value during the working day:

$$D = \frac{\max\left|N_i - \bar{N}\right|}{\bar{N}} \cdot 100\%$$

Temperature dependence of sensitivity is the variation of device readings when the environment temperature is changing :

$$k(t) = \frac{N(t) - N(t_o)}{t - t_o} \cdot 100\% ,$$

where $N(t)$ is the device reading when the environment temperature is t°C; $N(t_o)$ is the device reading when the environment temperature is t_o°C.

"Dead"time of the devices was determined using the "two sources technique":

- gamma or X-ray source was placed at a fixed point to provide the device counting rate of about 10^4 s^{-1}, the counting rate N_1 was measured;
- device and source remained immovable, the other source was placed in a position providing to make the counting rate $N_{12} \sim 2N_1$, then the counting rate N_{12} was measured;
- counting rate N_2 with the first source moved out was measured.

The "dead" time value τ was calculated by equation :

$$\tau = \frac{1}{N_{12}} \{1 - \sqrt{\frac{(N_{12} - N_1)(N_{12} - N2)}{N_1 N_2}}\}$$

The following results were obtained for the described prototype.
For X-ray channel:

- warming time is less than 30 min;
- reproducibility after turning off does not exceed 0.1 %;
- instability during the working day does not exceed 0.1%;
- temperature dependence of the sensitivity is 0.05%/°C;
- "dead" time $\tau = 1.21 \pm 0.01$ μs for first KX-detector
- "dead" time $\tau = 1.44 \pm 0.02$ μs for second KX-detector

For gamma-ray channel:

- warming time is less than 30 min;
- reproducibility after turning off does not exceed 0.1 %;
- instability during the working day does not exceed 0.1%;
- temperature dependence of the sensitivity is 0.05%/°C;
- "dead" time $\tau = 2.42 \pm 0.02$ μs.

The coincidence system resolving time τ_p was measured using a pulse generator and is equal 0,514, 1,004 and 2,018 μs for 1402 unit modes «½», «1» and «2» respectively. These τ_p values provided the random coincidence contribution less than 10% of coincidence counting rate.

The final result - activity value was calculated according to Campion (4) and Brian (5) equations.

Measurement modes selection.

The setup operating modes were the follow:

- The source-detector distance in any cases should minimize of summary events probability.
- The KX-channel energy «window» is configured to register the KX-radiation only. In γ-channel the integral operating mode with lower threshold higher than KX-radiation energy is used. It is accepted, that the KX-radiation registration efficiency by γ-detector is close to zero.
- The γ-channel lower threshold for ^{54}Mn and ^{88}Y activity measuring is adjusted above 255 keV to avoid coincidence registration with back scattered radiation.
- The γ-channel lower threshold for ^{65}Zn activity measuring is adjusted above 511 keV to avoid coincidence registration with annihilation radiation.
- The γ-channel lower threshold for ^{57}Co and ^{139}Ce activity measuring is adjusted in energy 80 keV and 100 keV respectively.
- For measuring ^{125}I activity in both KX-channels, the integral operating mode with lower threshold higher than the radiation emission peak (≥15 keV) is used.

Derivation of measurement equations

In general the measurement equations system for electron-capture radionuclide accompanied by internal conversion of γ–transition (^{125}I, for example), taking into account the summary events in each channel, will be follows:

$$\begin{cases} N_1 = N_0 \cdot (\varepsilon_{\gamma 1} I_\gamma + \varepsilon_{kx1}(I_{ec} + I_{ic}) - \varepsilon_{\gamma 1} I_\gamma \varepsilon_{kx1} I_{ec} - \varepsilon_{kx1}^2 I_{ec} I_{ic}) \\ N_2 = N_0 \cdot (\varepsilon_{\gamma 2} I_\gamma + \varepsilon_{kx2}(I_{ec} + I_{ic}) - \varepsilon_{\gamma 2} I_\gamma \varepsilon_{kx2} I_{ec} - \varepsilon_{kx2}^2 I_{ec} I_{ic}) \\ N_c = N_0 \cdot (\varepsilon_{\gamma 1} I_\gamma \varepsilon_{kx2} I_{ec} + \varepsilon_{\gamma 2} I_\gamma \varepsilon_{kx1} I_{ec} + 2\varepsilon_{kx1} I_{ec} \varepsilon_{kx2} I_{ic}) \end{cases} \quad (1)$$

Where: $N_1; N_2; N_c$ - pulse counting rates in γ-channel, KX channel and in coincidence channel, $\varepsilon_{\gamma 1}; \varepsilon_{\gamma 2}; \varepsilon_{kx1}; \varepsilon_{kx2}$ - efficiencies of γ and KX-detector to γ and KX-radiation; I_γ - emission probability of γ-radiation, $I_{ec} = P_k \omega_k$ - emission probability of KX-radiation due to electron capture, $I_{ic} = (\alpha_k \omega_k)/(1 + \alpha_t)$ - emission probability of KX-radiation due to internal conversion. The coincidences with LX – radiation are not considered for reasons described above.

In conditions of summary events low probability ($\varepsilon_{\gamma 1}; \varepsilon_{\gamma 2}; \varepsilon_{kx1}; \varepsilon_{kx2}$<5%) the equations (1) are simplified to (2).

$$\begin{cases} N_1 = N_0 \cdot (\varepsilon_{\gamma 1} I_\gamma + \varepsilon_{kx1}(I_{ec} + I_{ic})) \\ N_2 = N_0 \cdot (\varepsilon_{\gamma 2} I_\gamma + \varepsilon_{kx2}(I_{ec} + I_{ic})) \\ N_c = N_0 \cdot (\varepsilon_{\gamma 1} I_\gamma \varepsilon_{kx2} I_{ec} + \varepsilon_{\gamma 2} I_\gamma \varepsilon_{kx1} I_{ec} + 2\varepsilon_{kx1} I_{ec} \varepsilon_{kx2} I_{ic}) \end{cases} \quad (2)$$

The contribution of γ-radiation to KX-detector $N_2^\gamma = N_0 \cdot \varepsilon_{\gamma 2} I_\gamma$ is defined using aluminium filters (1mm for ^{54}Mn, ^{57}Co and ^{65}Zn and 5mm for ^{88}Y) and copper filter (1 mm for ^{139}Ce).

Modifying the equations (2) and computing I_γ, I_{ec} and I_{ic} from the data (1), we obtain measurements equation for each radionuclide. The numerical value of corrections standard uncertainty is indicated in brackets.

For ^{54}Mn

$$\frac{N_1 \cdot (N_2 - N_2^\gamma)}{N_c} = N_0 \quad (3)$$

For ^{65}Zn 1115 keV γ-transition only is taken into account.

$$\frac{N_1 \cdot (N_2 - N_2^\gamma)}{N_c} = N_0 \cdot \frac{(a \cdot I_{ec}^a + b \cdot I_{ec}^b)}{I_{ec}^a} = N_0 \cdot 0.989(9) \quad (4)$$

Where: $a; b$ - probability of electron capture to the 2 and 0 level for ^{65}Zn,

$I_{ec}^a; I_{ec}^b$ - emission probability of KX-radiation due to of electron capture to the 2 and 0 level.

For ^{139}Ce

$$\frac{N_1 \cdot (N_2 - N_2^\gamma)}{N_c} = N_0 \cdot \frac{(I_{ec} + I_{ic})}{I_{ec}} = N_0 \cdot 1.239(5) \quad (5)$$

For ^{88}Y 898 keV and 1836 keV γ-transitions are taken into account.

$$\frac{N_1 \cdot (N_2 - N_2^{\gamma})}{N_c} = N_0 \cdot \frac{(a \cdot I_{\gamma}^{898} + X \cdot I_{\gamma}^{1836}) \cdot (a \cdot I_{ec}^{a} + b \cdot I_{ec}^{b})}{(a \cdot I_{ec}^{a} \cdot (I_{\gamma}^{898} + X \cdot I_{\gamma}^{1836}) + b \cdot I_{ec}^{b} \cdot X \cdot I_{\gamma}^{1836})} = N_0 \cdot 0{,}989(10) \quad (6)$$

Where: $a;b$ - electron capture probability to the 2 and 1 level for ^{88}Y, $I_{ec}^{a}; I_{ec}^{b}$ - emission probability of KX-radiation due to electron capture to the 2 and 1 level, $I_{\gamma}^{898}; I_{\gamma}^{1836}$ - γ-radiation emission probability with energies 898 keV and 1836 keV, $X = \varepsilon_{\gamma 1}^{898} / \varepsilon_{\gamma 1}^{1836}$ - ratio of γ-radiation registration efficiency with energy 898 keV to the γ-radiation registration efficiency with energy 1836 keV in the selected «window» (≥400 keV).

The value of X =1,00(1) was calculated by Monte-Carlo method (6) for selected distances source-detector. The maximum contribution of X in correction standard uncertainty in the right part of the equation (6) was equal 0,1%.

For ^{125}I

$$\frac{N_1 \cdot N_2}{N_c} = N_0 \cdot \frac{(K_1 \cdot I_{\gamma} + I_{ec} + I_{ic}) \cdot (K_2 \cdot I_{\gamma} + I_{ec} + I_{ic})}{(I_{\gamma} \cdot I_{ec} \cdot (K_1 + K_2) + 2 \cdot I_{ec} \cdot I_{ic})} = N_0 \cdot 2.0064(42) \quad (7)$$

Where: $K_1 = \varepsilon_{\gamma 1} / \varepsilon_{kx1}; K_2 = \varepsilon_{\gamma 2} / \varepsilon_{kx2}$ - ratio of γ-radiation registration efficiency to the KX-radiation registration efficiency in each KX-detector in the selected energy «window» (≥15 keV).

The value of $K_1 = K_2$ = 1,215(45) were calculated by Monte-Carlo method (6) for selected distances source-detector. The maximum contribution of K_1 and K_2 in correction standard uncertainty in the right part of the equation (7) was equal 0,25%.

For ^{57}Co 14,4, 122 и 136 keV γ-transitions are taken into account.

$$\frac{N_1 \cdot (N_2 - N_2^{\gamma})}{N_c} = N_0 \cdot \frac{(K \cdot a \cdot I_{\gamma}^{136} + b \cdot I_{\gamma}^{122}) \cdot (I_{ec} + a \cdot I_{ic}^{136} + b \cdot I_{ic}^{122} + b \cdot I_{ic}^{14})}{(K \cdot a \cdot I_{ec} \cdot I_{\gamma}^{136} + b \cdot I_{ec} \cdot I_{\gamma}^{122} + b \cdot I_{\gamma}^{122} \cdot I_{ic}^{14})} = N_0 \cdot 1.016(9)$$

(7)

Where: $a;b$ - transition probability from 2 to 0 and from 2 to 1 level for ^{57}Co, $I_{\gamma}^{122}; I_{\gamma}^{136}$ - γ-radiation emission probability with energies 122 keV and 136 keV, $I_{ic}^{14}; I_{ic}^{122}; I_{ic}^{136}$ - KX-radiation emission probability due to γ-radiation internal conversion with energies 14,4 keV, 122 keV and 136 keV, $K = \varepsilon_{\gamma 1}^{136} / \varepsilon_{\gamma 1}^{122}$ - ratio of γ-radiation registration efficiency with energy 136 keV to the γ-radiation registration efficiency with energy 122 keV in the selected energy «window» (≥80 keV).

The value of K =1,060(4) was calculated by Monte-Carlo method (6) for selected distances source-detector. The maximum contribution of K in correction standard uncertainty in the right part of the equation (9) was equal 0,2%

Results

The ^{54}Mn, ^{57}Co, ^{65}Zn, ^{88}Y and ^{139}Ce radionuclide activity in film covered sources OSGI type was measured using KX-γ coincidences method. The results obtained are presented in table 1. In the last column of table 1 the deflection of these results from the same obtained by national activity standard of Russia Federation. The ^{54}Mn №5123 and ^{57}Co №5171 sources are the witnesses of international comparisons (7,8). Other radionuclides activity measurements results was traced to the results of key comparisons (9,10,11).

Table 1. The results.

Nuclide	Source number	Date	KX-γ coincidences activity, Bq	Uc, k=2 %	Activity, measured on the standard, Bq	Uc, k=2 %	Deflection, %
^{54}Mn	5123	01.01.09	12 956	1.0	12 860	1.0	0.8
	41-06	01.01.09	36 363	1.0	36 462	2.0	-0.3
	384-08	01.01.09	72 186	1.1	72 451	2.0	-0.4
^{65}Zn	5201	01.01.09	5 593	2.1	5 524	2.0	1.2
	16-08	01.01.09	41 130	2.1	41 221	2.0	-0.2
	387-08	01.01.09	90 294	2.1	90 236	2.0	0.1
	350-07	01.01.09	171 258	2.2	171 755	2.0	-0.3
^{88}Y	15-08	01.01.09	14 004	2.3	14 172	2.0	-1.2
	24-06	01.01.09	38 236	2.3	38 549	2.0	-0.8
	469-08	01.01.10	97 031	2.3	98 369	2.0	-1.4
^{139}Ce	14-08	01.01.09	18 446	1.8	18 340	2.0	0.6
	47-06	01.01.09	67 000	1.8	66 007	2.0	1.5
	471-06	01.01.10	150 746	1.9	149 330	2.0	1.0
^{57}Co	5171	01.01.09	8 229	2.0	8 108	1.0	1.5
	01	01.01.09	205 224	2.1	206 731	2.0	-0.7

^{125}I activity was measured in 5 film covered sources, prepared from one solution with well known masses. A detailed description of sources preparation procedure is given in (3). The specific activity is calculated as the average value of 5 results. The result obtained is given in comparison with specific activity (table 2), measured on the national activity standard of Russia Federation with KX-γ coincidences method.

Table 2. ^{125}I Specific activity.

Nuclide	Date	KX-γ coincidences specific activity, Bq/mg	Uc, k=2 %	Specific activity, measured on the standard, Bq/mg	Uc, k=2 %	Deflection, %
I-152	21.05.09	3084	2.0	3135	2.0	1.6

Discussion

Table 1 and 2 data analysis shows, results obtained using described prototype are in good agreement with national standard results. It means spectrometer-radiometer MKGB-01 can be used for activity measurements without preliminary calibration.
Moreover setup described makes it possible to measure radionuclides activity directly in mass-produced film covered sources (12).

On the basis of this investigations an original KX-γ coincidences setup construction is proposed (MKGB-01 units based primary converter, background shielding system, positioning device, secondary electronics).

Conclusions

A concept of creation of the setup, implements the KX-γ coincidences method, based on commercially available spectrometer-radiometer MKGB-01 is developed. The main requirements to the future KX-γ coincidences setup are formulated.

References

1. Bé M.-M. et.al. Table of Radionuclides – CEA/Saclay (France), 1998-2010.
2. Yu. T. Vydai, A. A. Kostantinov, T. E. Sazonova, S. V. Sepman "Ionizing radiation measurements measuring the activity of radionuclides by the coincidence method with 0.l-mm thick scintillation detectors" // Izmeritel'naya Tekhnika, 1989, No. 6, pp. 51-52.
3. E. E. Tereshchenko, M. A. Rasko, A. V. Zanevskii "Measurement of the specific activity of ^{125}I At the d. I. Mendeleev all-russia Research Institute of metrology" // Izmeritel'naya Tekhnika, 2006, No. 6, pp. 56-59
4. Campion P. J. // Intern. J. Appl. Rad. Isot. 1959. V. 4. P. 232.
5. Bryant J. // Intern. J. Appl. Rad. Isot. 1963. V. 14. P. 143.
6. K.A. Bagaev, S.S. Kozlovsky, I.E. Novikov "Computer code for 3D imitation modelling and registration system of ionizing radiation" // ANRI, 2007, No. 4. p. 35-40 in russian
7. G Ratel et al "BIPM.RI(II)-K1.Mn-54" Metrologia, 2008, 45
8. C Michotte et al "BIPM.RI(II)-K1.Co-57" Metrologia, 2009, 46
9. G Ratel and C Michotte "BIPM.RI(II)-K1.Zn-65" Metrologia, 2004, 41
10. G Ratel et al "BIPM.RI(II)-K1.Y-88" Metrologia, 2004, 41
11. G Ratel et al "BIPM.RI(II)-K1.Ce-139" Metrologia, 2005, 42
12. G Ratel et al "BIPM.RI(II)-K1.Cr-51" Metrologia, 2009, 46

Comparison of two techniques for low-level tritium measurement – gas proportional and liquid scintillation counting

Barešić, Jadranka; Horvatinčić, Nada; Krajcar Bronić, Ines; Obelić, Bogomil
Rudjer Bošković Institute, Zagreb, CROATIA

Abstract

Measurement of low-level tritium activities in natural/non-polluted waters, e.g. in precipitation and groundwater, requires special techniques for water pretreatment and detection of low-level radioactivity. Two methods for low-level tritium measurement have been developed in Zagreb Radiocarbon and Tritium Laboratory: gas proportional counting (GPC) and liquid scintillation counting (LSC). Method of electrolytic enrichment of water samples with tritium followed by measurement by LSC *Quantulus 1220* has been developed in 2008. Here we present the comparison of the two measurement techniques.

Our Laboratory participated in the intercomparison study organized by the IAEA, TRIC2008. The data evaluation of six samples revealed that all results measured by LSC are accepted, as well as four GPC results, while two GPC results of samples with low tritium activity (<2 TU) are in the warning level.

Introduction

Atmospheric thermonuclear tests during 1950es and 1960es introduced large amount of anthropogenic tritium into the atmosphere. The peak of tritium activity with up to 10 000 TU has been reached in 1963 in a monthly rain in North America. The anthropogenic tritium has been used as a global tracer in hydrogeology and meteorology studies (Rożanski at al. 1991). Tritium activity in surface, groundwater and precipitation was measured by a gas proportional counting (GPC) technique, and later on by liquid scintillation counting (LSC). However, the present tritium activity almost approached natural levels (5 – 10 TU), and measurement of samples without tritium enrichment is not precise enough any more.

In Zagreb Radiocarbon and Tritium Laboratory two measurement techniques of low-level tritium activities in natural/non-polluted waters, e.g. in precipitation and groundwater, have been used: gas proportional counting (GPC) and liquid scintillation counting (LSC). GPC technique for measurement of non-enriched samples has been used since 1978. A method of tritium measurement by LSC *Quantulus 1220* using electrolytic enrichment of water samples has been developed in 2008.

Material and methods

CH_4 is used as a counting gas in a multi-wire GPC. It is obtained by reaction of water (50 ml) with aluminium carbide at 150°C (Horvatinčić, 1980). The counting energy window is set to energies between 1 keV and 10 keV to obtain the best figure of merit. Gas quality control has been performed by simultaneous monitoring of the count rate above the tritium channel, i.e., above 20 keV (Krajcar Bronić et al. 1986). The limit of detection is 2.5 TU.

System of electrolytic enrichment consists of 20 cells of 500 ml volume (anodes: stainless steel, cathodes: mild steel) and equipments for primary and secondary distillations. The first step of sample pretreatment is primary distillation. If conductivity of distilled samples is <50 μS/cm, samples are ready for the enrichment procedure. Otherwise, samples have to be distilled again. For each enrichment run 3 spike and 2 dead-water (DW) samples are used for system control. Enrichment procedure lasts for 8 days (1420 Ah). Final volume of water sample after electrolysis is 19±1 ml. The enrichment factor (E) and the enrichment parameter (P) for each electrolysis run have been calculated using initial and final mass of water in cells and individual count rates of spike water before and after enrichment. The average enrichment factor (E) of several electrolysis runs is 21.4 ± 0.9, and the P parameter reached a value of 0.95.

Mixture of 8 ml of water and 12 ml of scintillation cocktail *Ultima Gold LLT* in plastic vials is used for counting in LSC. The measurement run contains 15 samples, 3 enriched spikes, 2 enriched DW samples, 1 non-enriched spike, 2 non-enriched DWs and a standard sample (activity 11 552 TU on 7.7.2008). The limit of detection is 0.3 to 0.5 TU, depending on the measurement duration.

Results

The results of GPC and LSC measurements of IAEA TRIC2008 intercomparison samples are presented in Table 1. The results were evaluated with the z-score and Final score evaluations. The z-score values were calculated using measured laboratory values (A_{lab}) and their sigma values (σ_{lab}) and IAEA true values (A_{IAEA}):

$$z = \frac{A_{lab} - A_{IAEA}}{\sigma_{lab}}$$

The Final score evaluations were determined by the evaluation criteria for both trueness and precision of the measurements (Gröning et al, 2009). In the final evaluation, both scores are combined and a result must obtain 'Acceptable' score in both criteria to be assigned final score 'Acceptable'.

According to the Final score evaluations all our LSC results are acceptable while two GPC results of samples T14 and T15 with low tritium activity are in warning level. The z-score evaluations showed that most of GPC results are lower than the IAEA true values (mean z-score is -0.44) and in the case of LSC results the deviations from the IAEA true values is smaller (mean z-score is -0.29). The comparison of both GPC and LSC results with the IAEA true values is presented in Fig.1.

Table 1. Comparison of GPC and LSC values measured in our Laboratory with IAEA TRIC2008 intercomparison results. The z-score and Final score evaluations are presented for both methods (A – acceptable, W – warning)

IAEA code	IAEA true value (TU)	GPC				LSC			
		Lab. code	Lab value (TU)	z-score	Final score	Lab. code	Lab value (TU)	z-score	Final score
T14	1.54 ± 0.05	T-3867	0.21 ± 0.81	-1.64	W	T-3906	1.25 ± 0.3	-0.97	A
T15	4.07 ± 0.05	T-3868	3.50 ± 0.96	-0.59	A	T-3907	4.11 ± 0.3	0.13	A
T16	7.74 ± 0.06	T-3869	6.60 ± 0.99	-1.15	A	T-3908	7.42 ± 0.3	-1.06	A
T17	14.46 ± 0.08	T-3870	14.23 ± 0.67	-0.34	A	T-3909	14.44 ± 0.4	-0.05	A
T18	0.67 ± 0.05	T-3871	0.03 ± 0.82	-0.78	W	T-3910	0.57 ± 0.3	-0.33	A
T19	568.7 ± 2.3	T-3872	579.24 ±5.70	1.85	A	T-3911	576.0 ± 13	0.56	A

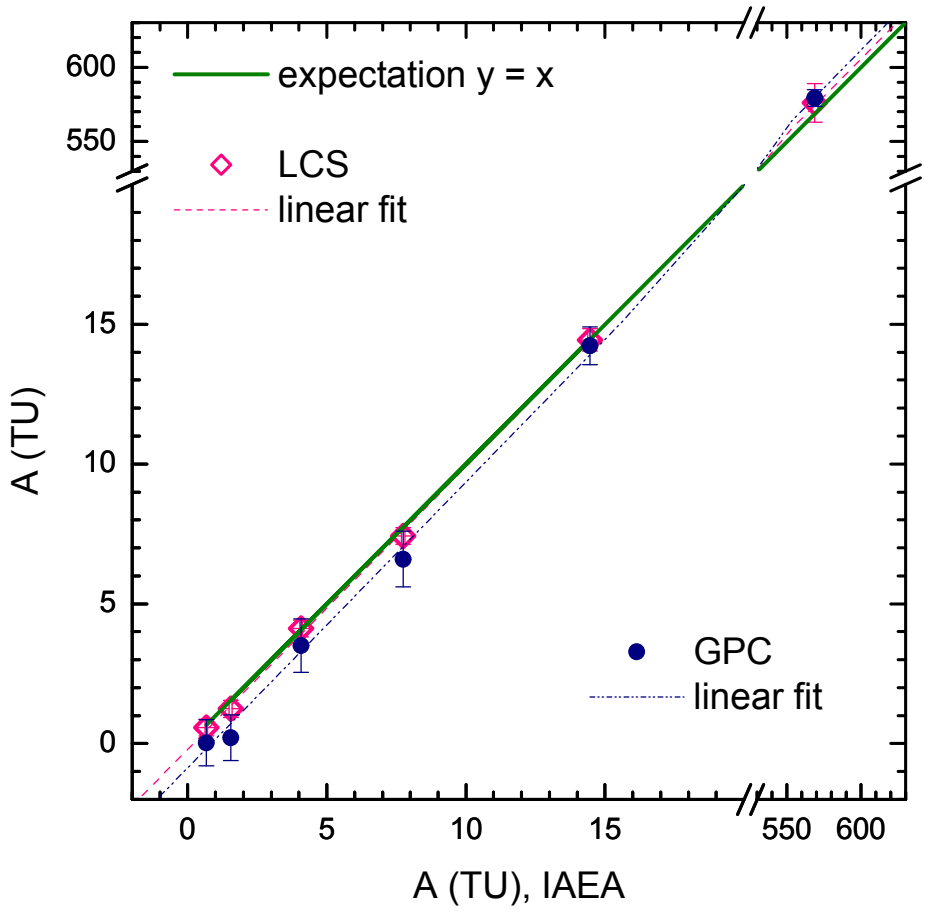

Fig. 1. The comparison of tritium activities of TRIC2008 intercomparison samples measured by GPC and LSC techniques with the IAEA true values.

For additional testing of both systems we measured tritium activity in several precipitation and groundwater samples by both GPC and LSC techniques. The results are presented in Fig. 2. Here we can see that all LSC results have smaller errors then GPC results. For the samples with low tritium activity (<10 TU, mostly groundwater) the GPC results are mainly lower then the LSC results while for the higher tritium activities (precipitation samples) the GPC results are lower than the LSC results. If we take into account also the IAEA intercomparison results obtained by both methods, we can conclude that for the low tritium activity the GPC system is not acceptable because of higher/worse detection limit (2.5 TU). LSC system with detection limit of 0.3 – 0.5 TU and with better precision (Table 1) is more suitable for most natural water samples including precipitation and groundwater samples.

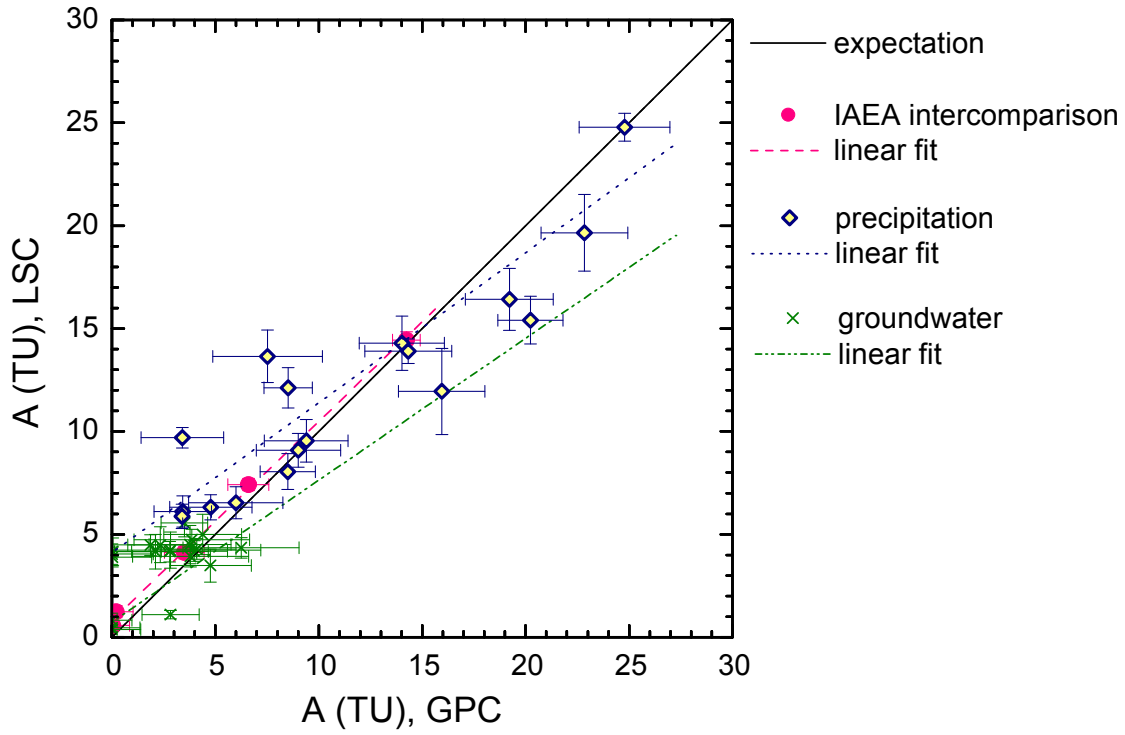

Fig. 2. Comparison of GPC and LSC results of groundwater and precipitation samples, as well as TRIC2008 intercomparison samples.

Conclusion

The data evaluation of six TRIC2008 samples (IAEA intercomparison) revealed that all results measured by LSC are accepted, and for GPC results four results are accepted and two results of low tritium activity (<2 TU) are in the warning level. Measurements of groundwater and precipitation samples show that GPC values are still valid for higher tritium activities (>10 TU), while lower activities can not be measured properly without enrichment and followed by LSC measurement.

Acknowledgments

The presented work was performed within the project 098-0982709-2741 and the project of bilateral scientific cooperation between Croatia and Slovenia entitled "Measurement of ^{3}H activity in natural waters by liquid scintillation spectrometry with electrolytic entrichment".

References

Gröning M, Tatzber H, Trinkl A, Klaus P, van Duren M. Eighth IAEA Interlaboratory Comparison on the determination of low-level tritium activities in water (TRIC2008). Report, IAEA, Vienna, 2009.

Horvatinčić N. Radiocarbon and tritium measurements in water samples and application of isotopic analysis in hydrology. Fizika 1980; 12 (S2): 201-218.

Krajcar Bronić I, Obelić B, Srdoč D. The simultaneous measurement of tritium activity and background count rate in a proportional counter by the Povinec method: Three years experience at the Rudjer Bošković Institute. Nuclear Instruments and Methods in Physics Research Section B - Beam Interactions with Materials & Atoms. 1986; B17, 5-6: 498-500.

Rożanski K, Gonfiantini R, Araguas-Araguas L. Tritium in the global atmosphere: distribution patterns and recent trends. J. Phys. G: Nucl. Part. Phys. 1991; 17: 523-536.

Multi-screen diffusion battery for radon progeny dispersion analysis

Zhukovsky, Michael; Bastrikov, Vladislav; Rogozina, Marina; Yarmoshenko, Ilya
Institute of Industrial Ecology, Ural Branch of Russian Academy of Science,
RUSSIAN FEDERATION

Abstract

The screen-type diffusion battery method was enhanced for size distribution measurements of radon progeny air particles. The measurement technique implies multisection arrangement of several dozens of screen stages and a backup filter during sampling with subsequent activity measurement of each component. Variations on quantity of screens, flow rate and screen meshness allows to obtain required cut-off diameters of the stages and essential operating size range in general. Serial mounting of screen blocks with continually narrowing penetration curve is also used. Optimal parameters were adjusted for radon progeny size distribution researches.

Size distribution measurements of radon progeny in the range of 1-400 nm were performed in the laboratory radon box with high radon equilibrium-equivalent concentration (5-20 kBq/m^3). Generally accepted modes of unattached and aerosol fractions were confirmed. The smallest mode is represented by the primary free particles (geometric mean diameter 1.75 nm, geometrical standard deviation $\sigma_g = 2.0$). It appeared that the nucleation mode consists of three modes (8.5, 20 and 40 nm with σ_g 1.5, 1.2 and 1.7, respectively). Two modes of the accumulation mode were also observed (120 and 300 nm with σ_g 1.5 and 1.2, respectively).

Knowledge of dispersion behaviour of natural radioactive aerosols and gases is critical for understanding human exposure and for appropriate measurement technique development, especially in the case of unattached fraction. Results obtained in the work have particular value from this point.

Introduction

Natural radioactive gas radon and its progeny form the most significant radiological hazard on the general population round the world. Inhalation dose due to radon progeny is highly dependent on the size of inhaled particles. Newly generated short-lived radon decay products usually exist as positively charged ions that rapidly attach on atmospheric aerosol particles and form radioactive aerosol. So the size distribution of radon progeny is directly related to the natural particle sizes that primarily assist at the atmosphere.

In order to have an appropriate estimate of radon dose one should determine aerosol size distribution along with the radon concentration. Traditional measurement instruments for dispersion analysis include diffusion battery and cascade impactor. The first is used for measurements in nanometer region, while the second – for micrometer region. In this work a screen-type diffusion battery was designed for the size distribution measurements in the wide range from fractions of nm to several hundreds of nm.

Investigations were conducted in the laboratory radon box in Radon laboratory of Ural State Technical University (Ekaterinburg, Russian Federation). High radon concentration values in the box allowed performing aerosol particle size distribution measurements with high accuracy.

Material and methods

Most commonly used methods for size distribution measurements of atmospheric ultrafine particles are based on their diffusion properties. The smaller particles have higher diffusivities than large ones and diffuse more rapidly to surfaces. In this work we use screen-type diffusion battery method optimized for wide range of particle sizes.

The measurement system consists of a number of wire screens with different penetration characteristics and several backup filters arranged sequentially in a series configuration. Activity collected on each wire screen and filter is measured after sampling with semiconductor alpha counter.

Three different wire screen types that appeared to be optimal for experiments were chosen. In Table 1 the main screen characteristics are summarized. Analytic aerosol filters with standard characteristics were used as backup filters.

Table 1. Wire screen characteristics.

Type	Mesh	Wire diameter, mm	Screen opening, mm	Screen thickness, mm	Screen mass, g	Density, g/cm^3
1	35	0.25	0.5	0.51	2.13	7.8
2	150	0.65	0.1	0.14	0.69	8.5
3	350	0.03	0.04	0.07	0.31	7.8

Particle penetration through a wire screen was described by semi-empirical equations of filtration theory (Cheng et al. 1980). Penetration through the screen depends on its characteristics, geometry, air flow velocity and particle size. From theoretical calculations and experimental testing of diffusion batteries with different screen combinations two main configurations were adjusted for wide range aerosol dispersion analysis (see Table 2).

It should be noticed that for Type II battery ultrafine particles with sizes less than 10 nanometers get stuck already on the first wire-screens. It allows to neglect a control of tube losses, which is significant only for slow motion of ultrafine particles.

Table 2. Multi-screen diffusion battery configurations.

Type	Screen mesh	Quantity of screens	Operating flow rate, l/min	Operating AMTD range, nm
I	35 150 350	5 5 14	25	0.78-27
II	150 350	6 28	0.8	11-400

Sampling procedures were performed in the laboratory radon box with a volume of 4 m^3. Radon was generated inside the box by placing a standard source of Ra with activity of 518 kBq and emanation coefficient 0.26. Equilibrium conditions between radon and its progeny were established before the sampling. The radon equilibrium-equivalent concentration in the box atmosphere was in the range from 4500 to 18000 Bq/m^3. The volumetric flow rate during sampling was kept constant.

Diffusion battery was placed inside the box via locking system in order to neglect particle concentration losses. By use of flexible tubes the device was connected to the air pump with adjustable volumetric flow rate. Sampling procedure was implemented during 10-40 minutes. Individual activity measurements of collecting elements were performed after 40 minutes delay in order to neglect the influence of equilibrium shift between short-lived radon daughters. The primary measurement results were presented as a set of equilibrium-equivalent concentrations, calculated from individual activities of each diffusion battery collecting element according to the Kusnetz method (Kusnetz 1956).

It is well known that aerosol particle distribution in the air is well described by the polymodal lognormal distribution. In the case of unimodal lognormal distribution integral probability function plotted on the log-probability graph is used for definition of the activity median thermodynamic diameter (Hinds 1999). The probability scale of log-probability graph compresses the percent scale near the median (50% point) and expands the scale near the ends such that a cumulative plot of a lognormal distribution will yield a straight line. A log-probability plot can be constructed by plotting the logarithm of diameter versus the probability function, expressed in cumulative percentages. This probability function is defined as:

$$f(D_i) = f(D_{i-1}) - \frac{C_{\mathrm{eq},i}}{\sum_{k=1} C_{\mathrm{eq},k}} \cdot 100\%,$$

where D_i is a 50% cut-off diameter of i wire-screen, $C_{\mathrm{eq},i}$ is an equilibrium-equivalent concentration, corresponding to i wire-screen. The value of the probability function $f(D_1)$ for the first wire-screen is fixed to 100%.

It is supposed that every screen of diffusion battery catches particles related to several modes of aerosol particle distribution. Probability function curve plotted for the full set of collecting elements have some inflections. By the analytical method each diffusion battery type was divided to several sections with specific number of wire screens. Thus, integral probability function curve of every section was linear and corresponded to lognormal distribution of one mode. An example of the probability function curves for one diffusion battery is presented in figure 1.

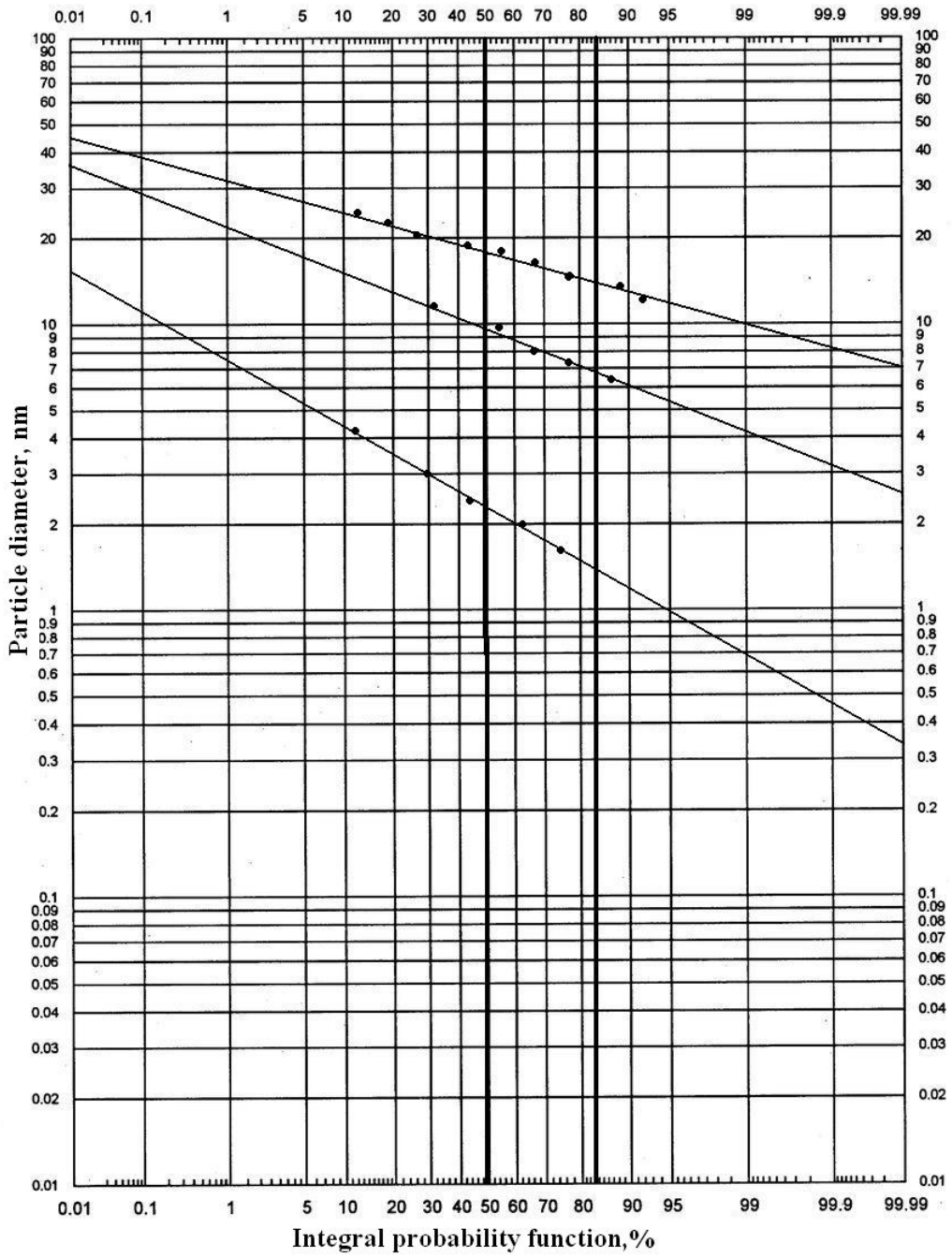

Fig. 1. Typical view of integral probability function for diffusion battery type I.

For a lognormal distribution the geometric standard deviation is defined as:

$$\sigma_g = \frac{d_{50\%}}{d_{84\%}},$$

where $d_{50\%}$ and $d_{84\%}$ are diameters, associated with values of probability function 50% and 84%, respectively.

Results and discussion

In the previous research with primary version of diffusion battery and aerosol cascade impactor four modes of radon progeny particle activity size distribution were observed (Salomatova 2009). In the present research variations of screen quantity, flow rate and screen meshness essentially expanded the overall diffusion battery operating size range. It allows to exclude impactor application which led to large uncertainty. New diffusion battery method produces more detailed data on aerosol dispersion.

For each experiment performed in the radon box total equilibrium-equivalent concentration, activity median thermodynamic diameter and geometric standard deviation were calculated. Six modes of radon progeny particles activity size distribution were defined. Characteristics of the defined modes are presented in the Table 3. Obtained radon progeny particles activity size distribution is shown on the Figure 2.

Table 3. Distribution modes characteristics.

Mode number	AMTD, nm	Geometric standard deviation	Fraction
1	1.75	2.0	0.4
2	8.5	1.5	0.03
3	20	1.2	0.07
4	40	1.7	0.1
5	120	1.5	0.26
6	300	1.2	0.14

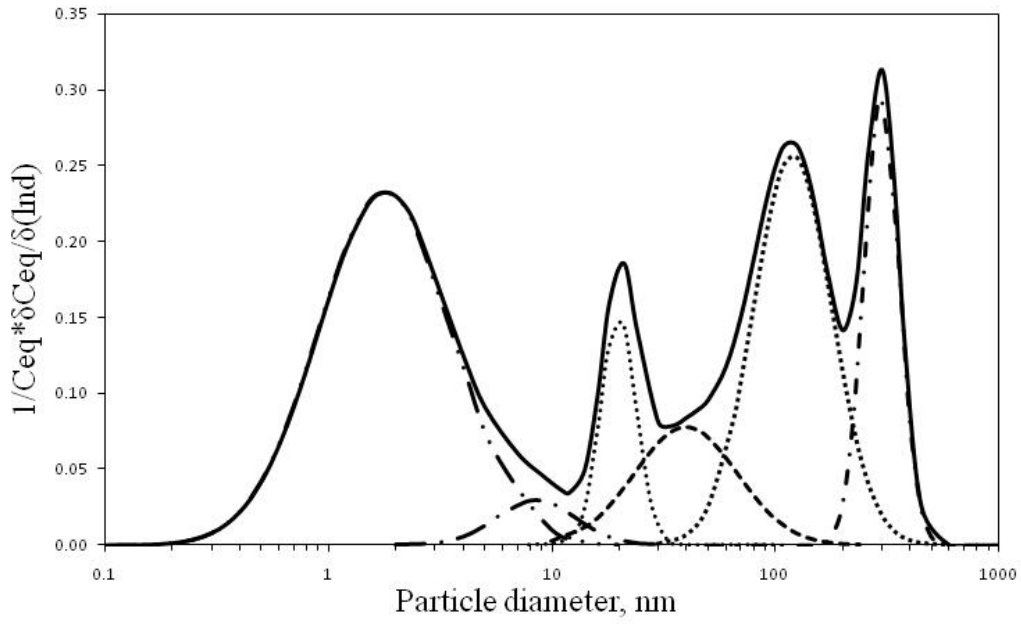

Fig. 2. Radon progeny activity size distribution.

A comparison with independent measurements of activity size distribution in earlier research (Porstendorfer 1996) is shown on the Figure 3.

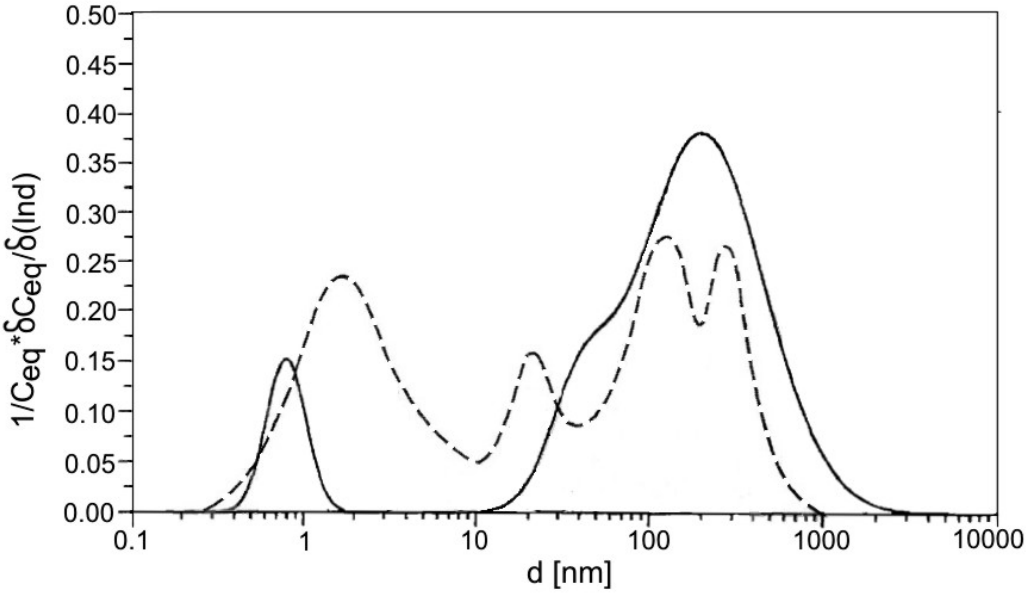

Fig. 3. Measured activity size distribution (dotted line) in comparison with typical distribution (solid line) for indoor air in dwellings (Porstendorfer 1996).

Air particles modes according to established classification could be identified as follows: 2 nm mode represents an unattached fraction of free radon progeny atoms; next five modes are formed by coagulation of unattached fraction atoms with atmospheric particles of different sizes. Thus, 8 nm corresponds to the group of natural particles, formed by the homogeneous nucleation; 20 nm and 40 nm modes are based on the particles, formed not only by homogeneous nucleation, but also condensation (heterogeneous nucleation). The largest modes 120 nm and 300 nm correspond to condensation particles.

On this basis it is possible to make an assumption that radon progeny particles activity size distribution can be an indicator of natural aerosol particles size distribution.

Conclusions

Several conclusions can be made as a result of the work performed.

The screen-type diffusion battery method was enhanced for radon progeny particle activity size distribution in the range from 1 to 400 nanometers with reduced geometric standard deviation in comparison with previous experiments with diffusion battery and cascade impactor.

Modes of the radon progeny particle activity size distribution corresponds to modes of the natural soluble particle size distribution. It is possible to measure concentration and size distribution of the fine soluble particles in the atmosphere through registration of radon progeny particles, coagulated with natural aerosols, by means of standard radiometric techniques.

The influence of atmospheric conditions parameters, such as humidity, temperature, aerosol particle concentration etc, is supposed to be investigated in the following work.

References

Cheng Y.S., Yeh H.C. Theory of screen type diffusion battery. Journal of Aerosol Science 1980; 11: 549–556.

Kusnetz H.L. Radon daughters in mine atmospheres: a field method for determining concentration. American Industrial Hygiene Association Quarterly 1956; 17: 85–88.

Hinds W.C. Aerosol technology. Properties, behavior and, measurement of airborne particles. 2nd ed. Wiley-Interscience; 1999.

Salomatova M.A., Ekidin A.A., Zhukovsky M.V. Radon progeny dispersion in the air. ANRI (Apparatura i Novosti Radiacionneekh Izmereniy) 2009; 3: 42–49 (in Russian).

Porstendorfer J. Radon: measurements related to dose. Environment International 1996; 22 (1): S563–S583.

Evaluating on-site monitoring cart conceptually developed for radiation workplace

Kawano, Takao; Nishimura, Kiyohiko
National Institute for Fusion Science, JAPAN

Abstract

In our previous study, an on-site radiation monitoring cart was developed by inspecting apparatuses necessary for radiation monitoring. These apparatuses were selected from those commercially available. It was found that all the equipment could be installed on an appropriately sized monitoring cart. Since the cart was too heavy, key methods for reducing the mass of the cart were suggested. The present study follows the previous study, and literature search was carried out to evaluate the performance of the cart from the viewpoint of radiation detection limits and radioisotope concentration. As a result, radiation detection limits were sufficiently lower than the legal limits stipulated by law in radiation workplaces radioisotope surface contamination, and radioisotope concentration in air, which are stipulated in the Japanese radiation law: The Law Concerning Prevention from Radiation Hazard due to Radioisotope etc.

1. Introduction

For developing an on-site radiation monitoring cart, radiation measurement apparatuses used for monitoring radiation at a radiation facility have been investigated recently. In our previous study (Kawano and Nishimura 2009), these apparatuses were properly selected from those commercially available, and they were investigated to see if they could be compactly installed on an appropriately-sized to be manhandled on-site monitoring cart. Furthermore, the feasibility of the cart and problems to be resolved were examined. It was found that all the equipment necessary for radiation monitoring could be installed on a monitoring cart of 164 cm (W) × 150 cm (H) × 80 cm (D), but the cart was too heavy. Thus, a more lightweight solution was required. Four key methods for reducing the mass of the cart were suggested.

Following the above-mentioned previous study, the cart was evaluated from the viewpoints of radiation detection limit and radioisotope concentration, assuming the selected apparatuses were installed onto the cart. The radiation detection limit was investigated through literature research, and compared with those stipulated in The Law Concerning Prevention from Radiation Hazard due to Radioisotope etc. of Japan (the Japanese radiation law is used as a abbreviated expression below) to evaluate the performance of the cart. It was concluded that the cart conceptually designed using only commercially available radiation measurement systems had a sufficient detection

capability for radiation monitoring in radiation facilities including radiation workplaces and radiation-controlled areas.

2. Conceptually designed monitoring cart

2.1. Radiation monitoring in work places

In radiation workplaces that mean radiation workplaces and radiation-controlled areas, and controlled areas means boundary of controlled areas in the present study, radiation monitoring has to be performed at regular intervals. According to the Japanese radiation law, three measurement obligations, the radiation dose in radiation workplaces, radioisotope surface contamination, and radioisotope concentration in air, are stipulated for radiation monitoring at a radiation workplace. In Table 1, radiation and radionuclides to be monitored and legal limits stipulated in the Japanese radiation law as typical cases are summarized.

Table 1. Regulation limits for work place and controlled areas.

Measurement item	Radiation or Nuclides	Legal limits	
		Work place	Controlled area
Radiation dose	Gamma ray Neutron	1000 μSv/40 h (25 μSv/h)	1300 μSv/520 h (2.5 μSv/h)
Radioisotope surface contamination	Alpha Others	4.0 Bq/cm^2 40 Bq/cm^2	0.4 Bq/cm^2 4.0 Bq/cm^2
Radioisotope concentration in air	^{3}H ^{14}C ^{32}P ^{35}S ^{125}I	5.0E-1 Bq/cm^3 4.0E-2 Bq/ cm^3 7.0E-3 Bq/cm^3 2.0E-2 Bq/cm^3 1.0E-3 Bq/cm^3	5.0E-2 Bq/ cm^3 4.0E-3 Bq/ cm^3 7.0E-4 Bq/ cm^3 2.0E-3 Bq/ cm^3 1.0E-4 Bq/ cm^3

Radiation dose limits are 1000 μSv/a week for a radiation workplace and 1300 μSv/3 months for a controlled area, assuming one week and three months are 40 and 520 hr (5 days/week, 8 hour/day and 13 weeks/3 months), the radiation dose limits correspond to 25 and 2.5 μSv/h, respectively. These dose limits are normally unrelated to radiation quality, gamma rays, neutrons, and beta rays. In the case of radioisotope surface contamination, the limits are stipulated under two categories, alpha-ray-emitting nuclides and other radiation-emitting nuclides. For alpha-ray-emitting nuclides, 4.0 and 0.4 Bq/cm^2 are the surface contamination limits for a workplace and a controlled area, respectively. For the other radiation-emitting nuclides, the limits are ten times larger, 40 and 4.0 Bq/cm^2. In the case of radioisotope concentration in air, limits are stipulated for respective radioisotopes. In Table 1, the limits of radioisotope concentration in air are listed for the five typical nuclides of ^{3}H, ^{14}C, ^{32}P, ^{125}I, and ^{35}S. These nuclides are used often in radiation facilities in Japan. Radioisotope concentration in water is not

stipulated by the Japanese radiation law because eating and drinking are not permitted in radiation facilities, including controlled areas.

2.2. Construction of on-site radiation monitoring cart

The conceptually designed on-site radiation monitoring cart discussed in the previous study is shown in Fig. 1, containing plan and side views. All the apparatuses used for monitoring radiation dose, surface contamination, and radioisotope concentration are mounted on a battery-powered rover rack, which one person can operate like an electric car. The dimensions of the rover rack are estimated to be 164 cm (W) × 150 cm (H) × 80 cm (D) . The rover rack has a running speed of 3.5 km/h and a running distance of 3.5 km when the battery is fully charged.

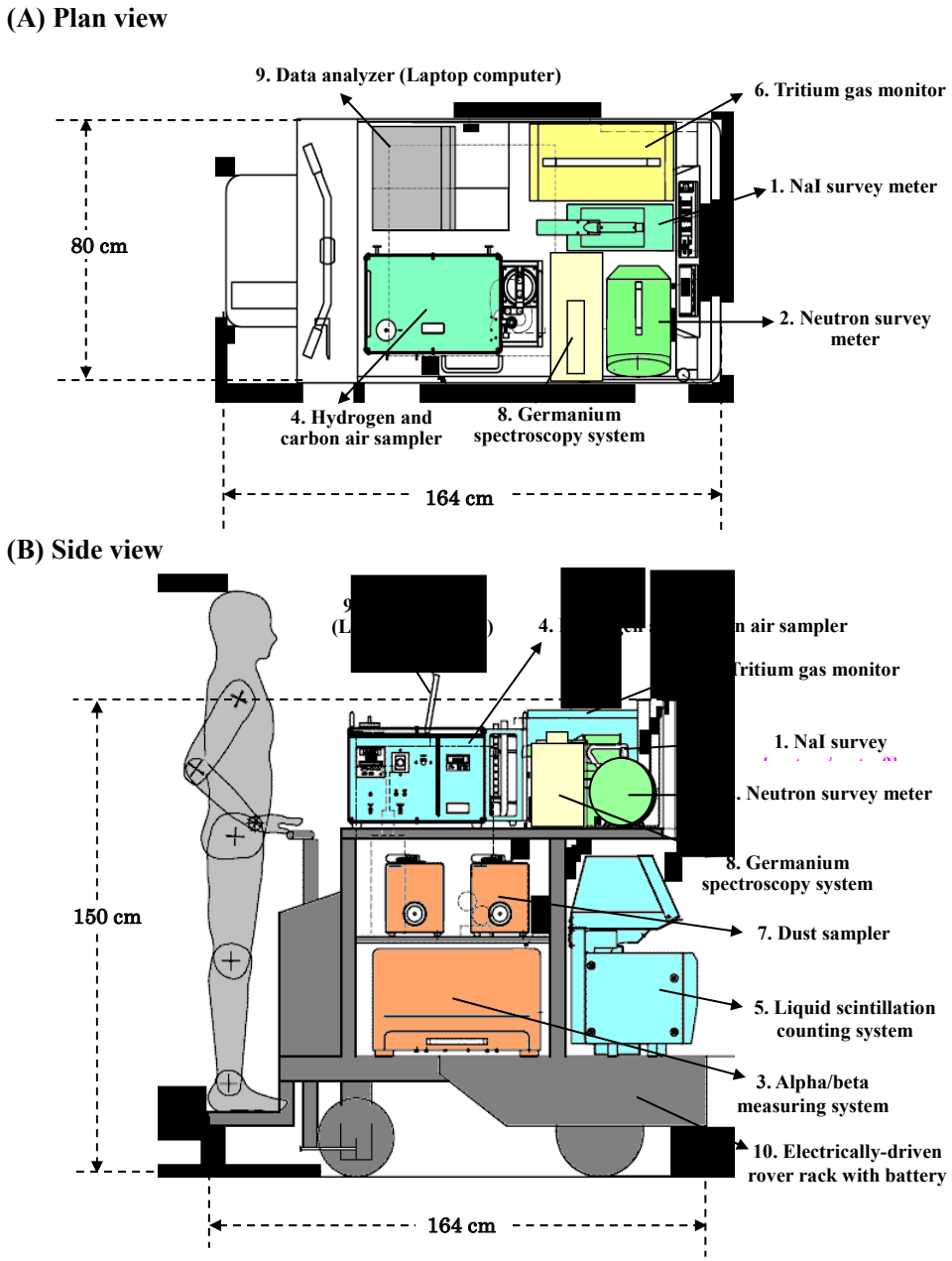

Fig. 1. Illustration of radiation monitoring cart.

(1) Monitoring radiation dose for gamma (X) rays and neutrons

A NaI(Tl) scintillation survey meter and a neutron survey meter are used to measure the radiation dose in radiation workplaces. The neutron survey meter is installed in a ^{3}He proportional counter for detecting neutron radiation. These survey meters are portable and can be replaced with other types of conventional survey meters, such as a Geiger Mueller (GM) survey meter and a tritium survey meter, as the need arises. For this radiation monitoring, alpha rays are ignored because their range in air is short and their penetrating power is weak.

(2) Monitoring radioisotope surface contamination

There are two methods for monitoring radioisotope surface contamination. One is a survey method and the other is a smear method. In the survey method, the above-mentioned survey meters, NaI(Tl) scintillation, neutron, GM, and tritium, can be used to directly detect radioisotope surface contamination. In the smear method, a smear paper is used to wipe up radioactive contamination from floors and the surfaces of devices, tools, etc. The radioactivity of contamination collected on the smear paper can be measured using the liquid scintillation counting system, alpha/beta radiation measurement system, or germanium spectrometer. The liquid scintillation counting system is used to measure tritium and carbon-14 contamination with high sensitivity. The alpha/beta radiation measurement system has a ZnS(Ag) scintillation detector and a plastic scintillation detector for measuring alpha and beta radiation, respectively. The germanium spectrometer is used to analyze gamma-ray-emitting nuclides contained in radioactive contamination. The smear method is highly sensitive but requires time a somewhat longer than the survey methods since it is an indirect measurement.

(3) Radioisotope concentration in air

There are also two methods for monitoring radioisotope contamination in air. One method is continuously measuring radioisotope concentration in air using a vent-type detector. An example of this type of monitor is a tritium gas monitor, which is installed in a vented ionization chamber and can provide live data. In the other method, a tritium and carbon air sampler and a dust sampler are used to collect radioisotope contained in air. With the hydrogen and carbon air sampler, tritium and carbon-14 contained in air are collected in the chemical forms of water and carbon dioxide by a cooled collection tube with dry ice-ethanol and a monoethanolamine tube, respectively. The radioactivity of the tritium collected in water and that of carbon-14 collected with monoethanolamine are measured using the liquid scintillation counting system mentioned above. The dust sampler is used to collect other radioisotopes that are bound to dust suspended in air on a filter paper or an activated charcoal filter. Radioactivity trapped on the filter can be measured using the liquid scintillation counting system, the alpha/beta radiation measurement system, or the germanium spectrometer, which is similar to the smear method.

A conventional laptop computer is installed on the on-site radiation monitoring cart as an on-site data analyzer. The computer can perform data acquisition, data storage, and data display. Consequently, the on-site radiation monitoring cart has the same functions as a conventional radiation measurement room. Furthermore, the cart is movable, allowing it to be brought into the radiation laboratory to carry out on-site

radiation monitoring and removed from the radiation laboratory on an as-needed basis. The cart is essentially a portable radiation measurement room.

3. Evaluation of detection limit

To certify that the cart is effective in detecting these radiation limits, a literature search was carried out. Table 2 lists the detection limits and their ratios to the legal limits set by the Japanese radiation law for the respective apparatuses conceptually installed for monitoring radiation dose in radiation workplaces, radioisotope surface contamination, and radioisotope concentration in air. For radioisotope concentration in air, detection limits are shown for five typical nuclides, ^{3}H and ^{14}C, ^{32}P, ^{125}I, and ^{35}S.

Table 2. Comparison of detection and regulation limits.

Measurement item	Radiation or Nuclides	Apparatuses installed	Detection limit	Detection limit/Legal limit	
				Work place	Controlled area
Radiation dose	Gamma ray	NaI(Tl) scintillation survey meters	0.1 μSv/h	4.00E-03	4.00E-02
	Neutron	Neutron survey meters	0.01 μSv/h	4.00E-04	4.00E-03
Radioisotope surface contamination	Arpha Others	Alpha/beta measuring system	0.04 Bq/cm^2 0.03 Bq/cm^2	0.01 7.50E-04	0.1 7.50E-03
Radioisotope concentration in air	^{3}H	Tritium and carbon air sampler and Liquid scintillation counting system	2.9E-5 Bq/ cm^3	5.80E-05	5.80E-04
	^{14}C		8.0E-6 Bq/cm^3	2.00E-04	2.00E-03
	^{3}H	Tritium gas monitor	1.1E-2 Bq/ cm^3	0.022	0.22
	^{32}P ^{35}S ^{125}I	Dust sampler and alpha/beta measuring system	3.8E-6 Bq/ cm^3 2.0E-6 Bq/ cm^3 2.5E-6Bq/ cm^3	5.43E-04 1.0JE-04 2.50E-03	5.43E-03 1.00E-03 2.50E-02

3.1. Radiation dose

For radiation monitoring in radiation workplaces, a NaI(Tl) scintillation survey meter and a neutron survey meter are used. Detection limits of the meters are 0.1 μSv/h and 0.01 μSv/h, respectively, as shown in Table 2. These detection limits can be compared to the legal limits shown in Table 1, the ratios are derived as 4.00E-03(1/250) and 4.00E-02(1/25) for gamma ray radiation and 4.00E-04(1/2500) and 4.00E-03(1/250) for neutron radiation in radiation workplace s and controlled areas. These results suggest that the radiation detection limits of these survey meters are sufficiently lower than those stipulated by law.

3.2. Surface contamination

Assuming the alpha/beta measuring system is regularly used to measure radioactive surface contamination with the smear method, the detection limits are 0.04 Bq/cm^2 for alpha-particle-emitting nuclides and 0.03 Bq/cm^2 for other nuclides. Comparing these detection limits to the legal limits for alpha-particle-emitting nuclides, the ratios are

derived as 0.01(1/100) and 0.1(1/10) for radiation workplaces and controlled areas. For other nuclides, the ratios are 7.50E-04(1/1000) and 7.50E-03(1/100) for radiation workplaces and controlled areas. The radiation limits of the smear method are sufficiently lower than the legal limits.

3.3. Radioisotope concentration in air

To measure the ^{3}H and ^{14}C concentrations in air, a tritium and a carbon air sampler and a liquid scintillation counting system are used. The detection limits of both nuclides are 2.9E-5 Bq/cm^3 and 8.0E-6 Bq/cm^3, respectively. The detection limits are smaller than the regulation limits, and the ratios are less than 5.80E-05(1/1000) and 5.80E-04(1/100) for radiation workplace s and controlled areas. If only tritium is measured, a tritium gas monitor can be used. The detection limit of the monitor is 1.1E-2 Bq/ cm^3. The ratios of the detection limits to the regulation limits are less than 0.022(1/45) and 0.22(1/4.5) for radiation workplace s and controlled areas.

For monitoring other nuclide concentrations in air, the dust sampler is used to collect dust in a filter. The filtrated dust containing radioisotopes can be measured using the alpha/beta measuring system. The detection limits of these measurements are 3.8E-6, 2.0E-6, and 2.5E-6 Bq/ cm^3 for the more commonly used nuclides ^{32}P, ^{125}I, and ^{35}S. The ratios of the detection limits to the regulation limits are less than 2.5E-03(1/400) and 2.5E-02 (1/40) for radiation workplace s and controlled areas.

The above results show that the on-site radiation monitoring cart conceptually designed using only commercially available radiation measurement systems performs well from the view point of radiation detection limits when used for monitoring radiation workplace s, including controlled areas.

4. Summary

An on-site radiation monitoring cart was developed by conceptually installing necessary apparatuses including a NaI(Tl) scintillation survey meter, neutron survey meter, alpha/beta measuring system, tritium and carbon air sampler, liquid scintillation counting system, dust sampler, and a tritium gas monitor. These apparatuses were all selected from those commercially available. The size of the cart was 635 mm × 800 mm × 1500 mm.

The performance of the cart was evaluated by inspecting its radiation detection limit. The ratios of the detection limits to the legal limits set by the Japanese radiation law were examined. As a result, the detection limit of the cart is, at worst, 1/100 and 1/10 smaller than the legal limits for radiation monitoring of radioisotope surface contamination, radioisotope concentration in air, and in radiation workplace s and controlled areas. The cart has sufficiently detected radiation in a radiation facility.

Reference

Kawano T. and Nishimura K. Conceptual Design of On-Site Monitoring Cart Available for Fusion Facility. 9th International Symposium on Fusion Nuclear Technology, October 11-16, 2009, P2-145, Dalian Chine, (2009)

A new AMS system for actinides isotopic ratio measurements at CIRCE (Caserta, Italy)

Sabbarese, Carlo[1]; Quinto, Francesca[1]; De Cesare, Mario[1]; Petraglia, Antonio[1]; Terrasi, Filippo[1]; D'Onofrio, Antonio[1]; Roca, Vincenzo[2]; Pugliese, Mariagabriella[2]; Palumbo, Giancarlo[2]; Alfieri, Severino[3]; Esposito, Alfonso[3]; Migliore, Gianluigi[3]

[1] CIRCE, Dept of Environmental Science – Second University of Naples, Caserta, ITALY

[2] Dept of Physics Science – University of Naples, Naples, ITALY

[3] SoGIN, Società di Gestione Impianti Nucleari, Sessa Aurunca (Caserta), ITALY

Abstract

Anthropogenic long-lived alfa-emitting radionuclides have been (and still are) released in the environment by nuclear testing, nuclear accidents, and operations of fuel reprocessing and plant decommissioning. Among these ^{239,240}Pu and ^{236}U are the most significant. The Accelerator Mass Spectrometry (AMS) technique surmounts the limitations of other techniques used.

In Italy no Nuclear Power Plant (NPP) is in operation, but the four dismissed NPPs are now being decommissioned; moreover, new generation of NPPs are reconsidered for future installations. Both the operations demand accurate investigations about the possible contamination by radioactive releases of nuclear sites and neighboring territory and of structural materials of the reactors. The monitoring activity requests ultrasensitive methodologies for the detection and quantification of ultralow activity radionuclides. Among radionuclides the alpha-emitting isotopes of actinide elements are the most critical also because of their toxicity. The radiation counting methods, due to the long half lives, do not provide the necessary sensitivity and, in some cases, resolution (e.g. ^{239}Pu-^{240}Pu).

The present contribution reports on the state of the art of a project, carried out at the AMS facility in the Center for Isotopic Research on Cultural and Environmental Heritage (CIRCE, Caserta, Italy), aiming to establish an ultrasensitive system for the measurement of concentrations and isotopic abundances of U and Pu, and to exploit this technique for the characterization, from the point of view of the contamination by U and Pu, of both environmental samples from the Garigliano NPP site and samples representative of the structural materials of the building and of the reactor of the same plant. At the same time the system provides a tool able to fulfill the analytical needs of IAEA for the campaigns for nuclear safeguards against illegal nuclear activities and the military use of weaponry with depleted uranium.

Introduction

Anthropogenic uranium and plutonium, and fission and activation products were widespread around the world due to human nuclear activities. Different sources of radionuclide contamination affect the environment on various scales of magnitude: plutonium from the atmospheric weapons test fallout is detectable globally in soils and sediments (Roca et al, 1989). In particular, the operation and decommissioning activities of a NPP could lead to airborne and liquid releases of radionuclides that would be mixed with contributions from larger and world scale sources. Useful tools to solve among different contributions are the isotopic ratios: $^{236}U/^{238}U$, $^{238}Pu/^{239+240}Pu$, $^{240}Pu/^{239}Pu$, $^{241}Pu/^{239}Pu$, $^{242}Pu/^{239}Pu$, given that the relative concentrations of plutonium and uranium isotopes depend on the nature of the source material and on its subsequent irradiation history. ^{239}Pu is produced from ^{238}U via neutron capture and subsequent beta decay of the resulting short-lived ^{239}U ($t_{1/2}$ = 23.47 min). In weapon-grade plutonium, ^{239}Pu is the most abundant isotope ($^{240}Pu/^{239}Pu < 0.07$). In weapon test fallout, $^{240}Pu/^{239}Pu$ varies, depending on the test parameters, in the range (0.10-0.35), the integrated ratio for the Northern hemisphere being about 0.18 (Koide et al., 1985); significantly different values (0.035-0.05) are found in Mururoa and Fangataufa atoll sediment, because of the peculiar nature of French testing (Chiappini et al., 1989).

In nuclear reactors, due to the different composition of fuels, uranium enrichment and burn-up degree, characteristic relative abundances of plutonium isotopes will be obtained: $^{240}Pu/^{239}Pu$ increases with irradiation time, which, in turn affects $^{238}Pu/^{239+240}Pu$. This ratio is useful to resolve between different sources in case they show similar $^{240}Pu/^{239}Pu$: e.g., irradiated nuclear fuel in a PWR with 7-20% ^{235}U and burn-up 1.4-3.9 GW·d reaches $^{240}Pu/^{239}Pu$ isotopic ratios of 0.13, a value, that could be ascribed also to global fall out; on the other side, these two sources show quite different $^{238}Pu/^{239+240}Pu$ activity ratio (0.025-0.04 for the global fallout and 0.45 for that nuclear fuel), (Buessler et al., 1995). Another valuable tool to identify a nuclear reactor origin of a radionuclide contamination is $^{236}U/^{238}U$ isotopic ratio. The dominant ^{236}U mode of formation is the capture of a thermal neutron by ^{235}U, a secondary contribution being the alpha decay of 240Pu; its concentration in nature has been heavily increased as a consequence of irradiation of enriched uranium in nuclear reactors. Several orders of magnitude of difference between the $^{236}U/^{238}U$ isotopic ratios in naturally-occurring uranium (10^{-9} to 10^{-14}) and in spent nuclear fuel (10^{-2} to 10^{-4}) imply that also a small contamination from irradiated nuclear fuel in natural sample is able to increase the $^{236}U/^{238}U$ measured in the whole sample. The measurement of U and Pu isotopic ratios requires the sensitivity of mass spectrometric techniques because ^{236}U and plutonium are present in environmental samples at ultra trace levels (^{236}U concentration is quoted to be in the order of pg/kg or fg/kg and ^{239}Pu around 100 pg/kg (Perelygin et al.,1997) and are long-lived radionuclides. To measure $^{236}U/^{238}U$ at natural level the unique able technique is the AMS, because of its capability to suppress background of isobaric molecules as it doesn't suffer of isobaric interferences from $^{235}UH^+$. The hydrides formation in ICPMS devices defines the detection limits of this technique for $^{236}U/^{238}U$ to 10^{-7}. Also, because of the interference from $^{238}UH^+$, the measurement of $^{239}Pu/^{240}Pu$ by ICPMS requires a higher decontamination of the plutonium fraction from uranium than AMS needs. However, no chemical procedure is efficient enough to separate uranium and plutonium fractions to allow the mass spectrometric measure of ^{238}Pu,

being the concentration of ^{238}U seven orders of magnitude higher than that of ^{238}Pu. Alpha-spectroscopy remains the only suitable technique for the measurement of ^{238}Pu concentration.

Material and methods

Sample preparation

The extraction of uranium and plutonium was performed following the procedures described in Kritil et al. (1979), applied to soil and sediment samples and adapted to our needs (Quinto et al., 2009). The samples were dried in a muffle furnace at 110°C, homogenized and combusted at 450 °C overnight. ^{236}Pu (30 mBq = $3.8x10^6$ atoms) and ^{232}U (86 mBq = $2.7x10^8$ atoms) were added as reference isotopes and also as radiotracers to determine the radiochemical yield of the extraction. The samples (2-12 g) were leached in 7.2 M HNO_3 and 0.5 g $NaNO_2$ for at least 3 h. The residue was centrifuged off and the supernatant was stored; fresh acid was added to complete the washing of the matrix. The combined leachates were brought to dryness and the residue was dissolved in 7.2 M HNO3. After adding of 0.2 g $NaNO_2$ the solution was heated until gas formation ceased and, after cooling, was loaded on an anion exchange column (6 ml Dowex 1x2, 100-200 µm particle size, previously conditioned with 7.2 M HNO_3). Plutonium present as Pu (IV) is retained on the resin. Uranium, mostly present as U (VI) is washed from the column with 45 ml of 7.2 M HNO_3. The original solution (now free of Pu) and the washing solutions were combined and kept for uranium determination. The column was washed with 30 ml of 32% HCl to remove thorium. Finally, plutonium was eluted with 50 ml of a mixture of 0.36 M HCl and 0.014 M HF into a teflon beaker containing already 5 ml 65% HNO_3. This solution was brought to dryness, then evaporated three times in 5 ml 65% HNO_3 with some drops of 30% H_2O_2 and another three times in 5 ml 37% HCl. The residue was dissolved in 6 ml fuming HCl, and subdivided in two halves for AMS measurement and alpha-spectrometry, respectively. The uranium fraction contained large amounts of iron. Therefore, the solution was evaporated to dryness and the residue dissolved in 20 ml 8 M HCl, from which iron was eliminated by diisipropylether liquid-liquid extraction. The iron free uranium fraction was evaporated to dryness, dissolved and evaporated twice in 50 ml 37% HCl, and finally dissolved in 80 ml 8M HCl. This solution was brought to a second anion exchange column (Dowex 1x2, 100-200 µm particle size, in 8 M HCl). Calcium and thorium were washed out with 50 ml 8 M HCl, then uranium was eluted with 90 ml 0.1 M HCl. The uranium solution was treated the same way as the plutonium solution; two subsamples for AMS and alpha-spectrometry were prepared. The chemical form of the AMS sample is $U+Fe_2O_3$ and $Pu+Fe_2O_3$, obtained by iron hydroxide co-precipitation and subsequent conversion to iron oxide by combustion at 700 °C. Uranium and plutonium fractions in iron oxide matrix were mixed with a similar volume of silver powder and pressed in aluminium sample holders suitable for the ion source of accelerator system. For alpha-spectrometry, plutonium and uranium fractions where co-precipitated with NdF_3 (Hindman, 1983) and deposited on membrane filters suitable for alpha-spectroscopy (Quinto et al., 2009).

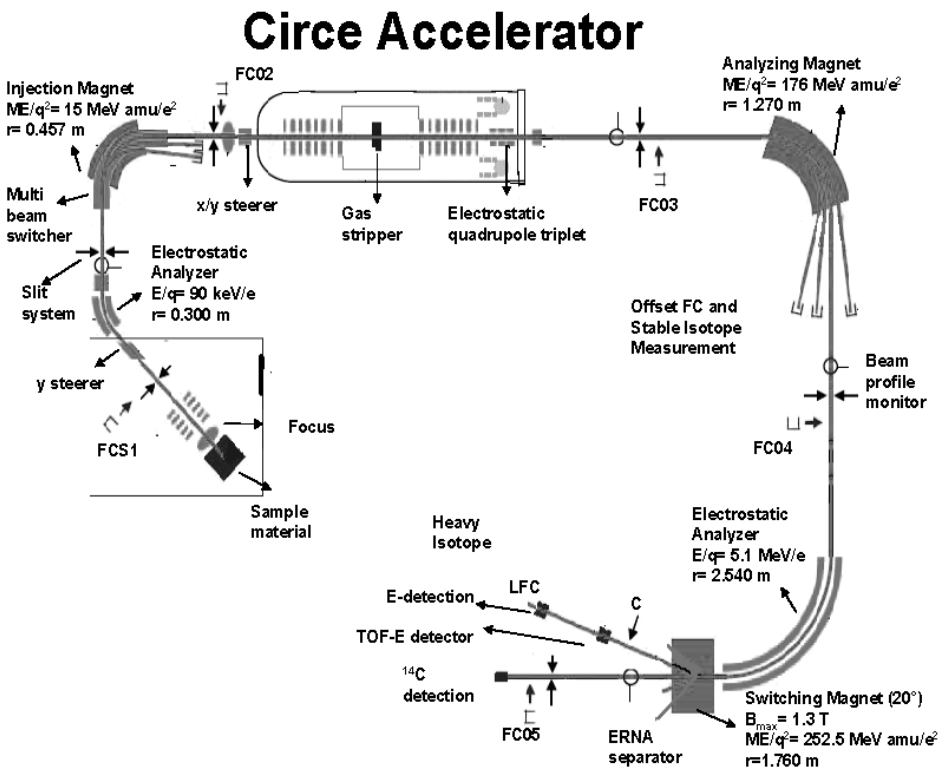

Fig. 1. The scheme of the +3 MV tandem accelerator of Pelletron type installed at the CIRCE.

The AMS measurement

The +3 MV CIRCE tandem accelerator of Pelletron type (Terrasi et al. 2008), similar to others installed in the past years in Europe and USA, is shown in Fig.1. Since the installation of CIRCE in 2005, we have extended the measuring capabilities of the original system with the installation of a switching magnet and a heavy isotope beamline (De Cesare et al., 2009; De Cesare et al., 2010).

The caesium sputter ion source is a 40-sample MC-SNICS. A typical output from 1 mm diameter samples pressed in Al cathodes for $^{12}C^-$ ions is 30 μA at 6 kV cathode voltage and a total injection energy of 67 keV and 0.3 μA for $^{238}U^{16}O^-$ molecules with a total injection energy of 50 keV. These ions are energy selected by a ±45° spherical electrostatic analyzer (r = 30 cm, plate gap = 5 cm) that is operated up to ±15 kV. Maximum electric field strength is 6 kV/cm, resulting in an energy/charge state ratio of 90 keV. The 90° double focusing Low Energy (LE) injection magnet (r = 0.457 m, vacuum gap= 48 mm, ME/q^2 = 15 MeV· amu) allows high resolution mass analysis for all stable isotopes in the periodic table. The insulated stainless steel chamber can be biased up to 15 kV for beam sequencing (e.g. between ^{12}C, ^{13}C, ^{14}C or between $^{238}U^{16}O$, $^{236}U^{16}O^-$).

The accelerator is contained inside a vessel filled with sulphur hexafluoride (SF6) at a pressure of about 86 psig. The terminal voltage (TV) is achieved and stabilized by GVM feedback on the charging system high voltage supply. The TV can be kept constant at 3.000 MV with a ripple of 1 kV. In the stripper, Argon (Ar) is recirculated by two turbo-pumps; the working pressure is about ~13 mTorr for $^{14}C^{3+}$ at 2.550 MV and ~7.3 mTorr for $^{238}U^{5+}$ at 2.875 MV, with an offset of ~6 mTorr

The double focusing 90° High Energy (HE) bending magnet has r= 1.27 m, ME/q^2 = 176 MeV.amu and $M/\Delta M$ = 725, with slit opening of ±1 mm both at object and image points, so that, e.g. $^{236}U^{5+}$ at 3 MV can be analyzed. The two 45° electrostatic spherical analyzers (r= 2.54 m and gap = 3 cm) are operated up to ±60 kV; energy resolution is $E/\Delta E$ = 700 for typical beam size.

Finally the selected ions are counted in a surface barrier detector.

In order to assess laboratory background for ^{236}U measurements, diluted samples of Joachimsthal uranium (0, 4, 40, 400 and ~104 μg) were prepared for each run. We used the U^{5+} current as an estimate of the uranium content. The effect of a mass-dependent background correction is almost negligible. The ^{236}U count rate, calibrated by the dilution series, was used to estimate the ^{236}U concentration. Results of such measurement are reported in Quinto et al. 2009.

In order to assess the accuracy of the $^{240}Pu/^{239}Pu$ isotopic ratio measurement, a Reference Material, IAEA 368 (sediment sample collected in the Pacific Ocean at Mururoa Atoll, a former French nuclear weapons testing site), was measured in three runs. Each measure of $^{240}Pu/^{239}Pu$ isotopic ratio was in agreement with the certified interval of values (0.035 to 0.05).

Results and discussion

Measurements have been performed with a position sensitive silicon detector with an active area of 58×58 mm², positioned 1.9 m downstream the 4 mm diameter collimator, positioned in turn 80 cm from the switching magnet. To measure the $^{236}U/^{238}U$ ratio a tuning of the transport elements up to the final detector is performed in order to maximize the ion optical transmission. The ^{236}U events are counted in the final detector and ^{238}U current is measured in FC04.

The tuning is made by setting the parameters of the beam line of the ^{238}U current to the Last Faraday Cup (LFC) positioned in front of the detector, using as target material uranium oxide (U_3O_8) obtained from Uranyl Nitrate ($UO_2(NO_3)_2 \cdot 6\ H_2O$) baked at 800°. This material originated from the uranium mines "K. k. Uranfabric Joachimisthal", and is the VERA (Vienna Environmental Research Accelerator) in-house U standard. In our case, the sample preparation provides uranium in form of $UxOy+Fe_2O_3$ from which xUyO- is sputtered. To select different injected masses the injection magnet bouncing system is used. The stripping yield for $^{238}U^{5+}$achieved by the Ar gas stripper of CIRCE is around 3.1%. At 3 MV terminal voltage, ME/q^2 is ~ 170 $MeV{\cdot}amu/e^2$ for $^{238}U^{5+}$ and ME/q^2 is ~ 221 $MeV{\cdot}amu/e^2$ for $^{238}U^{4+}$; since the double focusing HE magnet reaches a maximal ME/q^2= 176 MeV·amu, the 5+ represents the lowest charge state which can be bent by the HE magnet. For heavy ion measurements, the object and image slits of the injection magnet are closed to ±1 mm, the slits of the HE magnet are closed to ±2 mm and a collimator of 4 mm diameter is positioned just at the waist of the ESA. The current transmission between FCO4 and LFC is ~ 80 %. Once the setup for the pilot beam $^{238}U^{5+}$ is found, the voltage at the chamber of the injection magnet, the terminal voltage and the voltage of the analyzer ESA are scaled to the other wanted mass ($^{236}U^{5+}$).

The preliminary measurements for the isotopic ratio $^{236}U/^{238}U$ were performed by cycling between ^{238}U, which is measured by means of the current in the Faraday cup just after the HE magnet FC04, and ^{236}U, that is measured in the final 16-strips surface

barrier detector. We measured 2 samples: one with a nominal ratio $^{236}U/^{238}U \sim 10^{-8}$, obtained by adding a spike of ^{236}U to the KkU VERA in-house U standard, and the KkU itself with $^{236}U/^{238}U = (6.98 \pm 0.32) \times 10^{-11}$ (Steier et al. 2008). Also, samples with a "chemistry blank" have been prepared by the same treatment as the others. The contribution of the latter is of the order of 1 % of the KkU sample signal. Moreover, comparison with the spatial distribution obtained when the collimator was removed shows that interference from ions of higher magnetic rigidity with respect to $^{236}U^{5+}$ are largely suppressed by the 4 mm collimator; one can estimate that the residual interference background below the $^{236}U^{5+}$ peak, obtained as relative difference between the sum of the 4 central strips of the KkU (4mm C. out) and KkU (4mm C. in), is less than 80 % of the total, which is in turn the interference measured without the collimator. That indicates that "interference + chemistry" background in our $^{236}U/^{238}U$ measurements is $< 5 \times 10^{-11}$. This value has to be compared with previous result (3×10^{-9}, De Cesare et al 2009) obtained at 0°, before the installation of the switching magnet. De Cesare et al., (2009) have obtained a lower limit of $(9 \pm 1) \times 10^{-9}$ for the spike sample isotopic ratio, in agreement with the expected value. These results imply that with a background $< 5 \times 10^{-11}$, we are able to measure samples with an isotopic ratio value $\geq 10^{-10}$, without the use of an Energy Time Of Fligth system (TOF-E). In order to obtain the best $^{236}U/^{238}U$ isotopic ratio sensitivity of 10^{-12} (Steier et al., 2004), in samples including about 1 mg of U, a TOF-E system will be included. An upgraded of the CIRCE facility has been planned including the TOF-E system, with a flight path of 1.5 m, aiming to reach the necessary $^{236}U/^{238}U$ isotopic ratio sensitivity.

Further investigations are needed to identify the amount of ^{238}U that is under the peak of $^{236}U^{5+}$ and the amount of ^{235}U, that is also present. A Time of Flight–Energy (TOF-E) detection system (De Cesare et al. 2007; De Cesare et al. 2009) will be used, to discriminate between ^{236}U, ^{238}U and ^{235}U, with the start signal for the TOF measurement given by a MCP (MicroChannel Plate), in electrostatic mirror configuration, positioned about 70 cm from the 4 mm collimator. The energy information is given by the 16-strips silicon detector, which also provides the timing for the stop signal.

As an example of application to investigate the possible contamination of Garigliano Nuclear Power Plant (Caserta, Italy) activities, some soil samples were collected for the measurement of actinides in the neighbour of the plant. The values of activity and isotope ratios in environmental samples measured with AMS allow to identify the origin of the activity, due to the sensitivity of the technique used. The isotope ratio of $^{236}U/^{238}U$ and the specific activity of ^{236}U and ^{239}Pu in soils is shown in Figure 2, where are also reported the results of ^{137}Cs specific activity obtained from gamma spectrometry measurements.

It is evident a correlation between the specific activities of the three radionuclides, indicating a possible common origin. The isotope ratio values ranging between $4.5\ 10^{-10}$ and $1.3\ 10^{-8}$. These values are compatible with the value measured in a control sample

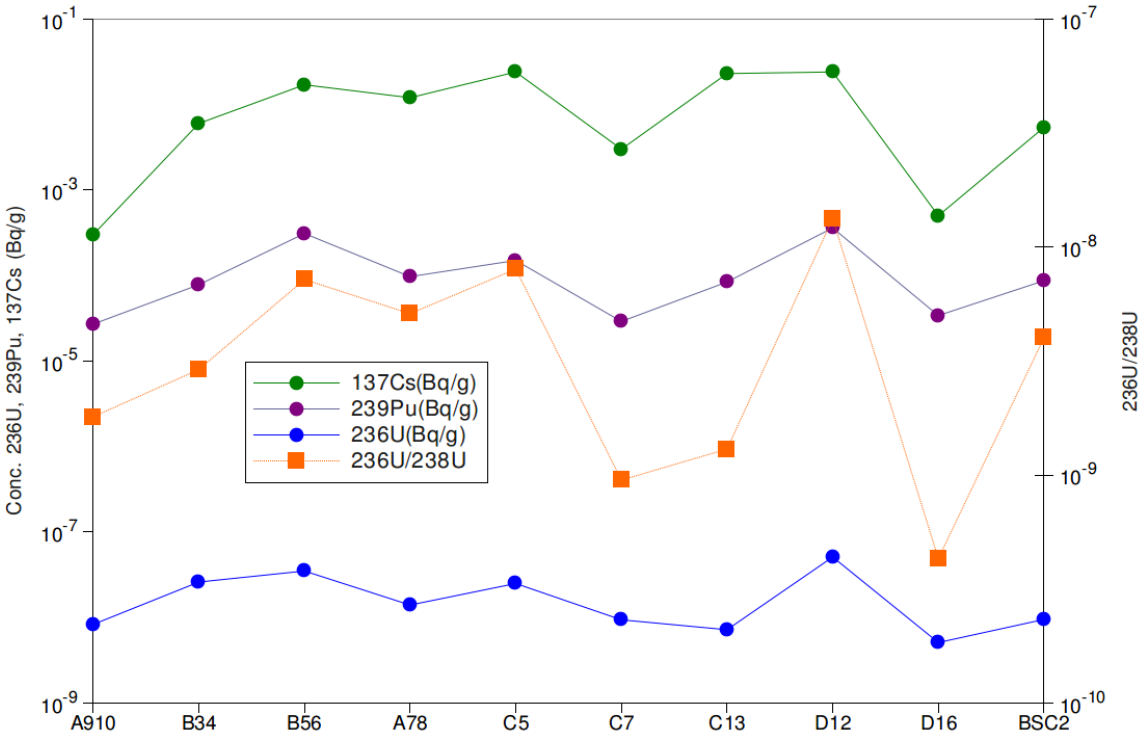

Figure 2. Results of ^{236}U, ^{239}Pu and ^{137}Cs specific activities and of $^{236}U/^{238}U$ ratio obtained on soil samples collected around the Garigliano Nuclear Power Plant (Caserta, Italy).

collected in the Sele plain (BSC2 sample), about 100 km far from the Garigliano NPP. Moreover, these values are consistent with values of global fallout [Sakaguchi et al., 2009] and are significantly lower than those measured in contaminated sites [Boulyga & Heumann, 2006]. Measurements of samples representative of the structural materials of the building and of the reactor of the same plant are also measured, but data not still available.

Conclusions

In this work an overview of the upgraded CIRCE facility for actinides measurements has been described in order to reach the necessary $^{236}U/^{238}U$ isotopic ratio sensitivity. The results of CIRCE laboratory are not far from those of ANU e VERA laboratories, but improvements are planning. Applications of method are carried out on soil sample to investigate possible contamination due to a NPP activities.

This system provides a tool able to fulfill the analytical needs of IAEA for the campaigns for nuclear safeguards against illegal nuclear activities and the military use of weaponry with depleted uranium.

References

S.F. Boulyga, K.G. Heumann, Journal of Environmental Radioactivity, 88, (2006),1-10.
K.O. Buessler, E.R. Sholkowitz, Geochim. Cosmochim. Acta, 51, (1987), 2623-2637; T.M. Beasley, J.M. Kelley, T.C. Maiti, L.A. Bond, Environ. Radioactivity, 38, (1997), 133-142; Y. Sivintsev, Report IAEA-IASAP-5, (1995); ANWAP, (1995).

R. Chiappini, F. Pointurier, JC. Millies-Lacroix, G. Lepetit, P. Hemet, Sci. Total Environ., 237-238, (1999), 269-276.

M. De Cesare, Y. Guan, N. De Cesare, A. D'Onofrio, L. Gialanella, A. Petraglia, F. Quinto, V. Roca, Sabbarese C., F. Terrasi (2009). Actinides measurements using 16-strip silicon detector at CIRCE (Caserta, Italy). Radiocarbon, ISSN: 0033-8222.

M. De Cesare, A. Petraglia, N. De Cesare, A. D'Onofrio, L. Gialanella, Y. Guan, F. Quinto, V. Roca, D. Rogalla, Sabbarese C., F. Terrasi (2010). Actinides AMS at CIRCE in Caserta (Italy). Nuclear Instruments & Methods in Physics Research. Section B, Beam Interactions with Materials and Atoms, vol. B268; p. 779-786, ISSN: 0168-583X.

F.D. Hindman, Anal.Chem. 55 (983) 2460-2461.

M. Koide, K.K. Bertine, T.J. Chow, E.D. Goldberg, Earth Planet. Sci. Lett., 1, (1985), 72.

J. Kritil, J. Mencel, A. Moravec, J. Radioanal.Nucl.Chem.Lett. 21 (1975) 115-120;

V.P. Perelygin and Yu.T. Chuburkov, Radiat. Meas., 28, 385, (1997)

F. Quinto, P. Steier, G. Wallner, A. Wallner, M. Srncik, M. Bichler, W. Kutschera, F. Terrasi, A. Petraglia, Sabbarese C. (2009). The first use of 236U in the general environment and near a shut down Nuclear Power Plant. Applied Radiation and Isotopes, ISSN: 0969-8043.V. Roca, M. Napolitano, P.R. Speranza, G. Gialanella, Journal of Environmental Radioactivity, 9, 2, (1989), 117-129.

A. Sakaguchi, K. Kawai, P. Steier, F. Quinto, K. Mino, J. Tomita, M. Hoshi, N. whitehead, M. Yamamoto, (2009). First results on 236U levels in global fallout. Sci. Tot. Env. 407.

P. Steier, R. Golser, W. Kutschera, V. Liechtenstein, A. Priller, A. Valenta, C. Vockenhuber, NIMB, 223-224, (2004), 67-71.

Terrasi F, A. D'Onofrio, N. De Cesare, C. Lubritto, Sabbarese C., D. Rogalla, F. Marzaioli, I. Passariello, M. Rubino, G. Casa, A. Palmieri, L, Gialanella, G. Imbriani, V. Roca, M. Romano, M. Sundquist, R. Loger (2008). High precision 14C AMS at CIRCE. Nuclear Instruments & Methods in Physics Research. Section B, Beam Interactions with Materials and Atoms, 266; 2221-2224, ISSN: 0168-583X

Neural network method for activity measuring in environmental samples

Finkel Felix[1]; Bystrov Eugeny[2]
[1] Russian Mendeleyev Research Institute for Metrology, RUSSIAN FEDERATION
[2] Atomtex, BELARUS

Neural network method for activity measuring in environmental samples. Theses.

The spectrometric method is one of the most popular methods for activity measuring in environmental samples. It provides application of semi-conductor and scintillation spectrometers. Despite high measurement accuracy, high price and some difficulties in operation make semi-conductor detectors difficult to apply. Scintillation spectrometers, which are cheaper, are applied to determine activity of natural radionuclides. But continuous spectrum image on the monitor permits the spectrometers to measure not so many radionuclides and, thus, it restricts application of the scintillation spectrometers.

One of the ways to solve the problem is to use sophisticated mathematical analysis of decomposition of scintillation spectra. Examination of different spectrum analyses and devices, produced by means of these methods, reveals that sometimes the above solution is quite improper and has weak solution stability. Besides, some problems appear while applying these methods in field devices, which are to carry out scale analysis without a computer. As a result, simplified methods are applied, which reduce accuracy of activity determination.

The current article describes the method of decomposition of scintillation spectra into spectrum components by means of artificial neural networks. The aim of the above method is to determine activity of radionuclides in the source under measurement according to its radiation spectrum. The spectrum is acquired by means of scintillation spectrometer. If applying a laboratory spectrometer, which, as a rule, is equipped with a computer, the spectrum is transferred from the ADC to the PC, which operates with the above method. If applying field spectrometers, spectrum is to be processed by either a smart sensor or operating control unit. Activity calculation algorithm is equal in both cases.

Introduction

Nowadays industry often has bad unwholesome influence on the environment and a human being. That is why environmental friendliness is one of the quality factors of production. It causes constant development of special equipment and methods for environmental monitoring. Radioactivity stands out from other quality factors to be controlled. High radiation contamination risks, on the one hand, and strict safety regulations, on the other hand, draw special attention to metrological parameters of modern equipment of radiation monitoring.

The spectrometric method is one of the most popular methods for activity measuring in environmental samples. It provides application of semi-conductor and scintillation spectrometers. Despite high measurement accuracy, high price and some difficulties in operation make semi-conductor detectors difficult to apply. Scintillation spectrometers, which are cheaper, are applied to determine activity of natural radionuclides. But continuous spectrum image on the monitor permits the spectrometers to measure not so many radionuclides and, thus, it restricts application of the scintillation spectrometers.

One of the ways to solve the problem is to use sophisticated mathematical analysis of decomposition of scintillation spectra. Examination of different spectrum analyses and devices, produced by means of these methods, reveals that sometimes the above solution is quite improper and has weak solution stability. Besides, some problems appear while applying these methods in field devices, which are to carry out scale analysis without a computer. As a result, simplified methods are applied, which reduce accuracy of activity determination.

The current article describes the method of decomposition of scintillation spectra into spectrum components by means of artificial neural networks. The aim of the above method is to determine activity of radionuclides in the source under measurement according to its radiation spectrum. The spectrum is acquired by means of scintillation spectrometer. If applying a laboratory spectrometer, which, as a rule, is equipped with a computer, the spectrum is transferred from the ADC to the PC, which operates with the above method. If applying field spectrometers, spectrum is to be processed by either a smart sensor or operating control unit. Activity calculation algorithm is equal in both cases.

Activity calculation of radionuclides

Since the spectrometric method under discussion is relative, calibration of the equipment is required. According to the neural network theory such calibration is called learning.

The step-by-step algorithm of activity calculation follows. Learning (calibration) is described in part 3 of the current article.

First of all, we describe input data. We have a spectrum of a working source N collected by means of a spectrometer. The source (sample) is measured in the preset geometry with the certain density $\rho_{и}$ and life time. We have also a background spectrum $N_{ф}$ measured under the same conditions. Background is usually measured by means of a spectrometer either with an empty shielding chamber or with an empty sample dish in the chamber.

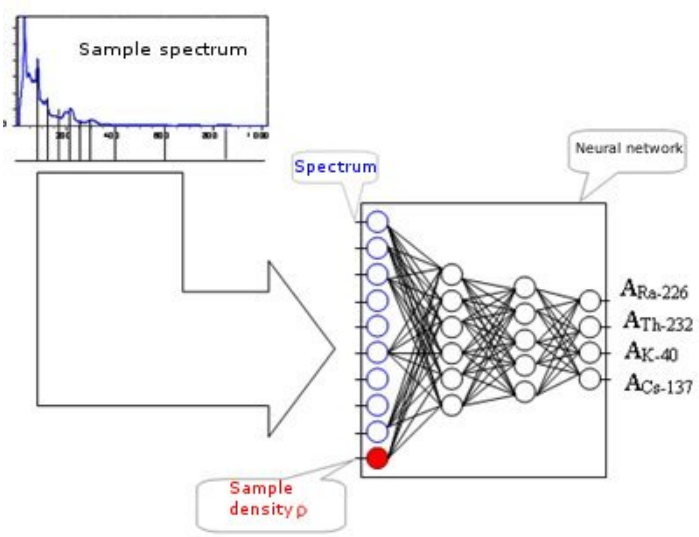

Pic.1. Diagram of activity measurement in samples by means the neural network method.

To reduce the spectrum to the energy scale, we should know energy calibration. Modern spectrometers provide the relation between a spectrum channel No. and energy, which are linearly dependent as follows:

$$E_i = E_0 + k \cdot i \quad (1)$$

where E_i – energy corresponding to the *i*-channel, keV; E_0, k – coefficients of energy calibration fixed during the device setting.

Data gained in the course of learning (calibration) is weights of neural network W, scales of each network input M_{in} and output M_{out} and energy windows where summing up R_E is carried out.

During calibration network parameters should be set up, including the number of layers and neurons in each layer and a type of activation function with parameters. The number of network inputs depends on the number of selected windows, plus one input for density. The number of network outputs corresponds to the number of radionuclides under detection.

First of all, we prepare input data for network calculation.

In the spectrum channels we define corresponding windows for each specified energy window. According to Eq.1:

$$R_{Lj} = \frac{R_{ELj} - E_0}{k}, \quad j=1..n \quad (2)$$

where R_{Lj} – channel No. in the spectrum of the left edge of the *j*-window; R_{ELj} – energy of the left edge of the *j*-window, keV; n – number of windows.

The similar equation is used for the right edge:

$$R_{Rj} = \frac{R_{ERj} - E_0}{k}, \quad j=1..n \quad (3)$$

where R_{Rj} – channel No. in the spectrum of the right edge of a *j*-window; R_{ERj} – energy of the right edge of a *j*-window, keV.

We define total counting rate in the specified windows for the source working spectrum and background spectrum:

$$S_j = \frac{1}{t} \cdot \sum_{i=R_{Lj}}^{R_{Rj}} N_i \quad , \text{ j=1..n} \tag{4}$$

$$S_{\phi j} = \frac{1}{t_\phi} \cdot \sum_{i=R_{Lj}}^{R_{Rj}} N_{\phi i} \quad , \text{ j=1..n} \tag{5}$$

where S_j and $S_{\phi j}$ – counting rates in the j-window of working and background spectra correspondingly, imp/sec; t и t_ϕ – real measurement time of working and background spectra correspondingly, sec. [1, 4].

Now we define input values of the neural network as follows:

$$X_j = \frac{S_j - S_{\phi j}}{M_{in\,j}} \quad , \text{ j=1..n} \tag{6}$$

where X_j – value of the j-output of the neural network; $M_{in\,j}$ – scale value for the j-output. Eq. 6 reveals that the value X_j can vary from 0 to 1, which is caused by principles and architecture of neural network.

The number of network inputs m=n+1, with another special input for density, is defined as follows:

$$X_m = \frac{\rho_u}{M_{in\,m}} \tag{7}$$

where $\rho_и$ – density of the sample under measurement, g/cm^3; $M_{in\ m}$ - scale for density input, g/cm^3.

Input data is gathered now and should be put in calculation of the neural network. Network calculation means definition of states and outputs of neurons within inner layers and the last output layer [2]. These are outputs of the last layer, which are desired unscaled activities of radionuclides. One should remember that the number of outputs is not fixed and defined according to research tasks. It means that if activity of a certain radionuclide is to be determined in the sample with a radionuclide mixture, the network can have one output corresponding to a specified radionuclide. In this case network learning is carried out by means of spectra of unmeasured radionuclides.

Network calculation is made in a layer-by-layer manner. Calculation of neuron states for the first layer is not necessary, since their outputs, or network inputs, are known. Thus, neuron states for the second layer are calculated as follows:

$$C_j^{II} = \sum_{i=1}^{P_1} X_i \cdot W_{1,i,j} \quad , \text{ j=1..P}_2 \tag{8}$$

where P_1 - number of neurons in the first layer, similar to the number of network outputs; P_2 – number of neurons in the second layer; $W_{1,i,j}$ – weight between the i-neuron of the first layer and j-neuron of the second layer, the index *l* depicts a layer, which has a link output (the first layer for Eq. 8).

Neuron output is regarded as the function of its state:

$$y_j^{II} = f(C_j^{II}) \text{ , j=1..P}_2 \quad (9)$$

where y_j^{II} - output of the j-neuron in the second layer; f – activation function, defined as:

$$f(c) = \frac{1}{1+\exp(-\alpha \cdot c)} \quad (10)$$

where c – argument of the function or, in this case, neuron state; α – coefficient, which determines the slope of the function graph (Pic.2). The coefficient α is determined in the course of calibration and can vary from 0.5 to 3.

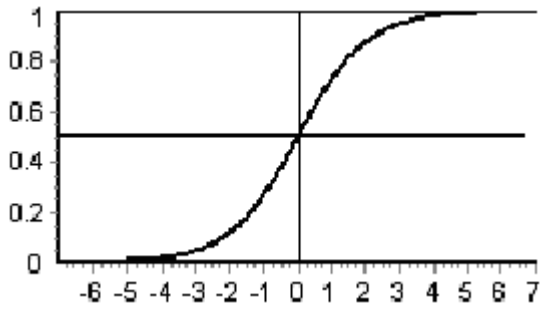

Pic. 2. Sigmoid activation function [3].

Despite vast variety of activation functions, the research revealed that the above type of the activation function provides particularly successful and accurate calculation.

Neuron states for the third layer are calculated as follows:

$$C_j^{III} = \sum_{i=1}^{P_2} y_i^{II} \cdot W_{2,i,j} \text{ , j=1..P}_3 \quad (11)$$

As shown by Eq. 11, the network inputs are replaced by the outputs of the second layer. Thus, we have got the following equation, similar to Eq. 9:

$$y_j^{III} = f(C_j^{III}) \text{ , j=1..P}_3 \quad (12)$$

where y_j^{III} - output of the j-neuron in the third layer.

The network for the rest of layers, including the output layer [2, 3], is calculated on the same principle as illustrated above. In this case, the output layer is described as follows:

$$C_j^Z = \sum_{i=1}^{P_{Z-1}} y_i^{Z-1} \cdot W_{Z-1,i,j} \quad (13)$$

$$y_j^Z = f(C_j^Z) \text{ , j=1..P}_Z \quad (14)$$

where y_j^Z - output of the j-neuron in the last layer; Z – number of layers in the network.

To turn directly to calculation of radionuclides activities, output scales determined during the calibration should be used.

$$A_j = (y_j^Z - k_{кр}) \cdot (\frac{M_{out\,j}}{k_{ум}}) \quad , \; j=1..P_Z \tag{15}$$

where A_j – activity of the j-neuron in order, Bq; $M_{out\,j}$ - scale for j-output of the network; $k_{кр}$ –boundary coefficient, which enables not to use the non-linear range of a sigmoid function and is defined as 0.1; $k_{ум}$ – coefficient introduced to correct a scale disturbed by the boundary coefficient. More detailed description of the above coefficients follows.

Calibration (learning)

To train the neural network, calibration spectra are required, which should be spectra of separate radionuclides measured in calibration samples with different densities (Pic.3).

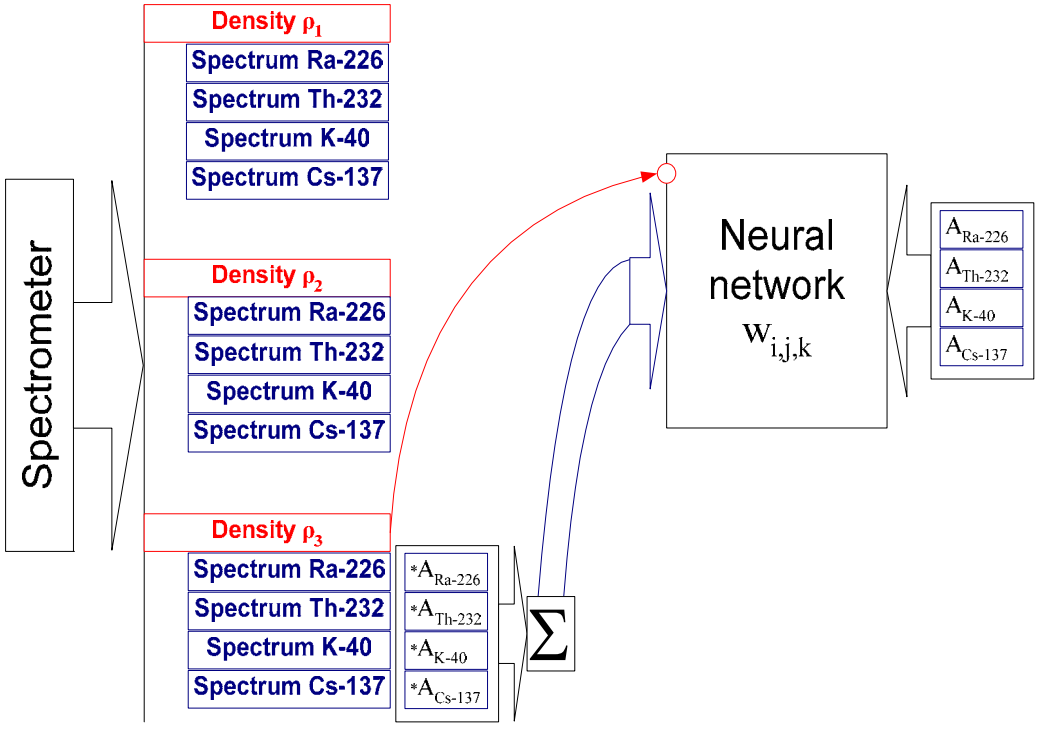

Pic. 3. Example of choosing calibration spectra for learning.

These available calibration spectra should be included into the learning sample, where each component is a spectrum with different radionuclide content and density. To get such spectra, the additivity concept of simple spectra of radionuclides is to be applied. Thus, the equation for a sample spectrum with activities A_j, where j=1..n (n – number of nuclides in a source) will be the following:

$$Q_i = Q_{\phi i} + \sum_{j=1}^{n} q_{ij} \cdot A_j \ , \quad \text{i=1..v} \tag{16}$$

where Q_i – counting rate in the i-channel of the mixed spectrum of the sample, imp/sec; $Q_{\phi i}$ – counting rate in the i-channel of the background spectrum, imp/sec; q_{ij} – counting rate in the i-channel for the simple spectrum of the corresponding j-radionuclide, imp; v- number of channels in a spectrum. Eq. 16 can be applied provided that energy calibration of both simple spectra and the background spectrum is similar. If the above condition is not met, the value of energy calibration is to be made equal for all the spectra by means of Eq. 1. Besides, one should take into account that simple spectra *q* are collected for samples with one and the same density.

Simple spectra *q* are calculated as follows:

$$q_{ij} = \frac{\frac{N_i}{t} - \frac{N_{\phi i}}{t_\phi}}{A_j} \ , \quad \text{i=1..v, j=1..n} \tag{17}$$

where N_i– counting in the i-channel in the real j-radionuclide spectrum, imp; $N_{\phi i}$– counting in the i-channel in the background spectrum, imp; A_j – sample activity of the j-radionuclide, Bq; t and t_ϕ – life time for measuring source spectra and background spectra correspondingly, sec [4].

As shown by Eq. 15, while changing the value A_j we can acquire the required spectrum Q for a non-existent sample with the density similar to that one, for which simple spectra q were collected. Thus, Eq. 15 can be put down as follows:

$$Q_i^k = Q_{\phi i} + \sum_{j=1}^{n} q_{ij}^k \cdot A_j^k \ , \quad \text{i=1..v , k=1..r} \tag{18}$$

where r – number of densities; k – density No. in order.

Thus, Eq. 17 is the main one for making both learning and testing samples. The variable k, i.e. density, and variables A_j are subject to variation, or the so-called randomization. And this is the acquired spectrum Q, which is the learning element. There can be as many similar elements as possible. It means that the more information the neural network learns, the more accurate and precise results are achieved.

Now we describe the learning algorithm in details. We have simulated spectra of radionuclide mixtures Q and the activity vector A_B corresponding to each of the spectra. Thus, according to the algorithm described in part 2 of the current article, initialization of the matrix weights W should be carried out by means random variables from 1 to 0.3 [2]. Then, we put different spectra from the learning sample Q in random order to the network input, calculate forward the network by means of Eqs. 1 – 15 and, as a result, get the simulated vector of radionuclide activity A_M. In this case we have already got activity vector A_B from the learning sample for the spectrum Q.

The matrix weights are corrected in the opposite way to the network distribution. Thus, an auxiliary j-variable can be illustrated as follows:

$$g_j^Z = y_j^Z \cdot (1 - y_j^Z) \cdot (y_j^Z - y_{Bj}) \quad , \ \text{j=1..P}_Z \tag{19}$$

where y_j^Z - j-neuron output of the last layer; Z – number of network layers; $y_{B\,j}$ - target value of the j-output, calculated according to the following:

$$y_{B\,j} = \frac{A_{B\,j}}{M_{out\,j}}\ ,\ \text{j=1..P}_\text{Z} \tag{20}$$

where $M_{out\,j}$ - scale for j-output of the network.

Now we calculate the coefficient of weight correction:

$$\Delta W_{Z-1,i,j}^T = -\eta \cdot g_j^Z \cdot y_i^{Z-1} + \mu \cdot \Delta W_{Z-1,i,j}^{T-1}\ ,\quad \text{i=1..P}_{\text{Z-1}}\ ,\text{j=1..P}_\text{Z} \tag{21}$$

where T- number of learning iteration, if T=1 (i.e. at the beginning of learning) variables $\Delta W_{Z-1,i,j}^{T-1}$ are equal to 0; η – parameter, which determines learning rate, can vary from 0 to 1; μ – learning coefficient (Part 2) can vary from 0 to 1. The minus sign "-" in front of the first component of Eq.21 is caused by the fact that the weight changes in the opposite way to that one indicated by the derivative of error surface.

Weight correction is carried out according to the following equation:

$$W_{Z-1,i,j}^T = W_{Z-1,i,j}^{T-1} + \Delta W_{Z-1,i,j}^T\ ,\quad \text{i=1..P}_{\text{Z-1}}\ \text{j=1..P}_\text{Z} \tag{22}$$

The above weight correction (Eqs. 19 – 22) is carried out in the opposite way to the network distribution for each pair of layers. This approach is called "backward error distribution".

For the next pair of inner (hidden) layers (***not for the last and next to last ones***) weights change in the following way:

$$g_j^{Z-1} = y_j^{Z-1} \cdot (1 - y_j^{Z-1}) \cdot \delta_j\ ,\ \text{j=1..P}_{\text{Z-1}} \tag{23}$$

where

$$\delta_j = \sum_{k=1}^{P_Z} g_k^Z \cdot W_{Z-1,j,k}^T \tag{24}$$

Eq. 23 differs from Eq. 19 on the error of a hidden layer δ_j, which does not correspond directly to target output values. That is why weight correction of the hidden layer is proportional to its "contribution" to the error of the next layer.

Then, weight correction is carried out in a similar way to Eqs. 21 and 22:

$$\Delta W_{Z-2,i,j}^T = -\eta \cdot g_j^{Z-1} \cdot y_i^{Z-2} + \mu \cdot \Delta W_{Z-2,i,j}^{T-1}\ ,\ \text{i=1..P}_{\text{Z-2}}\ ,\text{j=1..P}_{\text{Z-1}} \tag{25}$$

$$W_{Z-2,i,j}^T = W_{Z-2,i,j}^{T-1} + \Delta W_{Z-2,i,j}^T\ ,\quad \text{i=1..P}_{\text{Z-2}}\ \text{j=1..P}_{\text{Z-1}} \tag{26}$$

As far as next layers are concerned, weights are transformed according to Eqs. 23 – 26 if correction is carried out from the end of the network to its beginning [2, 3].

After correction completion, another spectrum Q with a density parameter is put into the input the network to start learning. The network is calculated forward and the

results are compared with target values of the vector y_{B_j} specified by the spectrum Q.

Then, learning is carried out in the opposite way. There can be as many learning iterates as possible (about $5 \cdot 10^6$). It stands to reason that only a computer can calculate the above. The higher capacity computers have, the greater interest to artificial neural networks is aroused in different spheres of physics.

References

1. Vartanov, N. & Samoylov, P. (1975). Applied scintillation gamma spectrometry.
2. Kalan, R. (2003). Main concepts of neural networks.
3. Osovski, S. (2004). Neural networks for information processing.
4. Pegoev, A. (1980). Data processing methods in applied gamma spectrometry.

Whole body counting with large plastic scintillators as a tool in emergency preparedness – determination of total efficiency and energy resolution

Nilsson, Jenny; Isaksson, Mats
Department of Radiation Physics, Institute of Clinical Sciences, The Sahlgrenska Academy, University of Gothenburg, SU/Sahlgrenska, 413 45 Gothenburg, SWEDEN

Abstract
The measured total efficiencies for large plastic scintillators (NE 102 A), 91.5 × 76.0 × 24.5 cm^3, has been compared with Monte Carlo calculated total efficiencies. For ^{54}Mn the results show a good agreement except close to detector edges. To investigate light losses the Monte Carlo calculated deposited energy spectrum was converted into emitted light spectrum. The amount of emitted light was then changed depending on where the energy was deposited in the scintillation material. The emitted light per unit energy was calculated with Birks formula, with *kB* set to 9.65 mg cm^{-2} MeV^{-1}. Even for small light losses the emitted light spectrum resolution was affected.

Introduction and Theory
Increased demands on emergency preparedness have lead to a renewed interest in whole body counting. It is hard to know beforehand the energy and source distributions that will be of interest in a situation and a fast and accurate calibration method is therefore sought after. One possible solution is to do a Monte Carlo calibration of the whole body counter, WBC, system.

The University of Gothenburg has a low-activity laboratory equipped with two WBCs, one with four large plastic scintillators (NE 102A) and one with two large NaI(Tl)-detectors. The ambition is to do a Monte Carlo calibration for both systems, and presented in this work are the preliminary results for the plastic scintillator system.

To verify the WBC model, calculated total efficiencies for several nuclides were compared with measured. This was a relatively straight forward work; a much more demanding task is to obtain a calculated energy deposition spectrum whose energy resolution is comparable to a measured spectrum.

In scintillator spectrometry systems a spectrum is broadened due to multiple processes between the initial energy deposition and the final signal from the photomultiplier tube, PMT. The processes can be divided into five major parts (Valentine 1998): 1) production of scintillation photons; 2) the scintillation photons are collected at the PMT photocathode; 3) production of photoelectrons; 4) the photoelectrons are collected at the first dynode in the PMT; and 5) multiplication in the

PMT. Breitenberger (1955) has given a statistical description of the spectrum broadening in scintillator spectrometers, equation 1, using a theoretical model where the steps 2-4 are combined into a single transfer function. The relative variance V of the number of electrons Q to arrive at the PMT anode is given by

$$V_Q = V_T + \frac{1+V_M}{\overline{X}\,\overline{T}} \tag{1}$$

Each index indicates the quantity that contributes to the variance: X is the number of photons, M the multiplication including after-effects in the PMT and T the probability for one photocathode electron to reach the first dynode in the PMT per scintillation photon. The number of scintillation photons/MeV is known for NE 102A and V_M should, according to Breitenberger, be considered an instrumental parameter that is adjusted for each individual case. To determine T for the plastic scintillators is still a work in progress and investigated in this work are the effects on spectrum broadening due to nonlinear light yield and loss of scintillation photons, for example by light absorption in the scintillation material.

To convert the calculated deposited energy into emitted light the following relation first proposed by Birks (1964) was used

$$dL/dr = S(dE/dr)(1+kB(dE/dr))^{-1} \Leftrightarrow dL/dE = S(1+kB(dE/dr))^{-1} \tag{2}$$

where r is the range in the scintillator expressed in g cm^{-2}, dL/dr the specific fluorescence, S the absolute scintillation efficiency, dE/dr the specific energy loss, kB a constant expressed in mg cm^{-2} MeV^{-1}, and dL/dE the emitted fluorescent light per unit deposited energy. Birk's equation accounts for nonlinear light yield.

The code used was MCNPX 2.60, Monte Carlo N-Particle eXtended. The calculated energy depositions spectra are scored with MCNPX's f8 tally; it is possible to use a Gaussian energy broadening, GEB, function together with the f8 tally. However, since the broadening process consists of several steps, each with its own probability and variance, which are not necessarily Gaussian, the ambition is to use Breitenberger's equation instead of the GEB function.

Material and methods

The WBC consists of four large plastic scintillators made of NE 102A (NE 102A is equivalent to BC-400) each measuring 91.5 × 76.0 × 24.5 cm^3. Each detector is equipped with two PMTs (EMI 9545A) mounted on a perspex light guide and the stainless steel detector housing has a 0.397 mm copper window. The signal from the photomultiplier tubes are amplified (Canberra Amplifier 816A) and the output fed to an Ortec pulse-height analyser (Ortec ASPEC-927). Fig. 1 shows the detector configuration.

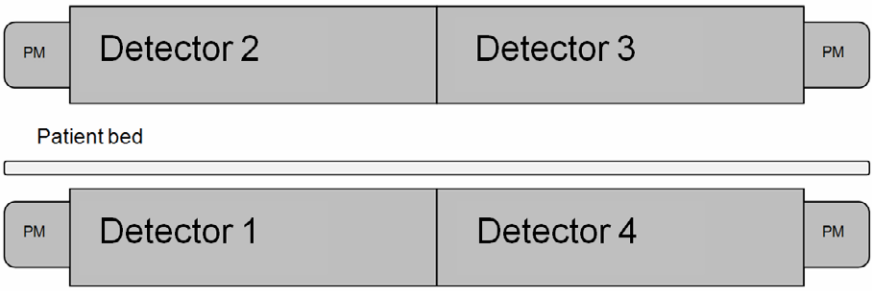

Fig. 1. Two detectors above and two below the patient bed gives, roughly, a 3π geometry. PM stands for photomultiplier tube. Medial direction: along the patient bed, -100 to 100 cm; lateral direction: across patient bed, -40 to 40 cm.

The Monte Carlo model of the WBC included the scintillation material, detector housing with Cu window, light guides, patient bed and a 3 mm lead wall coating of the surrounding steel chamber. Adding more wall or floor material gave a very little difference in total efficiency and it was therefore excluded in the model.

Four button sources were used: ^{137}Cs, ^{54}Mn, ^{65}Zn and ^{60}Co; only the result for ^{54}Mn is presented here.

Total efficiency

The total efficiency was measured and simulated for the source placed along the axis of symmetry in medial and lateral direction with 10 cm intervals. Medial direction: along the patient bed; lateral direction: across patient bed. The total number of counts was compared to the calculated number of counts scored with the f8 tally.

Spectrum broadening

The calculated deposited energy in MeV was converted into MeVee (MeV electron equivalent, a deposited energy of 1 MeV generates 1 MeVee in light output at linear light yield). This was done using the MCNPX's pulse height light tally, PHL. When using PHL, *dL/dE* for all energies has to be stated in the MCNPX input file. *dL/dE* was calculated with equation 2, where *S* was set to 3.0 (Mukhopadhyaya 2004); *dE/dr* was calculated with ESTAR (NIST 2005). For high electron energies the response is linear for NE 102A (Saint-Gobain Crystals 2005) and *kB* was changed until the ^{54}Mn photo absorption energy peak at 0.835 MeV lead to a photo absorption emitted light peak at 0.835 MeVee.

To investigate how light losses, depending on energy deposition site, affected the emitted light spectrum, each detector material cell in the MCNPX model was divided in medial direction into 9 smaller cells, all with the same material properties but with a different *dL/dE* depending on the distance from the light guide. The emitted light per particle track was scored with the f8 tally, and when used together with PHL, f8 sums the emitted light per particle track in MeVee from all 9 cells. Light absorption or light leaving the detector material was represented by multiplying *dL/dE* with a factor A_i (i=1:9; $A_i \leq 1$). A was calculated with the equation $A_i = -Cx_i + 1$ where C is a constant and x_i the distance from the light guide to the middle of each of the 9 detector cells. However, this it is not necessarily considered an accurate description of the detector

material. The value for C was changed in steps of 0.0005 from 0.0005 to 0.0025, for the box furthest away from the light guide A_9 varied from 0.956 to 0.778.

Results

Total efficiency

In fig. 2 and 3 the medial and lateral total efficiencies for ^{54}Mn are showed for detector 1. The results show a good agreement between measured and calculated efficiencies except close to the detector edges.

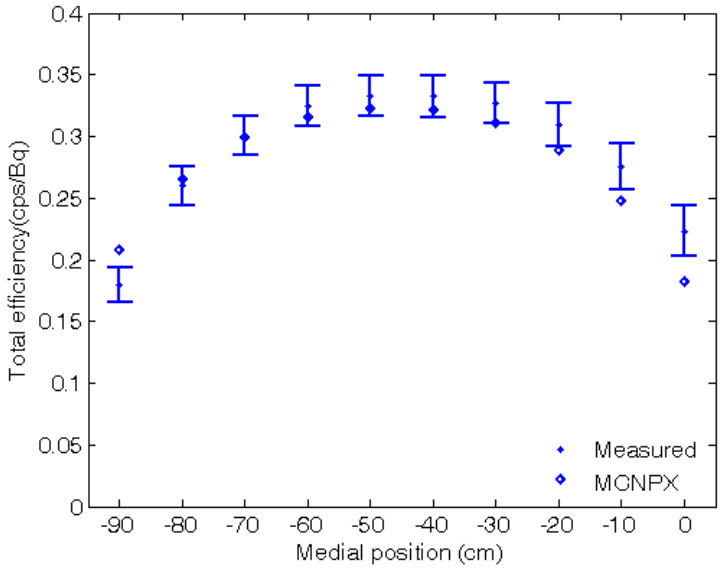

Fig. 2. The total efficiencies for ^{54}Mn placed at different positions along the medial direction. Lateral position was 0 cm in all measurements.

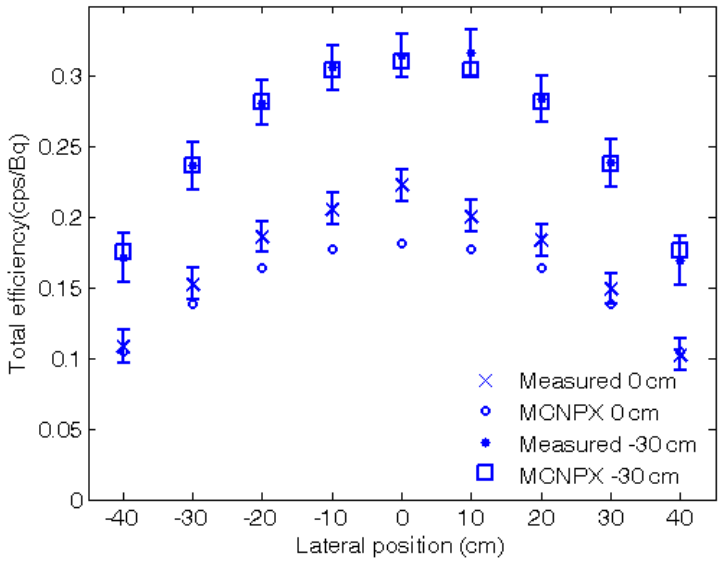

Fig. 3. The total efficiencies for ^{54}Mn placed at different positions along the lateral direction. Medial position was 0 and -30 cm, respectively.

Spectrum broadening

For kB=9.65 mg cm^{-2} MeV^{-1} the photo absorption energy peak at 0.835 MeV lead to a photo absorption emitted light peak at 0.835 MeVee, for lower energies small differences were noticed between linear and nonlinear light yield.

For detector 1, the deposited energy spectrum, and thereby also the emitted light spectra for all A_i=1, were nearly identical when the source was placed at -30 and -60 cm in medial direction, lateral position 0 cm. Fig. 4 and 5 show the emitted light spectrum for both positions for all Ai<1. In fig. 4 C=0.0005 and in fig. 5 C=0.0025. It is obvious that even for a small assumed absorption the emitted light spectra differs for the two source positions and the photon absorption emitted light peaks are shifted.

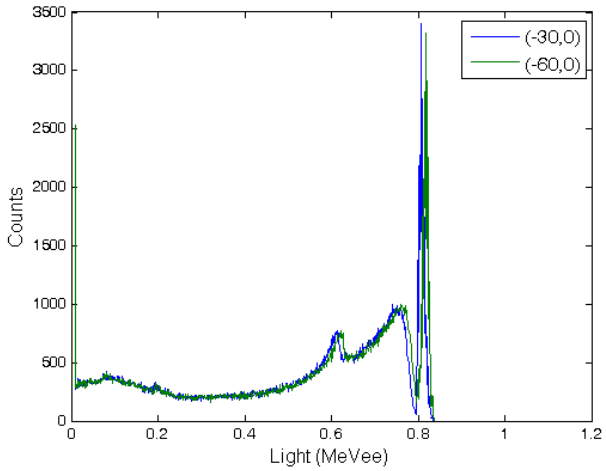

Fig. 4. The blue and green spectra show the emitted light in MeVee for ^{54}Mn placed at -30 respectively -60 cm in medial direction, lateral 0 cm for both. *C*=0.0005 and *A*=0.956 for the detector cell furthest away from the light guide, i.e. a small light loss.

The multiple peaks for C=0.0025 is due to the relative large differences in A between the 9 detector cells. If there was a continuing decrease of A the spectrum would most likely be more smeared without narrow peaks.

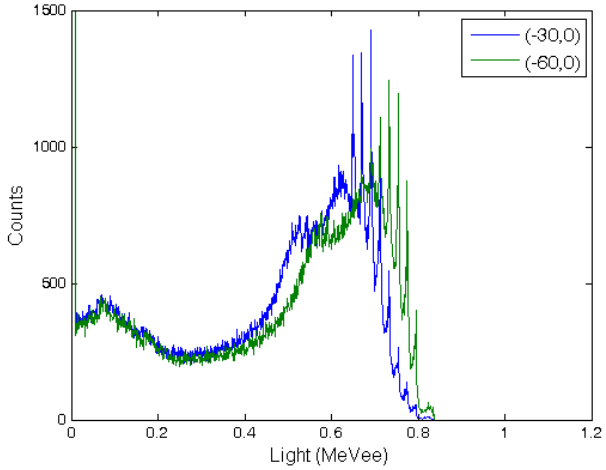

Fig. 5. The blue and green spectra show the emitted light in MeVee for ^{54}Mn placed at -30 respectively -60 cm in medial direction, lateral 0 cm for both. *C*=0.0025 and *A*=0.778 for the cell furthest away from the light guide, i.e. a rather high light loss.

Discussion

The comparison between calculated and total efficiency showed a good agreement for most source positions. Close to the detector edges the accuracy of the source position is quite important, and some deviations between measured and calculated efficiencies could be caused by a difference in stated and actual distance between detector housing and scintillation material. Also, when the source was placed at medial positions, it was assumed that the displacement was only in the medial direction when calculating the uncertainties, and vice versa for the lateral positions. Further analyses of the data results will give larger uncertainties and the calculated results might then be within the measured uncertainties limits.

Birk's constant *kB* was determined to be 9.65 mg cm^{-2} MeV^{-1}, for which there is a nonlinear response for energies below the photo absorption emitted light peak. But, there are other formulas describing the nonlinear light yield and it is also possible to use a linear response for all energies, the question is: what is most accurate? Birk's formula might not be the most accurate description, but it was easy to use together with the PHL tally, and for a detector described in this work the eventual nonlinear effects on spectrum broadening will most likely disappear in other more dominating broadening effects such as multiplication in the PMTs. Even if it is barely noticeable, the results does not imply that any formula would do, but it ought to be acceptable to use Birk's formula as long as one is aware of the assumptions that lie behind equation 2, which is carefully described by Birks (1964).

The results for different *A*, trying to mimic light absorption and light leaving the detector material, show that even for a small light loss the spectrum will be affected. For such large detectors as in this case it seems unlikely that light losses cannot be ignored and must be determined more exactly if an accurate spectrum broadening function is to be made. If so, a better representation of light losses must be done, the method described here gave crude results and how *A* is to be calculated must relate to the physical properties of the material. The attenuation length for NE 102A is 250 cm (Saint-Gobain 2005). The attenuation is described with Beer's law, but the conditions in the plastic scintillators, where light can be reflected, differs from the conditions described in Beer's law where incoming light is assumed to be parallel and attenuation is defined as light absorbed or scattered out of a narrow beam. This suggests that the absorption length would be longer than 250 cm, but how long and if the absorption increases linearly with length is not known. One possibility would be to do a Monte Carlo calculation of the light's path inside the detector material, but then one must know the reflecting index for the material surrounding the plastic scintillators and how long a particle track should be followed. The results show that the light losses are important, but at this moment it is yet to be determined how it should be modelled. The PHL tally has the advantage of being relatively easy and straight forward to use, and once the relationship between light losses and absorption site is more known, it ought to be possible to use the PHL tally to account for it.

Conclusion

Monte Carlo calculated total efficiencies correspond well with measured for several source positions relative to the detector. The effects of light losses are noticed in emitted light spectrum resolution, and for large detectors this ought to be properly accounted for when doing a spectrum broadening.

References

Birks J.B. The theory and practice of scintillation counting. London: Pergamon Press; 1964.

Breitenberger E. Scintillation spectrometer statistics. Prog in Nuc. Phys. Vol. 4; 1955. p 56-94.

Mukhopadhyaya S. Plastic gamma sensors: an application in detection of radioisotopes, Proc. SPIE Annual Meeting. 2003 August 3-8; San Diego, CA, US. Vol. 5198, p 62-72; 2004

NIST- National Institute of Standards and Technology, U.S. Department of Commerce. ESTAR-Stopping Power and Range Tables for Electrons. http: //physics.nist.gov/ PhysRefData/Star/Text/contents.html. Online: October 1998, last updates: August 2005

Saint-Gobain Crystals. Scintillation Products. Organic Scintillators Brochure; 2005.

Valentine J.D. The light yield nonproportionality component of scintillator energy resolution. IEEE Trans. Nucl. Sci. Vol 45 (3); 1998

Examination of patients using the whole body gamma ray counter that is calibrated according to the individual anatomy properties

Yatsenko, V. N.; Borisov, N. M.; Korzinkin, M. B.
Burnasyan Federal Medical Biophysical Center, Moscow, RUSSIA

Abstract

Recently G.H. Kramer, K. Capello and E. Cardenas-Mendez [1] concluded that "whole body counters can now be calibrated more accurately using voxel phantoms, but the improvement is not as great as one might expect".

However, we have a slightly different view on the usefulness of voxel phantoms during the whole body counter-assisted examination of patients. Although the merits of voxel phantoms during calibration of whole body counters using the standard voxel phantoms are really not very significant, during the examination of patients the properties of individual anatomy can introduce considerable corrections into the whole body counting efficiencies (for low-energy gamma emitters, it may lead to the 2-fold increase/decrease of the assessed activity).

As an example, we performed whole body counter calibration and examination of patients, using both standard plastic phantom (developed by the Livermore laboratory, USA) and voxel phantom method (using the OEDIPE software developed at IRSN, France, and the well-known Monte Carlo code MCNP [2]). During our studies, we obtained the correction factors that are needed for the transition from the Livermore plastic phantom to the individual voxel phantom.

Introduction

Monitoring of internal radiation exposure for involved workers is one of the most actual problems in radiation hygiene of nuclear industry. Usually, the routine monitoring is performed using the so-called whole body and organ counters (WBC), i.e. generally semiconductor, more rarely scintillation gamma spectrometers that register the gamma rays, which are emitted by the incorporated radionuclides. In vivo monitoring data are especially important to make solutions on the medical measures that are to be taken in case of accidental radionuclide contamination of the nuclear workers. Modern in vivo counters possess high counting efficiencies for gamma rays through wide energy range, and provide high resolution in terms of absorbed energy values. However, they require the calibration procedure, i.e. determination of spectrometer counting efficiency (in other words, a relational factor between activities of incorporated radionuclides and counting intensities in the pulse-height-spectra of the gamma spectrometers).

The most biologically significant incorporated radionuclides (like ^{239}Pu and ^{241}Am) emit low-energy (13-60 keV) gamma rays. As a result, determination of WBC counting efficiencies is hampered due to intensive absorption and scattering of radiation in the patient's body. To circumvent these obstacles, one could use mathematical simulation (particularly Monte Carlo method as almost the only valid calculation method for such a purpose) rather than measurement of reference phantoms. However, such calculations require an adequate model of the patient's anatomy. This anatomy model could be described in terms of small rectangular boxes (voxels) with certain density and chemical composition.

Material and methods

The OEDIPE software

To provide the adequacy of mathematical simulation regarding to the physical measurements, the voxel representation of the patient's anatomy is retrieved from the x-ray computed tomography (CT) or magnetic resonance imaging (MRI) data. The software OEDIPE has been developed for creation of voxel phantoms of individual patients to conduct MCNP calculations. MCNP is a general-purpose Monte Carlo code, which performs transport calculations for gamma rays, neutrons and electrons in wide energy range. MCNP describes the transport geometry in terms of first- and second-order surfaces, as well as toroidal surfaces, thus enabling voxel representation of the patient's anatomy.

The MCNP input data file is automatically written by the OEDIPE interface. It contains the information on the patient's body in voxel representation, source characteristics, detector materials and geometry (described in terms of standard surfaces rather than voxels), the tally of interest (pulse-height-spectrum of the detector or dose distribution inside the body). To accelerate the calculations, the neighbor voxels with the same density and chemical composition are coupled into larger rectangular boxes using the maximal rectangular area technique. To visualize the transport geometry written in the MCNP input data file, the Sabrina software is used.

Whole body counting lab at FMBC

At the Burnasyan Federal Medical Biophysical Center (FMBC, Moscow, Russia), four Canberra germanium WBCs are placed into a shielded canyon, which shielding is made of exceptionally old steel. This steel was produced in 1930s, i.e. before the nuclear weapon tests had begun. Thus, this special shielding, which does not contain the artificial radionuclides, provides low radiation background inside the canyon. Moreover, the air inside the canyon is being ventilated during the in vivo examination, thus decreasing the radon activity, and creating the exceptionally low background intensity.

The preliminary test of the experimental equipment, measurement technique and voxel phantom-assisted calibration of whole body counters was done by whole body counting of plastic torso phantom developed by Livermore National Lab. ^{241}Am was to be measured using the Canberra whole body counters. This radionuclide is usually incorporated together with other actinides in the lungs of nuclear workers; it has the relatively high (59.54 keV) energy of major portion of emitted gamma rays. During the

measurements, perforated lungs of the Livermore phantom contained 27 capsules with ^{241}Am of 3165 Bq total activity. Measurements were conducted by two spectrometers placed at the "chest" of the phantom in from of right and left lung.

Using these WBC devices, we examined exam three patients of the FMBC clinic (see Fig.1). Case histories of all patients (retired employees of Seversk Chemical Plant (Seversk town, Tomsk region) indicate to both inhalation (under routine operations) and wound intake (puncture wounds of hands during industrial operations) of non-soluble actinides, including ^{241}Am compounds in 1960-ties. Within long period of time, patients were regularly examined (natural excreta analysis, whole body counting) and treated (intravenous administration of Ca-DTPA (Pentacin), soft tissue dissection in the wound site) in medical facilities of FMBA of Russia (former 3rd Major Department of the USSR Ministry of Health).

To obtain the voxel phantoms of the patients as well as the Livermore plastic mannequin, we scanned the ex-workers and the Livermore phantom using the Toshiba Aquillion CT machine.

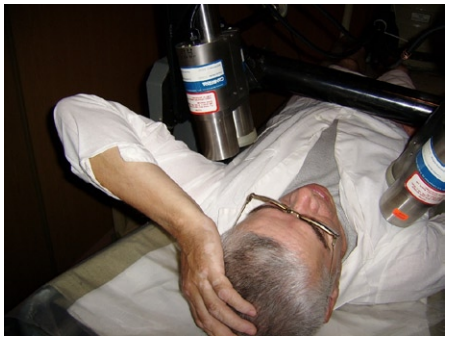

Fig. 1. Lung examination in patients at FMBC clinic.

Results and Discussion

Experiments with the Livermore plastic phantoms

The Livermore phantom counting conditions were simulated using the MCNP software in voxel geometry (256x256x51 voxel resolution) that was retrieved using the OEDIPE software from the CT images obtained at the Burnaysan FMBC clinic. Fig. 2 provides results of OEDIPE software calculations: separation of major organs in the phantom image (panel a) and radiation transfer geometry record in the input data file of MCNP code (panel b). MCNP calculations for plastic phantom have used the source term as multiple points; the point positions were determined by the capsule places in the CT images of the phantom.

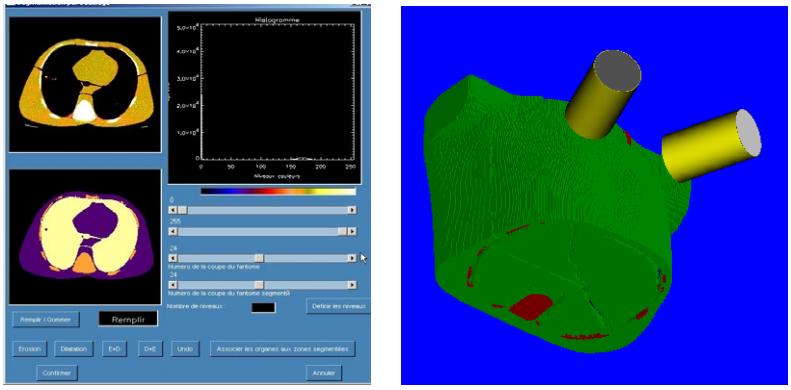

Fig. 2. The Livermore phantom CT images processing for WBC calibration. Panel a: separation of organs and tissues applying OEDIPE software. Left upper window: initial CT image and segmented image below (colors are related to the tissue types); right upper window: spectrum of initial image according to the pixel brightness. Panel b: radiation transfer visualization with Sabrina software, which was recorded by OEDIPE software as the input data file for MCNP calculations. The color corresponds to the type of the tissue or substance. Number of voxels: 256×256×51.

The experimental and calculated spectra of whole body counter detectors placed in front of left (panel a) and right (panel b) lung of the phantom are shown by Fig. 3. Table 1 contains data on recalculation factor between the intensity of the photo peak (59.54 keV) and the total activity of ^{241}Am for right and left detector twins. Calculations did not use either counting efficiency correction versus the absorbed energy or spectrum standardization, so the calculated values of Fig. 2 and Table 1 are absolute ones rather than relative ones. The average quadratic deviation in the maximum pulse counting channel for calculated spectrum is about 6% for 1 million histories of random tests, which requires about 20 minutes of calculation time at personal computer (3 GHz, 512 Mb RAM).

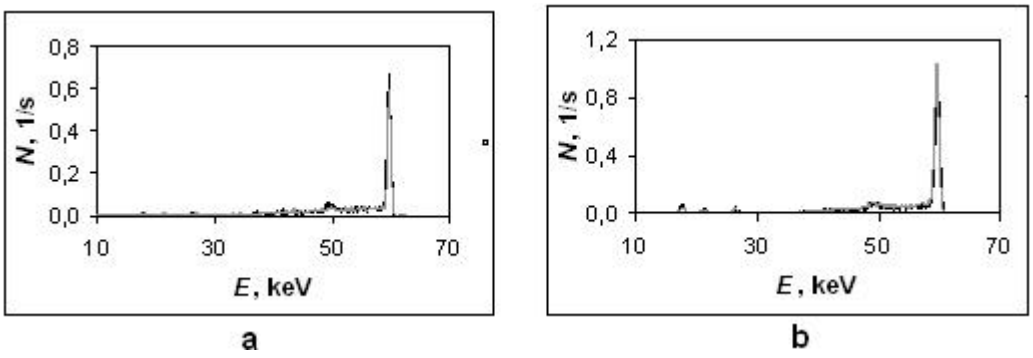

Fig. 3. Experimental (light colored) and calculated (dark colored) spectra of the left (panel a) and right (panel b) counting of ^{241}Am gamma radiation for lungs of Livermore National Lab plastic phantom.

Table 1. Experimental and calculated factors for recalculation of the photo peak (59,54 keV) intensity and the total activity of ^{241}Am for Livermore phantom and detectors placed in front of left and right lung.

Detector	Calculation (*C*), $s^{-1}\cdot kBq^{-1}$	Experiment (*E*), $s^{-1}\cdot kBq^{-1}$	Difference $D = (C-E)/C*100\%$
Left	0.85	0.78	+9
Right	1.41	1.55	-6

The comparison of calculation/measurement demonstrates that calculations have 10% and better accuracy to reproduce absorbed energy spectrum of Canberra Industries detectors both in the photo peak and in the Compton scattering range.

Examination of retired nuclear workers

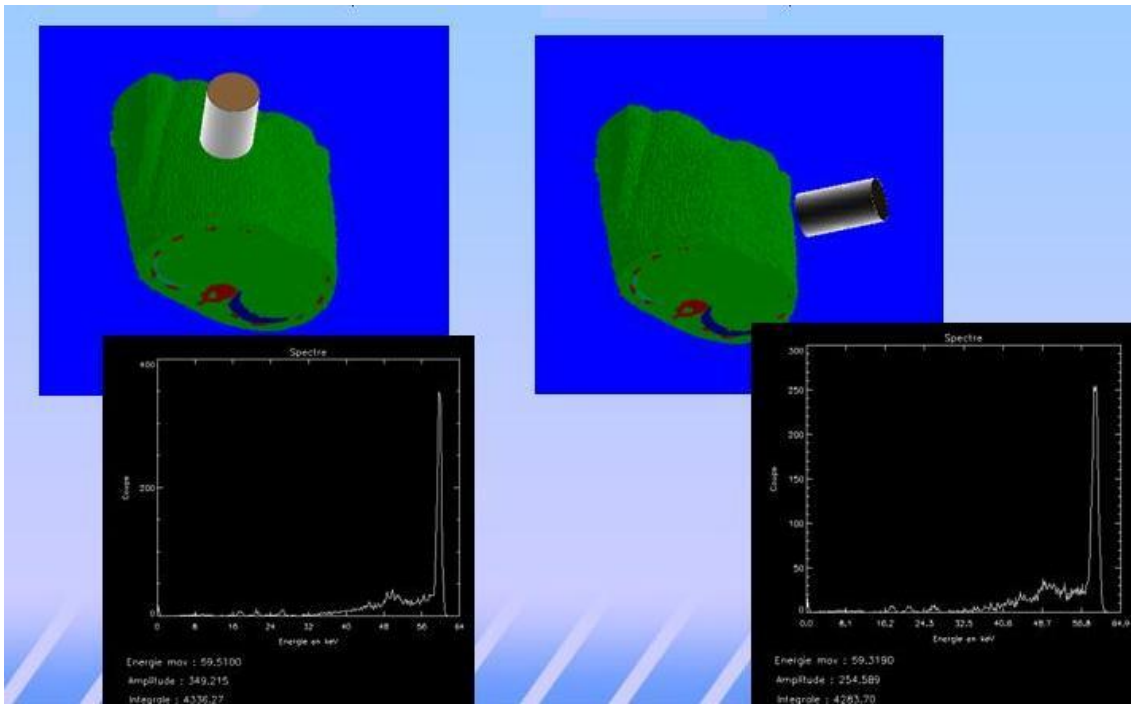

Fig. 4. ŒDIPE computer code application to assess re-calculation factors for counts in the spectrometry channels into ^{241}Am incorporated activity for one of retired employee of atomic industry. In the top: MCNP phantoms (Sabrina software applied for visualization). In the bottom: absorbed energy spectra calculated according to MCNP computer code for homogeneous lung distribution of ^{241}Am of one unit of activity (ŒDIPE software applied for visualization).

To determine ^{241}Am calibration factors in different spectrometry channels, ŒDIPE software was used basing upon CT chest images of patients (256x256pixel resolution for each slice) to create their MCNP voxel phantoms (Fig. 4, on the top). When preparing MCNP phantoms, the incorporated radionuclide distribution was adopted to be homogeneous in each lung.

Applying MCNP4c2 computer code, absorbed energy spectra were calculated for each of detectors placed in front of left and right lung of each patient; the homogeneously distributed ^{241}Am source of one unit of the activity was adopted. The photopeak intensity corresponding to the energy of major portion of photons emitted by ^{241}Am (59.54 keV) has provided the assessment of re-calculation factors.

Experimental calibration factors were determined by Livermore phantom measurement and set of ^{241}Am point sources placed in the "lungs" of phantom. ^{241}Am and ^{239}Pu measurement results are given by Table 2 for patients.

Table 2. ^{241}Am and ^{239}Pu measurement results for patients

Patient	Patient B.		Patient S.		Patient O.	
Lung	left	right	left	right	left	right
Full absorption peak intensity at 59,56 кэВ (N), c^{-1}	10,3	1,8	< 0, 1	0,80	0,43	1,25
Individual (OEDIPE+MCNP) assessment of ^{241}Am lung burden, ($A_C = N/K_C$), кБк	5,1	0,90	< 0, 04	0,31	0,39	0,95
Assessment of ^{241}Am lung burden using the Livermore calibration phantom, ($A_L = N/K_L$), кБк	6,9	0,6	< 0, 07	0,26	0,28	0,40
Relative error in lung burden assessment of ^{241}Am activity, $\eta = (AC - AL)/AC \cdot 100\%$	-35%	+33%	-75%	+16%	+28%	+57%
Correction factor $K_u=A_L/A_C$	1,35	0,67	1,75	0,84	0,72	0,42

The current value of radionuclide burden is proportional to the current value of the internal exposure dose rate. Concerning the internal exposure dose accumulated within long period of time since the examination and, moreover, concerning the

retrospective internal exposure dose assessment, such values depend on biokinetics parameters of incorporated actinides, which are subjected to the significant individual variability as well as depend on medical measures accelerating radionuclide body excretion.

Besides, neither the exact portions of different intake pathways, nor the initial isotope composition of the intake are not known well. Large number of unknown factors affecting the internal exposure accumulated dose makes its assessment very approximate. To increase the accuracy and reliability of accumulated dose assessment, it is convenient to elaborate the periodical monitoring of radionuclide burdens in different organs and tissues of the patient.

Conclusions

1. The developed computational and experimental method for internal exposure monitoring was implemented for whole body counting of incorporated actinide patients.
2. The original technique for incorporated radionuclide in vivo measurement is elaborated, which not only increases the measurement accuracy significantly (with excluding the error component related to the incompliance of plastic phantom structure to the individual patient's anatomy) but also provides the uncertainty assessment of routine measurement technique based on plastic phantom calibration for WBC measurement result interpretation.
3. ŒDIPE computer code also provides the internal exposure dose distribution, which finding was tested, when solving industrial hygiene task (radioactive contaminated wound assessment).
4. The application of radiometric monitoring combined with Monte Carlo computational method as the long term program for persons involved in the internal exposure accident victims would significantly increase the reliability of in vivo monitoring of incorporated radionuclides and assessments of cumulated doses of internal exposure.

References

1. G.H. Kramer, K Capello and E. Cardenas-Mendez "Voxel Phantoms: NORMAN vs. VIP-Man, What Differences Are There?", Supplement to Health Physics vol. 96, No.2
2. Brown F. B. MCNP 5.0 // The Monte Carlo Method: Versatility Unbounded in a Dynamic Computing World / American Nuclear Society. Chattanooga, TN, 2005.

An extrapolation ionization chamber for α-ray detection and measurement

Bercea, Sorin; Cenusa, Constantin; Celarel, Aurelia;
Sahagia, Maria; Stochioiu, Ana; Ivan, Constantin
"Horia Hulubei" National Institute of R&D for Physics and Nuclear Engineering,
Bucharest, ROMANIA

Abstract

The extrapolation ionization chamber is a special type of the cavity ionization chamber, developed by Böhm (Böhm, 1983) for the absolute measurement of the absorbed dose rate in β-ray beams. The cavity theory was first created for the absorbed dose measurement in photon radiation, but it was also created for charged particles. In the radiation metrology laboratory from IFIN-HH we built such an extrapolation chamber for β-ray, but we tried to find how it would work when irradiated with α-ray.

Firstly, we obtained the experimental curves of the ionization current versus the polarizing voltage, *U*, the former have quite a net saturation region. Then, we measured the saturation current of the chamber for different values of the distance between the electrodes (i.e. different values of the sensitive volume of the chamber). When we represented the graph of the ionization (saturation) current against the distance between the chamber's electrodes, we noticed that this curve is quite analogous to the same curve obtained for β-ray irradiation.

So, by analogy, we concluded that for this chamber, the main requirements of the cavity theory are also fulfilled when the chamber is irradiated with α-ray.

This paper presents the results of the measurements concerning the *I=I(U)* and *I=I(x)* characteristic curves of the extrapolation chamber when it is irradiated with α-ray from a Pu-239 radioactive source. Some concluding remarks are also included, concerning the possibility of developing an absolute method for the measuring the absorbed dose for α-ray, based on the cavity theory.

Introduction

The detection and measurement of α-rays are procedures that repeat the general requirements that are imposed to ionizing radiations. In the same time, they must take notice of the characteristics of this type of radiations.α-rays are He nuclei (and therefore have a big rest mass- He^4_2 and (2+) electrical charge) that undergo Coulombian interactions which make them release energy quickly into the medium they pass through. It is for this reason that the path of the α-rays in various mediums is considerably smaller (for example 3.75 cm through air). In solid mediums, α-rays have

much smaller paths and are completely absorbed in depths of tens or hundreds of microns.

The properties mentioned above impose that specific methods are elaborated and adequate detectors are designed. One of the methods for the detection and measurement of ionizing radiation is the ionometric method, which is based on the collecting and measuring of the electrical charges produced by ionization inside the gas from the sensitive volume of the detector.

As far as α-rays are concerned, it is necessary that the detector (for example an ionization chamber) have a sufficiently thin window that permits the passing of particles without significant loss of energy; hence, the particles that reach the sensitive volume can produce a sufficient number of ionizations. The ionizations lead to the outcome of an electrical signal that can be measured with adequate precision at the output of the detector.

Initially, the cavity theory, which correlates the generation of ionization electrical charges inside the gas from a cavity, with the energy released in the material surrounding the cavity, was elaborated for photon radiation. Further on the theory was adapted also for radiations made of particles with rest mass and electrical charge Trott (Trott, 1966).

The most complex elaboration of the cavity theory for β-particles was presented by Böhm (Böhm, 1983) he also designed an ionization cavity-chamber with variable volume (the extrapolation chamber). The latter is destined to measure the absolute value of the released energy (meaning the absorbed dose) in a particular medium for the β-radiation.

Material and methods

This type of ionization chamber (extrapolation chamber) was also put into practice by the Radiation Metrology, Testing and Dosimetry Team (CMRID) of the Horia Hulubei National Institute for R&D in Physics and Nuclear Engineering, IFIN-HH.

Description of the ionization (extrapolation) chamber built by IFIN-HH

The ionization chamber has a cylinder shape with plane-parallel electrodes Fig. 1. The voltage electrode (polarization electrode) is made up of an electroconductory layer (an aluminium layer with a thickness of a few microns), which is placed on one of the sides of a very thin sheet of Mylar (70 mg/cm^2); this electrode is also the input window of the detector. The collector electrode is made up of a graphite layer placed on a polystyrene block. This graphite layer is electrically isolated from the guard electrode (guard ring). The latter consists of a circular layer of graphite. The guard ring is connected to the detector's ground and is designed to define the sensitive volume of the detector from an electrical point of view.

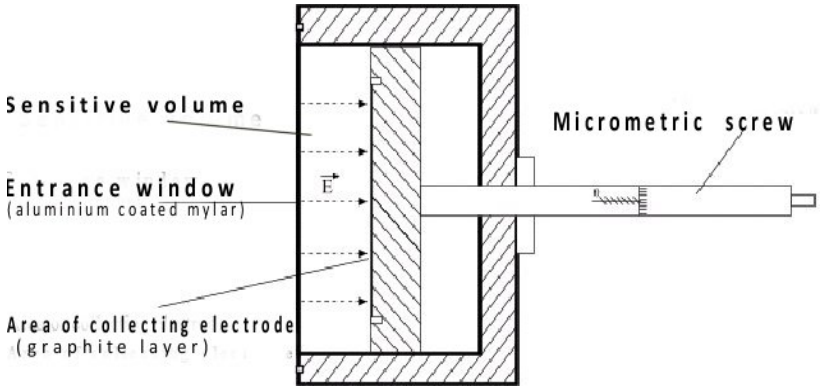

Fig. 1. Schematic view of the extrapolation chamber.

The sensitive volume of the detector can be modified mechanically by varying the distance between the polarization electrode and the collector electrode with a micrometric screw, in the range of 5-16 mm. In Fig. 2 we present the shape and size of the electrodes.

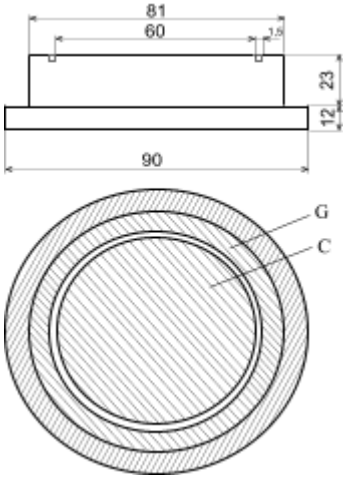

C – collecting aria, G – guard ring electrode

Fig. 2. The shape and size of the electrodes of the extrapolation chamber.

In figure 3 we present the electrical circuit used for measuring the ionization charge (or current) of the ionization chamber, Bercea et al (Bercea et al. 2008a, Bercea et al. 2008b).

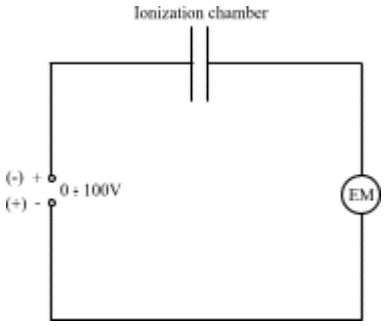

EM - electrometer

Fig. 3. The electrical circuit for measuring the ionization charge / current.

The experiment

As we have shown in our introduction, in order to calculate the rate of the absorbed dose, $\dot{D}_\alpha$, we use the relationship (1). This includes the slope of the curve ionization current versus distance $I=I(x)$, $\left(\frac{\partial I}{\partial x}\right)$, in the range where it is linear. This is extrapolated for $x\to 0$, meaning where the perturbator effect on the radiation that interacts with the solid medium that surrounds the cavity filled with gas (air) disappears.

$$\dot{D}_\alpha = K\frac{W}{eS\rho}\left(\frac{\partial I}{\partial x}\right)_{x\to 0} \qquad (1)$$

K - constant which takes in to account the units of measure
W - the average energy required to produce the air ionization
e - the elementary electric charge
S - the aria of the collecting electrode
ρ - the air density in the sensitive volume of the ionization chamber

In order to see to what extent the ionization chamber made by IFIN-HH acts according to the cavity theory, which refers to α-radiation, the following experiments were made.

The experimental drawing of the curves ionization current versus polarization voltage, $I=I(U)$, for a given source of α-radiations in a well-defined geometry. The geometry corresponded to the various distances between the polarization electrode and the collector electrode, x, and also the detecting of the range of values of the polarization voltage, values within which the detector is functional.

Choosing a value for the polarization voltage that lies within the saturation range for all the values of the distance between the electrodes, x, the graphical representation of the curve that gives the ionization current I versus the distance between the electrodes of the chamber, is determined experimentally.

Results

The measurement of the ionization current

The ionization current generated by the detector was measured in the presence of a source of α-rays, in a fixed irradiation geometry. The α-ray source used in this case was a Pu^{239} source having the following characteristics:

– -extended, circular source with a diameter of 120 mm;
– -emission rate: ε= 13 601 α/s in 2πsr.

The source was positioned with the aid of a special support ring placed at a distance of 2 mm from the surface of the window of the ionization chamber.

The ionization current was measured with a Keithley 617 electrometer.

The arrangement used for measuring the ionization chamber is given in Fig. 4.

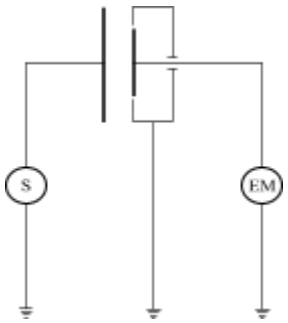

S – voltage source; EM - electrometer

Fig. 4. The experimental arrangement for measuring the ionization current.

Considering the order of magnitude of the ionization current (about 1 pA) during the measurements, certain precautions had to be made, in order to reduce the influence of the working conditions on the results of the measurement. Thus, in the working chamber, the temperature was held constant (20 ± 2º C); any actions that may cause powerful noises or vibrations were avoided, as well as the movement of people in the proximity of the measurement stand (less than 1.5 meters from the stand).

Before installing the radioactive source on the stand, we measured the current of the ionization chamber for the value "0" of the polarization voltage. The value we obtained in this case was $\pm 5.6 \times 10^{-15}$A. After installing the Pu^{239} source on the stand, we waited 2 hours before starting the measurements.

The first important observation was that for $U = 0$ in the presence of the radioactive source, the ionization chamber presented a positive current , whose values depended on the value of the distance between the electrodes of the chamber (Table 1). A first assumption is that it could be due to the alpha particles reaching the collecting electrode, in absence of any polarization.

Table 1. The values of the ionization current (I) for 3 values of the air gap, for $U = 0$.

x (mm)	I (A)
5	$1.0074 \cdot 10^{-12}$
7	$1.960 \cdot 10^{-12}$
9	$0.2388 \cdot 10^{-12}$

For the three values chosen for the distance between the electrodes, x, we experimentally obtained the characteristic curves I=I(U). The results we obtained are presented in Fig. 5.

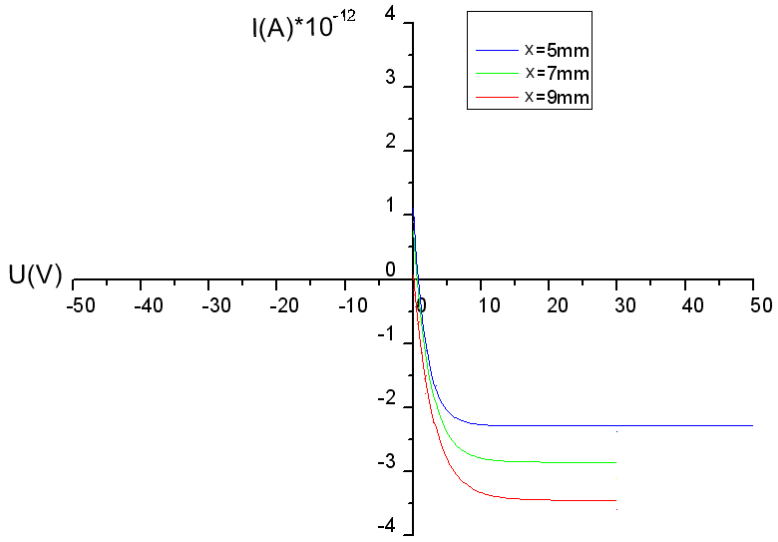

Fig. 5. The I=I(U) curves for three values of x.

For the value of the polarization tension U=15 V situated in the saturation region of the $I = I(U)$ curve we made measurements of the ionization current and we also obtained the curve that expresses the ionizing current versus the distance between the electrodes (the gap depths), x, respectively the volume of the chamber (V), considering the fact that $V = S*x$, and the surface of the collector electrode S = constant.

The results obtained are presented in table 2 and the curve that resulted is presented in Fig. 6.

Table 2. The ionization current corresponding value of the gap depth (*x*).

x (mm)	I*10^{-12} (A)
1	0.48
1.5	0.7
2	1
2.5	1.22
3	1.52
3.5	1.7
4	2
4.5	2.3
5	2.4
5.5	2.5

x (mm)	I*10^{-12} (A)
6	2.8
6.5	3
7	3.1
7.5	3.2
8	3.4
8.5	3.6
9	3.8
9.5	4
10	4.2
10.5	4.3

x (mm)	I*10^{-12} (A)
11	4.4
11.5	4.5
12	4.5
12.5	4.5
13	4.5
13.5	4.5
14	4.5
14.5	4.5
15	4.5

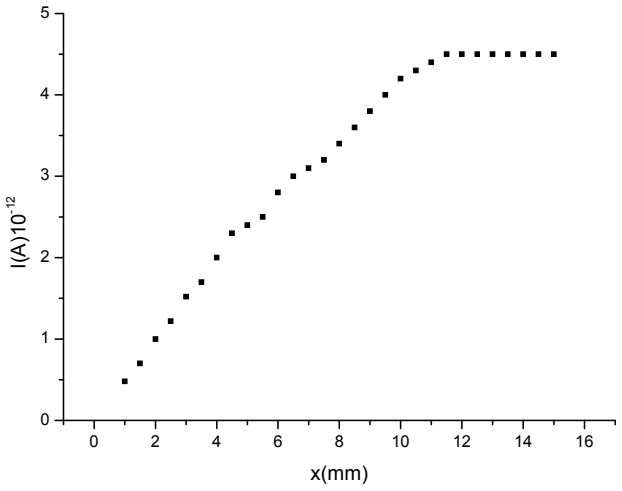

Fig. 6. The *I = I(x)* characteristic curve.

Discussion

The analysis of the results obtained regarding the *I=I(U)* characteristic of the ionization chamber, in the presence of a α-radiation field, as above presented Fig. 5, leads to the conclusion that in the presence of these radiations, the detector has a typical behaviour. The ionization current reaches the saturation value fairly quickly for all the possible values of the distance between the electrodes.

In saturation conditions, we have concluded that the *I = I(x)* curve also has a typical behaviour for this type of detector, respectively, for $x \rightarrow 0$, the ionization current is proportional to the distance between the electrodes, *x*, in the range 0 to 4.5 mm, such as the Figure 6 shows, and thus, with the sensitive volume of the chamber. This behaviour indicates the fact that, in the presence of a α-radiation field, the ionization chamber with a variable volume produced by IFIN-HH has the same behaviour as when irradiated with β-radiations.

Conclusions

The experimental results we obtained, especially the shape of the *I=I(x)* curve, which is linear within the range 0 to 4 .5 mm, and consequently when $x \rightarrow 0$, are an experimental confirmation for the fact that the cavity theory, as presented for the β-radiations /1/, may also be used, in the same experimental configuration, for measuring the absorbed doze in α-radiation fields and beams. All that is left is that further research leads to the identification of all the quantities necessary for obtaining the absorbed doze of α-rays. This relation would connect the absorbed dose rate $\dot{D}_{\alpha}$, to the variation of the ionization current, $\left(\frac{\partial I}{\partial x}\right)$, which would be analogous to the relation for the β ray.

Acknowledgements

The research wich lead to these results was suported by the National Authority for Scientific Research in the Project PN 09 37 02 05.

References

Bercea S., Sahagia M., Celarel A. ,Razdolescu C. Ionizing Radiation Metrology Laboratory from IFIN-HH, Romania Presentation .„Simposio de Metrologia" Santiago de Queretaro, Mexic, 22-24 oct. 2008

Bercea S., Cenusa C., Celarel A., Neacsu, B., Patrascu S. On the electrical parameters of the ion – chamber detector, „1st International Symposium RMO 2008 - Regional Metrology Organizations" Dubrovnik - Cavtat, Croatia, November 12 – 15, 2008

Böhm J .Standardization and Calibration in beta dosimetry – International Beta Dosimetry Symposium Washington, D.C., USA, Febr. 15-17, 1983

Trott N.G. Design and operation of an extrapolation chamber with removable electrodes. Int. J. Appl. Rad. Isotopes, 1966, vol I , pp. 103 - 111